MULTIPHASE PARTICLE-SIZE-GROUPING MODEL OF PRECIPITATION AND ITS APPLICATION TO THERMAL PROCESSING OF MICROALLOYED STEEL

BY

KUN XU

DISSERTATION

Submitted in partial fulfillment of the requirements
for the degree of Doctor of Philosophy in Mechanical Engineering
in the Graduate College of the
University of Illinois at Urbana-Champaign, 2012

Urbana, Illinois

Doctoral Committee:

Professor Brian G. Thomas, Chair and Director of Research
Professor Petros Sofronis
Professor Pascal Bellon
Professor Jian-Min Zuo

ABSTRACT

The formation and presence of second phase precipitates greatly influence the properties of metal alloys, and varies with alloy composition and temperature history. In microalloyed steel, for example, precipitates may lead to beneficial grain refinement or detrimental transverse surface cracks. A comprehensive set of models has been developed to determine precipitate formation during metal processing. They include an equilibrium precipitation model and kinetic models for single-phase and multiphase precipitation, and are applied together with heat transfer, grain growth, and other models to predict precipitation and related microstructural parameters and properties during thermal processing of microalloyed steel.

First, the equilibrium precipitation model predicts the equilibrium concentrations of dissolved elements and precipitated phases as a function of the steel composition and temperature, which is used to provide the supersaturation or driving force for the kinetic model. Next, a kinetic growth model based on population balance and Particle-Size-Grouping (PSG) method gives the volume fraction and size distribution of precipitates evolving with time. The method features geometrically-based thresholds between each size group, reasonable estimates of border values in order to accurately include intra-group and inter-group diffusion, and an efficient implicit solution method to integrate the equations. The kinetic model is generalized to predict multiphase precipitation to incorporate more realistic heterogeneous complex/mixed precipitates. The corresponding population balance and PSG equations are developed, including mutually-exclusive precipitates and mutually-soluble precipitates. From the results, an austenite grain growth model is applied to predict austenite size evolution under the influence of pinning precipitates.

The three models are each extensively validated, including the equilibrium model matching with analytical solutions, the commercial package JMatPro, and experimental measurements of precipitate amounts, types and compositions. The kinetic models are validated by matching with exact solutions of the population balance equations, with each other for special cases, and with experimental measurements of precipitated fraction and size evolution, and a Precipitation-Temperature-Time diagram.

By taking advantage of the temperature, phase-fractions, and segregated-composition histories from previous models, the models developed in this work are finally applied together to

predict precipitate formation and grain growth at different locations during continuous casting of steel slabs for realistic steel grades and casting conditions. The models track the evolution of the amount, composition, and size distribution of precipitates. In addition, austenite grain size, ductility and estimated susceptibility to transverse cracks, are expected to be explained by the microstructure of particle-containing materials in processes. The results are important to control steel grades and cooling practice to assure product quality, and present new insights into precipitate formation and transverse cracks during continuous casting.

In this work, the nucleation, growth and coarsening are modeled as a continuous competing process, and all of the model parameters have physical significance and no fitting parameters are introduced. Although the current work focuses on precipitation in microalloyed steels, if the necessary database is available, the current models can be applied to simulate diffusion-driven precipitation in any materials and processes.

ACKNOWLEDGEMENTS

I would like to express my deep appreciation to my advisor, Prof. Brain G Thomas, for all of his sincere guidance, support and encouragement for this project. It is my fortune to learn a great deal from him both academically and personally. Also thanks to my committee members, Prof. Petros Sofronis, Prof. Pascal Bellon and Prof. Jian-Min Zuo, to offer guidance for my thesis.

The financial support of the member companies of the Continuous Casting Consortium at the University of Illinois at Urbana-Champaign, which includes ABB, Arcelor-Mitta, Baosteel, Corus, Delavan/Goodrich, LWB Refractories, Nucor, Nippon Steel, Postech, Steel Dynamics and Ansys-Fluent, are gratefully acknowledged. I would like to thank Professor John G. Speer and David K. Matlock, and previous graduate student Myra S. Dyer from Colorado School of Mines, Adam J. Shutts from Nucor Steel-Hickman, for their plant experimental measurements and helpful discussion. Thanks to Dr. Don O'Malley at Nucor Steel Decatur, for his help to validate our equilibrium model using JMatPro.

I would also like to thank all graduate students in the Continuous Casting Consortium for their help and discussion in my past graduate years at University of Illinois, including Seid Koric, Hemanth Jasti, Kai Jin, Lance C. Hibbeler, Petrus Bryan, Rowan Matt, Rui Liu, Varun Singh, Xiaoxu Zhou, Yonghui Li *et al*.

Special thanks are given to my parents, who have always believed in me, offered support and love along the way when I grow up.

Thank you for everything,
Kun

TABLE OF CONTENTS

LIST OF FIGURES

LIST OF TABLES

LIST OF ABBREVIATIONS

CSP : Compact Strip Production

EDS : Energy-Dispersive X-ray Spectroscopy

ICP-AES : Induction Coupled Plasma – Atomic Emission Spectrometry

PDAS : Primary Dendrite Arm Spacing

PSG : Particle-Size-Grouping

PTT : Precipitation-Temperature-Time

RA : Reduction of Area

SANS : Small-Angle Neutron Scattering

TEM : Transmission Electron Microscopy

NOMENCLATURES

a : Activity of dissolved element or precipitate phase

c : Lattice parameter (m)

e_i^j : Interaction coefficient of element i as affected by element j ($wt\%^{-1}$)

f : Transformed fraction in phase transformation

i_M : Number of pseudomolecules for the largest agglomerated particle in simulation

m_j : Number of pseudomolecules contained in PSG characteristic volume V_j

$m_{j-1,j}$: Number of pseudomolecules contained in PSG threshold volume $V_{j-1,j}$

n : Exponent to measure resistance to grain boundary motion in the presence of impurities and alloying elements

n_0 : Initial total number density of single pseudomolecules in solution ($\#\cdot m^{-3}$)

$n_{1,eq}$: Equilibrium number density of dissolved single pseudomolecules ($\#\cdot m^{-3}$)

n_{1i} : Equilibrium number density of single pseudomolecules at surface of size i particles ($\#\cdot m^{-3}$)

n_i : Number density of size i particles ($\#\cdot m^{-3}$)

n_s : Total number density of single pseudomolecules in steel composition ($\#\cdot m^{-3}$)

n_j^C : Number density of particles at the center of size group j ($\#\cdot m^{-3}$)

n_j^L : Number density of border particles, representing the smallest particles in size group j ($\#\cdot m^{-3}$)

n_j^R : Number density of border particles, representing the largest particles in size group j ($\#\cdot m^{-3}$)

p_i^s : Molar fraction of precipitate s for size i particles

r_1 : Radius of single pseudomolecule

r_i , r_j : Characteristic radius of size i particles, or size group j particles (m)

$r_{j-1,j}$: Threshold radius to separate size group j-1 and size group j particles in PSG method (m)

r_c : Critical radius of precipitate for nucleation (m)

$\overline{r}_P$: Average radius of precipitate particle (m)

w_P : Weight concentration of precipitate (%)

t : Average precipitate particle size (m)

Δt : Time step size in numerical computation (s)

A_i , A_j : Surface area of size *i* particles, or size group *j* particles (m^2)

A_M : Atomic mass unit of element M ($g \cdot mol^{-1}$)

$A_{M_xN_y}$: Atomic mass unit of precipitate M_xX_y ($g \cdot mol^{-1}$)

B : Coefficient related to the pinning efficiency of the precipitates

C_M : Molar concentration of element M in matrix

C_R : Cooling rate ($^oC \cdot s^{-1}$)

D : Diameter of austenite grain (m)

D_M : Diffusion coefficient of element M in matrix ($m^2 \cdot s^{-1}$)

D_f : Fractal dimension for precipitate morphology

G_M : Number of size groups for the largest agglomerated particle in PSG method

G_T : Truncating size group in PSG method to match experimental resolution

K : Rate function for nucleation and growth in KJMA model

$K_{M_xX_y}$: Solubility product of precipitate M_xX_y (wt%*wt%)

M : Kinetic constant that represents mobility of grain boundary or interface ($m^2 \cdot s^{-1}$)

M_0 : Total mass concentration of alloying element M in steel composition (wt%)

$[M]$: Dissolved mass concentration of alloying element M (wt%)

N_j : Total number density of size group *j* particles in PSG method ($\#\cdot m^{-3}$)

N_A : Avogadro number (6.022×10^{23} $\#\cdot mol^{-1}$)

N_M : Total number density of pseudomolecules ($\#\cdot m^{-3}$)

N_P : Total number density of measured precipitate particles ($\#\cdot m^{-3}$)

N_s : Number of atoms per unit area across the interface ($\#\cdot m^{-2}$)

N_T : Total number density of all precipitate particles ($\#\cdot m^{-3}$)

P_j^s : Molar fraction of precipitate s for size group *j* particles

Q_{app} : Apparent activation energy for grain growth (J/mol)

R_g : Gas constant (8.314 $J \cdot K^{-1} \cdot mol^{-1}$)

R_V : Particle volume ratio between two neighboring particle size groups

T : Absolute temperature (K)

V_i, V_j : Characteristic volume of size *i* particles; or size group *j* particles (m^3)

$V_{j-1,j}$: Threshold volume to separate size group *j-1* and size group *j* particles in PSG method (m^3)

V_P : Molar volume of precipitated phase ($m^3 \cdot mol^{-1}$)

Z_s : Number of bonds per atom across a given surface

Z_l : Coordinate number of nearest neighbors within the crystal lattice

α_i : Dissociation rate of size *i* particles ($m^{-2} \cdot s^{-1}$)

β_i : Diffusion growth rate of size *i* particles ($m^3 \cdot \#^{-1} \cdot s^{-1}$)

χ_P : Molar concentration of precipitate

δ : Relative lattice misfit across the interface between pairs of precipitate and matrix atoms

$\delta_{i,k}$: Kronecker's delta function ($\delta_{i,k}=1$ for $i=k$, $\delta_{i,k}=0$ for $i \neq k$)

ε : Turbulent energy dissipation rate ($m^2 \cdot s^{-3}$)

φ_V : Volume fraction of measured precipitate phase

λ_1 : Primary dendrite arm spacing (μm)

μ : Shear modulus (Pa)

ν : Poisson's ratio

ρ : Density ($kg \cdot m^{-3}$)

σ : Interfacial energy between precipitated particle/matrix ($J \cdot m^{-2}$)

υ : Kinematic viscosity ($m^2 \cdot s^{-1}$)

$\Phi_{i,k}$: Collision frequency between size *i* and size *k* particles ($m^3 \cdot \#^{-1} \cdot s^{-1}$)

Π : Supersaturation

Δg_{chem} : Volume chemical driving force for nucleation

ΔE_0 : Heat of solution of precipitate in a dilute solution of matrix ($J \cdot mol^{-1}$)

ΔG_V : Change of Gibbs free energy per unit volume during precipitation ($J \cdot m^{-3}$)

ΔH : Heat of formation of precipitate ($J \cdot mol^{-1}$)

Superscripts:

$*$: Dimensionless value

$-$: Average value

e: Effective value

z : precipitate type

L, R, C: Left, right border-size and center-size particles in each size group

Subscripts:

eq: Equilibrium value

i : size group in population balance equations

j : size group in PSG model equations

M: For matrix phase

P: For precipitate phase

I: For matrix/precipitate interface

Functions:

$ceil(x)$: The smallest integer which is not less than real number x

$floor(x)$: The largest integer which is not larger than real number x

CHAPTER 1
INTRODUCTION

Many important properties of metal alloys, such as their mechanical strength, toughness, creep and corrosion resistance, magnetic and superconducting properties, ductility and related cracking problems, are greatly affected by the presence of second phase precipitate particles. These phenomena include the strengthening and embrittlement of steel, and precipitation hardening of nonferrous alloys. A fundamental understanding of the thermodynamics and the kinetics of precipitation reactions in metallic solids, resulting in an ability to predict the important microstructural features of precipitates, and their influence on material properties, is thus of great interest to materials researchers.

Precipitates in alloys display a variety of different morphologies and size distributions, ranging from spherical, cruciform to needle shape, sizes from nm to μm and locations of inside the grains, on the grain boundaries or on dislocations, such as shown in Figure 1.1 [1-5]. The contribution of microstructure changes due to precipitate formation can have many different effects on material property. Large grain size decreases ductility and toughness, by allowing strain to concentrate at the grain boundaries to decrease strength and ductility. In addition to precipitation strengthening, a dispersion of fine precipitates can retard grain growth and recrystallization due to a pinning force to inhibit grain boundary movement, and thereby encourage grain refinement [6]. An unfortunate side effect is to decrease high temperature ductility and cause cracking, such as transverse cracks of microalloyed steel in continuous casting [7, 8]. If large numbers of fine precipitates accumulate along weak grain boundaries at elevated temperatures, they may cause a phenomenon called as precipitate embrittlement, in which voids and concentrated strains are produced near the grain boundaries to initialize and propagate the cracks [8]. There is a critical balance governing precipitate effects. If the precipitates are very fine, they are beneficial to refine the grain size, but also likely to cause cracks. If they grow too large, they are less damaging to ductility, but may lose the ability to restrict grain growth, and will themselves cause quality problems by causing stress concentration and fatigue failure in final products.

The composition, morphology, amount, spatial and size distribution of precipitates are all very important to alloy performance. The microstructure of mixed matrix and second phase

precipitates is, in turn, controlled by the alloy composition and temperature history in the process. The solubility of the precipitates always decreases with lowering temperature, so there is a critical temperature when precipitates start to form. The alloy composition affects the temperature range of precipitates formation and function, and the corresponding grain growth restriction and hot ductility decrease. A slower cooling rate generally increases the amount and size of precipitates, due to more time allowed for precipitation and coarsening. A lower ductility is expected for intermediate cooling rates when there is enough time for fine precipitates to occur, but not enough time for further growth or coarsening. Therefore it is important to control the alloy composition and cooling practice to produce optimal temperature and stress histories that avoid subjecting the material to high strains during those critical time periods when the grain size is large, embrittling precipitates are present and the alloy is susceptible to crack formation.

1.1 Techniques for Characterizing Precipitate

The experimental techniques for characterizing precipitates are abundant and still in rapid development. These methods measure the different properties of precipitates (spatial location, chemical composition, morphology, size distribution, and volume fraction), and have different resolution limits, sample preparation requirements and working conditions. The spatial region measured ranges from very tiny regions (TEM) to the entire sample (macro-etching), and limits the precipitate size that can be detected. The smallest detectable precipitate size can range from the atomic scale (for AFM) to micron scale, (for optical microscopy) and the sample usually must satisfy certain requirements of dimension (maximum size or thickness) and property (electrically conductive or not). The required working conditions for the measurements range from vacuum (TEM) to ambient air, or even liquid environment (AFM). In order to accurately recognize and measure the existing precipitate properties and to efficiently simplify the sample preparation and operation cost, the technique must be chosen carefully.

For an experimental technique to characterize precipitates for practical application, it must distinguish unambiguously if the precipitate-forming elements are in solid solution or in precipitate form. The method may be direct, by identifying and measuring the precipitates themselves, or indirect, by detecting a certain physical property change in the samples due to precipitate formation. The available direct and indirect methods for characterizing precipitates will be briefly introduced in the next two sections. Further details of the background, test

procedures, instrumentation, data acquisition and analysis methods can be found elsewhere [9-28].

Direct Methods

Direct methods to measure the properties of precipitates include the Energy-Dispersive X-Ray Spectroscopy (EDS or EDX) and X-Ray Diffraction (XRD) for precipitate composition, chemical extraction or related method for precipitate amount, Transmission Electron Microscopy (TEM), Scanning Electron Microscopy (SEM), Field Ion Microscopy (FIM), Scanning Tunneling Microscopy (STM), and Atomic Force Microscopy (AFM) for precipitate amount and size.

The EDS/EDX or XRD techniques are mainly applied for chemical characterization and crystallographic structure of precipitates. When a focused X-ray beam interacts with regular, repeating planes of atoms, part of the beam is transmitted, part is absorbed by the sample, part is refracted and scattered, and part is diffracted. Each element has a unique atomic structure allowing X-rays that are characteristic of atomic structure to be identified uniquely from one another. EDS/EDX measures the number and energy of the emitted X-rays relative to lateral position on the sample [10], while XRD measures the intensity of the reflected radiation versus the detector angle to calculate the inter-atomic spacing and structure [11] based on Bragg's law to identify the precipitate phase and composition.

The chemical extraction method separates the precipitates by dissolving the metal matrix, and then determines the alloying element in the filtered residue. By choosing a suitable etchant, the metal matrix can be dissolved without dissolving the precipitates, and the insoluble precipitate particles are then separated through filtration and measured. The most commonly-used chemical dissolution technique is that developed by Beeghly, which was first used to determine the nitrogen combined with aluminum in steel [12]. Electrochemical separation is also frequently used to get better extraction [13]. But these chemical methods are often criticized for the lack of sensitivity to small particles, of less than 10nm in size, and failure to isolate the elements that make up the different precipitates [12].

Due to the relatively large wavelength (~380-780nm) and diffraction effect of visible light, the resolution of an optical microscope can not resolve less than 200nm. The observation of nano-scale and even atomic scale microstructure became possible when the electron

microscope was developed. TEM is the most common method for characterizing precipitate size. Specimens for TEM must be prepared with very small thicknesses (~50-100nm) to allow electrons to transmit through them. SEM allows thicker samples, but only the surface can be scanned and measured. Both techniques require a vacuum to avoid reactions such as oxidation. Because the wavelength of electrons is inversely proportional to the charged voltage, the highest resolution of TEM can reach ~0.2nm under very high voltage, which is around one order magnitude beyond that of SEM.

FIM is the first microscope technique to fully achieve atomic resolution and to spatially resolve individual atoms at the surface of a sharp needle-sharp metal tip (<100nm radius). Atoms of filled imaging gas adsorbed on the tip are ionized by the strong electric field in the vicinity of the tip, and the positive charged gas ions are repelled perpendicularly away from the tip to hit a screen. The arrangement and chemical composition of individual atoms can be clearly discerned as bright dots on the image. Application of FIM is limited to materials which can be fabricated into a sharp tip, used in ultra-high vacuum environment and tolerates the high electrostatic fields.

STM is the first well-accepted instrument to obtain real-time three dimension imaging based on quantum tunneling at the atomic level, due to its easy specimen preparation and few constraints of test material and environment. It can reach lateral resolution of 0.1nm and depth resolution of 0.01nm, and works in vacuum, air, water and various liquid or gas surroundings, and at temperatures ranging from near several kelvins to several hundred centigrade. The specimen for STM requires being extremely flat (<10nm variation in height), and precision of the scanning tip requires being extremely high to get accurate measurements. Similar to SEM and TEM, nonconductive specimens need to be coated with a conductive layer.

In order to maintain atomic scale resolution and overcome the disadvantages of STM, a series of new probe microscope techniques have recently been developed. For example, AFM uses a cantilever with a mechanical probe at its end to replace the tunneling tip in STM. The tiny deflection of the cantilever that is caused by the atomic force between the specimen and tip is measured using a laser spot into an array of photodiodes, instead of the flow of tunneling current in STM. It can be used to distinguish individual atoms on the surface of any material and can handle nonconductive samples directly. In order to prevent collision between tip and surface, a constant distance or force is carefully maintained with feedback mechanism for these probe microscopy techniques. Example applications of TEM study on precipitation in Cu-Co alloy [14],

SEM study on coarsening of precipitates in Fe-Ni-Al alloy [15], FIM study on precipitation in Ti-Nb steel [16], STM study of precipitates in microalloyed steel [17] and AFM study of precipitates in aluminum alloy [18] are given elsewhere.

Indirect Methods

Direct methods are accurate but often very costly. The investigated volume is always limited to a volume on the order of a few thousand of nm^3, so the measured properties may be highly local and provide no global information. The measurement of precipitate size distribution often requires a large number of data and heavy statistical treatment. The estimation of volume fraction of phases may be also tedious and inaccurate with local direct techniques. Instead, indirect methods can be used for global characterization, which spatially average the property changes in much larger samples, due to precipitate formation.

The measured responses may be thermal (differential thermal analysis [18], differential scanning calorimetry [19]), electric (thermoelectric power [20], electrical resistivity [21]), magnetic (nuclear magnetic resonance spectroscopy [22]), mechanical (internal friction [23], peak strain measurement [24], stress relaxation [25], creep test [26]), or radiative (small angle neutron scattering [27], or small angle X-ray scattering [28]).

Indirect measurement methods must be chosen carefully chosen, because the global properties may be influenced not only by precipitation, but also by recrystallization, dislocation networks and other evolving microstructure features. For these techniques, a reference sample without precipitation is always investigated together with the test samples, and the differences recorded, are attributed to the formation of precipitates. The results should be validated with direct measurements to prove their accuracy.

Although intense work on experimental techniques to characterize precipitate formation in metal alloys has been conducted over many years, there is still no single accepted method which can unambiguous provide reliable and satisfactory quantitative analysis of all necessary properties of precipitates. Chemical methods, for example, may dissolve small precipitates, and thus underpredict their presence. Microscope methods, on the other hand, may miss rare large precipitates, owing to the small sample region measured. It is better to combine several direct and indirect techniques together simultaneously to give a comprehensive picture of the precipitate characteristics.

1.2 Numerical Modeling of Precipitation and Grain Growth

Considering the high cost and complexity of experimental techniques, numerical modeling is becoming an attractive alternative method for characterizing precipitates, which is much less expensive and easier to be applied. Moreover, after a numerical model has been validated with reliable experimental measurements, it is able to predict the behavior of a broad range of alternative materials or processing routes, for parametric investigation and optimization.

A general schematic of microstructure modeling is shown in Figure 1.2. The temperature history of the process is first determined using a heat transfer model. Then an equilibrium model and a kinetic model give the corresponding equilibrium concentration, and the volume fraction, and size distribution of precipitate evolution with time. Then, a grain growth can be applied to simulate the grain size evolution of the alloy of interest including the effect of the precipitates. Finally, the material properties of interest are determined from the temperature, precipitate and grain size histories, considering the mixed matrix and precipitate microstructure.

The temperature history is readily modeled by heat transfer models, which have been well developed in many commercial software packages, such as Abaqus [29] and Ansys [30], and by in-house codes for special-purpose processes, such as CON1D for continuous casting of steel. By correctly setting the boundary conditions and solving the transient heat conduction equation, computations at the macroscopic size scale can accurately give the temperature history.

Equilibrium precipitation behavior is frequently determined by the minimization of Gibbs free energy. The Gibbs free energy continuously decreases when the system evolves, and approaches its minimum at equilibrium. This is well developed in CALPHAD methods (CALculation of PHAse Diagram), and is applied in commercial software packages, such as Thermo Calc [31, 32], FactSage [33], ChemSage [34], and JMatPro [35]. An alternative method for predicting equilibrium precipitation in a multi-component system is to simultaneously solve systems of equations based on solubility products, which represent the limits of how much a given precipitate can dissolve in the matrix [36]. Both methods have been proven to give good agreement with experimental measurements.

Kinetic models predict the rate to approach the equilibrium state, and the corresponding evolution of the precipitated amount and size distribution. The phenomenon is governed by Fick's equation for diffusion. Classical precipitation theory separates the precipitation process into nucleation [37], growth [38] and coarsening [39] stages. Random thermal diffusion creates

unstable clusters of chemically-bonded pseudomolecules called “embryos”, which grow into stable “nuclei” if they exceed a critical size to make the volume energy decrease exceed the surface energy increase. Just after nucleation, a high supersaturation causes particles of all size to grow, which defines the growth stage. Once the supersaturation has decreased to equilibrium, the larger particles are surrounded by low concentration, and can only grow by diffusion from the surrounding smaller particles, because of the shortage of free pseudomolecules the in matrix. Recently, numerical models of these stages have been developed, including kinetic Monte Carlo models [40-42], phase field methods [43-45], Matcalc [46-48], and cluster dynamics models [49-51]. These models can be used to simulate precipitation as one continuous process, and are more fundamental because fewer assumptions are introduced.

The thermodynamic driving force for grain growth is the decrease of total grain boundary area, which is directly related to the interfacial energy and curvature of the grain boundaries. When second phase precipitates exist, they may exert pinning forces to inhibit grain boundary movement and grain growth. A general equation to describe grain growth in metals and alloys in the presence of growing and dissolving precipitates was first suggested by Anderson and Grong [52], and this model is further used by Bernhard to predict the austenite grain size of continuously-cast steel slabs [53]. Good matches with measurements were found if the necessary parameters were well determined [53].

1.3 Crack Formation and Hot Ductility of Microalloyed Steel

Precipitate formation in microalloyed steel is an important example to demonstrate the influence of precipitation on strength, ductility, toughness and weldability of metal alloys. Increasing demand for better steel properties continues to drive improvements in design and production of steel. With a good combination of microalloyed additions and thermomechanical processing, a set of desirable mechanical properties is attained through microstructure control. Microalloyed steel typically has a low carbon content (0.05-0.15 wt%), with up to 2% manganese, and small quantities of niobium, titanium, vanadium and aluminum (0.10wt% or less).

Cracks have been observed at almost every conceivable location in cast steel sections as shown in Figure 1.3 [54]. In the interior, cracks can be seen near the corners, at the centerline or diagonally between opposite corners. On the surface, transverse and longitudinal cracks can

appear in both the center and corner regions. No matter the kind of crack, the fundamental terms related to its formation are the low ductility at high temperature region and an excessive applied operating stress or strain.

Ductility is often measured from simple tensile tests and quantified by "reduction of area (RA)". In general, the ductility of steel at elevated temperatures is excellent. However, there are at least three distinct temperature regions where ductility drops remarkably, as shown in Figure 1.4 [55]. The first one appears at high temperatures around within 50^{o}C of the solidus temperature. The ductility in this region is virtually zero and is responsible for hot tearing, which is caused by the presence of liquid film in the interdendritic regions that do not freeze until the temperature drops well below the solidus temperature. The microsegregation of sulfur and phosphorus residuals at solidifying dendrite interfaces lowers the local solidus temperature, and is most harmful on the ductility and solidification cracking sensitivity in this temperature range. The resulting fracture surface exhibits a smooth, rounded appearance, characteristic of the presence of a liquid film during failure [55, 56].

The second zone of low ductility in steel appears in the austenite temperature range of 800^{o}C to 1200^{o}C. The low ductility around 1200^{o}C is mainly attributed to the formation of MnS and FeS, and grain boundary decohesion due to segregation of sulfur. Around temperature 900^{o}C, the low ductility is associated to the precipitation of AlN, BN or Nb(C,N) on austenite grain boundaries and the corresponding grain boundary sliding. Low ductility fractures are always intergranular along austenite grain boundaries, and lots of fine precipitates and ductile dimples around these precipitates are present. Due to the low temperature involved, the low ductility below 900^{o}C is believed to only influence the formation of surface cracks [55, 56].

The third low ductility zone occurs in the temperature range of 600-900^{o}C when austenite transforms to ferrite, which is caused by an accelerated precipitation in ferrite and strain concentration in soft thin deformation-induced ferrite films around austenite grain boundaries. When most of austenite has been transformed to ferrite, because the ferrite is much softer with finer and more equiaxed grains than that of the austenite, strain distribution between austenite and ferrite becomes more uniform. Thus a recovery of good ductility is always observed at the end of transformation. Fractures surface are always characterized by intergranular failures, and often associated with void formation around fine precipitates [56].

The factors that directly influence hot ductility include precipitate formation, grain size and strain rate. Generally speaking, the ductility is lowered quantitatively with an increase of precipitate amount [57, 58]. The finer the precipitate size the worse is the ductility. Precipitates are proved to reduce ductility when they are smaller than 50nm in size, and likely to cause a reduction of area ~25% when their size is around ~10nm [57]. The precipitates on austenite grain boundary are more detrimental than those inside matrix, because they encourage void nucleation and growth either during grain boundary sliding or within ferrite films. Precipitate free zones are often observed adjacent to austenite grain boundaries, and may lead to strain concentration at these boundaries.

Refining grain size can lead to improvement of ductility. Although the influence of precipitates and grain size on ductility often can not be clearly separated and distinguished, some tests on the precipitate-free steel proved that finer grain size causes reductions of both the depth and width of the high-temperature ductility trough [59]. This is possibly due to a decrease of the grain boundary sliding rate, or by the difficulty in propagation of grain boundary cracks formed on sliding through triple points of connecting grains. The minimum reduction of area is approximately proportional to $D^{-1/2}$ for grain size less than 500μm [60].

An increase of strain rate is also beneficial to improve ductility. An increase of strain rate by an order of magnitude between 10^{-4} to 10^{-1} s^{-1} often increases the RA values by ~20%, and changes the fracture appearance from intergranular to ductile [61, 62]. These effects are maybe caused by reduced grain boundary sliding, insufficient time for strain-induced precipitation and formation of voids next to the precipitates and prevention of deformation-induced ferrite.

The distinction between low ductility regions of steel is mainly determined by the stability of the different precipitates. Because of a relatively larger amount of manganese in microalloyed steel and the serious segregation of sulfur, the MnS precipitate is likely to form during solidification or in the high temperature range of austenite. The MnS particles are thus possibly coarse in size and often not very damaging for the hot ductility. A high level of Mn/S ratio is more beneficial to ductility because the sulfur tends to be tied to the precipitated MnS in the matrix, and not predominantly at austenite grain boundaries. Because the amount of alloying manganese is always more than 10 times of other elements, the effect of modifying the activities and diffusivity of elements by manganese addition is maybe important. For example, a significant decrease of dynamic precipitation rate of Nb(C,N) [63] and TiC [64] with increasing

manganese amount was found. The low ductility trough due to MnS precipitation is only apparent at high strain rates, which is not significant for transverse crack formation during continuous casting process.

The most detrimental precipitates for decreasing hot ductility of steel are maybe Nb(C,N) and AlN, which are preferable to nucleate and grow as fine precipitates on austenite grain boundaries or dislocations. The Nb(C,N) precipitates, which form at austenite grain boundaries with a size of a few tenths of nanometers or less, delay the onset of dynamic recrystallization and grain boundary mobility that can otherwise isolate occasional cracks formed by other mechanisms. Concurrently, when grain boundary sliding is active as a process of plastic deformation, Nb(C,N) particles will encourage the development of cracks [65]. The precipitation of AlN has the similar effect [66], but it is always sluggish and mainly occurs in rolling process because of the different h.c.p. structure of AlN and f.c.c. structure of austenite.

Vanadium is believed to have the similar precipitation behavior with niobium, but shows a reduced effect in decreasing ductility and promoting transverse cracks due to a higher solubility of V(C,N). The vanadium nitride and carbide is always coarser in size, and less detrimental than those of niobium. In order to cause a same effect with niobium steel, a much larger amount of vanadium addition is often required [67].

Titanium is maybe the most possible alloying element that can effectively improve ductility. Because of its low solubility, TiN precipitates form during solidification or at high temperature. They are so much coarser in size, less harmful and randomly distributed, and can provide the heterogeneous nucleation and growth sites for further precipitation of niobium and vanadium. The preferential combination of nitrogen with titanium also prevents the precipitation of more detrimental precipitation of fine AlN particles. The coarse size of TiN precipitates or more complex (Ti,Nb)(C,N) precipitates is possible to restrain grain growth at high temperature, but not small enough to initialize and propagate cracks. All these influences of titanium are beneficial to ductility [60].

The microstructure of steel is, in turn, controlled by the steel composition and temperature histories in test. A suitable increase of alloying precipitate-forming elements could favor precipitation and worse ductility. The additions of microalloy also change the phase transformation temperatures of microalloyed steel, and thus alter the temperatures at which ductility trough occurs.

Temperature profile is also very important for precipitation formation of steel. A longer holding time increases both the fraction and size of precipitate. Temperature oscillation in the spray cooling zones of continuous casting also decreases ductility, if the temperature falls into a favorable range of precipitation in austenite, or even below the austenite to ferrite transformation temperature to enhance a much faster precipitation in ferrite [68].

When tensile stress is applied in the temperature range of low ductility, the cracks are possibly initialized. The formation of transverse surface cracks is a vital problem after the very early time of continuous casting, and still limits both productivity and quality of the steel industry these days. These cracks are believed to form in the mold, and possibly in the vicinity of oscillation marks, which is caused by the low melting points of these regions associated with segregation and higher temperature due to reduced heat transfer across gap filled with air or slag [69]. The carbon concentration is vital, if some peritectic solidification occurs, which may cause transformation strains during solidification and increase the occurrence of transverse cracks. The highest frequency of transverse cracks is found to appear in a carbon range of ~0.12% for C-Mn-Al steels [70].

The grain size beneath oscillation marks is often coarse, and tends to favor the propagation of cracks. The notch geometry near oscillation marks also favors the stress concentration. These defects continues to become larger and more numerous below mold, as a result of further tensile stresses. During slab straightening, the strains are tensile on the upper surface of the strand and compressive on the lower surface. The strains are of course reversed for bending. The observation of most numerous transverse cracks on the top surface of the slab suggests that much transverse crack propagation is induced by the stresses experienced in the straightening process. The cracks generally follow austenite grain boundary, and can be several dozens of nm in length.

The rapid cooling in continuous casting causes steep temperature gradients in the solid shell that can change rapidly and generate thermal strains when it expands or contracts. When the solid shell moves through the casting machine, it is subjected to various stresses caused by friction in the mold, ferrostatic pressure, roll pressure, misalignment, bending and straightening operations. Cracks are possibly initialized when the accumulated stresses are overcritical.

In summary, a typical mechanism for transverse surface crack formation in continuous casting is shown in Figure 1.5 [8]. Surface grains can grow extremely large due to locally high

temperature and strain, especially beneath deep oscillation marks. Because the slab is cooled from the surface to the center during casting, precipitates first begin to form and microcracks initiate along these "blown" grain boundaries. With formation of more precipitates, existing microcracks grow and new ones form, and finally propagate into visible cracks on the top surface of the strand under tensile strain. Figure 1.6 obviously displays larger grains and a transverse crack under an oscillation mark of a 0.2% carbon steel slab [8], which proves this mechanism of transverse crack formation.

1.4 Objectives

Although extensive studies have been conducted on the precipitation kinetics in microalloyed steels, a fundamentally-based model to treat the entire precipitation as one continuous and competing process and cover the precipitate ranging from atomic size to coarse size is still lacking. Such a comprehensive model must combine both the thermodynamic and the kinetics of the multi-component and multi-phase steel, and simulate the evolution of precipitate size distribution, instead of mean precipitate size variation with time. Furthermore, the models for multiphase precipitation, which is frequently observed in reality, are developed. The purposes of this work include:

1). To develop an efficient, fundamental new model to simulate the precipitate formation. These models include an equilibrium precipitation model to predict the amounts and compositions of the precipitates at equilibrium, and kinetic models to predict the amount and size distribution evolution of the precipitates with time;

2). The suggested precipitation model needs to combine the thermodynamics and kinetics simultaneously. The nucleation, growth and coarsening are attempted to be simulated as one continuous and competing process with significant parameters in physics, and cover a larger size range with reasonable computation cost.

3). Kinetic model of multiphase precipitation is necessary to simulate more realistic heterogeneous complex/mixed precipitates. The number densities and the molar fraction of each precipitate phase of particles with different size must be included.

4). From the result of the precipitation model, an austenite grain growth model is required to predict the austenite grain size in the presence of precipitates. The influence of precipitates on inhibiting grain growth must be included.

5). In order to introduce less uncertainties and demonstrate its accuracy, it is better to validate each model separately first. Then all models are used together to simulate the precipitate formation for commercial steel grades and practical continuous casting processes. This work is done by taking advantages of an existing heat transfer model, which is applied to calculate the histories of temperature and steel phases within the casting slab.

6). Combined with other models, the results from the models in this work are used to explain the low ductility and transverse cracks in continuous casting, where precipitates and grains have important effects.

An overview of this project is shown in Figure 1.7. The first step is to predict temperature and steel phase fraction histories throughout the strand using an existing heat transfer model, CON1D. Then an equilibrium precipitation model and kinetic model are used to predict the composition, volume fraction and size distribution evolution of precipitates. A multiphase precipitation model is also necessary to compute the complex precipitation behavior. For the solute rich region, such as grain boundaries, a segregation model is required to compute the enriched composition first, and then precipitate formation can be modeled by the same sequence. An austenite grain growth model is applied to calculate austenite grain size evolution with the pinning effect of precipitates. Finally, the ductility and susceptibility to cracking of steel product can be determined by considering the coupled influence of grain size and precipitate histories, and empirical formulae from experiments.

This work aims to improve our ability to control and utilize the effects of precipitates in steels. The set of equilibrium, diffusion and mass balance equations are solved simultaneously for each individual precipitate phase and particle. The developed models aim to provide a physical basis for quantitatively interpreting how various variables such as steel composition and casting processes affect the precipitate formation in industrial processes. The model is intended to be generally applicable to wide ranges of different precipitates in different alloy systems. It should be useful in the optimization of material design and generate subsequent improvements to current material manufacturing.

1.5 Tables and Figures

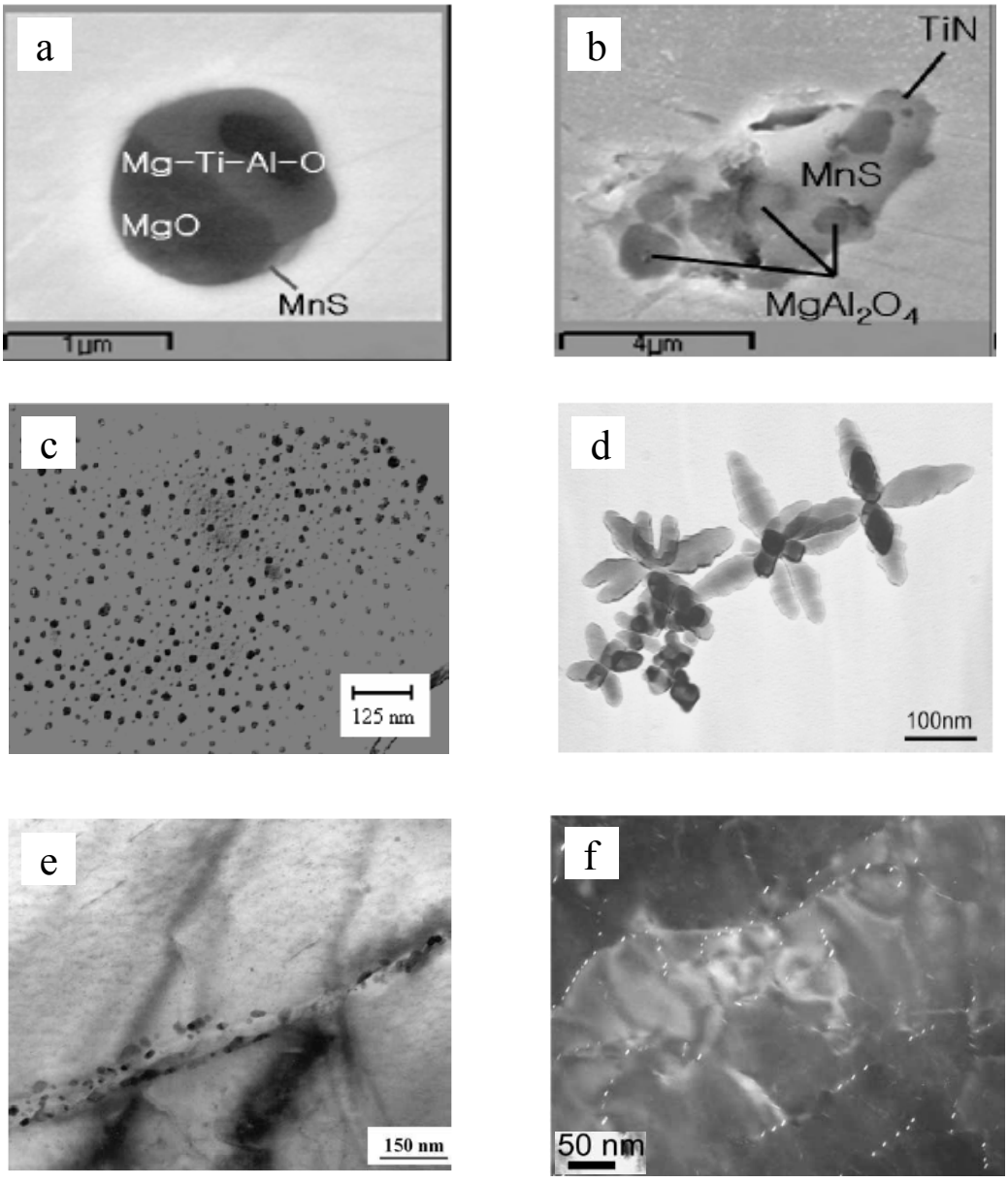

Figure 1.1: Example precipitates in microalloyed steels: (a), (b).Coarse complex multiple-phase precipitates by heterogeneous nucleation [1],
(c).Fine spherical AlN [2], (d).Cruciform (Ti,V)N [3], (e).(Ti,Nb)C on grain boundaries [4], (f). NbC along dislocations in ferrite [5]

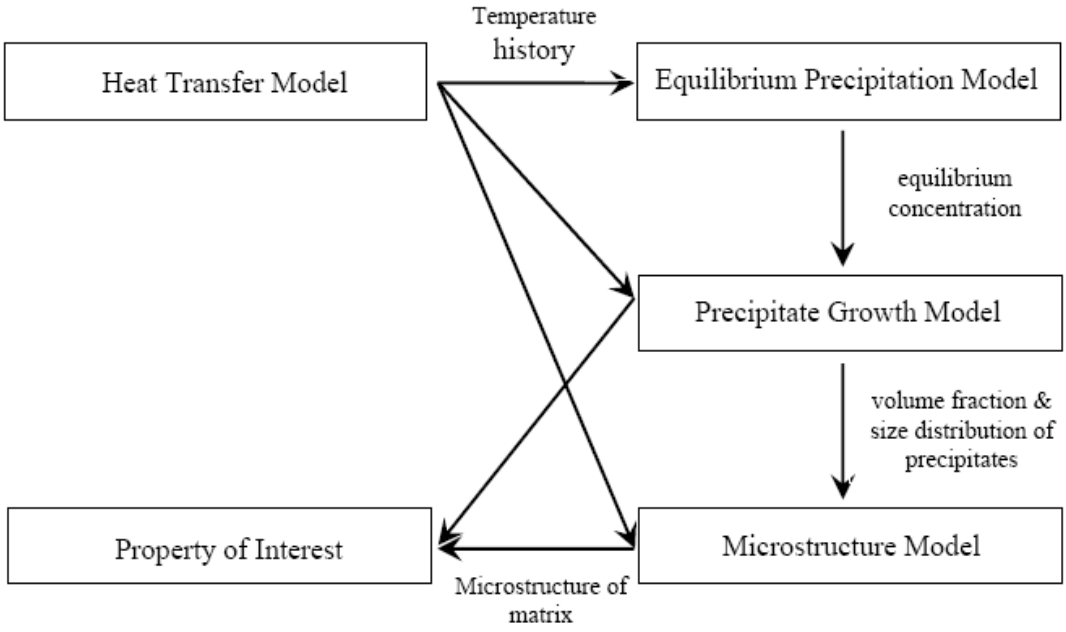

Figure 1.2: Schematic of modeling of precipitate and related phenomena

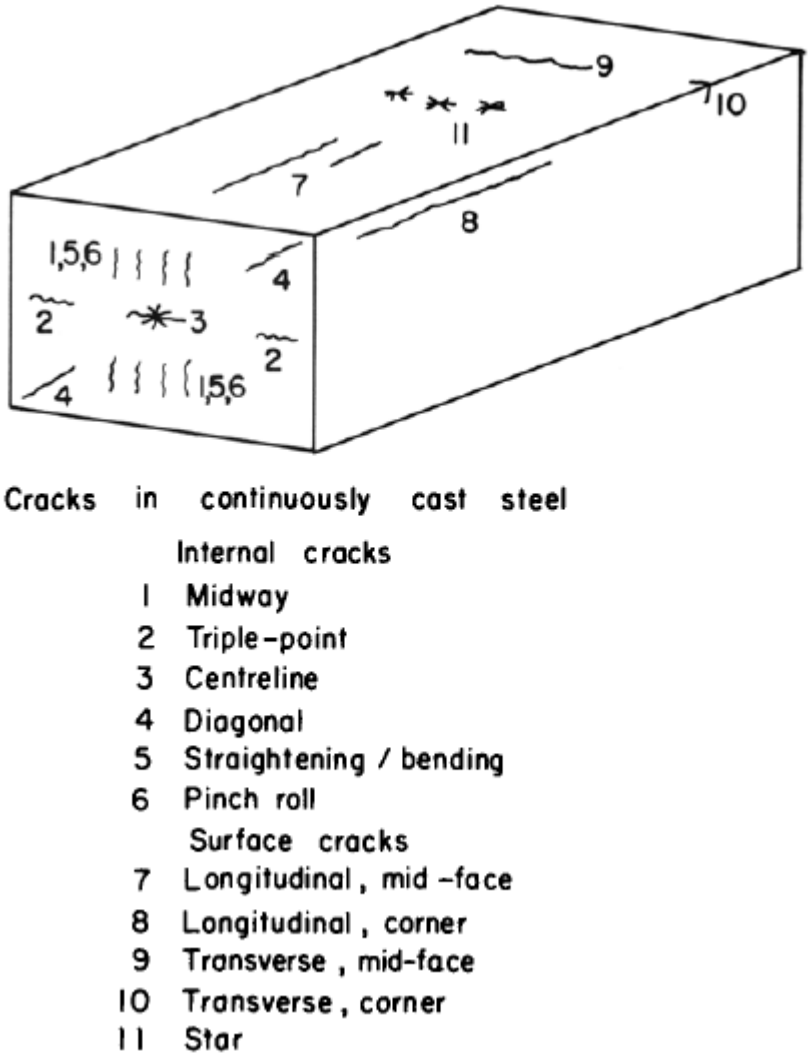

Figure 1.3: Schematic of cast section showing different types of cracks [54]

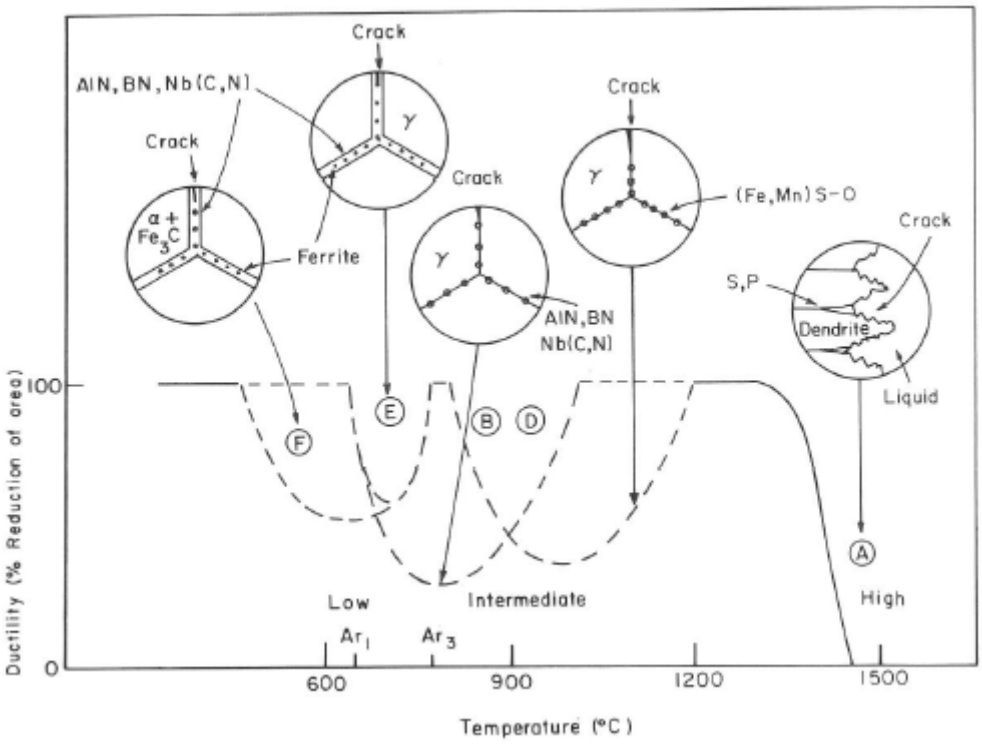

Figure 1.4: Schematic of temperature zones of reduced hot ductility of steel [55]

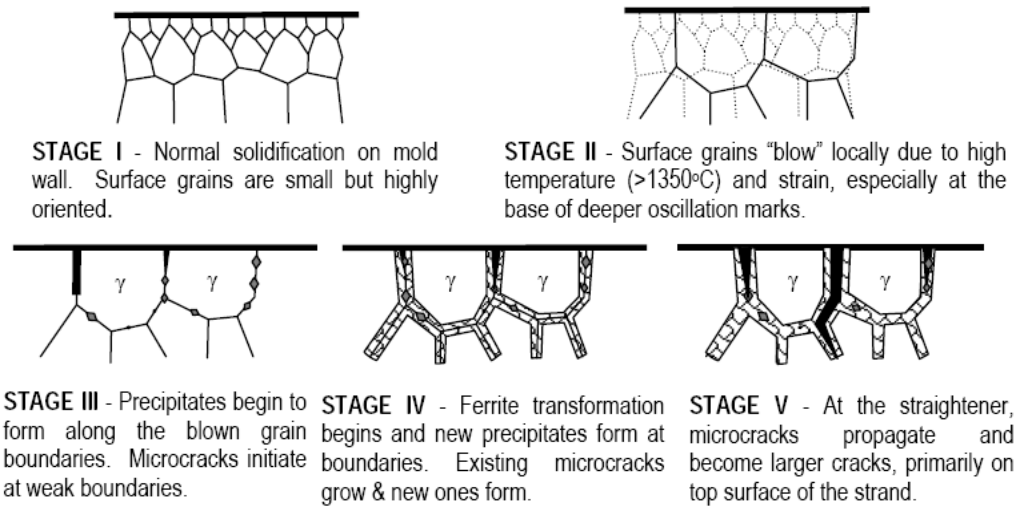

Figure 1.5: Mechanisms of surface crack formation with precipitate embrittlement in continuous casting [8]

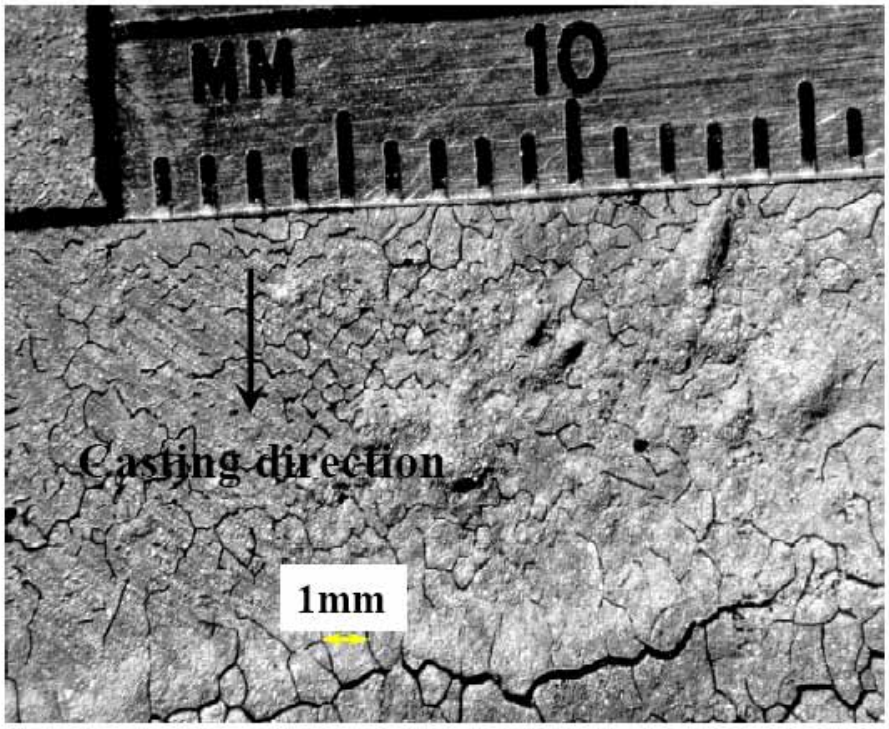

Figure 1.6: Transverse crack at the base of an oscillation mark on the top surface of a 0.2%C steel slab [8]

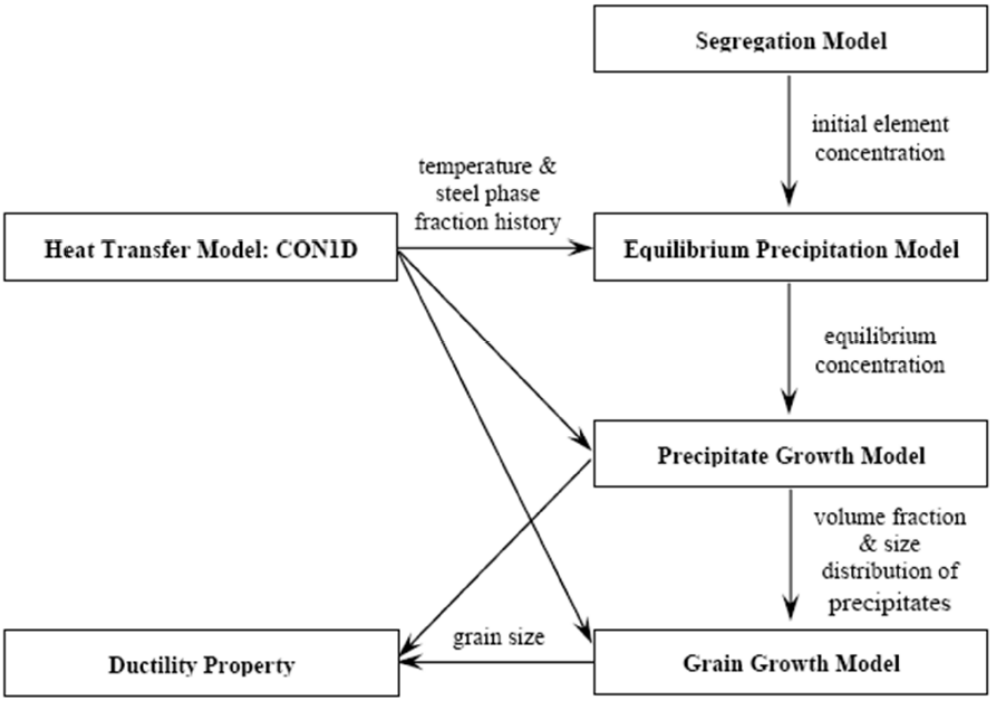

Figure 1.7: Overview of the project

CHAPTER 2
EQUILIBRIUM PRECIPITATION MODEL

An accurate modeling for precipitate growth has at least 2 steps: 1) equilibrium thermodynamic analysis, 2) kinetic effects. The equilibrium model could predict occurrence and stability of precipitates at equilibrium, and then the kinetic model could tell the rate to approach the equilibrium, and the amounts and particle size distributions evolution with time.

The first crucial step to model precipitation behavior is to predict the phases, compositions and amounts of precipitates present at equilibrium for a given composition and temperature. This represents the maximum amount of precipitate that can eventually form when the solubility limit is exceeded. It is also critical for calculating the supersaturation, which is the composition extent of going beyond the solubility limit and the driving force for precipitate growth. Thus, a fast and accurate model of equilibrium precipitation is a necessary initial step towards the development of a comprehensive model of precipitation kinetics.

2.1 Previous Work

Minimization of Gibbs free energy is the most popular method to determine the equilibrium phases present in a multi-component material. The total Gibbs energy of a multi-component system is generally described by a regular solution model [71]. In addition to the Gibbs energy of each pure component, the extra energy terms come from the entropy of mixing, the excess Gibbs energy of mixing due to interaction between components, and the elastic, magnetic or other energies if stored in the system. For a binary-solution phase, such as disordered solid solutions, the regular solution type model gives the total Gibbs energy as

$$G^{\varphi} = \chi_A G_A^0 + \chi_B G_B^0 + RT[\chi_A \ln \chi_A + \chi_B \ln \chi_B] + \chi_A \chi_B \sum_{i=0}^{n} G_i (\chi_A - \chi_B)^i \qquad \textbf{(2.1)}$$

where χ_A and χ_B are the mole fractions, and G_A^0 and G_B^0 are the reference energies of component A and B, respectively. The first two terms correspond to Gibbs energy of a mechanical mixture of the constituents of the phase, and the third term is the entropy of mixing for an ideal solution. The fourth term is for the excess Gibbs energy from interaction. The sum of the terms $G_i(\chi_A - \chi_B)^i$ is called as Redlich-Kister polynomial [72], which is the commonly used polynomial to describe the deviation from the regular solution.

A higher component system can be calculated from thermodynamic extrapolation of the constituent subsystems. Muggianu's method is often recommended because it can be easily generalized to multi-component system [73]. For example, the Gibbs energy of a ternary-solution phase is extrapolated from the binary energies using as

$$G^{\varphi} = \chi_A G_A^0 + \chi_B G_B^0 + \chi_C G_C^0 + RT[\chi_A \ln \chi_A + \chi_B \ln \chi_B + \chi_C \ln \chi_C]$$
$$+ \chi_A \chi_B \sum_{i=0}^{n_{AB}} G_i^{AB} (\chi_A - \chi_B)^i + \chi_B \chi_C \sum_{i=0}^{n_{BC}} G_i^{BC} (\chi_B - \chi_C)^i + \chi_C \chi_A \sum_{i=0}^{n_{CA}} G_i^{CA} (\chi_C - \chi_A)^i \quad \textbf{(2.2)}$$

For the ordered solution phases, the sublattice model is generally adopted [74]. The basic idea for this model is to assign a sublattice for each distinct site in the crystal structure. The terms in expression increases exponentially with the number of sublattices, and the interactions between atoms on different sublattices must be considered. Thus although the model can be easily generalized to an arbitrary number of sublattices in theory [75], it has been always limited for two sublattices in simulation. These ideas are adopted to develop CALPHAD method [76]. In recent years, many researchers have used software packages based on these Gibbs energy minimization methods, including Thermo Calc [31, 32], FactSage [33], ChemSage [34], JMatPro [35] and other CALPHAD models [77, 78], to calculate equilibrium precipitation behaviors in multi-component steels.

One application example of these models is given by Lee for a Fe-Nb-Ti-C-N steel system with self-consistent thermodynamic parameters [78]. The carbonitride phase was modeled using a two sublattice model with (Fe,Nb,Ti)(C,N,Vacancy), where the two sublattices represent the substitutional metal atoms and the interstitial atoms separately. Since not all positions are occupied by interstitial atoms, vacant sites were introduced. Mutual interaction energies between components incorporated up to ternary interactions, and accuracy was confirmed by comparing predictions with thermodynamic properties of Nb-Ti carbonitrides measured under equilibrium conditions for a wide range of steel compositions.

Although these models based on minimizing Gibbs free energy can accurately predict the equilibrium amounts of precipitates, and have the powerful ability to predict the precipitates to expect in a new system, the accuracy of their databases and their ability to quantitatively predict complex precipitation of oxides, sulfides, nitrides and carbides in microalloyed steels are still in question. In addition, the solubility limit of each precipitate is a logarithmic function of free energy, so a small inaccuracy in the free energy function could cause a large deviation in

calculating the amount precipitated [79]. Finally, the required free energy curves and interaction parameters become tedious for microalloyed steels containing dozens of components, and are very interdependent and so must be refit to incorporate new data.

An alternative method to predict the equilibrium phases in a multi-component alloy is to simultaneously solve systems of equations based on experimentally measured solubility products, which represent the limits of how much a given precipitate can dissolve per unit mass of metal. The origin of this equilibrium constant concept can be traced back to Le Chatelier's Principle of 1888 [80]. The incorporation of mutual solubility was first suggested by Hudd [81] for niobium carbonitride, and later extended by Gladman [36] to Ti-Nb-C-N steel. This alternative method is proved to be more concise and easier for personal programming.

Recently, Liu [82] developed a model to predict the equilibrium mole fractions of precipitates Ti(C,N), MnS and $Ti_4C_2S_2$ in microalloyed steel. The solubility products are calculated from standard Gibbs energies, and the interaction between alloying elements and the mutual solubility of Ti(C,N) are counted. The precipitation of complex vanadium carbonitrides and aluminum nitrides in C-Al-V-N microalloyed steels was discussed by Gao and Baker [83]. They utilized two thermodynamic models by Adrian [84] and Rios [85], and produced similar results. Park [86] calculated the precipitation behavior of MnS in austenite including two different sets of solubility products for $Ti_4C_2S_2$ and TiS [31, 82], and assuming these sulfides and carbonitrides (Ti,V)(C,N) are mutually insoluble. In both works [83, 86], the solution energy of mixing for C-N was assumed to be constant (-4260J/mol) with all other solution parameters setting as zero. The Wagner interaction effect was neglected for this dilute system and ideal stoichiometry was assumed for all sulfides and carbonitrides.

Previous solubility-product based models often neglect effects such as the differences between substitutional and interstitial elements during precipitation, mutual solubility between precipitates and the Wagner effect between solutes, so are only suitable for particular steel grades and precipitates. Moreover, the analysis of molten steel and ferrite is lacking as most works only focus on precipitation in the austenite phase.

Although many previous attempts have been made, an accurate model of equilibrium precipitation behavior in microalloyed steel has not yet been demonstrated. The complexity comes from many existing physical mechanisms during precipitation processes, such as solubility limits of precipitates in different steel phases, change of activities due to Wagner

interaction between elements, treatment of mutually exclusive and soluble properties among precipitates and mass conservation of all elements.

This chapter aims to establish and apply such a thermodynamic model to efficiently predict the tendency, sequence and amounts of typical oxides, sulfides, nitrides and carbides in microalloyed steels. Mutual solubility is incorporated for appropriate precipitates with similar crystal structures and lattice parameters. Wagner interaction parameters between solutes are widely collected from the available literatures. Mass balance of each alloying element is guaranteed during precipitation. After the system of equations is established, it is solved by suitable numerical method. The model is applied to investigate the effect of mutual solubility. It is then validated with analytical solution of simple cases, numerical results from commercial package JMatPro and previous experimental results. Finally, the model is applied to predict equilibrium precipitation in two commercial microalloyed steels with different casting speeds in practical continuous casting condition. The details of this equilibrium model have been published in our previous paper [87].

2.2 Model Description

The equilibrium precipitation model developed here computes the composition and amount of each precipitate formed for a given steel composition and temperature, based on satisfying the solubility products of a database of possible reactions and their associated activity interaction parameters. The database currently includes 18 different oxide, sulfide, nitride and carbide precipitates, (TiN, TiC, NbN, $NbC_{0.87}$, VN, V_4C_3, Al_2O_3, Ti_2O_3, MnO, MgO, MnS, MgS, SiO_2, TiS, $Ti_4C_2S_2$, AlN, BN, Cr_2N*)*, and 13 different elements, (N, C, O, S, Ti, Nb, V, Al, Mn, Mg, Si, B, Cr*)*, in Fe, and is easily modified to accommodate new reactions and parameters.

2.2.1 Solubility Products

For each reaction between dissolved atoms of elements *M* and *X* to give a solid precipitate of compound M_xX_y.

$$xM + yX \leftrightarrow M_xX_y \tag{2.3}$$

The equilibrium solubility product, $K_{M_xX_y}$, is defined as

$$K_{M_xX_y} = a_M^x \cdot a_X^y / a_{M_xX_y} \tag{2.4}$$

where a_M , a_X and $a_{M_xX_y}$ are the activities of M, X and M_xX_y respectively.

It is always measured as a function of temperature in experiments as

$$K_{M_xX_y} = -\frac{A}{T} + B \qquad \textbf{(2.5)}$$

where parameters A and B can be determined by fitting experiments. Since A is always positive, thus the solubility products decrease with lowing temperature, and there is usually a critical temperature below which precipitates can form, if sufficient time is given.

The solubility products of the precipitates in liquid steel, ferrite and austenite used in this study are listed in Table I. The solubilities in liquid are about 10-100 times larger than those in austenite, which are about 10 times greater than those in ferrite at the same temperature. These observed ratios are assumed to estimate unknown solubility products for oxides in solid steel and for the other precipitates in liquid steel. As shown in Figure 2.1, the solubility products generally decrease from carbides, to nitrides, to sulfides, to oxides, which correspond to increasing precipitate stability. Thus, oxides is very stable and often precipitate first, forming almost completely in the liquid steel, where they may collide and grow very large and be far less damaging than other precipitates, leaving coarse oxide particles (inclusions) and very little free (dissolved) oxygen remaining in the solid phase after solidification. In addition, oxide precipitates in the solid often act as heterogeneous nucleation cores of complex precipitates which form later at lower temperature [126, 127].

The solubilities and amounts of nitrides and carbides added to microalloyed steels typically result in these precipitates forming in the austenite phase as small (nm-scale) second-phase particles which inhibit grain growth. A notable precipitate is TiN, which is roughly 100-1000 times more stable than other nitrides and carbides. The large variations between the ratio of carbide and nitride solubility products also depends greatly on the alloying elements. This ratio is about 10 for niobium, so $NbC_{0.87}$ precipitates are commonly observed in steels because carbon is always relatively plentiful. This ratio is about 100-1000 for titanium and vanadium so these elements typically precipitate as nitrides. When the concentration of sulfur is high enough, the corresponding sulfides and carbosulfides are also observed in these steels.

For the low solute contents of the steels, the activity a_i, of each element i, (wt%) is defined using Henry's law as follows:

$$a_i = \gamma_i[\%i] \text{ where } \log_{10}\gamma_i = \sum_{j=1}^{13} e_i^j[\%j] \quad \textbf{(2.6)}$$

where γi is the activity coefficient, e_i^j is the Wagner interaction coefficient of element i as affected by alloying element j, and $[\%i]$ is the dissolved mass concentration of element i (wt%). The summation covers interactions from all alloying elements, including element i itself. This relation comes from the Taylor series expansion formalism first proposed by Wagner [128] and Chipman [129] to describe the thermodynamic relationship between logarithm of activity coefficient and composition of a dilute constituent in a multi-component system. Larger positive Wagner interaction parameters encourage more precipitation. If the alloying concentrations were higher, then higher-order interaction coefficients using the extended treatment by Lupis and Elliott [130] should be used. Since alloy additions are small in the microalloyed steels of interest in this work (<~1wt%), they are assumed to be dilute so only first-order interaction coefficients were collected. Relative to the solubility product effects, these interaction parameters are a second order correction to precipitation in these steels. Each referenced value was determined in either the liquid melt or solid steel. They are assumed independent of steel phase and are summarized in Table II.

During phase transformations, when the steel has more than one phase (liquid, δ-ferrite, austenite and α-ferrite), the solubility product of the precipitate M_xX_y is defined with a weighted average based on the phase fractions as follows:

$$K_{M_xX_y} = f_l \cdot K^l_{M_xX_y} + f_\delta \cdot K^\delta_{M_xX_y} + f_\gamma \cdot K^\gamma_{M_xX_y} + f_\alpha \cdot K^\alpha_{M_xX_y} \quad \textbf{(2.7)}$$

where f_l, f_δ, f_γ and f_α are the phase fractions of liquid, δ-ferrite, austenite and α-ferrite in steel.

2.2.2 Treatment of Mutual Solubility

Although many different precipitates are included in the previous section, several groups are mutually soluble, as they exist as a single constituent phase. There is ample experimental evidence to show the mutual solubility of (Ti,Nb,V)(C,N) carbonitride in steels. The treatment of mutual solubility follows the ideas of Huud [81], Gladman [36], Speer [131] e*t al*, and assumes ideal mixing (regular solution parameters are zero) for mutually soluble precipitates. The activities of precipitates which are mutually exclusive with each other remain at unity

because they exist separately in the steel. On the other hand, the activities of mutually soluble precipitates are less than unity because they always appear together with other precipitates. Instead their activities are represented by their respective molar fractions in the mixed precipitates, so the sum of the activities of the precipitates that comprise a mutually soluble group is unity. The crystal structures and lattice parameters of the precipitates are given in Table I. Precipitates with the same crystal structures and similar lattice parameters (within 10%), are assumed to be mutually soluble, and this assumption could be adjusted by further experimental observations.

According to the above criterion, the 18 precipitates in the current work are separated into the following 10 groups: (Ti,Nb,V)(C,N), (Al,Ti)O, (Mn,Mg)O, (Mn,Mg)S, SiO_2, TiS, $Ti_4C_2S_2$, AlN, BN, Cr_2N. Precipitates can form from the element combinations that comprise each of these groups, including those for the 4 mutually soluble groups shown in Table 2.3. The 18 solubility limits provide the following constraint equations:

$$a_{M_xX_y} = \frac{a_M^x \cdot a_X^y}{K_{M_xX_y}} \tag{2.8}$$

The activity of precipitate M_xX_y, $a_{M_xX_y}$, is determined differently for mutually soluble and exclusive precipitates. Its value is one for the 6 mutually exclusive precipitates (SiO_2, TiS, $Ti_4C_2S_2$, AlN, BN, Cr_2N). For the 4 mutually soluble precipitate groups, the precipitate activities must satisfy:

$$a_{TiN} + a_{NbN} + a_{VN} + a_{TiC} + a_{NbC_{0.87}} + a_{V_4C_3} = 1 \tag{2.9}$$

$$a_{Al_2O_3} + a_{Ti_2O_3} = 1 \tag{2.10}$$

$$a_{MnO} + a_{MgO} = 1 \tag{2.11}$$

$$a_{MnS} + a_{MgS} = 1 \tag{2.12}$$

The *y/x* ratio of each precipitate *MxXy* is easily calculated from Table I, and is often a non-stoichiometric fraction, according to experimental observations. With wide uncertainties in measured solubility products [36], further research is needed to modify these data to best match new measurements.

Since not all the precipitates are always formed, Eq. (2.8) is required to be used cautiously. The criteria for determining whether the certain kind of precipitate from or not is first given by

$$\frac{a_M^x \cdot a_X^y}{K_{M_xX_y}} \geq a_{M_xX_y} \tag{2.13}$$

This condition needs to be calculated and judged iteratively each time after the dissolved concentrations of elements are calculated and updated. If this condition is true, then both sides in the above equation must be imposed to be equal as Eq. (2.8) to satisfy the solubility requirement. If this is not true, Eq. (2.8) is not satisfied anymore because the dissolved alloy concentrations are under the solubility limit, and the following equation is imposed instead, which states that precipitate *MxXy* does not form at present:

$$\chi_{M_xX_y} = 0 \tag{2.14}$$

For the mutually soluble precipitate groups, such as (Ti,Nb,V)(C,N), the criteria is given as

$$a_{TiN} + a_{NbN} + a_{VN} + a_{TiC} + a_{NbC_{0.87}} + a_{V_4C_3} \geq 1 \tag{2.15}$$

If this is true, the equations (2.8) for all TiN, TiC, NbN, $NbC_{0.87}$, VN, V_4C_3 need to be all satisfied. Otherwise, $\chi_{(Ti,Nb,V)(C,N)} = 0$, and the activities of a_{TiN}, a_{NbN}, a_{VN}, a_{TiC}, $a_{NbC_{0.87}}$, $a_{V_4C_3}$ can be randomly chosen to satisfy Eq. (2.9) because these values have no physical meaning when this group of precipitates does not form yet.

2.2.3 Mass Balance on Alloying Elements

The total of the molar fractions of each group of precipitates in the steel is

$$\chi_{total} = \chi_{(Ti,Nb,V)(C,N)} + \chi_{(Al,Ti)O} + \chi_{(Mn,Mg)O} + \chi_{(Mn,Mg)S} + \chi_{SiO_2} + \chi_{TiS} + \chi_{Ti_4C_2S_2} + \chi_{AlN} + \chi_{BN} + \chi_{Cr_2N} \tag{2.16}$$

The following equations must be satisfied for the mass balance of each of the 13 alloying elements, by summing over all 18 precipitate types, as summarized in Table 2.4:

$$\chi_{M_0} = (1 - \chi_{total})\chi_{[M]} + \sum_{i=1}^{18}\left(x\chi_{M_xX_y}\right)_i \tag{2.17}$$

$$\chi_{X_0} = (1 - \chi_{total})\chi_{[X]} + \sum_{i=1}^{18}\left(y\chi_{M_xX_y}\right)_i \tag{2.18}$$

where $\chi_{M_0} = A_{steel}M_0/(100A_M)$ and $\chi_{[M]} = A_{steel}[M]/(100A_M)$ are the molar fractions of the total mass concentration, M_0 (wt%,) of the given element in the steel composition, and the dissolved concentration [M] (wt%) for the element *M*. A_{steel} and A_M are the atomic mass of the steel

matrix and element *M*. A similar relation holds for element *X* in Eq. (2.18). It indicates that total concentration of each alloying element is divided into that in solution and that in precipitate form. The molar fraction $\chi_{M_xX_y}$ of precipitate M_xX_y is the product of the activity of this precipitate and its corresponding molar fraction of the precipitate group:

$$\chi_{M_xX_y} = a_{M_xX_y}\chi_g \tag{2.19}$$

where χ_g is the molar fraction of mutually soluble precipitate group *g* which contains precipitate M_xX_y. For example, the group $g = (Ti, Nb, V)(C, N)$ contains M_xX_y precipitates *TiN*, *NbN*, *VN*, *TiC*, $NbC_{0.87}$ and/or V_4C_3.

Generally, there are **P** equations for the solubility limits of **P** precipitates, **M** equations for mass balances of **M** alloying elements, and **Q** extra constraint equations for **Q** groups of mutually soluble precipitates. The total number of equations is **P+M+Q**. In addition, there are **M** unknown dissolved concentrations of the **M** alloying elements, **R** molar concentrations of the **R** groups of mutually exclusive precipitates, **Q** molar concentrations of the **Q** groups of mutually-soluble precipitates, and **P-R** mutually soluble coefficients. Thus the total number of unknowns is also **M+Q+P**. The current study includes **P=18** precipitates, **M=13** alloying elements, and **Q=4** mutually soluble groups, giving **35** equations and **35** unknowns. With an equal number of equations and unknowns, the equation system can be solved by suitable numerical method. It is also worth to mention that most of the above equations are general and satisfied for the whole precipitation process no matter whether the system is under equilibrium. But if solubility product equation (2.4) is satisfied, the calculated values are all for equilibrium state. In order to clear the ambiguity, the equilibrium values in this work are labeled by an under script such as $[M]_{eq}$, comparing with the transient concentration [M], which changes from the initial concentration M_0 to the equilibrium concentration $[M]_{eq}$ during precipitation.

2.2.4 Numerical Solution Details

The above equations are solved simultaneously using a simple iterative scheme. To achieve faster convergence, the method takes advantage of the fact that results are desired over a wide temperature range, as it runs incrementally from above the solidus temperature to below the austenite to α-ferrite transformation temperature. Starting at a high temperature in liquid steel, complete solubility of every precipitate phase is obtained. Temperature is lowered at each time

step, using the results from the previous step as the initial guess. The 35 equations are solved by Newton-Raphson method until the largest absolute error between left and right sides of all equations converges to less than 10^{-6}. The (35×35) matrix of the derivatives of the equations with respect to the unknowns is calculated analytically. The solution of this system of equations F_i is given as

$$z_{k+1} = z_k - \lambda J(z_k)^{-1} F(z_k) \tag{2.20}$$

The Jacobian matrix J is computed from

$$\{J(z)\}_{ij} = \frac{\partial F_i(z)}{\partial z_j} \tag{2.21}$$

The parameter λ is continuously halved from unity until the norm of the equations system decreases. After solving the equations, the dissolved concentrations of each alloying element and the amounts of each precipitate formed at equilibrium are stored at each temperature.

The computational time is typically smaller than 0.1s for each temperature, so the current model gives a relatively quick prediction of the equilibrium phases for microalloyed steels. Such an efficient model is efficient for coupling into a kinetic model.

The molar concentration of precipitate can be transformed to the mass concentration or volume fraction in steels. For precipitate M_xX_y, its mass concentration $w_{M_xX_y}$ (wt%), and volume fraction $\varphi_{M_xX_y}$ are calculated from its molar fraction $\chi_{M_xX_y}$, as follows:

$$w_{M_xX_y} = \frac{100 A_{M_xX_y}}{A_{steel}} \chi_{M_xX_y} \tag{2.22}$$

$$\varphi_{M_xX_y} = \frac{\rho_{steel}}{\rho_{M_xX_y}} \frac{A_{M_xX_y}}{A_{steel}} \chi_{M_xX_y} \tag{2.23}$$

where A_{steel} and $A_{M_xX_y}$ are the atomic mass, and ρ_{steel} and $\rho_{M_xX_y}$ are the density of the steel matrix and precipitate separately. As the alloy additions are small, these properties of steel are simply taken to be constants (55.85g/mol and 7500kg/m^3).

2.3 Influence of Mutual Solubility

2.3.1 Validation with Analytical Solutions of Mutually Exclusive Precipitates

For simple single-precipitate systems with y/x=1, such as NbN, Wagner interaction can be neglected and the element activities are equal to their dissolved mass concentration in the very

dilute systems. The first precipitate occurs when the product of the initial concentrations, Nb_0 and N_0, exceeds K_{NbN}. After NbN forms, the solubility limit requires

$$[Nb]_{eq}[N]_{eq} = K_{NbN} \tag{2.24}$$

The stoichiometry requirement for this chemical reaction is

$$\frac{Nb_0 - [Nb]_{eq}}{A_{Nb}} = \frac{N_0 - [N]_{eq}}{A_N} \tag{2.25}$$

The analytical solution can be summarized as

(a). At high temperature, when $Nb_0 * N_0 \leq K_{NbN}$, there are no precipitates

(b). At lower temperature, when $Nb_0 * N_0 > K_{NbN}$

$$[N]_{eq} = \frac{(A_{Nb}N_0 - A_N Nb_0) + \sqrt{(A_{Nb}N_0 - A_N Nb_0)^2 + 4A_{Nb}A_N K_{NbN}}}{2A_{Nb}}$$

$$[Nb]_{eq} = \frac{-(A_{Nb}N_0 - A_N Nb_0) + \sqrt{(A_{Nb}N_0 - A_N Nb_0)^2 + 4A_{Nb}A_N K_{NbN}}}{2A_N}$$

$$(w_{NbN})_{eq} = (A_{Nb} + A_N)\left(\frac{(A_{Nb}N_0 + A_N Nb_0) - \sqrt{(A_{Nb}N_0 - A_N Nb_0)^2 + 4A_{Nb}A_N K_{NbN}}}{2A_{Nb}A_N}\right) \tag{2.26}$$

For mutually exclusive precipitates composing with y/x=1, if these precipitates do not share any alloying elements, the analytical solution is simply two sets of equations like those for NbN. Alternatively, if they share a common element, such as with Nb-Al-N system with NbN and AlN, all of the different possible conditions, such as $Nb_0 * N_0 > K_{NbN}$ and $Al_0 * N_0 > K_{AlN}$, are tested to find which precipitate forms first. After one precipitate forms, the initial nitrogen concentration is replaced with its dissolved value to judge whether the other precipitate forms or not and the results change if both precipitates form.

If both precipitates form, the solubility limits and chemical reaction require

$$[Nb]_{eq}[N]_{eq} = K_{NbN} \tag{2.27}$$

$$[Al]_{eq}[N]_{eq} = K_{AlN} \tag{2.28}$$

$$\frac{Nb_0 - [Nb]_{eq}}{A_{Nb}} + \frac{Al_0 - [Al]_{eq}}{A_{Al}} = \frac{N_0 - [N]_{eq}}{A_N} \tag{2.29}$$

The solution can be summarized as

(a). At high temperature, when $Nb_0 * N_0 \leq K_{NbN}$ and $Al_0 * N_0 \leq K_{AlN}$, there is no precipitate

(b). At low temperature, when either $Nb_0*N_0>K_{NbN}$ and $Al_0*N_0>K_{AlN}$ is satisfied

(i). If $Nb_0*N_0>K_{NbN}$, the solution is given like a single NbN case

(ii). If $Al_0*N_0>K_{AlN}$, the solution is similar to Eq. (2.26), but all values of Nb are replaced with the corresponding values of Al instead.

(c). If the temperature continues to decrease so that both $Nb_0*N_0>K_{NbN}$ and $Al_0*N_0>K_{AlN}$ are satisfied, Nb_0*N_0/K_{NbN} and Al_0*N_0/K_{AlN} are computed and compared

(i). If Nb_0*N_0/K_{NbN} is larger, the following condition is checked

$$Al_0 * [N]_{eq} > K_{AlN} \tag{2.30}$$

If true, then both precipitates form. Otherwise, only NbN precipitates exist.

(ii). If Al_0*N_0/K_{AlN} is larger, the next condition is checked

$$Nb_0 * [N]_{eq} > K_{NbN} \tag{2.31}$$

If true, then both precipitates form. Otherwise, only AlN precipitates exist.

(iii). If both precipitates form

$$[N]_{eq} = \frac{[A_{Nb}A_{Al}N_0 - A_N(A_{Nb}Al_0 + A_{Al}Nb_0)]}{2A_{Nb}A_{Al}} + \frac{\sqrt{[A_{Nb}A_{Al}N_0 - A_N(A_{Nb}Al_0 + A_{Al}Nb_0)]^2 + 4A_{Nb}A_{Al}A_N(A_{Nb}K_{AlN} + A_{Al}K_{NbN})}}{2A_{Nb}A_{Al}}$$

$$[Nb]_{eq} = \frac{-K_{NbN}[A_{Nb}A_{Al}N_0 - A_N(A_{Nb}Al_0 + A_{Al}Nb_0)]}{2A_N(A_{Nb}K_{AlN} + A_{Al}K_{NbN})} + \frac{K_{NbN}\sqrt{[A_{Nb}A_{Al}N_0 - A_N(A_{Nb}Al_0 + A_{Al}Nb_0)]^2 + 4A_{Nb}A_{Al}A_N(A_{Nb}K_{AlN} + A_{Al}K_{NbN})}}{2A_N(A_{Nb}K_{AlN} + A_{Al}K_{NbN})}$$

$$[Al]_{eq} = \frac{-K_{AlN}[A_{Nb}A_{Al}N_0 - A_N(A_{Nb}Al_0 + A_{Al}Nb_0)]}{2A_N(A_{Nb}K_{AlN} + A_{Al}K_{NbN})} + \frac{K_{AlN}\sqrt{[A_{Nb}A_{Al}N_0 - A_N(A_{Nb}Al_0 + A_{Al}Nb_0)]^2 + 4A_{Nb}A_{Al}A_N(A_{Nb}K_{AlN} + A_{Al}K_{NbN})}}{2A_N(A_{Nb}K_{AlN} + A_{Al}K_{NbN})}$$

$$(w_{NbN})_{eq} = (A_{Nb} + A_N)\left[\frac{K_{NbN}(A_{Nb}A_{Al}N_0 + A_N(A_{Al}Nb_0 - A_{Nb}Al_0)) + 2A_{Nb}A_N Nb_0 K_{AlN}}{2A_{Nb}A_N(A_{Nb}K_{AlN} + A_{Al}K_{NbN})} - \frac{K_{NbN}\sqrt{[A_{Nb}A_{Al}N_0 - A_N(A_{Nb}Al_0 + A_{Al}Nb_0)]^2 + 4A_{Nb}A_{Al}A_N(A_{Nb}K_{AlN} + A_{Al}K_{NbN})}}{2A_{Nb}A_N(A_{Nb}K_{AlN} + A_{Al}K_{NbN})}\right]$$

$$(w_{AlN})_{eq} = (A_{Al} + A_N)\left[\frac{K_{AlN}(A_{Nb}A_{Al}N_0 + A_N(A_{Nb}Al_0 - A_{Al}Nb_0)) + 2A_{Al}A_N Al_0 K_{NbN}}{2A_{Al}A_N(A_{Nb}K_{AlN} + A_{Al}K_{NbN})} \right.$$

$$\left. - \frac{K_{AlN}\sqrt{[A_{Nb}A_{Al}N_0 - A_N(A_{Nb}Al_0 + A_{Al}Nb_0)]^2 + 4A_{Nb}A_{Al}A_N(A_{Nb}K_{AlN} + A_{Al}K_{NbN})}}{2A_{Al}A_N(A_{Nb}K_{AlN} + A_{Al}K_{NbN})} \right] \quad \textbf{(2.32)}$$

For mutually-exclusive precipitates which share alloying elements, the formation of the first precipitate phase changes the dissolved concentration of shared elements and delays the formation of other precipitates. The interaction parameters are all set to zero for numerical simulation of these test cases. Figure 2.2 shows that the numerical results match the analytical solution very well for all three hypothetical steels. By adding 0.02%Al into steel with 0.02%Nb and 0.02%N, AlN forms first, consumes some of the dissolved nitrogen which delays the formation of NbN precipitate, and decreases the equilibrium amount of NbN. Instead, if 0.01%B is added to the 0.02%Nb and 0.02%N steel, the early precipitation of BN delays NbN to form at an even lower temperature. This is because BN has a lower solubility limit and reacts with more nitrogen in forming BN because of a lower atomic mass of boron.

A precipitation diagram for the Nb-Al-N-Fe system at different temperatures in austenite was calculated from the current model and shown in Figure 2.3. The sum of the mass concentration of elements Nb, Al and N is set as 0.05wt%. Each curve in this diagram shows the boundary between stable and unstable precipitation of AlN or NbN in these hypothetical steels. At 1300^{o}C, AlN forms first because of its lower solubility limit. The composition region for stable AlN precipitation increases with decreasing temperature. When temperature drops below 1150^{o}C, either AlN or NbN may exist for certain compositions. Finally, at temperatures below 1125^{o}C, either AlN, NbN or both precipitates could coexist. Similar progressions occur in other systems.

2.3.2 Calculation for Mutual Soluble Precipitates

A prediction of mutually-soluble precipitation is shown in Figure 2.4 for a hypothetical Ti-Nb-N steel with 0.01%Nb, 0.01%N and 0.005%Ti. The precipitates form as the single group (Ti,Nb)N, and even for this simple example of mutually-soluble system, an analytical solution could not be found. In addition to precipitate amounts, Figure 2.4 shows how the precipitate composition evolves with decreasing temperature. For example, at 1300^{o}C, the precipitate group composition is 72%Ti, 6%Nb and 22%N, which corresponds to the molar-fraction expression

$Ti_{0.48}Nb_{0.02}N_{0.50}$. When titanium is present, TiN is the dominant precipitate at high temperature, owing to its high stability. Its molar fraction $(f_{TiN})_{eq}$ decreases at lower temperature, as NbN forms from the remaining N, and increases the Nb content of the precipitate. This result is consistent with experimental findings, such as Strid [132] and Craven [133], where the core of complex carbonitrides is mainly TiN. The model suggests that precipitates generated at high temperature are Ti-rich, and the precipitate layers that form later become richer in Nb as the temperature lowers. Figure 2.4(a) also shows results for the same steel without Ti. With mutual solubility, adding titanium remarkably increases the initial precipitation temperature and decreases the equilibrium activity of NbN, which allows more NbN to form. If TiN and NbN were mutually exclusive, then adding titanium would decrease NbN precipitation. This result illustrates the importance of proper consideration of mutual solubility in the model.

2.4 Validation with Commercial Packages and Experimental Measurements

2.4.1 Validation with Commercial Package

The chemical composition of the two commercial steels in this work, 1004 LCAK (low carbon aluminum killed) and 1006Nb HSLA (high strength low alloy), are given in Table 2.5. The results from the commercial package JMatPro 5.0 with general steel submodule [134] and the current model are compared in Figure 2.5. The JMatPro predicts separate precipitation of a TiN-rich "MN" phase at higher temperatures and a NbC-rich "M(C,N)" phase at lower temperatures. These are treated together as a single (Ti,Nb,V)(C,N) phase with evolving composition in the current model, as previously mentioned. The oxide M_2O_3 predicted by JMatPro corresponds with the (Al,Ti)O phase in the current model.

The comparison shows qualitative agreement for the predicted precipitate types, and the amounts of (Al,Ti,)O, MnS, and (Ti,Nb,V)(C,N) between the two models are all similar. For the latter phase group, JMatPro predicts a double-humped curve, owing to its two precipitate groups, MN and M(C,N), which is roughly approximated by a single smooth curve with the current model. The composition of (Ti,Nb,V)(C,N) in the current model also matches reasonably with the average composition of the two precipitate groups in JMatPro. For example, in 1006Nb steel the calculated composition is $Ti_{0.48}Nb_{0.02}V_{0.00}C_{0.00}N_{0.50}$ at 1304°C and $Ti_{0.28}Nb_{0.22}V_{0.00}C_{0.23}N_{0.27}$ at 804°C for JMatPro, and $Ti_{0.47}Nb_{0.03}V_{0.00}C_{0.02}N_{0.48}$ at 1304°C and $Ti_{0.29}Nb_{0.21}V_{0.02}C_{0.14}N_{0.35}$ at 804°C for the current model. The current model predicts that (Ti,Nb,V)(C,N) and MnS first form

in the δ-ferrite phase, but dissolve after the transformation to austenite, where the solubilities are larger. This trend is missing in JMatPro. JMatPro consistently predicts more AlN than the current model, likely due to having less solubility for this precipitate in its database. Below 800°C, a jump in AlN is predicted by JMatPro. This is because cementite transformation is ignored in the current model. The carbon-rich Fe_3C phase provides plenty of carbon to allow MN and M(C,N) to form nearly as pure carbide, which leaves more nitrogen to react with Al. In conclusion, the differences between the two models are not considered to be significant, considering that both models neglect the important effects of kinetics.

2.4.2 Validation with Measured Equilibrium-Precipitated Nb Amount

Zajac and Jansson [135] investigated equilibrium precipitation in several Nb-based industrial microalloyed steels, including the two compositions shown in Table 2.6. The steels were first solution treated at 1300°C or 1350°C for 1 hour to dissolve precipitates followed by quick water quenching. Then, specimens were heated and aged at two different temperatures isothermally for 24 to 48 hours. The precipitated amount of Nb in Nb(C,N) was measured by the inductively coupled plasma (ICP) emission method on electrolytically extracted compounds for each sample. Figure 2.6 compares these experimental measurements with calculated results of precipitated niobium amount for these two steels, and shows that the current model matches well with the experimental data.

2.4.3 Validation with Observed Titanium Precipitate Types

Titanium sulfide and titanium carbosulfide are also observed in high-titanium steels. The equilibrium precipitation behavior of titanium stabilized interstitial free steels was studied quantitatively using dissolution experiments by Yang *et al* [103]. Several steels with different compositions were reheated at different temperatures varying from 1100°C to 1350°C and the holding time to reach the equilibrium state varied from 1.5 to 3 hours for different reheating temperatures. The steel compositions and the types of precipitates observed at each holding temperature in the experiments are listed in Tables 2.7 and 2.8 respectively. The calculated molar fractions of the precipitates in these steels with temperature are shown in Figure 2.7. The model predictions are consistent with the observed stability of these precipitates. The oxide Al_2O_3 begins to form in the liquid steel, so was likely removed by the flux/slag, and not recorded

in the experiments.

2.4.4 Validation with Measured Inclusion Compositions for Welding

Inclusion formation in steel welds is important to decide the final microstructure and improve toughness in welds. It is also a good resource to validate the current model since many measurements are available in the literature. Kluken and Grong [136] measured the inclusion compositions in term of average element concentrations of aluminum, titanium, manganese, silicon, sulfur and copper in nine submerged arc welds with different steel compositions using the wavelength dispersive X-ray (EDX) intensity analysis and carbon extraction replicas method. The observed inclusions in the solidified weld pool consist of an oxide core forming due to reoxidation in the liquid state, and are covered partially by sulfides and nitrides on their surfaces. Simple empirical relations were suggested to compute the dissolved concentrations of alloying elements to match the measurements, and the order of precipitate formation was always Al_2O_3, Ti_2O_3, SiO_2, MnO, MnS and TiN regardless of the weld composition.

Hsieh [137] used Thermo-Calc software to predict inclusion development in these low-alloy-steel welds. Multi-phase equilibrium between oxides and liquid steel was assumed since the precipitation reactions are very fast at these high temperatures. The oxidation sequence was found to be sensitive to small changes in the weld composition. The calculation stopped at liquidus temperature 1527^{o}C, so the possible formation of sulfides, nitrides and carbides after solidification was not found.

The distributions of various precipitated compounds in the inclusions are computed by the current model as functions of steel composition. Since precipitates including copper are not considered in this study, the original measured inclusion composition data were normalized to make the sum of the mass concentration of aluminum, titanium, manganese, silicon and sulfur total 100%, in order to allow for a proper comparison. The chemical compositions of the experimental welds are given in Table 2.9. A comparison of the calculated inclusion compositions at 1527^{o}C in liquid steel and 1250^{o}C in austenite with the measurements is shown in Figure 2.8, and reasonable agreement is found especially at 1250^{o}C, after high temperature solid-state reactions alter the normalized compositions, but before kinetics stops the diffusion (slope=0.644 and correlation coefficient=0.911 at 1527^{o}C, slope=0.988 and correlation coefficient=0.932 at 1250^{o}C). It indicates that the current model can be used as a first

approximation to describe the formation of complex inclusions for different weld metal compositions. The agreement is likely adversely affected by the lack of consideration of kinetics and segregation during solidification in the current model.

2.5 Tables and Figures

Table 2.1: Lattice parameters and solubility products of precipitates

Composition (mass percent)	**Crystal form Lattice parameter**	$\log_{10} K_l$	$\log_{10} K_{\alpha,\delta}$	$\log_{10} K_\gamma$
Al_2O_3 $[\%Al]^2[\%O]^3$	Hexagonal[88] $a = 4.76\,\text{Å}, c = 13.0\,\text{Å}$	$-\frac{64000}{T} + 20.57$[96]	$-\frac{51630}{T} + 7.55$*	$-\frac{51630}{T} + 9.45$[101]
Ti_2O_3 $[\%Ti]^2[\%O]^3$	Hexagonal[89] $a = 5.16\,\text{Å}, c = 13.6\,\text{Å}$	$-\frac{56060}{T} + 18.08$[97]	$-\frac{56060}{T} + 14.08$*	$-\frac{56060}{T} + 15.98$*
MgO [%Mg][%O]	f.c.c[88] $a = 4.21\,\text{Å}$	$-\frac{4700}{T} - 4.28$[98]	$-\frac{4700}{T} - 6.28$*	$-\frac{4700}{T} - 5.33$*
MnO [%Mn][%O]	f.c.c[90] $a = 4.45\,\text{Å}$	$-\frac{11749}{T} + 4.666$[99]	$-\frac{11749}{T} + 2.666$*	$-\frac{11749}{T} + 3.616$*
SiO_2 $[\%Si][\%O]^2$	Trigonal[91] $a = 4.91\,\text{Å}, c = 5.41\,\text{Å}$	$-\frac{30110}{T} + 11.40$[100]	$-\frac{30110}{T} + 9.40$*	$-\frac{30110}{T} + 10.35$*
MnS [%Mn][%S]	f.c.c[92] $a = 5.22\,\text{Å}$	$-\frac{9020}{T} + 3.98$*	$-\frac{9020}{T} + 1.98$*	$-\frac{9020}{T} + 2.93$[102]
MgS [%Mg][%S]	f.c.c[92] $a = 5.20\,\text{Å}$	$-\frac{9268}{T} + 2.06$*	$-\frac{9268}{T} + 0.06$*	$-\frac{9268}{T} + 1.01$[103]
TiS [%Ti][%S]	Trigonal[93] $a = 3.30\,\text{Å}, c = 26.5\,\text{Å}$	$-\frac{13975}{T} + 6.48$*	$-\frac{13975}{T} + 4.48$*	$-\frac{13975}{T} + 5.43$[104]
$Ti_4C_2S_2$** $[\%Ti]^4[\%C]^2[\%S]^2$	Hexagonal[93] $a = 3.30\,\text{Å}, c = 11.2\,\text{Å}$	$-\frac{68180}{T} + 35.8$*	$-\frac{68180}{T} + 27.8$*	$-\frac{68180}{T} + 31.6$[104]
AlN [%Al][%N]	Hexagonal[36] $a = 3.11\,\text{Å}, c = 4.97\,\text{Å}$	$-\frac{12950}{T} + 5.58$[100]	$-\frac{8790}{T} + 2.05$[100]	$-\frac{6770}{T} + 1.03$[100]
BN [%B][%N]	Hexagonal[94] $a = 2.50\,\text{Å}, c = 6.66\,\text{Å}$	$-\frac{10030}{T} + 4.64$[100]	$-\frac{14250}{T} + 4.61$[100]	$-\frac{13970}{T} + 5.24$[100]
NbN [%Nb][%N]	f.c.c[36] $a = 4.39\,\text{Å}$	$-\frac{12170}{T} + 6.91$*	$-\frac{12170}{T} + 4.91$[100]	$-\frac{10150}{T} + 3.79$[100]
$NbC_{0.87}$ $[\%Nb][\%C]^{0.87}$	f.c.c[36] $a = 4.46\,\text{Å}$	$-\frac{9830}{T} + 6.33$*	$-\frac{9830}{T} + 4.33$[100]	$-\frac{7020}{T} + 2.81$[100]
TiN [%Ti][%N]	f.c.c[36] $a = 4.23\,\text{Å}$	$-\frac{17040}{T} + 6.40$[100]	$-\frac{18420}{T} + 6.40$[100]	$-\frac{15790}{T} + 5.40$[100]
TiC [%Ti][%C]	f.c.c[36] $a = 4.31\,\text{Å}$	$-\frac{6160}{T} + 3.25$[100]	$-\frac{10230}{T} + 4.45$[100]	$-\frac{7000}{T} + 2.75$[100]
VN [%V][%N]	f.c.c[36] $a = 4.12\,\text{Å}$	$-\frac{9720}{T} + 5.90$*	$-\frac{9720}{T} + 3.90$[100]	$-\frac{7700}{T} + 2.86$[100]
V_4C_3** $[\%V]^4[\%C]^3$	f.c.c[36] $a = 4.15\,\text{Å}$	$-\frac{28200}{T} + 24.96$*	$-\frac{28200}{T} + 16.96$[100]	$-\frac{26240}{T} + 17.8$[100]
Cr_2N $[\%Cr]^2$ [%N]	Trigonal[95] $a = 4.76\,\text{Å}, c = 4.44\,\text{Å}$	$-\frac{1092}{T} - 0.131$*	$-\frac{1092}{T} - 2.131$*	$-\frac{1092}{T} - 1.181$[105]

* Estimated values used in the present work; temperature is in Kelvin

** For consistency, these solubility products are rewritten in the form M_xX_y, according to the relationship $\log_{10} K_{M_xX_y} = x \log_{10} K_{MX_{y/x}}$

Table 2.2: Selected interaction coefficients in dilute solutions of microalloyed steel

Element j	e_N^j	e_C^j	e_S^j	e_O^j	e_{Ti}^j	e_{Nb}^j
N	6294/T[106]	5790/T[109]	0.007[100]	0.057[113]	19500/T+8.37[110]	-
C	0.06[100]	8890/T[107]	0.11[100]	-0.42[96]	-221/T-0.072[96]	-
S	0.007[100]	0.046[100]	-8740/T-0.394[108]	-0. 133[113]	-0.27[96]	-
O	0.05[100]	-0.34[100]	-0.27[100]	1750/T+0.76[96]	-3.4[96]	-
Ti	-5700/T+2.45[110]	-55/T-0.015[96]	-0.072[113]	-1.12[96]	0.042[96]	-.
Nb	-235/T+0.055[111]	-66257/T[117]	-.	-	-	-2[109]
V	356/T+0.0973[112]	-	-	-	-	-
Al	-0.028[113]	0.043[100]	0.035[113]	-1.17[96]	0.93[121]	-
Mn	-8336/T-27.8 +3.652lnT[114]	-5070/T[118]	-0.026[100]	-0.021[96]	-0.043[96]	-
Mg	-	-0.07[113]	-	-1.98[96]	-1.01[122]	-
Si	-286/T+0.202[115]	162/T-0.008[113]	0.063[100]	-0.066[96]	177.5/T-0.12[115]	77265/T-44.9[117]
B	1000/T-0.437[116]	-	-	-	-	-
Cr	65150/T+24.1[114]	21880/T+7.02[119]	-0.011[113]	-0.046[120]	-0.016[120]	216135/T+140.8[117]

Element j	e_V^j	e_{Al}^j	e_{Mn}^j	e_{Mg}^j	e_{Si}^j	e_B^j	e_{Cr}^j
N	-.	0.058[113]	-	-	-	-	-
C	-	0.091[96]	-0.0538[96]	-0.25[122]	0.18[96]	-	-0.12[113]
S	-	0.035[96]	28418/T+12.8[102]	-	0.066[96]	-	153/T+0.062[113]
O	-	-1.98[96]	-0.083[96]	-3[96]	-0.119[96]	-	-0.14[113]
Ti	-	0.004[121]	-0.05[96]	-0.51[122]	1.23[96]	-	0.059[113]
Nb	-	-	-	-	-	-	-
V	470/T-0.22[123]	-	-	-	-	-	-
Al	-	0.043[96]	0.027[124]	-0.12[122]	0.058[96]	-	0.023[120]
Mn	-	0.035[124]	175.6/T+2.406[106]	-	-0.0146[96]	-	0.0039[96]
Mg	-	-0.13[122]	-	-	-	-	0.042[125]
Si	-	0.056[96]	-0.0327[96]	-0.088[96]	0.103[96]	-	-0.0043[113]
B	-	-	-	-	-	0.038[116]	-
Cr	-	0.012[120]	0.0039[96]	0.047[122]	-0.0003[96]	-	-0.0003[113]

-.: not found value in literature, they are assumed to be zero in current calculation

Table 2.3: Mutually-soluble precipitate groups and their precipitates

Mutually-soluble precipitate group	Precipitate types involved
(Ti,Nb,V)(C,N)	*TiN*, *NbN*, *VN*, *TiC*, $NbC_{0.87}$, V_4C_3,
(Al,Ti)O	Al_2O_3, Ti_2O_3
(Mn,Mg)O	*MnO*, *MgO*
(Mn,Mg)S	*MnS*, *MgS*

Table 2.4: Precipitates considered for each alloying-element mass balance

Element	Groups of precipitates	Types of precipitates
N	*(Ti,Nb,V)(C,N)*, *AlN*, *BN*, Cr_2N	*TiN*, *NbN*, *VN*, *AlN*, *BN*, Cr_2N
C	*(Ti,Nb,V)(C,N)*, $Ti_4C_2S_2$	*TiC*, $NbC_{0.87}$, V_4C_3, $Ti_4C_2S_2$
S	*(Mn,Mg)S*, *TiS*, $Ti_4C_2S_2$	*MnS*, *MgS*, *TiS*, $Ti_4C_2S_2$
O	*(Al,Ti)O*, *(Mn,Mg)O*, SiO_2	Al_2O_3, Ti_2O_3, *MnO*, *MgO*, SiO_2
Ti	*(Ti,Nb,V)(C,N)*, *(Al,Ti)O*, *TiS*, $Ti_4C_2S_2$	*TiN*, *TiC*, Ti_2O_3, *TiS*, $Ti_4C_2S_2$
Nb	*(Ti,Nb,V)(C,N)*	*NbN*, $NbC_{0.87}$
V	*(Ti,Nb,V)(C,N)*	*VN*, V_4C_3
Al	*(Al,Ti)O*, *AlN*	Al_2O_3, *AlN*
Mn	*(Mn,Mg)O*, *(Mn,Mg)S*	*MnO*, *MnS*
Mg	*(Mn,Mg)O*, *(Mn,Mg)S*	*MgO*, *MgS*
Si	SiO_2	SiO_2
B	*BN*	*BN*
Cr	Cr_2N	Cr_2N

Table 2.5: Compositions of 1004 LCAK and 1006Nb HSLA steels (weight percent)

Steel	Al	C	Cr	Mn	Mo	N	Nb	S	Si	Ti	V	O
1004 LCAK	0.040	0.025	0.025	0.141	0.007	0.006	0.002	0.0028	0.028	0.0013	0.001	0.00015
1006Nb HSLA	0.0223	0.0472	0.0354	0.9737	0.0085	0.0083	0.0123	0.0013	0.2006	0.0084	0.0027	0

Table 2.6: Compositions of Nb-based microalloyed steels (wt%)

Steel	C	Si	Mn	P	S	Nb	Al	N	V	Ti
Nb4	0.158	0.28	1.48	0.008	0.002	0.010	0.016	0.005	0.013	0.003
Nb8	0.081	0.31	1.44	0.010	0.002	0.033	0.017	0.004	0.011	0.003

Table 2.7: Compositions of Ti-based microalloyed steels (wt%)

Steel	C	Si	Mn	P	S	Al	Ti	N	O
B	0.0036	0.0050	0.081	0.011	0.0028	0.045	0.095	0.0019	0.0028
C	0.0033	0.0040	0.081	0.011	0.0115	0.037	0.050	0.0022	0.0036

Table 2.8: Precipitates observed after holding several hours at different temperatures

Steel	1300°C	1250°C	1200°C	1150°C	1100°C
B	TiN	TiN,TiS*	TiN,TiS	TiN,$Ti_4C_2S_2$	TiN,$Ti_4C_2S_2$
C	TiN,TiS	TiN,TiS	TiN,TiS	TiN,TiS	TiN,<TiS>,$Ti_4C_2S_2$

Note: * means very scarce and < > means minor amount

Table 2.9: Compositions of experimental weld steels (wt%)

Weld	C	O	Si	Mn	P	S	N	Nb	V	Cu	B	Al	Ti
1	0.09	0.034	0.48	1.86	0.010	0.010	0.005	0.004	0.02	0.02	0.0005	0.018	0.005
2	0.09	0.037	0.55	1.84	0.010	0.009	0.005	0.005	0.02	0.03	0.0006	0.020	0.025
3	0.10	0.035	0.69	1.88	0.012	0.010	0.008	0.004	0.02	0.03	0.0008	0.028	0.063
4	0.10	0.030	0.52	1.87	0.010	0.007	0.005	0.007	0.01	0.06	0.0004	0.041	0.005
5	0.09	0.039	0.58	1.95	0.009	0.009	0.005	0.005	0.02	0.03	0.0006	0.037	0.022
6	0.09	0.040	0.69	1.97	0.009	0.009	0.006	0.007	0.02	0.03	0.0006	0.044	0.058
7	0.09	0.032	0.53	1.90	0.009	0.008	0.005	0.006	0.02	0.03	0.0004	0.062	0.008
8	0.10	0.031	0.62	1.92	0.010	0.010	0.005	0.005	0.02	0.03	0.0006	0.062	0.032
9	0.09	0.031	0.62	1.78	0.011	0.007	0.006	0.004	0.01	0.08	0.0006	0.053	0.053

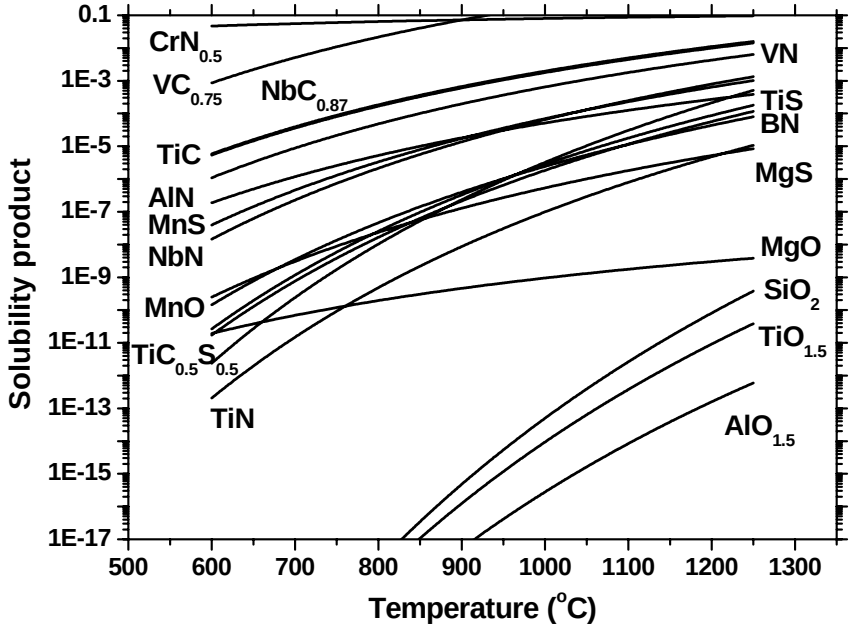

(a). Austenite

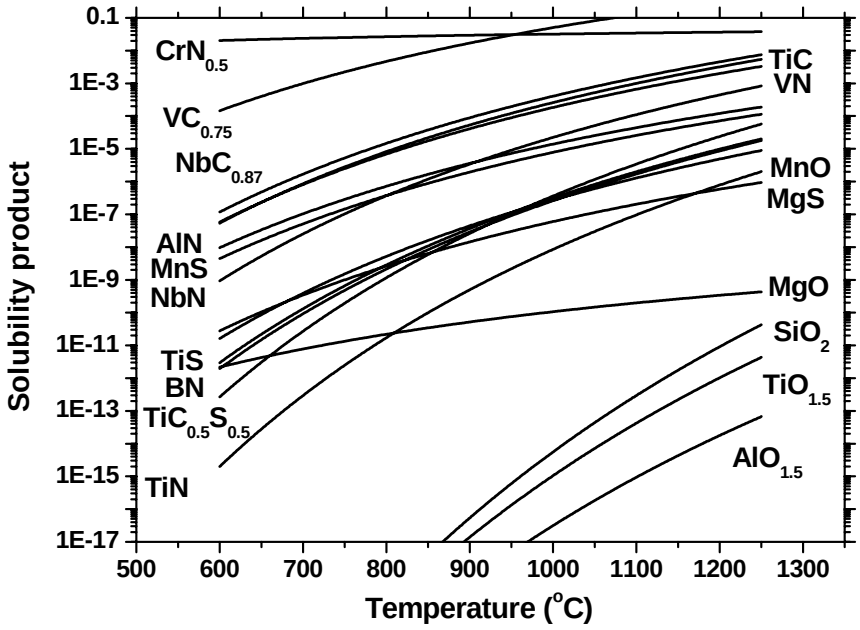

(b). Ferrite

Figure 2.1: Solubility products of various precipitates in austenite and ferrite

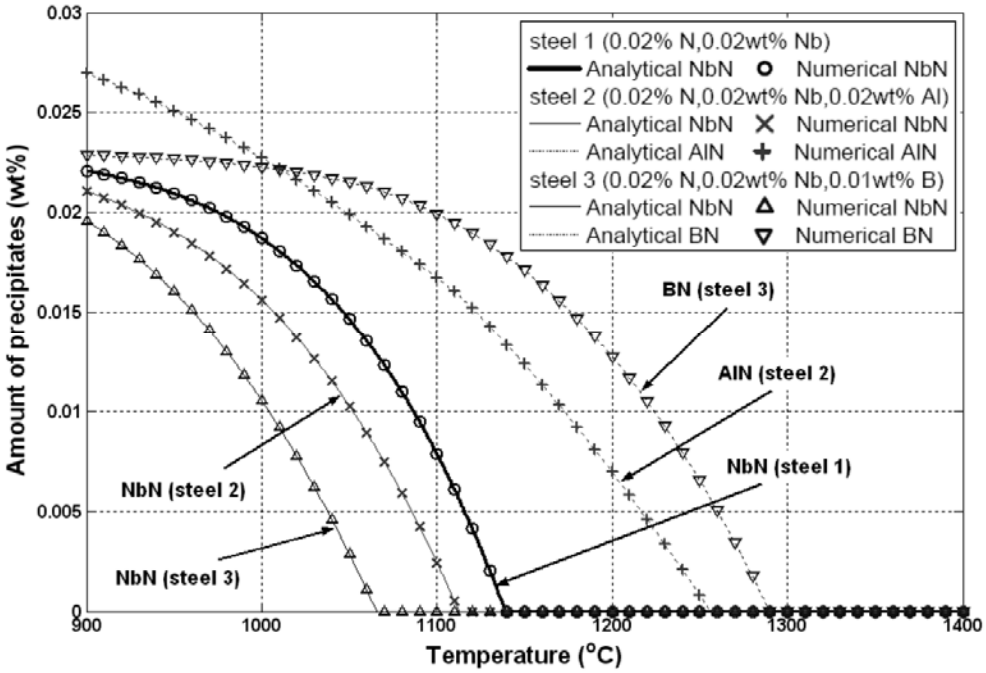

Figure 2.2: Comparison of mutually-exclusive precipitation model predictions with analytical solution in austenite for 3 Fe alloys containing 0.02%N and 0.02%Nb, and either 0.02% Al or 0.01% B

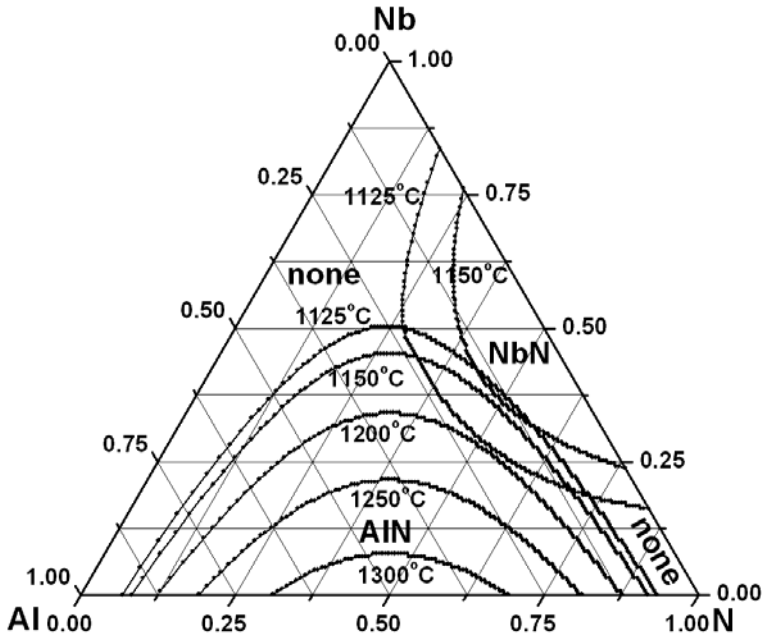

Figure 2.3: Calculated precipitation phase diagram for quaternary Nb-Al-N system with 99.95%Fe

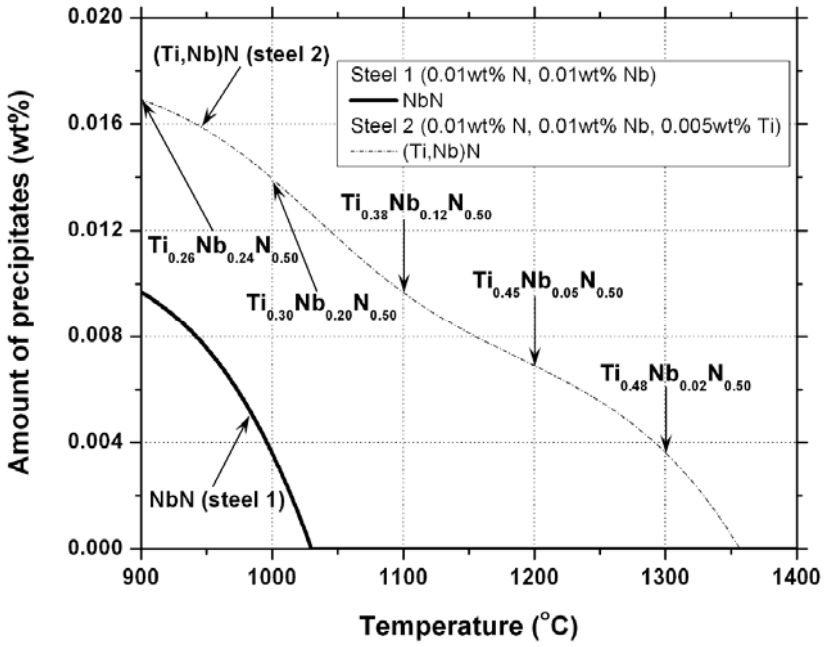

(a). Precipitate amount

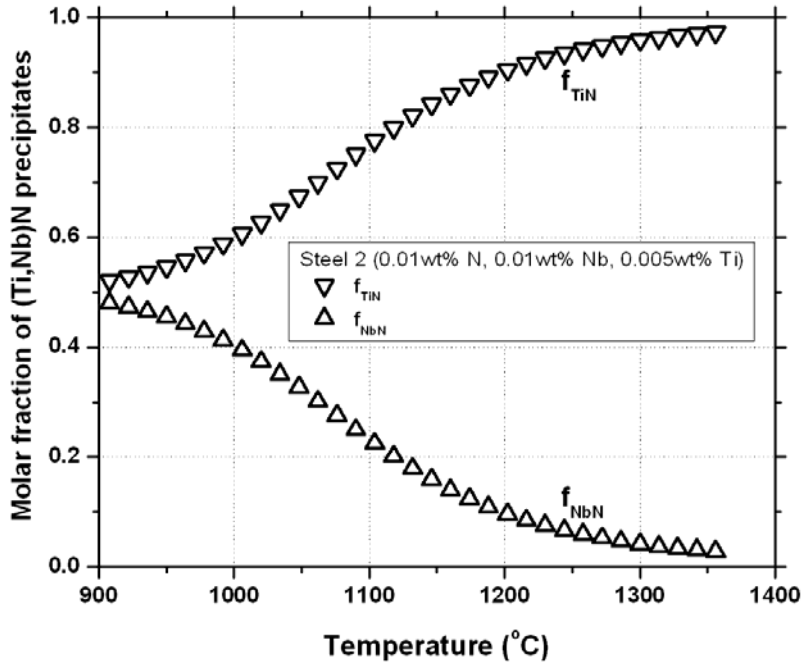

(b). Molar fraction of (Ti,Nb)N precipitates

Figure 2.4: Model calculation of mutually-soluble precipitation in austenite for 2 Fe alloys containing 0.01%N and 0.01%Nb, with and without 0.005%Ti

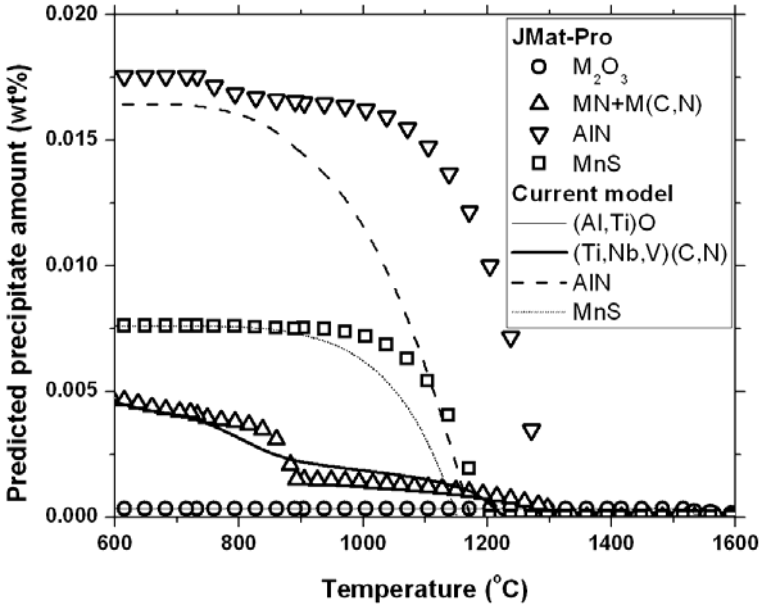

(a). 1004 LCAK steel

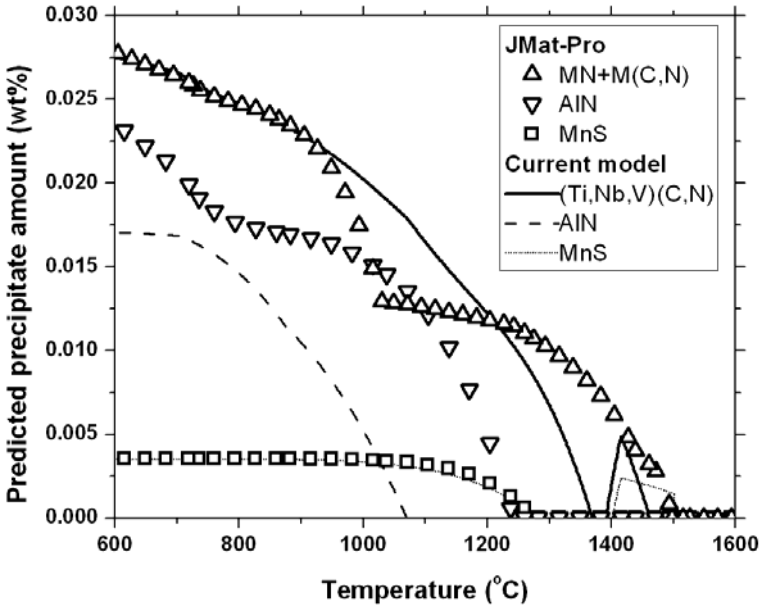

(b). 1006Nb HSLA steel

Figure 2.5: Comparison of precipitate calculations by software JMatPro and the current model

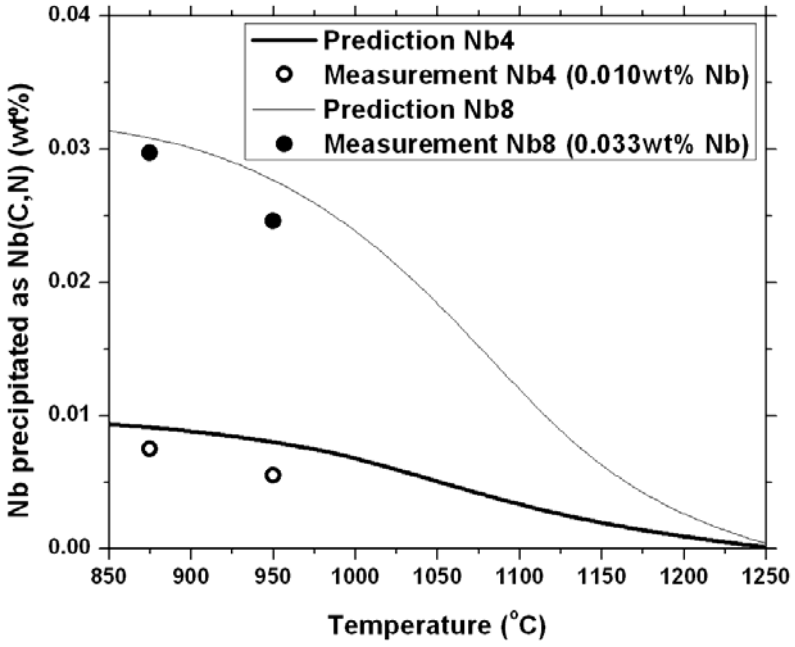

Figure 2.6: Comparison of predicted amounts of Nb precipitation with experimental measurements at different temperatures (Table 2.6 steels [135])

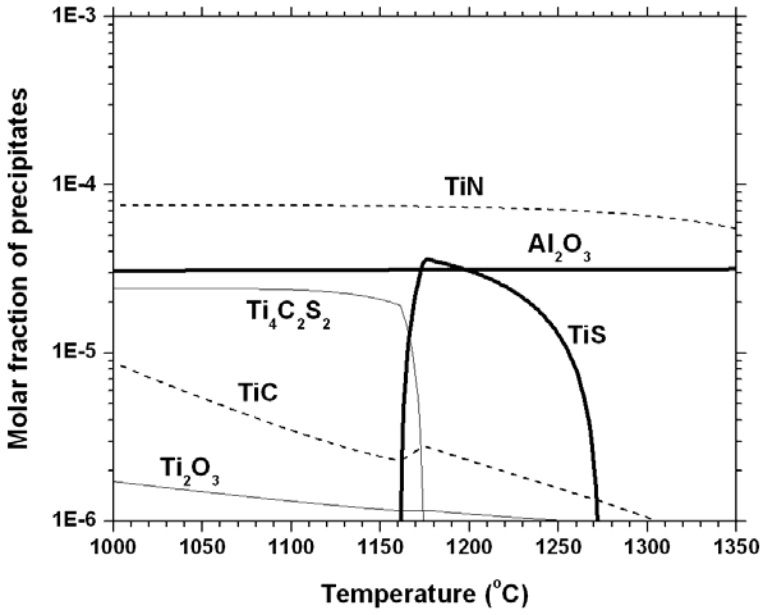

(a). Steel B

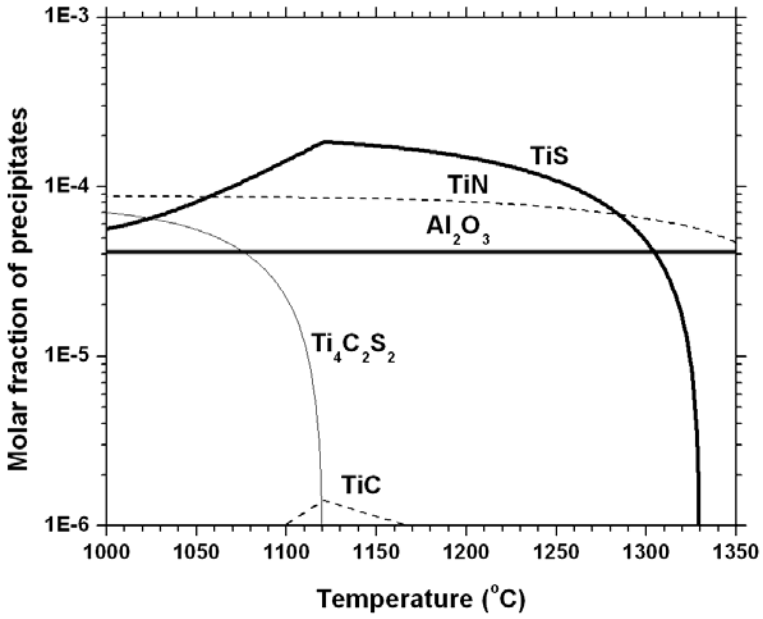

(b). Steel C

Figure 2.7: Calculated molar fractions of precipitates for Ti-steels in Table 2.7

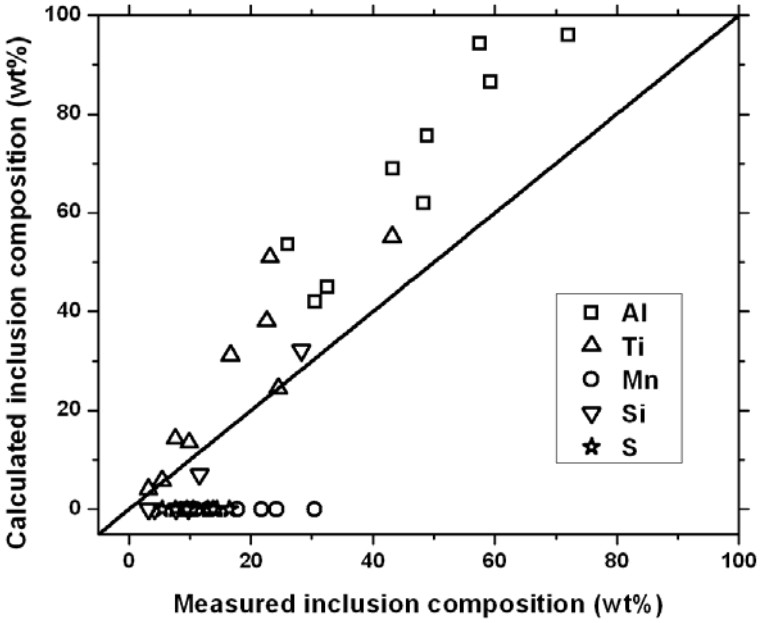

(a). 1527°C (liquidus temperature)

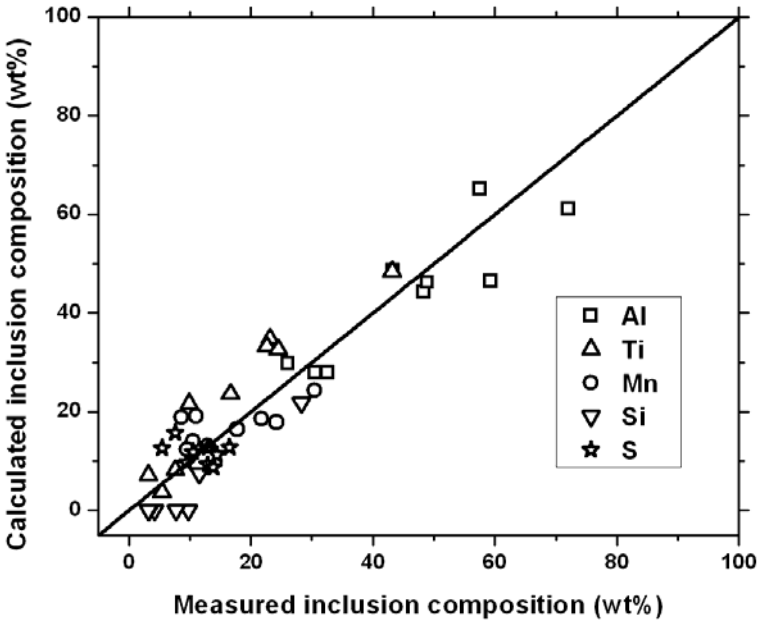

(b). 1250°C

Figure 2.8: Comparison of calculated and measured inclusion compositions for welding metals [136]

CHAPTER 3
KINETIC MODEL OF SINGLE-PHASE PRECIPITATION

An equilibrium model developed in chapter 2 can predict the occurrence, stability, compositions and amounts of precipitates at equilibrium, for the different steel compositions, phases, and temperatures. Theoretically, precipitates start to form when the solubility limit is exceeded, and they can form at different rates, stages and locations during steel processing, including in the liquid steel due to rapid diffusion and collision, the mushy-zone between dendrites and grains due to rapid diffusion in the segregated liquid, and in the solid state due to slow diffusion inside the grains, faster diffusion at the grain boundaries, or along the advancing austenite-ferrite interphase boundary. These different mechanisms cause the precipitate particles to show a variety of compositions, morphologies and size distributions.

The precipitation may be sluggish even if it is thermodynamically most favored in reality, and it is verified in experiments that precipitation may take 10-30 minutes to start, and 1-24 hours to reach equilibrium in undeformed austenite even at a favorable temperature range [21, 138]. For most casting and reheating processes of steels, especially under low temperatures and deformation, equilibrium is seldom approached due to a limited time. From kinetic point, driving forces for precipitation in solid are diffusion rate and supersaturation. Near the high temperature just after the solubility limit is exceeded, the low supersaturation causes a slow precipitation although the diffusion is high. At low temperature, the low diffusion makes the precipitation slow although the supersaturation is high. Thus the Precipitation-Temperature-Time (PTT) curve always shows a "C" shape, and a quick precipitation is often restricted to happen near a "nose" temperature for various precipitates in different steel phases [139-143]. The equilibrium model is also unable to predict the size of precipitates, which is important for hot ductility [57, 60].

It is generally acknowledged that the temperature history and alloy chemistry are important to determine the final precipitate properties [63-64,144-146]. The precipitation is also greatly accelerated by 10-1000 times with deformation strain [24, 147], such as occurs during controlled rolling, and a finer precipitate size distribution is also observed simultaneously [148, 149]. This is because deformation introduces the favorable nucleation sites and diffusion paths of precipitation, such as dislocation networks and vacancy clusters. This kind of precipitation is

always named as “dynamic precipitation”, comparing with “static precipitation” when no deformation is applied. The precipitation is maybe hastened by a γ→α phase transformation because of the larger diffusion rate and smaller solubility limit of this precipitates in ferrite, which is well documented for AlN precipitation [1, 150]. This also causes “interphase precipitation”, which generally takes place at transformation interfaces during austenite decomposition and results in non-random dispersions of the precipitates in rows or sheets [151]. All of these factors determine the size distribution, spatial distribution and morphological characteristics of the precipitate particles, thus are important to influence the steel properties.

There are growing needs to develop a kinetic model of the precipitate growth to describe the precipitation rate under non-equilibrium conditions, and to quantify the evolution of the particle size distribution with time, which is essential to make realistic predictions, especially for carbonitride precipitates in microalloyed steels.

3.1 Previous Work

An early effort to predict phase transformation kinetics is the KJMA model, by Kolmogorov [152], Johnson, Mehl [153] and Avrami [154], which is widely used to study precipitation processes and to generate Precipitation-Temperature-Time (PTT) diagrams. The general isothermal KJMA equation to describe transformed fraction, f, as a function of time, t, is given by [155]

$$f(t) = 1 - \exp(-K \cdot t^n) \quad \textbf{(3.1)}$$

where K is the rate function for nucleation and growth which depends on chemical composition and temperature, and n is the Avrami exponent, typically ranging from 1-4, which depends on growth dimensionality (1-D, 2-D or 3-D), nucleation index (zero, decreasing, constant or increasing nucleation rate), and growth index (interface-controlled or diffusion-controlled). The parameters K and n are determined from experimental measurements at different test temperatures and compositions, and often vary during precipitation. Although this model has been further developed by Duit *et al* for isothermal precipitation of aluminum nitride and for non-isothermal continuous precipitation using additivity rule, and can match many precipitated fraction measurements [156], its empirical nature prevents it from describing alternate thermomechanical processes without refitting the parameters with further measurements.

Moreover, size distributions cannot be predicted in the original KJMA model, which is expanded later as so-called Populational KJMA model to enable a prediction of size evolution [157].

3.1.1 Classical Precipitation Kinetics Models-Sharp Interface Model

The most exact and straightforward method of simulating precipitation kinetics is to solve the diffusion equation directly. By taking some assumptions to make the problem solvable, it causes the early development of classical precipitation models. These models treat precipitate particles to be cut from the precipitate phase and embedded into the matrix. The interface between the matrix and precipitate phase in these models is assumed to be mathematically sharp and zero in length, and concentration change from precipitate phase to interface is a step function. Thus these models are often called as "sharp interface model". As shown in Figure 3.1, a precipitation process always includes induction period, nucleation, growth and coarsening stages, which are always separated to be modeled by in classical precipitation theories.

Nucleation

The nucleation often includes an incubation period to form stable nuclei, and the stable nuclei are continuously generated from the solid solution afterwards. Random thermal diffusion creates unstable clusters of chemically-bonded pseudomolecules called "embryos", which grow into stable "nuclei" if they exceed a critical size, which makes the total free energy to decrease with increasing particle size.

In the earliest theory on nucleation, Volmer and Weber [158] assumed that number of clusters larger than critical size decay artificially into zero. Becker and Döring [159] stated that a decay or dissolution of supercritical droplets, which is a little larger than critical size, becomes possible and these clusters are considered to belong to the size distribution by introducing Zeldovich factor [160]. The isothermal nucleation rate, J(t), which is the number of nuclei per unit volume per unit time, is suggested as [159]:

$$J(t) = \Theta Z \beta^* \exp\left(-\frac{\Delta G_c}{k_B T}\right)\exp\left(-\frac{\tau}{t}\right) \qquad \textbf{(3.2)}$$

where Θ is the number of active nucleation sites per unit volume, Z is the Zeldovich non-equilibrium factor, β^* is the atomic impingement rate at which atoms are attached to the critical nucleus, ΔG_c is the free activation energy for the formation of a critical nucleus, k_B is

Boltzmann's constant, T is the absolute temperature, τ is the incubation time for establishing steady state nucleation conditions and t is the isothermal precipitation time. The parameters Θ, Z, β^*, ΔG_c and τ are all specific to the system and the type of nucleation process.

For spherical precipitates, the parameters in nucleation model can be evaluated as [37]:

$$\Theta = \frac{\rho_D}{c} \tag{3.3}$$

$$Z = \left[\frac{-1}{2\pi kT} \frac{\partial^2 \Delta G}{\partial i^2}\bigg|_{i_c} \right]^{1/2} \tag{3.4}$$

$$\beta^* = \frac{4\pi r_c^2 D_M C_0}{c^4} \tag{3.5}$$

$$\tau = \frac{1}{2Z\beta^*} \tag{3.6}$$

where ρ_D is the dislocation density, c is the lattice parameter of the matrix, r_c and i_c are the critical radius and number of a stable nucleus, D is the diffusion rate of precipitation, C_0 is the initial concentration. The effect of deformation is considered into the model by using dislocation density as a fitting parameter.

After incubation time, a steady nucleation rate is approached for the remaining time after $t>>\tau$, as follows

$$J_s = Z\beta^*\Theta \exp\left(-\frac{\Delta G_c}{k_B T} \right) \tag{3.7}$$

For the steady state nucleation, a constant nucleation rate causes the number of stable nuclei to linearly increase with time. With more nuclei form, the concentration of solutes in matrix decreases, which will cause a decrease of nucleation rate simultaneously.

The evaluation of free energy is critical in the classical nucleation theory since it is embedded in an exponent term. The formation of a coherent spherical droplet with radius r which gives rise to some elastic coherency strains, leads to a change of free energy [161]

$$\Delta G(r) = V(\Delta g_{chem} + \Delta g_{el}) + A\xi\sigma = (\Delta g_{chem} + \Delta g_{el})\frac{4\pi r^3}{3} + 4\pi r^2 \xi\sigma \tag{3.8}$$

where negative Δg_{chem} is the volume chemical driving force for nucleation, Δg_{el} is the volume strain energy created from the formation of nucleus, σ is the interface energy between matrix/precipitate and ξ is a modified factor of interface energy falling between 0 and 1,

associated with relaxing of the lattice mismatch due to the presence of dislocations, grain boundaries or other defects in crystal structure. The first term which scales with r^3 accounts for the gain of negative energy on forming the droplet, and second term which scales with r^2 is an positive energy required to form the a new interface. As shown in Figure 3.2, a combination of these two terms makes the total free energy to be positive and increase at small size scale. After passing a maximum, the total energy continues to decrease with increasing size. It means that if a growing particle becomes larger enough to overcome this energy barrier, there is no obstacle to prevent its further growth. Thus it is stable and always tends to grow. On the other hand, a smaller particle needs extra energy to grow, thus it is unstable and tends to dissolve if it is below this critical size.

The critical size of the nucleation, r_c, is obtained by differentiating the Eq. (3.8)

$$r_c = -\frac{2\xi\sigma}{\Delta g_{chem} + \Delta g_{el}} \tag{3.9}$$

The critical free energy is thus given as

$$\Delta G_c = \Delta G(r_c) = \frac{16\pi}{3}\frac{\xi^3\sigma^3}{(\Delta g_{chem} + \Delta g_{el})^2} \tag{3.10}$$

The chemical driving force is generally approximated by supersaturation, which is given as [32]:

$$\Delta g_{chem} = -\frac{R_g T}{V_P}\ln\frac{C_0}{[C]_{eq}} \tag{3.11}$$

where V_P is the molar volume of precipitate phase, and $[C]_{eq}$ is the dissolved concentration of precipitate in matrix at equilibrium.

For spherical particles, the elastic strain energy stored can be evaluated as [162]

$$\Delta g_{el} = \frac{2}{3}\mu_M \delta_V^2 \frac{\alpha}{\alpha + (1-\alpha)(2+3/(1-\upsilon_M))\mu_M/(2+3/(1-\upsilon_P)\mu_P} \tag{3.12}$$

where δ_V is the volumic dilatation associated with the elastic deformation, $\alpha=(1+\upsilon_M)/3(1-\upsilon_M)$, μ and υ are the shear modulus and Poisson's ratio of material, and subscript "M" and "P" stand for the matrix and precipitate phase.

Liu and Jonas [163] modified the steady nucleation theory to predict the starting time for the strain-induced precipitation of Ti(C,N) in austenite. The start time for precipitation is thus given as

$$P_s = N_c / J_s = \frac{N_c a^3}{D_M \rho X_{Ti}} \exp\left(\frac{\Delta G_c}{k_B T}\right) \quad \textbf{(3.13)}$$

where N_c is the critical number of nuclei, which must be formed for precipitation to be detectable. It could be chosen as a fitting parameter with experiments. The calculated precipitation start times are proved to match the experiments of Ti(C,N) [163] and Nb(C,N) [164] for various compositions and temperatures quite well.

Other similar formulae were also developed. Detta and Sellars [165] derived a semi-empirical model for stain-induced precipitation of niobium carbonitride. The effect of strain rate on precipitation was introduced by using the Zener-Hollomon parameters [166]. The 5% precipitation time of the total precipitated Nb(C,N) in austenite is proposed as

$$t_{5\%} = A[Nb]^{-1} \varepsilon^{-1} Z_H^{-0.5} \exp\left(\frac{270000}{RT}\right) \exp\left(\frac{B}{T^3 (\ln \Pi)^2}\right) \quad \textbf{(3.14)}$$

where $Z_H = \dot{\varepsilon} \exp(Q/RT)$ is the Zener-Hollomon parameter, [Nb] is the soluble niobium content (wt%), ε is the strain, $\dot{\varepsilon}$ is the strain rate, Π is the supersaturation, A and B are constants with optimum values by fitting the experimental data. It can be concluded that precipitation start time is inversely proportional to the strain and strain rate from the expression, which is consistent with experimental observations.

The main shortcomings of the classical nucleation theory are that supersaturation is assumed as constant and the cluster size is assumed to distribute in the vicinity of the critical radius. But these assumptions are not consistent with the fact that many growing precipitates larger than the critical size gradually form and the supersaturation decreases continuously with the formation of stable nuclei in the nucleation stage, and may be only reasonable during the earliest nucleation stage. Moreover, a deterministic function of nucleation rate seems not suitable to describe the stochastic and random nature of nucleation.

Growth

After nucleation, the stable nuclei are embedded in a still supersaturated matrix. The particles are surrounded by a high concentration field which can provides adequate driving force for diffusion growth, and could cause all size particles to growh, which defines the classical growth stage.

For diffusion controlled transformation of a particle in a spherically symmetrical system, Fick's second law gives equation as follows

$$D_M\left[\frac{\partial^2 C}{\partial a^2}+\frac{2}{a}\frac{\partial C}{\partial a}\right]=\frac{\partial C}{\partial a} \tag{3.15}$$

Assuming the precipitates uniformly distribute in a finite matrix, each particle is considered to locate at the center of a spherical cell with radius L, where 2L is the average distance between two neighboring particles. Let r be the average radius of the particle within the spherical cell. When L>>r, the solute concentration at the cell boundary is assumed to equal the matrix concentration C_M, which changes slowly with time, Thus the boundary conditions are given as

$$C = C_I \quad when\ a = r \tag{3.16}$$

$$C = C_M \quad when\ a = L(L >> r) \tag{3.17}$$

where C_I is the solute concentration in the matrix at the particle/matrix interface.

If C_I and C_M are assumed to be constant, the concentration profile could be determined by the stationary interface approximation developed by Whelan [167]. The diffusion field is assumed to have no memory of the past motion of the interface, thus the above equation could be solved for a≥r

$$C - C_M = (C_I - C_M)\frac{r}{a}erfc\left(\frac{a-r}{2\sqrt{D_M t}}\right) \tag{3.18}$$

where erfc(x) is the complementary error function as

$$erfc(x) = \frac{2}{\sqrt{\pi}}\int_x^\infty \exp(-z^2)dz \tag{3.19}$$

From the mass conservation of the solute in the matrix, the flux of solute at the interface equals to the rate of loss or gain of solute in the precipitate. Thus the flux balance at the interface is written as [168]

$$-4\pi r^2(C_P - C_I)dr = -4\pi r^2 D_M \left.\frac{\partial C}{\partial a}\right|_{a=r}\cdot dt \tag{3.20}$$

where C_P is the solute concentration in the precipitate phase.

The velocity of the precipitate/matrix interface is obtained as

$$v = \frac{dr}{dt} = \frac{D_M}{C_P - C_I}\left.\frac{\partial C}{\partial a}\right|_{a=r} = \frac{C_M - C_I}{C_P - C_I}\left[\frac{D_M}{r}+\left(\frac{D_M}{\pi t}\right)^{1/2}\right] \tag{3.21}$$

Within a short period of time, the equation is a good approximation when both C_I and C_M change slowly and are close to be constants in this period. During calculation, both C_I and C_M are updated after each infinitesimal increment of time.

Under steady state, the term with $t^{-1/2}$ of the transient part can be ignored, and the above equation is simplified as

$$\frac{dr}{dt} = \frac{C_M - C_I}{C_P - C_I}\frac{D_M}{r} = k\frac{D_M}{r} \tag{3.22}$$

where the coefficient is defined as $k = (C_M - C_I)/(C_P - C_I)$. It is seen from this equation that a particle grows only when k>0 and it dissolves when k<0. C_P is normally a constant determined from precipitates phase composition. C_M is only a function of time, but C_I can be a function of precipitate size. Therefore for a multi-particle system, it is possible for some particles to dissolve while other particles to grow at the same time. The size of each individual particle r_i could be determined by integrating the previous differential equation for each individual size.

At the beginning of the precipitate growth, C_M is much larger than C_I when most solutes still dissolve in the matrix instead of being precipitated out. Size effect of C_I is not so significant when computing the difference between C_M and C_I. Thus all particles can grow no matter what sizes they have at growth stage. Zener [169] initially assumed a mono-dispersive size distribution, and $C_I = C_{eq}$ for very large particles at t→∞, and $C_M = C_0$. Thus integrating Eq. (3.22) yields

$$r(t) = \left(2\frac{C_0 - C_{eq}}{C_P - C_{eq}}\right)^{1/2}(D_M t)^{1/2} \tag{3.23}$$

This relationship shows that the precipitate size grows with time according to a parabolic rate in the so-defined growth stage. However, the precipitation regime strictly following Eq. (3.23) seldom exists. The growth always consumes the dissolved solutes from matrix, and the matrix concentration, C_M, continuously decreases with time. A possible correction to compute matrix concentration is that

$$C_M(t) = C_0 - \frac{\varphi_V(t)}{V_P} \tag{3.24}$$

where $C_M(t)$, $\varphi_V(t)$ and V_P are the transient matrix concentration, volume fraction and molar volume of precipitates. $\varphi_V(t)$ can be estimated from the number density and size of precipitate, as follows

$$\varphi_V(t) = \sum_{i=1}^{N_V(t)} \frac{4}{3}\pi r_i^3 \approx N_V(t)\frac{4}{3}\pi \bar{r}^3 \quad \textbf{(3.25)}$$

where "number density", $N_V(t)$, is the number of precipitate particles per unit volume.

The assumption of size-independent interface concentration is only valid for very large particles, which is contradictory with the fact that there are always very small particles with size around or below critical value in matrix. This factor can be considered by well-known Gibbs-Thomson equation [170, 171], to describe the concentration at interface of each particle with its size in a dilute solid solution:

$$C_I(r) = C_{eq} \exp\left(\frac{2\sigma V_P}{R_g T}\frac{1}{r}\right) \quad \textbf{(3.26)}$$

where C_{eq} is the equilibrium concentration of solute with a plane interface, σ is the precipitate/matrix interfacial energy, R_g is the gas constant, and T is the absolute temperature. This equation indicates that an increase of particle radius causes the nearby solute concentration to decrease greatly. According to Eq. (3.26), it is possible for small particle to dissolve, and large particles to grow simultaneously at a certain time, if the matrix concentration is between these two concentrations at interface.

The capillary length, L_c, is defined as

$$L_c = \frac{2\sigma V_P}{R_g T} \quad \textbf{(3.27)}$$

For typical precipitates in steels, σ=0.5J/m^2, V_P=1.2×10^{-5}mol/m^3, T=1000^{o}C, the calculated capillary length is ~1.1nm, which is around 7 times of the single pseudomolecule for the same precipitate phase. In order to make $C_I(r)$ to approach the value of C_{eq}, the particles must have size larger than 20nm.

The largest problem of Zener diffusion growth model is only describing the time evolution of precipitates with uniform size. However, a polydispersed precipitate size must be involved at the end of nucleation as well as the beginning of coarsening stage. Thus this model is not expected to correctly predict the measured growth kinetics quantitatively between the nucleation and growth stages even if they are well separated on the time scale. Instead, a size distribution of precipitate and the size-dependent concentrations are often necessary in calculation.

Coarsening

Nature always involves particles with various sizes, not simply a uniform size, dispersed in the matrix. Once the supersaturation has decreased to approach equilibrium, a majority of solutes exists in the precipitate form and few solutes remain the matrix. Then capillary effects become important, causing a phenomenon called as coarsening or Ostwald ripening [172]. Governed by a minimization of the total surface energy, coarsening is driven by the difference in concentration gradients near precipitate particles of different sizes. The larger particles are surrounded by low concentration, so grow by diffusion from the high concentration surrounding smaller particles, which are less stable and shrink. Typical concentration profiles in growth and coarsening are shown in Figure 3.3. In growth, many solutes dissolve in matrix, and the matrix concentration is much larger than interface concentrations of both particles, thus it can make both particles to grow. Instead, this is not true anymore in coarsening, at which the solute concentrations in the matrix and at the precipitate/matrix interface are comparable. Only the larger particles that produce a lower solute concentration than matrix concentration can grow, and the smaller with a solute concentration higher than matrix concentration must shrink. These different diffusion directions of solute to distinguish the growth and coarsening are shown in Figure 3.4. As a result, the net number density of particles decreases with time. Usually, coarsening is considered to be the last stage of a precipitation reaction. But the capillargy effect actually exists for the entire precipitation process, and may become important in the growth stage, or even while the system is still in nucleation.

The classical theory describing coarsening from the above ideas was derived simultaneously and independently by Lifshitz and Slyozov [173] and Wagner [174]. Their treatment is now often referred to as the LSW coarsening theory, and the main assumptions are:

1). The volume fraction of precipitate is small. In such as dilute system, diffusional interactions between particles occurring in more concentrated alloys can be neglected, and particles only interact with the nearby matrix.

2). The volume fraction of precipitates is kept as constant ,which means the decomposition is close to completion and equilibrium state is approached. No more free solutes exist in the matrix, and the larger particle can grow only by the shrinkage of smaller particles. Furthermore, a predetermined size distribution of particles is necessary to initialize coarsening, which limits the application of some nucleation and growth models with uniform size to simulate coarsening.

3). The particle size in coarsening is quite large, and the Gibbs-Thomson equation can be linearized as

$$C_I(r) = C_e\left(1+\frac{2\sigma V_P}{R_g T}\frac{1}{r}\right) \tag{3.28}$$

This linearized Gibbs-Thomas equation gives less than 5% error for particles of $r>2.82L_c$, but large errors are produced for very small particles.

The LSW theory gives the following equations to describe the coarsening process:

$$\overline{r}^3 = \frac{8D_M\sigma V_P C_{eq}}{9R_g T}t \tag{3.29}$$

$$N_V = \frac{27R_g T\varphi_V}{32\pi D_M\sigma V_P C_{eq}}t \tag{3.30}$$

where $\overline{r}$ is mean precipitate radius at time t. These equations show that the third power of the mean particle size increases linearly with time, as opposed with squared in growth, which proves the coarsening is a much slower process. The number density of particles, N_V, decreases with time, and the total volume fraction of precipitate, φ_V, is kept as a constant.

The density function of particle size in LSW coarsening theory is given as

$$f(\frac{r}{\overline{r}}) = \frac{4}{9}\left(\frac{r}{\overline{r}}\right)^2\left(\frac{3}{3+(r/\overline{r})}\right)^{7/3}\left(\frac{1.5}{1.5-(r/\overline{r})}\right)^{11/3}\exp\left(\frac{r/\overline{r}}{(r/\overline{r})-1.5}\right) \quad for\ 0<\frac{r}{\overline{r}}<1.5 \tag{3.31}$$

$$f(\frac{r}{\overline{r}}) = 0 \quad for\ \frac{r}{\overline{r}}\geq 1.5 \tag{3.32}$$

This size distribution is predicted to be independent of the initial distribution, with a maximum particle size of $1.5\overline{r}$. This distribution satisfies the normalization condition as follows

$$\int_0^\infty f(\frac{r}{\overline{r}})dx = \int_0^{1.5\overline{r}} f(\frac{r}{\overline{r}})dx = 1 \tag{3.33}$$

A more general form of coarsening kinetics is given by Sun *et al* [175]:

$$\overline{r} - r_0 = K_c(t-t_0)^{1/n} \tag{3.34}$$

where r_0 is the mean precipitate radius at the initial time t_0 when the coarsening starts, and K_c is the coarsening parameter. The denominator of the fractional exponent n in this equation depends on the specific rate-limiting mechanisms: n=3 if the coarsening is controlled by

bulk diffusion [173, 174], n=4 if controlled by grain boundary diffusion [176], or n=5 if controlled by pipe diffusion [177].

From the description of classical precipitation kinetic models, it has shown that some assumptions are idealized and not close to reality. Although these models capture some important mechanisms in each individual precipitation stage, there is no physical reason to split an entire precipitation process into the consecutive nucleation, growth and coarsening stages. The nucleation, growth and coarsening are always one continuous, competing and overlapping process especially when the size distribution evolves dramatically in a rather short period. Furthermore, some of these models only describe the time evolution of precipitates with uniform size, but it certainly has to deal with a dispersed precipitate microstructure in order to match the reality. The different precipitate size distributions even with the same mean size could have quite different pining effects to restrict the grain growth, which will be discussed in Chapter 5.

In summary, there must be many mechanisms involving in precipitation, such as supersaturation, diffusion and capillary effect. The different mechanisms may become dominant in the different stage of precipitation. In order to treat incubation, nucleation, growth and coarsening as one continuous process, rather than consecutive stages on the time scale, many researchers tried to model the precipitation as more concomitant as possible within the framework of existing classical theories. This kind of model is firstly attempted by Langer, Schwartz and Kampmann, Wagner (LS or Modified LS model) [178, 179], and later by Kampmann and Wagner [180] (KWN Model).

MLS Model

For MLS model [178,179], only particles larger than the critical size are counted as precipitate phase, and the shape of size distribution is predetermined to match the LSW coarsening theory. The total number density and the mean size of precipitate are defined as N_{LS} and $\overline{r}_{LS}$. Thus $\overline{r}_{LS} > r_c$ holds for all stages of precipitation. An apparent density for particles with critical size is introduced as

$$f_a(r_c,t) = N_{LS}\frac{b}{\overline{r}_{LS} - r_c} \tag{3.35}$$

The constant b=0.317 is chosen to match the LSW coarsening rate when t→∞. Due to the nucleation rate J and dissolution, N_{LS} changes with time as follows

$$\frac{dN_{LS}}{dt} = J - f_a(r_c, t)\frac{dr_c}{dt} \tag{3.36}$$

The continuity equation requires

$$(C_P - C_M)N_{LS}\frac{4\pi}{3}\overline{r}_{LS}^3 = C_0 - C_M \tag{3.37}$$

The influence of the assumed shape of size distribution to match the LSW coarsening thoery in MLS theory is in doubt. Another shortcoming of MLS model is the assumption that only particles larger than critical size are counted as precipitated phase. In coarsening stage, the critical size continuously increases and approaches the mean precipitate size. This assumption causes that only few large particles are counted, but lots of particles with relatively smaller size are missing in this model.

KWN Model

In order to introduce fewer assumptions and get better accuracy, Kampmann and Wagner [180] had devised an algorithm from classical nucleation and growth theories, which is termed as the Numerical Model (KWN Model). Unlike the MLS model, the shape of size distribution is computed, instead of being assumed, and all particles no matter which are larger or smaller than critical size are counted.

For the KWN model, the size distribution is subdivided into discrete intervals $[r_j, r_{j+1}]$ with $\left|r_{j+1}\text{-}r_j\right|/r_j << 1$, and N_j particles in the j-th interval with mean size $\overline{r}_j$.

The total number and mean radius of precipitate particles are defined as

$$N_T = \sum_{j=1}^{G_M} N_j \tag{3.38}$$

$$\overline{r}_j = \frac{1}{2}(r_j + r_{j+1}) \tag{3.39}$$

$$\overline{r} = \frac{1}{N_T}\sum_{j=1}^{G_M} N_j \overline{r}_j \tag{3.40}$$

The continuity equation in the N model requires

$$(C_p - C_M)\sum_{j=1}^{j_M} N_j \frac{4\pi}{3}\overline{r}_j^3 = C_0 - C_M \tag{3.41}$$

The equations (3.21), (3.24) and (3.26) are used for calculation, and the particles with different size have different growth rate. It treats the classically defined "growth" and "coarsening" stages as one continuous process, and causes all particles to grow at the beginning of process, and large particles to grow and small particles to shrink later. The nucleation rate calculated from Eq. (3.2) and (3.11) needs to be revised to consider influence of a decreasing matrix concentration during precipitation. The initial concentration must be replaced by the transient value, thus the nucleation rate continuously decreases and reaches zero when the transient concentration becomes equal to the equilibrium value. The time steps in calculation are chosen in such a way that within each corresponding time interval the changes of all radius and concentrations remain sufficient small. Thus both the nucleation and growth rates can be considered as being constant in each time step.

The KWN model is believed to be the best combined and most accurate one from the classical precipitation theories, especially when an accurate description of nucleation is available or a previous size distribution has existed. It is widely modified and applied to simulate precipitation of AlN in austenite and on grain boundaries of low-carbon steels [168], Nb(C,N) in austenite [164], and NbC on dislocations in ferrite [181]. From a comparison with experimental data of precipitated fraction and size distribution, the N model is also used to determine the crucial precipitation parameters which are difficult to measure, such as diffusion coefficient and interface energy of the particular alloy system [180, 182], or evaluate the applicability of other kinetic models of precipitation [180, 183].

The main shortcoming of KWN model is still to require a deterministic time and concentration dependent function to describe the nucleation rate, and its ability to count the stochastic nature of nucleation is in doubt.

3.1.2 Recent Modeling Developments of Precipitation Kinetics

Taking advantage of faster computers, more computational models of precipitation kinetics have recently been developed. All of these models aim to simulate the precipitation as continuous as possible based on the fundamental physics. These new tools include kinetic Monte Carlo model, phase field method, Matcalc method and cluster dynamics model.

Kinetic Monte Carlo Model

At the atomic scale, kinetic Monte Carlo model statistically describes the diffusion through vacancy jumps toward nearest-neighbor atoms, and the vacancy exchange frequency is a thermal activated function as follows

$$\Gamma_{XV} = v_X^0 \exp\left\{-\frac{\Delta Q_X}{k_B T}\right\} \tag{3.42}$$

where v_X^0 is an attempt frequency, which is assumed to depend on the nature of the atoms X. The activation energy ΔQ_X is the energy change required to move the atom X from its initial stable position to the saddle point position. At each Monte Carlo step, a vacancy can undergo exchange with its nearest neighbors for the substitutional atoms, and the interstitial atom can exchange its site with nearest free interstitial sites. One of these exchanges is chosen according to the residence time algorithm described elsewhere [40]. The total energy of the system is counted as the sum of pair interaction energies, and it decreases and finally reaches a minimum in simulation.

The calculation of Monte Carlo model is always limited in a small scale, thus it can be only suitable for very fine particles, especially the early nucleation stage. Some applications are illustrated by the kinetics simulation of Al_3Zr and Al_3Sc in aluminum [41], and Y_2O_3 in ferrite [42]. The largest size of precipitates is often limited to be less than several hundred atoms.

Phase Field Method

The main idea in phase field method is that microstructure evolution takes place to reduce the total free energy. It describes microstructure as a whole by using a set of continuous field variables, and becomes one of the most powerful methods for modeling microstructure.

For an isolated precipitate phase growing into a matrix phase, this two-phase microstructure is described in terms of composition C(r,t) (conserved variable) and order parameter η(r,t) (non-conserved variable) in a periodic domain. The order parameter η is defined in such a way that η=0 for matrix phase, η=1 for precipitate phase, and 0<η<1 for the matrix/precipitate interface.

The chemical free energy could be given by the following function

$$G_{chem} = N_V \int_V [g(C,\eta) + \kappa_C (\nabla C)^2 + \kappa_\eta (\nabla \eta)^2] dV \tag{3.43}$$

where $g(C,\eta)$ is the bulk free energy per atom, κ_C and κ_η are the energy coefficients for composition gradients and order parameter, respectively.

The bulk free energy density can be given by

$$g(C,\eta) = g_M(C)(1-W(\eta)) + g_P(C)W(\eta) + P\eta^2(1-\eta)^2 \quad \textbf{(3.44)}$$

where $g_M(C)$ and $g_P(C)$ are the free energies of matrix and precipitate phase, W(η) is an interpolation function of order parameter, and P is a constant describing the height of the free energy barrier between the matrix and precipitate phase.

The elastic contribution to the free energy is

$$G_{el} = \frac{1}{2}\int_V (\sigma_{ij})_{el}(\varepsilon_{ij})_{el}dV \quad \textbf{(3.45)}$$

where σ_{el} and ε_{el} are elastic stress and strain tensors, respectively. The microstructure evolution is governed by the Cahn-Hillard equation [184] and Allen-Cahn equation [185]:

$$\frac{\partial C}{\partial t} = \nabla\cdot(M\nabla\mu) \quad \textbf{(3.46)}$$

$$\frac{\partial \eta}{\partial t} = -L\frac{\partial(F/N_V)}{\partial \eta} \quad \textbf{(3.47)}$$

where M is the atomic mobility, μ is the chemical potential and L is the relaxation coefficient for the order parameter. Chemical potential μ is defined as the variational derivative of the total free energy per atom with respective to the local composition:

$$\mu = \frac{\partial(F/N_V)}{\partial C} \quad \textbf{(3.48)}$$

A thin interface with finite thickness is always described in phase field method, instead of a sharp interface in classical precipitation models. Some application of phase field model could be found for effects such as strain, interface curvature and diffusivity on growth of an isolated precipitate in a supersaturated matrix [43, 44], and $M_{23}C_6$ carbide in steel [45].

Matcalc Method

Recently, a commercial precipitation-kinetics software package, Matcalc, has been developed based on thermodynamic extremum principles [46-48]. The evolution of the system is governed by the following set of equations [186, 187]

$$\frac{\partial G}{\partial q_i} = -\frac{1}{2}\frac{\partial Q}{\partial \dot{q}_i} \tag{3.49}$$

where G is the total Gibbs energy of the system, Q is total Gibbs energy dissipation rate, and q_i are the suitable independent state parameters of a closed system.

The system consists of a matrix and precipitates. There are *s* substitutional components and *p* interstitial components in the system, and the total number of components *n*=*s*+*p* is fixed. Let χ_i (i=1,…,n) be a fixed number of moles of component i, *m* the number of precipitate in the system, r_k (k=1,…,*m*) the radius of a spherical precipitate *k*, u_{ki} (k=1,…,m,i=1,…,n) the mean site fraction of component *i* in the precipitate *k*.

For simplicity, the partial molar volumes of the substitutional components are the same for all substitutional components in all phases and partial molar volumes of all interstitial components are zero. When site fraction of vacancies is negligible, the volume corresponding to one mole of site positions is set as Ω, which is independent of the chemical composition and phase. The mean concentration in the precipitate, C_{ki} (k=1,…,m, i=1,…,n) can be calculated as

$$C_{ki} = -\frac{u_{ki}}{\Omega}, \quad k = 1,...,m, i = 1,...,n \tag{3.50}$$

The number of moles and the mean concentration of component *i* in the matrix are given as

$$N_{Mi} = \left(N_{0,i} - \sum_{k=1}^{m} \frac{4\pi r_k^3 C_{ki}}{3} \right), \quad i = 1,...,n \tag{3.51}$$

$$C_{Mi} = \frac{N_{M,i}}{\Omega \sum_{i=1}^{s} N_{M.i}}, \quad i = 1,...,n \tag{3.52}$$

where $N_{0,i}$ is the number of moles of component *i*. The system is uniquely described by the state parameters *m*, r_k (k=1,…,*m*) and C_{ki} (k=1,…,m, i=1,…,n). Let μ_{Mi} (i=1,…,n) be the chemical potential of component i in the matrix and μ_{ki} (k=1,…m, i=1,…,n) be the chemical potential of component i in the precipitate *k*. All of these chemical potentials can be expressed as functions of the concentrations and unknowns. The total Gibbs energy of the system is given by

$$G = \sum_{i=1}^{n} N_{Mi}\mu_{Mi} + \sum_{k=1}^{m} \frac{4\pi r_k^3}{3}(\lambda_k + \sum_{i=1}^{n} C_{ki}\mu_{ki}) + \sum_{k=1}^{m} 4\pi r_k^2 \sigma_k \tag{3.53}$$

where σ_k is the interface energy and λ_k accounts for the contribution of the elastic energy and plastic work due to volume expansion of precipitates. By this definition, $\partial G / \partial q_i$ (q_i includes r_k, k=1,…,m and C_{ki}, k=1,…,m, i=1,…,n) in Eq. (3.49) can be calculated, which represent generalized driving forces for the state parameters.

The total Gibbs energy dissipation rate in Eq. (3.49) is also required to be evaluated. It includes three parts: migration of interfaces characterized by their mobolities M_k, k=1,…,m; diffsuion of all components in the precipitates characterized by diffusion coefficients D_{ki}, k=1,…,m, i=1,…,n; diffusion of all components in the matrix characterized by diffusion coefficients D_{Mi}, i=1,…,n. These contributions to energy dissipation are thus evaluated as

$$Q_1 = \sum_{i=1}^{n} \frac{4\pi r_k^2 \dot{r}_k}{M_k} \tag{3.54}$$

$$Q_2 = \sum_{k=1}^{m} \sum_{i=1}^{n} \int_0^{r_k} \frac{RT}{c_{ki} D_{ki}} 4\pi r^2 j_{ki}^2 dr \tag{3.55}$$

$$Q_3 = \sum_{k=1}^{m} \sum_{i=1}^{n} \int_{r_k}^{\infty} \frac{RT}{c_{Mi} D_{Mi}} 4\pi r^2 J_{ki}^2 dr \tag{3.56}$$

The radial diffusive flux in the precipitate (j_{ki}), at the precipitate/matrix interface (J_{ki}^*) and in the matrix surrounding the precipitate (J_{ki}) are suggested as

$$j_{ki} = -\frac{r \dot{c}_{ki}}{3}, \quad 0 \le r \le r_k \tag{3.57}$$

$$J_{ki} = J_{ki}^* \frac{r_k^2}{r^2} \frac{Z^3 - r^3}{Z^3 - r_k^3}, \quad r_k \le r \le Z \tag{3.58}$$

$$J_{ki}^* = \dot{r}_k (C_{Mi} - C_{ki}) - \frac{r_k \dot{C}_{ki}}{3} \tag{3.59}$$

where $Z >> r_k$. According to these definitions, the terms $\partial Q / \partial \dot{q}_i$ in right side of Eq. (3.49) can be also evaluated. Thus these equations give the change rate of $\dot{r}_k$ and $\dot{C}_{ki}$, and the new values of r_k and C_{ki} are able to be computed at a new time step.

The largest benefit of Matcalc method is to determine the kinetics of the multi-component system without the necessity of knowing the concentration profiles and the constant conditions for chemical potentials at the migrating interface. It offers an easy approximate solution to the kinetics of the precipitation of different composition and different sizes with a

sufficient accuracy. It is suitable for application to complex systems. But Matcalc also requires a proper theory of multiphase nucleation to start the simulation, which may limit the application of Matcalc method. Some details and applications of Matcalc for precipitation, including separate models within the matrix [46, 47], and on the grain boundaries [48] are available elsewhere.

Cluster Dynamics Model

In cluster dynamics, the system is seen as a gas of mesoscopical clusters, or called "nanoparticles", made of monomers that can be solute atoms, vacancies, self-interstitial atoms. The total volume fraction occupied by the clusters must be small. The evolution of clusters of each size is treated within the framework of the chemical rate theory, and no explicit laws for the individual nucleation, growth and coarsening stage is required.

A fundamental assumption of cluster dynamics is that exchanges between clusters involve only monomers. Reactions between neighboring clusters are considered by the condensation and evaporation rates, based on a thermodynamic model of the free energy of the system [49-51]. The evolution of clusters of size i>1 is coupled with its two adjacent neighbors as follows

$$C_i = (\alpha_{i+1} C_{i+1} + \beta_{i-1} C_{i-1}) - (\alpha_i + \beta_i) C_i \tag{3.60}$$

where C_i is the atomic concentration of clusters of size i, β_i and α_i are called as "condensation rate" and "evaporation rate", which are the probability for one solute atom to impinge and leave a cluster of size i per unit time.

The condensation rate is obtained by solving the diffusion problem in the solid solution around a spherical precipitate. The stationary diffusion equation in a spherical coordinate is given as

$$D \frac{1}{r^2} \frac{\partial}{\partial r} \left(r^2 \frac{\partial C_1(r)}{\partial r} \right) = 0 \tag{3.61}$$

The boundaries conditions are set as $C_1(r = r_i) = 0$ at the matrix/cluster interface and $C_1(r = \infty) = C_1^{\infty}$ far away from the cluster. It is worth to mention that the actual monomer concentration should equal to the corrected value from Gibbs-Thomson equation (3.26). Taking this concentration as zero here is to assume that the cluster does not emit any monomers.

The monomer concentration around the precipitate is solved as

$$C_1(r) = C_1^{\infty} \frac{r - r_i}{r}, \quad r > r_i \tag{3.62}$$

The condensation rate is given by integrating over the cluster surface of the incoming flux of monomers

$$\beta_i = -4\pi r_i^2 \frac{D_M}{\Omega} \frac{\partial C_1}{\partial r}\bigg|_{r=r_i} = 4\pi r_i \frac{D_M}{\Omega} C_1^{\infty} \tag{3.63}$$

The evaporation rate is obtained assuming that it is an intrinsic property of the cluster and therefore does not depend on the solid solution surrounding the cluster. In an under-saturated solid solution of nominal concentration χ_{eq} at equilibrium, the cluster size distribution is given by

$$C_{i,eq}(\chi_{eq}) = \exp\left[-(G_i - 2i\mu(\chi_{eq}))/kT\right] \tag{3.64}$$

where G_i is the free energy of a cluster containing i monomers, and $\mu(\chi_{eq})$ is the effective chemical potential in the solid solution, which is half the difference between the chemical potentials of the solute and the solvent atoms. At equilibrium, all fluxes between size i and size i+1 clusters are zero.

$$\alpha_{i+1} = \alpha_{i+1,eq}(\chi_{eq}) = \beta_{i,eq}(\chi_{eq}) \frac{C_{i,eq}(\chi_{eq})}{C_{i+1,eq}(\chi_{eq})} \tag{3.65}$$

It finally leads to the following expression of the evaporation rate

$$\alpha_{i+1} = 4\pi r_i \frac{D_M}{\Omega} \exp\left[\left(G_{i+1} - G_i - G_1\right)/kT\right] \tag{3.66}$$

For Al_3Zr and Al_3Sc, the cluster formation free energy into a volume and interface contributions:

$$G_i - 2i\mu(\chi_{eq}) = 4i\Delta G_{nuc}(\chi_{eq}) + (36\pi i^2)^{1/3} c^2 \sigma_i \tag{3.67}$$

where ΔG_{nuc} is the nucleation free energy, which is the free energy change when nucleating a precipitate out of the solid solution. σ_i is the interface free energy of cluster containing i solute atoms, and c is lattice parameter. Thus evaporation rate is given as:

$$\alpha_{i+1} = 4\pi r_i \frac{D_M}{\Omega} \exp\left[(36\pi)^{1/3} c^2 \left((i+1)^{2/3}\sigma_{i+1} - i^{2/3}\sigma_i - \sigma_1\right)/k_B T\right] \tag{3.68}$$

The evaporation rate is shown to be independent of the nucleation free energy, which is important in the classical nucleation theory but play no role in cluster dynamics model.

The largest benefits of cluster dynamics are that it describes the precipitation as one continuous process, and does not require explicit laws for the individual nucleation, growth or coarsening stages. Due to its low computer cost, it claimed to have the potential to link between atomistic simulations and macroscopic models, and can handle long term evolution that cannot be obtained by Kinetic Monte Carlo or phase field methods [49]. The main drawback of cluster dynamics is its inability to cover the vast size scales. Further drawbacks are of hypothesizing of uniform distributions of clusters, and no explicit consideration of spatial correlations between clusters [188].

3.1.3 Continuous Model

In order to simulate the precipitation as a continuous process, the fundamental models such as Smoluchowski [189] and Kampmann [190] are attractive because the particles agglomerate automatically, particles of all sizes are tracked, and the few parameters come with physical significance. The fundamental unit of these models is "pseudomolecule", which is an "embryo" or stoichiometric cluster of atoms consisting of as few as a single metallic/interstitial atom pair. The evolution of number of particles per unit volume, or called as "number density" is the key parameter to determine.

Particle Collision Model

Collisions between particles and rapid diffusion in the liquid phase increase the number of large particles, and enhance inclusion removal by flotation. The population balance model for collision first suggested by Smoluchowski is [189]:

$$\frac{dn_i}{dt} = \frac{1}{2}\sum_{k=1}^{i-1} \Phi_{k,i-k} n_k n_{i-k} - n_i \sum_{k=1}^{\infty} \Phi_{i,k} n_k \qquad \textbf{(3.69)}$$

where n_i is the number of size i particles per unit volume, or "number density", and $\Phi_{i,j}$ is the collision frequency between size i and size j particles. The first term on the right-hand side generates size i particles due to the collision of two smaller particles, and the second term decreases the number of size i particles by their collision with particles of any size to become larger particles. The generation term is halved to avoid counting collision pairs twice. However, when two particles generating size i particles have same size, the generation term should not be halved because the collision pair is unique. Moreover, the loss term should be doubly counted

when size i particles collide with themselves. The number of pseudomolecules composing the largest agglomerated particle must be a finite number i_M in numerical computation. Making these appropriate changes gives the following improved expression:

$$\frac{dn_i}{dt} = \frac{1}{2}\sum_{k=1}^{i-1}(1+\delta_{k,i-k})\Phi_{k,i-k}n_k n_{i-k} - n_i\sum_{k=1}^{i_M}(1+\delta_{i,k})\Phi_{i,k}n_k \quad \textbf{(3.70)}$$

where $\delta_{i,k}$ is the Kronecker delta, $\delta_{i,k}=1$ for $i=k$ and $\delta_{i,k}=0$ for $i\neq k$. When $i=1$, the population balance for dissolved single pseudomolecules simplifies to:

$$\frac{dn_1}{dt} = -n_1\sum_{k=1}^{i_M}(1+\delta_{1,k})\Phi_{1,k}n_k \quad \textbf{(3.71)}$$

Thus the number density of single pseudomolecules always decreases with collisions. This model has been successfully applied for various collision mechanisms, including turbulent collision [191], Stokes collision [192], Brownian collision [193] and gradient collision [194].

The mass is proved to be conserved if i_M is chosen to be large enough, by satisfying the following equation

$$\sum_{i=1}^{\infty} i\frac{dn_i}{dt} = 0 \quad \textbf{(3.72)}$$

Evaluating equations (3.70)-(3.71) requires summing over and tracking every possible size from 1 to i_M pseudomolecules, so is not practical for realistic particle sizes. Results from these equations, however, comprise the exact solution for collision test problems.

Precipitate Particle Diffusion Model

Kampmann [190] suggested the following diffusion-controlled model to treat the kinetics of nucleation, growth and coarsening as one continuous and simultaneous process:

$$\frac{dn_i}{dt} = -\beta_i n_1 n_i + \beta_{i-1}n_1 n_{i-1} - \alpha_i A_i n_i + \alpha_{i+1}A_{i+1}n_{i+1} \quad (i \geq 2) \quad \textbf{(3.73)}$$

where β_i, α_i and A_i are the diffusion growth rate, dissociation rate and reaction sphere surface area for a size i particle containing i pseudomolecules. A pseudomolecule (or called a "monomer" [195, 196]) is a stoichiometric cluster of atoms that consists of as few as a single metallic/interstitial atom pair. Random thermal diffusion creates unstable clusters of chemically-bonded pseudomolecules called "embryos", which grow into stable "nuclei" if they exceed a critical size. The first and second terms on the right-hand side account for the loss and

generation of size *i* particles due to "diffusion growth" by adding a single pseudomolecule to size *i* and *i*-1 particles respectively. The third and fourth terms account for the loss and generation of size *i* particles due to particle "dissociation" by losing a single pseudomolecule from size *i* and *i*+1 particles respectively. For single pseudomolecules, *i*=1, the special cases of double loss when two pseudomolecules react with each other and double generation of single pseudomolecules when size 2 particles dissociate are not counted exactly in Kampmann's initial work. Thus the following revised balance equation is suggested here:

$$\frac{dn_1}{dt} = -n_1 \sum_{k=1}^{i_M} (1+\delta_{1,k})\beta_k n_k + \sum_{k=2}^{i_M} (1+\delta_{2,k})\alpha_k A_k n_k \qquad \textbf{(3.74)}$$

Assuming a uniform spherical concentration field of single pseudomolecules with a boundary layer thickness approximated by r_i around each size *i* particle, the diffusion growth rate of size *i* particles is expressed by [190]:

$$\beta_i = 4\pi D_M r_i \qquad \textbf{(3.75)}$$

where D is the diffusion coefficient in the matrix phase, and r_i is the radius of size *i* particles. As precipitation reactions always involve more than one element, this coefficient is chosen for the slowest-diffusing element, which is assumed to control the diffusion rate. As shown in Table 3.2 and Figure 3.5, the diffusion of interstitial elements such as O, S, N and C is much faster, so the diffusion rate is usually determined by the diffusion coefficient of the alloying metal element in the precipitate.

The following relation is assumed for the dissociation rate, which is the number of pseudomolecules lost per unit surface area of size *i* particles per unit time, based on a mass balance of a particle in equilibrium with the surrounding matrix phase [190]:

$$\alpha_i = \beta_i n_{1i} / A_i = D_M n_{1i} / r_i \qquad \textbf{(3.76)}$$

The concentration of single pseudomolecules, n_{1i}, in equilibrium around the surface of the size *i* particle is needed to evaluate this equation. It is estimated using the Gibbs-Thomson equation, and decreases with increasing particle size as follows [170, 171]:

$$n_{1i} = n_{1,eq} \exp\left(\frac{2\sigma V_P}{R_g T}\frac{1}{r_i}\right) \qquad \textbf{(3.77)}$$

where $n_{1,eq}$ is the number density of dissolved single pseudomolecules in equilibrium with a plane interface of the precipitate phase. This equation indicates that increasing particle radius causes the nearby solute concentration to decrease greatly, by several orders of magnitude.

The balance is also satisfied for a large i_M by satisfying

$$\sum_{i=1}^{\infty} i \frac{dn_i}{dt} = 0 \tag{3.78}$$

Equations (3.73)-(3.77) include the effects of equilibrium, diffusion growth, dissociation, curvature effects and mass conservation, with parameters all having appropriate physical significance. Results from these equations are regarded as the exact solution for diffusion test problems.

It is worth to notice that the above equations are completely identical to those of cluster dynamics model after transforming concentrations to the number densities, except that the definitions of "dissociation rate" and "evaporation rate" are different. Both two rates reflects a decreasing interface concentration with increasing size, but the different quantity and influence of two terms on the precipitation kinetics are not clear yet, and may be compared and discussed in future. Similar to cluster dynamics, the free energy of nucleation is not explicitly shown in this model. The evolution of all particles is determined by the same differential equations, and whether the particle becomes stable or unstable is determined by the model itself.

3.1.4 Introduction of Particle-Size-Grouping Method

The pseudomolecule-based models described above are attractive because the particles evolve automatically without any explicit laws for individual stage in precipitation, particles of all sizes are tracked, and the few parameters are fundamental physical constants themselves. Unfortunately, these models encounter inevitable difficulties when they are applied to simulate the precipitation in real materials such as steel, where the precipitate particle size ranges greatly from a single "pseudomolecule" of ~0.1nm, to coarsened particles larger than 100μm. Realistic particles range in size over at least 6 orders of magnitude, and contain from 1 to 10^{18} pseudomolecules. With such an overwhelming linear scale, it is impossible to solve realistic problems using traditional models based on pseudomolecules.

Attempting to overcome this difficulty, the Particle-Size-Grouping (PSG) method has been introduced in several previous studies and has proven to be very effective in calculating the

evolution of particle size distributions for collision-coagulation growth over a large size range [203-208]. Rather than tracking each individual particle size, the main idea of this technique is to divide the entire possible particle size range into a set of size "groups", each with a specific mean size and size range. Careful attention is required to formulate the equations to ensure proper interaction and mass conservation [203]. Several researchers have applied the PSG method to simulate inclusion agglomeration in liquid steel due to collisions, coagulation and removal. Such models have been applied to RH degassers [204], continuous casting tundishes [205, 206] and ladle refining [207, 208]. To start these PSG models, an initial size distribution is often required, which can be found from either experimental measurements or assumptions.

To make the PSG method more usable, Nakaoka *et al.* [209] used different volume ratios between neighboring size groups to test the accuracy of PSG method, and took advantage of the exponential increase in sizes that accompany powers of 2. This innovation allows modeling from single monomers to realistic particle sizes with only 20-80 size groups. Particle collisions were modeled, considering both inter-group and intra-group interactions, and numerical results agreed well with experimental agglomeration curves for various particle concentration and agitation speeds.

However, very little work has been done to apply the PSG method to diffusion, which is the dominant mechanism for precipitate growth in many processes including steel casting and rolling. The particle size may not be actually be expanded by addition of one pseudomolecule in the size group manner because addition of a monomer to a particle in a certain group can seldom support enough particle growth to jump into the neighboring larger size group. This is apparently inconsistent with real precipitation kinetics. One study by Zhang and Pluschkell [210], coupled both collision and diffusion into a PSG model, but inter-group diffusion was not considered, and thus diffusion itself still can never make particles to grow into the neighboring larger group. Zhang [195, 196] included a discrete-sectional technique by Gelbard [211] and Wu [212] into the PSG model, but this introduces a discrete regime before PSG-sectional regime which linearly increases with number of containing monomers and thus weakens the efficiency of the PSG method itself. The inter-group diffusion was considered by assuming a uniform size distribution in every size group, which is often not a good estimation and may give a poor accuracy comparing with real distribution. No previous study has demonstrated an accurate simulation and an insurance of mass conservation of diffusion only by using an efficient PSG method.

The purpose of this chapter is to develop accurate, robust, and versatile PSG methods to simulate precipitate growth due to both collision and diffusion mechanisms. The standard PSG method for collision problem is developed first, and a new PSG method for diffusion is created. Both methods are verified by comparison with exact solutions of the primary population equations in test problems. The new PSG method is shown to be a very time-efficient calculation using a small number of size groups with complete mass balance and high accuracy. The new PSG method is applied to simulate several practical precipitation processes in solid steels, and compared with experimental measurements. Finally, the influence of the different variables on precipitation kinetics is discussed. Some of these works have been published in a previous paper [213].

3.2 Introduction of Particle-Size-Grouping Method

From a theoretical point of view, the pseudomolecule-based population-balance models in the previous sections are accurate and the integration of their set of governing equations is straight forward. However, the computational cost quickly becomes infeasible for realistic particle sizes. The PSG method is introduced here to overcome this difficulty. The fundamental concept of the PSG method is shown schematically in Figure 3.6. In this method, the particles are divided into different size groups (size group number j) with characteristic volume V_j and characteristic radius r_j. The number density of particles of size group j is defined as

$$N_j = \sum_{V_{j,j+1}>V>V_{j-1,j}} n(V) \tag{3.79}$$

This summation covers all particles whose volume lies between two threshold values. The threshold volume that separates two neighboring size groups, $V_{j,j+1}$, is assumed to be the geometric average of the characteristic volumes of these two groups, instead of the arithmetic average used in previous works [209, 210]:

$$V_{j,j+1} = \sqrt{V_j V_{j+1}} \tag{3.80}$$

If a newly-generated particle has its volume between $V_{j-1,j}$ and $V_{j,j+1}$, it is counted in size group j. The increase of number density of size group j particles is then adjusted according to the difference between the volume of the new particle and V_j, in order to conserve mass.

The volume ratio between two neighboring size groups is defined as

$$R_V = \frac{V_{j+1}}{V_j} \tag{3.81}$$

To generate regularly-spaced threshold values, R_V is usually varied. However, for constant R_V, the PSG characteristic and threshold volumes can be simply expressed as:

$$V_j = R_V^{j-1} V_1,\ V_{j,j+1} = R_V^{(j-1/2)} V_1 \tag{3.82}$$

where the volume of the unit cell that contains one single pseudomolecule, V_1, is computed using the molar volume of its precipitate crystal structure, V_P:

$$V_1 = \frac{V_P}{N_A} \tag{3.83}$$

where N_A is Avogadro's number, and the small effects of temperature change and vacancies are neglected. Since V_1 is the volume of the unit cell instead of single pseudomolecule, consideration of the packing factor is not needed. The number of pseudomolecules contained in a given PSG volume is

$$m_j = \frac{V_j}{V_1},\ m_{j,j+1} = \frac{V_{j,j+1}}{V_1} \tag{3.84}$$

In the PSG method, it is easy to introduce fractal theory to consider the effect of particle morphology. The effective radius of a particle can be expressed by

$$r_j = r_1 \left(\frac{V_j}{V_1} \right)^{1/D_f} \tag{3.85}$$

where D_f is the fractal dimension, which can vary from 1 (needle-shaped precipitates) to 3 (complete coalescence into smooth spheres). Tozawa [214] proposed D_f=1.8 for Al_2O_3 clusters in liquid steel, and D_f=3 is adopted everywhere in this thesis for simplicity.

After the number of single pseudomolecules composing the largest agglomerated particles i_M is determined, the corresponding total number of size groups G_M must be large enough for the second largest size group to contain the largest agglomerated particle, i_M. Thus, for constant R_V, G_M must satisfy:

$$G_M \geq ceil(\log_{R_V} i_M) + 2 \tag{3.86}$$

The largest size group is a boundary group which always has zero number density. The accuracy of the PSG method should increase with decreasing R_V, as more size groups are used. From the logarithm relation shown above, it can be seen that the PSG method is very efficient for

real problems with a large range of particle sizes. For example, Table 3.1 shows the relationship between the particle size and size group for constant R_V=2 and R_V=3 for precipitate AlN. The calculation indicates in order to cover the particle size up to 100μm, it only needs a number of less than 60 groups for R_V=2 and 40 groups R_V=3.

3.2.1 PSG Method for Collision

Applying the PSG method to model colliding particles involves the following rules, affecting size group *j*:

1). A size group *j* particle colliding with a small particle, from group 1 to $k_{c,j}$, remains in group *j*, and increases the number density, N_j.

2). A group *j* particle colliding with a relatively large particle, from a group larger than $k_{c,j}$, generates a particle in group *j*+1 or higher.

3). A group *j*-1 particle colliding with a particle from group $k_{c,j}$ to *j*-1 generates a group *j* particle.

Combining these rules gives the following equation, where the coefficients involving mean volumes are needed to conserve volume,

$$\frac{dN_j}{dt} = N_j \sum_{k=1}^{k_{c,j}} \frac{V_k}{V_j} \Phi_{j,k} N_k - N_j \sum_{k=k_{c,j}+1}^{G_M} \left[(1+\delta_{j,k}) \Phi_{j,k} N_k \right] + \sum_{k=k_{c,j}}^{j-1} \frac{V_{j-1}+V_k}{V_j} \Phi_{j-1,k} N_{j-1} N_k \quad (j \geq 2) \tag{3.87}$$

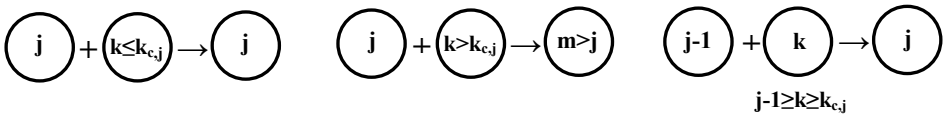

$$\text{with } k_{c,j} = \begin{cases} j-1 & 4.000 > R_V > 2.148 \\ j-2 & 2.148 > R_V > 1.755 \\ j-3 & 1.755 > R_V > 1.587 \end{cases} \tag{3.88}$$

The R_V ranges in Eq. (3.89) are found by solving the following equations, after inserting the Eq. (3.83) expressions:

$$V_j + V_{k_{c,j}+1} > V_{j,j+1} \tag{3.89}$$

Finally, the number density of single pseudomolecules is calculated by

$$\frac{dN_1}{dt} = -N_1 \sum_{k=1}^{G_M} (1+\delta_{1,k}) \Phi_{1,k} N_k \tag{3.90}$$

Equations (3.87), (3.88) and (3.90) are integrated over time for all size groups. The small number of size groups enables the model to simulate practical problems.

3.2.2 PSG Method for Diffusion

Applying the PSG method to solid-state diffusion processes would appear to involve fewer rules than the particle collision method just presented, because precipitate growth by diffusion involves gain or loss of only one individual pseudomolecule at a time. However, adding a single pseudomolecule to a particle very rarely gives enough particle growth to count it in the next larger size group. In addition, size groups j-1, j and j+1 all influence the evolution of size group j number density for a given time interval. Thus, some knowledge of the particle distribution inside each size group is necessary, especially near the size group thresholds where the inter-group interaction occurs. It requires careful consideration of diffusion growth and dissociation both inside and between size groups. Some previous work [195, 196] assumed a uniform size distribution inside each size group, and the number density of particles near thresholds can be easily estimated by the total number density and the covered interval of each size group, but this assumption apparently can seldom match the real size distribution, thus a better estimation of these number densities for intra-group diffusion is required.

All particles inside a size group j will still stay in group j even after a diffusion growth or dissociation event, except for those "border sizes" which fall on either side of the threshold sizes which define the neighboring size groups: n_j^L (closest to $V_{j-1,j}$) and n_j^R (closest to $V_{j,j+1}$). Size group j particles also can be generated if particles n_{j-1}^R from size group j-1 jump into size group j by diffusion growth or particles n_{j+1}^L from size group j+1 fall into size group j by dissociation. At the same time, size group j particles can be lost if particles n_j^R jump to size group j+1 by diffusion growth or particles n_j^L fall to size group j-1 by dissociation. These considerations are incorporated into a new PSG method, taking care to conserve mass, as follows [213]:

$$\frac{dN_j}{dt} = \frac{m_1}{m_j}\beta_j N_1 (N_j - n_j^R) - \frac{m_1}{m_j}\alpha_j A_j (N_j - n_j^L)$$

$$+ \frac{ceil(m_{j-1,j})}{m_j}\beta_{j-1}^R N_1 n_{j-1}^R + \frac{floor(m_{j,j+1})}{m_j}\alpha_{j+1}^L A_{j+1}^L n_{j+1}^L$$

$$-\frac{floor(m_{j,j+1})}{m_j}\beta_j^R N_1 n_j^R - \frac{ceil(m_{j-1,j})}{m_j}\alpha_j^L A_j^L n_j^L \quad (j \geq 2) \tag{3.91}$$

where n_j^L is the number density of those particles in size group j which fall into size group j-1 by losing one pseudomolecule, and n_j^R is the number density of those particles in size group j which jump into size group j+1 by gaining one pseudomolecule. Function *ceil* calculates the smallest integer which is not less than the given real number, and *floor* for the largest integer which is not larger than the given real number. In Eq. (3.91), the first and second terms on the right-hand side account for the diffusion growth and dissociation inside size group j, and the third and fourth terms account for the generation of size group j particles by inter-group diffusion growth and dissociation of neighboring groups. The last two terms are for loss of size group j particles due to the diffusion growth and dissolution of size group j particles themselves.

Single pseudomolecules are a special case because they comprise the only group which interacts with all other size groups. Thus, the new PSG method for diffusion uses the following population balance equation for j=1:

$$\frac{dN_1}{dt} = -N_1\sum_{k=1}^{G_M}(1+\delta_{1,k})\beta_k(N_k - n_k^R) + \sum_{k=2}^{G_M}\alpha_k A_k(N_k - n_k^{L\cdot})$$

$$-N_1\sum_{k=1}^{G_M}(1+\delta_{1,k})\beta_k^R n_k^R + \sum_{k=2}^{G_M}(1+\delta_{2,k})\alpha_k^L A_k^L n_k^L \tag{3.92}$$

No matter what the values of number densities n_j^L and n_j^R for the border size are chosen, the mass is proved to be conserved in PSG method by satisfying

$$\sum_{j=1}^{\infty} m_j \frac{dN_j}{dt} = 0 \tag{3.93}$$

The diffusion growth rate β_j, and dissociation rate α_j of size group j particles needed to solve Eqs. (3.91)-(3.92) are calculated with Eqs. (3.75)-(3.77) using the characteristic (mean) radius given by Eq. (3.85). The radius, diffusion growth rate, and dissociation rate for the border-sized particles are:

$$r_j^L = \left(ceil\left(m_{j-1,j}\right)\right)^{1/D_f} r_1,\ r_j^R = \left(floor\left(m_{j,j+1}\right)\right)^{1/D_f} r_1 \tag{3.94}$$

$$\beta_j^L = 4\pi D_M r_j^L,\ \beta_j^R = 4\pi D_M r_j^R \tag{3.95}$$

$$\alpha_j^L = \frac{\beta_j^L N_{1,eq}}{A_j^L}\exp\left(\frac{2\sigma V_P}{R_g T}\frac{1}{r_j^L}\right),\ \alpha_j^R = \frac{\beta_j^R N_{1,eq}}{A_j^R}\exp\left(\frac{2\sigma V_P}{R_g T}\frac{1}{r_j^R}\right) \tag{3.96}$$

The particle number densities for the border sizes n_j^L and n_j^R are estimated from a geometric progression approximation

$$n_j^L = n_{j-1}^C\left(\frac{n_j^C}{n_{j-1}^C}\right)^{\frac{ceil(m_{j-1,j})-m_{j-1}}{m_j-m_{j-1}}},\ n_j^R = n_j^C\left(\frac{n_{j+1}^C}{n_j^C}\right)^{\frac{floor(m_{j,j+1})-m_j}{m_{j+1}-m_j}} \tag{3.97}$$

In order to propagate particle growth, if $n_j^C \neq 0$ and $n_{j+1}^C = 0$, n_j^R is calculated by

$$n_j^R = n_j^L\left(\frac{n_j^C}{n_j^L}\right)^{\frac{floor(m_{j,j+1})-ceil(m_{j-1,j})}{m_j-ceil(m_{j-1,j})}} \tag{3.98}$$

The particle number density at the center of each size group j is calculated by assuming two geometric progressions inside each size group

$$n_j^C = \frac{N_j}{\sum_{k=1}^{m_j-ceil(m_{j-1,j})}(1/q_j^L)^k + 1 + \sum_{k=1}^{floor(m_{j,j+1})-m_j}(q_j^R)^k} \tag{3.99}$$

$$\text{with } q_j^L = \left(\frac{\overline{n}_j}{\overline{n}_{j-1}}\right)^{\frac{1}{m_j-m_{j-1}}},\ q_j^R = \left(\frac{\overline{n}_{j+1}}{\overline{n}_j}\right)^{\frac{1}{m_{j+1}-m_j}} \tag{3.100}$$

The average number density of size group j is calculated as

$$\overline{n}_j = \frac{N_j}{floor(m_{j,j+1})-ceil(m_{j-1,j})+1} \tag{3.101}$$

Since the boundary (*ceil*, *floor*) and mean values of size groups are used directly and R_V is not explicitly found in these equations, this model is very flexible to apply. This allows arbitrary size increments between groups in a single simulation, making it easy to improve accuracy with smaller R_V in size ranges of interest and to improve computation with larger R_V in other sizes. Alternatively, the group sizes can be chosen to produce linearly-spaced particle radius intervals, needed to compare with experiments.

3.3 Validation with Exact Solution for Collision and Diffusion

3.3.1 Collision Test Problem

Saffman [191] suggested the turbulent collision frequency per unit volume of liquid medium to be:

$$\Phi_{ij} = 1.3A(\varepsilon/\upsilon)^{1/2}(r_i + r_j)^3 \quad \textbf{(3.102)}$$

where ε is turbulent energy dissipation rate and υ is kinematic viscosity. The empirical coefficient A was suggested by Higashitani [215] and is assumed constant here. This model has been often applied to study inclusion agglomeration in liquid steel [195-196, 204-208, 210]. It is chosen here as a test problem to validate the collision model, using the complete integer-range equations in Section 3.1.3 as the exact solution.

Substituting into the dimensionless form of number density and time:

$$n_i^* = n_i / n_0 \,,\; t^* = 1.3A(\varepsilon/\upsilon)^{1/2} r_1^3 n_0 t \quad \textbf{(3.103)}$$

where n_0 and r_1 are the initial number density and the radius of single pseudomolecules. The initial condition is given by $n_i^*=1$ for $i=1$ and $n_i^*=0$ for $i>1$. The size of the largest agglomerated particle is $i_M=12000$, so that accuracy within 0.05% error in the total particle volume is guaranteed up to $t^*=1$. The boundary condition is always zero number density of the largest agglomerated particle (exact solution) and for the largest size group (PSG method). The Runge-Kutta-Gill method is applied for time integration with a time step of $\Delta t^*=0.0025$. Smaller time step sizes produce negligible difference.

The total dimensionless number density of pseudomolecules and particles are defined as

$$N_M^* = \sum_{i=1}^{i_M} i \cdot n_i^* \,,\; N_T^* = \sum_{i=1}^{i_M} n_i^* \;\text{ for exact solution}$$

$$N_M^* = \sum_{j=1}^{G_M} m_j \cdot N_j^* \,,\; N_T^* = \sum_{j=1}^{G_M} N_j^* \;\text{ for PSG method} \quad \textbf{(3.104)}$$

The mass balance requires N_M^* to be constant (=1) through the entire calculation. Figure 3.7 shows the total particle volume is conserved for both the exact solution and PSG method. There is also good agreement between both cases for $R_V=3$ and $R_V=2$ for the total particle number density, which decreases with time due to agglomeration. Figure 3.8 shows that the evolution of the number densities of each size group with time from the PSG method also agrees reasonably with the exact solution for both R_V cases. With smaller R_V, accuracy of the PSG method increases as expected.

As time increases, collisions form large particles, leaving fewer smaller particles. For example, size group N_{10} in R_f=2 contains all particle sizes from 363 to 724 pseudomolecules, with a central size of 512 pseudomolecules. The number density of intermediate size groups increases at early times, reaches a maximum, and decreases at later times. The exact solution has limited maximum time, owing to its prohibitive computational cost. The tremendous computational efficiency of the PSG method is seen by examination of Table 3.3.

3.3.2 Diffusion Test Problem

To validate the PSG diffusion model, a test problem is chosen where the total number density of single pseudomolecules in the system is produced by an isothermal first order reaction [190]

$$n_s^*(t^*) = n_s(t^*)/n_{1,eq} = \sum_{i=1}^{i_M} i \cdot n_i^* = 9[1-\exp(-0.1t^*)] \quad \textbf{(3.105)}$$

The number density of dissolved single pseudomolecules must be adjusted with time, to match the increase of n_s^*. This increase with time can be interpreted as an increase in supersaturation due to decreasing temperature in a practical cooling process. The dimensionless terms are defined as

$$n_i^* = n_i / n_{1,eq}\,,\; t^* = 4\pi D_1 r_1 n_{1,eq} t \quad \textbf{(3.106)}$$

To calculate the dissociation rate in Eq.(3.76), $2\sigma V_P/(R_g T r_1)$=3.488 [190]. The initial condition is no particles, or n_i^*=0 for $i\geq 1$.

The boundary condition is always zero number density for the largest agglomerated particle (exact solution) or for the largest size group (PSG method). The maximum size of agglomerated particle is chosen as i_M=50000, to ensure that mass conservation is satisfied up to t^*=10000. The explicit Runge-Kutta-Gill method was used for integration with time step size of Δt^*=0.01 chosen for accuracy. The maximum time step for stability is roughly Δt^*=0.04 for both methods for this problem.

As shown in Figure 3.9, the total volume of particles is conserved for both the exact solution and the PSG method. This total increases with time and asymptotes at 9, according to Eq. (3.105). The number density histories from all 3 cases also agree. Its behavior can be explained by examining Figure 3.10.

Figure 3.10 shows how the particle size distribution evolves, due to the changing concentration gradients near particles of different size groups. At early times, all size group particles grow owing to the driving force of increasing supersaturation. At later times, the results show Ostwald ripening. The large particles have low concentrations, so tend to grow at the expense of smaller particles, which have high local concentrations, and eventually shrink. For example, size group N_1 (dissolved single pseudomolecules) reaches its peak and starts to decrease in number after $t^*=20$. There is reasonable agreement for both total particle number density and number densities of each size group between the PSG method and the exact solution for both cases of $R_I=3$ and $R_I=2$. Results for $R_I=2$ naturally match the exact solution more closely.

The comparison of dimensionless average particle radius, $\bar{r}/r_1$ with time between PSG method and exact solution is shown in Figure 3.11. By choosing the different truncating size, both $R_I=3$ and $R_I=2$ give good matches with exact solution. The slope of average radius with time shows a clear transition from ~0.5 at growth stage to ~1/3 at coarsening stage, which is expected in the classical precipitation theories. It is no surprise that the slopes at growth stage can be larger than 0.5 in this test problem, because it is accompanied by the continuous nucleation for a quick precipitation reaction.

According to Eqs. (3.97)-(3.101), the calculated "border number densities" of size groups at in PSG method can be used to generate the size distribution of each individual particle. The comparison of number densities with exact solution for different times is shown in Figure 3.12. It demonstrates that PSG method generally gives reasonable match of particle size distribution with exact solution, but a deeper trough and a larger number density are observed at the first minimum point and the maximum size separately. It suggests a better estimation of border number densities in PSG method is maybe possible in future.

3.3.3 Comparison of Computational Cost between PSG Method with Exact Solution

The computation times for both test problems are listed in Table 3.3. All the calculations are run with Matlab on Dell OPTIPLEX GX270 with P4 3.20GHz CPU and 2GB RAM in order to enable a fair comparison. The computational cost dramatically reduces for the PSG method. It is interesting to note that the computation cost for the collision problem is proportional to i_M^2 for the exact solution or G_M^2 for the PSG method, while it is proportional to i_M or G_M

respectively for the diffusion problem. Because the details of particle distribution inside the size groups must be captured to enable an accurate solution in a diffusion problem, the time saving is not as large. The savings increase exponentially with increasing maximum particle size. This is enough to make practical precipitation calculations possible, considering that less than 60 size groups covers particle sizes up to 100μm with constant R_V=2 for typical nitrides or carbides in microalloyed steels as shown in Table 3.1.

3.4 Practical Applications

When the PSG method is applied to model a real precipitation process, additional models are needed for the temperature history and for the mass concentrations of each element dissolved at equilibrium. This chapter assumes the temperature history is known in advance and the equilibrium precipitation model in chapter 2 is used for equilibrium calculation.

For a given steel composition and temperature history, the first step is to use the equilibrium model to compute the dissolved concentrations of every element at every temperature, and to identify the critical element which restricts the number of single pseudomolecules available to form the precipitate of interest, as a function of time. The initial condition starting from the liquid state is complete dissolution with the number density of single pseudomolecules, $N_1(t=0)$, equal to the total number density, n_s, of the precipitate of interest. For a given steel composition containing M_0 of element M, and X_0 of element X, then n_s for precipitate M_xX_y is

$$n_s = \min\left(\frac{M_0}{100}\frac{\rho_{steel}}{xA_M}N_A, \frac{X_0}{100}\frac{\rho_{steel}}{yA_X}N_A\right) \quad \textbf{(3.107)}$$

where A_M and A_X are the atomic masses of elements M and X, and ρ_{steel} is the density of the steel matrix ($7500 kg \cdot m^{-3}$). All other particle sizes have zero number densities initially.

Sometimes, such as after a solution treatment, some of the initial processing steps from the liquid state can be ignored or replaced with a measured initial distribution. Because the model in this chapter can handle only one precipitate, the initial composition must be the dissolved concentration available for that precipitate after taking away the other precipitates that form first. For example, in the cases of nitride AlN formation, a new Al concentration is used after subtracting the more stable oxide Al_2O_3.

The equilibrium number density of single pseudomolecules of the precipitate in the steel, $n_{1,eq}$, is calculated from the dissolved mass concentrations $[M]_{eq}$ and $[X]_{eq}$ at equilibrium in the same way:

$$n_{1,eq} = \min\left(\frac{[M]_{eq}}{100} \frac{\rho_{steel}}{xA_M} N_A, \frac{[X]_{eq}}{100} \frac{\rho_{steel}}{yA_X} N_A \right) \tag{3.108}$$

Although the current model only calculates size distributions for a single precipitate, other alloys may affect the results by forming other precipitates which change the equilibrium dissolved concentrations of the elements in the precipitate of interest. These effects are included through the equilibrium model, in addition to Wagner interactions [87].

The PSG kinetic model is then run, knowing the history of the equilibrium number density of single pseudomolecules of the chosen precipitate. The diffusion coefficients and dissociation rates in Eqs. (3.75)-(3.77) and (3.93)-(3.95) are updated for each time step according to the temperature history. This model calculates how the particle size distribution evolves with time.

When running the PSG model, time steps must be large enough to enable reasonable computation cost, while avoiding stability problems due to dissociation exceeding diffusion growth. Thus, the implicit Euler scheme is adopted here to integrate Eqs. (3.91)-(3.101) through time:

$$\left[1 + \Delta t \left(\frac{m_1}{m_j} \alpha_j A_j + \frac{floor(m_{j,j+1})}{m_j} \beta_j^R N_1^{i+1} + \frac{ceil(m_{j-1,j})}{m_j} \alpha_j^L A_j^L \right) \right] N_j^{i+1}$$

$$= N_j^i + \Delta t \left[\frac{m_1}{m_j} \beta_j N_1^{i+1} (N_j^{i+1} - n_j^R) + \frac{m_1}{m_j} \alpha_j A_j n_j^L + \frac{ceil(m_{j-1,j})}{m_j} \beta_{j-1}^R N_1^{i+1} n_{j-1}^R + \frac{floor(m_{j,j+1})}{m_j} \alpha_{j+1}^L A_{j+1}^L n_{j+1}^L \right.$$

$$\left. + \frac{floor(m_{j,j+1})}{m_j} \beta_j^R N_1^{i+1} (N_j^{i+1} - n_j^R) + \frac{ceil(m_{j-1,j})}{m_j} \alpha_j^L A_j^L (N_j^{i+1} - n_j^L) \right] \quad (j \geq 2) \tag{3.109}$$

where i is the time-step index. This implicit scheme allows over 10^4–fold increase in time step size comparing with the original explicit scheme, for realistic precipitate/matrix interfacial energies ~0.5J/m^2. The above equation system is solved with the iterative Gauss-Seidel method until the largest relative change of N_j^{i+1} converges to within less than 10^{-5} between two iterations. The upper limits of n_j^L and n_j^R are N_j^{i+1}, and are evaluated at each iteration. Although this scheme is stable for any time step size, its accuracy may deteriorate if the time step is too large.

Thus a reasonable time step must be chosen where results stay almost the same with a smaller time step.

Having validated mass conservation with test problems, the number density of single pseudomolecules is then computed as follows, instead of Eq. (3.92)

$$N_1^{i+1} = n_s - \sum_{j=2}^{G_M} m_j N_j^{i+1} \tag{3.110}$$

Because single pseudomolecules is the only size group to react with all particles, this choice saves around half of computational cost. To post-process the results, the total number density of precipitate particles N_p, fraction precipitated f_P, mean precipitate particle radius $\overline{r}_P$ and precipitate volume fraction φ_P are computed from the number densities as follows:

$$N_P = \sum_{j=G_T}^{G_M} N_j \tag{3.111}$$

$$f_P = \frac{\sum_{j=G_T}^{G_M} m_j N_j}{n_s} \tag{3.112}$$

$$\overline{r}_P = \frac{\sum_{j=G_T}^{G_M} r_j N_j}{n_P} \tag{3.113}$$

$$\varphi_P = f_P \frac{n_s}{n_s - n_{1,eq}} \frac{\rho_{steel}}{\rho_P} \frac{(w_P)_{eq}}{100} \tag{3.114}$$

where size group G_T, which contains particles just larger than a "truncating" threshold radius $r_{T-1,T}$, is introduced to define the split between "dissolved" and measurable particles. This parameter must be introduced because all experimental techniques have resolution limits, while the current PSG model simulates particles of all sizes including single pseudomolecules. ρ_P is the density of the precipitate phase, and w_P^e is the mass concentration of precipitate at equilibrium (wt%). All of these values with subscript "P" here are clearly dependent on the choice of truncating size, which is not required for numerical simulation but can be given by the resolutions of different experimental techniques. The complete PSG model is applied here to three different example precipitate systems, where measurements are available for validation.

3.4.1 Precipitated Fraction for Isothermal AlN Precipitation

The first validation problem for the PSG diffusion model was to simulate the isothermal precipitation of AlN in a 0.09%C, 0.20%Si, 0.36%Mn, 0.051%Al and 0.0073%N steel for the experimental conditions measured by Vodopivec [138]. Specimens were solution treated at 1300^{o}C for 2 hours, "directly" cooled to the precipitation temperature of 840^{o}C in austenite or 700^{o}C in ferrite, aged for various times, and quenched. The AlN content in steel was measured using the Beeghly method [12].

The initial experimental measurements (zero and short aging times) report 6.4% of the total N (N_0=0.0073%) precipitated as AlN, perhaps because the cooling stages were not fast enough. The final precipitated amounts of nitrogen as AlN do not reach the predictions of the equilibrium model, even after long holding times, when the precipitated fraction becomes nearly constant. This might be due to nitrogen consumed into other types of nitrides. Thus the measurements are normalized to zero at zero aging time, and $(N_0-[N]_{eq})/N_0$ at long times.

As shown in Figure 3.13, the equilibrium model [87] predicts AlN to start forming at 1236^{o}C, and the equilibrium dissolved concentration of nitrogen in steel is ~0.00022wt% at 840^{o}C and ~0.0000031wt% at 700^{o}C. A sharp decrease of equilibrium dissolved aluminum concentration can be seen over the $\gamma \rightarrow \alpha$ phase transformation, 865^{o}C to 715^{o}C, due to the lower solubility limit of AlN in ferrite predicted by the equilibrium model.

Isothermal precipitation simulations of 1 hour at 700^{o}C and 3 hours at 840^{o}C were run, neglecting the cooling histories before and after, which were not clearly reported. The molar volume of AlN is 12.54×10^{-6}m^3/mol [36], and the diffusion coefficient of Al in austenite and ferrite is taken from Table 3.2. The interfacial energies for these two precipitation temperatures are calculated in the appendix A, where the value is seen to be 10% higher at 700^{o}C in ferrite than at 840^{o}C in austenite. The number densities of precipitate particles are calculated based on the nitrogen concentration, because this element is insufficient when reacting with aluminum to form AlN for this steel composition. Constant R_V=2 and 32 size groups are used in the simulation, which covers particle radii up to around 200nm. The time step is 0.001s with ~1000 decreasing to ~100 iterations required within each time step for convergence of the implicit method with Gauss-Seidel solver. Because it has been suggested that the Beeghly technique cannot detect very fine precipitate particles which could pass through the filter [216, 217], the truncating precipitate radius is set to 2.0nm in the simulation to match the measurements.

The predicted AlN precipitate fractions are shown and compared with experimental measurements in Figure 3.14. Reasonable matches are shown at both temperatures. The calculation verifies the experimental observation of much faster precipitation in ferrite than in austenite, due to the lower solubility limit of AlN and the faster diffusion rate of aluminum in ferrite than in austenite. The disagreement could be due to AlN precipitation on the grain boundaries, because the physical properties assumed in the simulation are based on homogeneous precipitation in the steel matrix. The same mismatch in predicting AlN precipitation has been found and discussed by other researchers [218, 219].

3.4.2 Size Distribution for Isothermal Niobium Precipitation

The second validation problem is to simulate the size distribution of niobium precipitate particles in steel containing 0.079%Nb, 0.011%C, 0.001%N, 0.002%Mn, 0.0023%S, 0.001%P, 0.006%Al and 0.0013%O, to compare the PSG simulation predictions with the niobium precipitate distribution measured in ferrite [220]. The alloy was vacuum induction melted, cast into ingots, and hot rolled from 50mm to 5mm thickness. After homogenization at 1350^{o}C for 45 min, the specimens were rapidly quenched to an aging temperature of 700^{o}C and held for various times. Small-angle neutron scattering (SANS) and transmission electron microscopy (TEM) were used to measure precipitate amount and size.

The equilibrium calculation in Figure 3.13 predicts that the niobium precipitates in this steel first become stable at 1054^{o}C, and the equilibrium dissolved mass concentration of the niobium is calculated as 0.0002506wt% at 700^{o}C [87]. For the PSG precipitation simulation, the diffusion coefficient of Nb is taken from Table 3.2, molar volume of NbC is 13.39×10^{-6}m^3/mol [36], density of NbC is 7.84×10^{3}kg/m^3 [36], and the interfacial energy is calculated in the appendix A. The composition of the niobium precipitates in the simulation was regarded as $NbN_{0.08}C_{0.80}$, according to the predictions of the equilibrium model, for this steel composition, where pctC > pctN. This composition agrees with the experimental observation of "niobium carbide" precipitates, and the non-stoichiometric ratio of $NbC_{0.87}$ measured in other work [36]. Lacking data for this complex niobium precipitate, property data were taken for NbC, which are believed to be very similar, as the lattice constants of NbC and $NbC_{0.87}$ differ by only ~0.2% [221].

In order to compare with the experimental measurements, R_V was set equal 2 for particles with radius smaller than 0.3nm and larger than 10nm, and varied to give constant 0.2nm size groups for 0.3-8.5nm, and 0.5nm size groups for 8.5-10nm. A total of 50 size groups were used to model particle radius up to 10nm to cover the largest particle observed in the experiments. The implicit time step was 0.01s, with less than 10 iterations needed for convergence at most times, resulting in ~2.5 days of total CPU time on a 3.20GHz processor PC for the 600,000s (~7 days) simulation. Rapid quenching from solution treatment to aging temperature and from aging to ambient is assumed, so only an isothermal simulation at 700^{o}C was performed.

Predicted evolutions of precipitate mean size, size distribution and volume fraction results from the PSG simulation are shown in Figures 3.15 and 3.16, and compared with available measurements [220]. Because many dislocations in the matrix due to the prior deformation may relax the lattice mismatch and decrease the interface energy, they become favored locations for precipitation. Figure 3.15 shows that lowering the interface energy to 0.3J/m^2 (corresponding to a modified factor of 0.7) and choosing a truncating radius of 0.7nm gives the best match of both mean precipitate size and volume fraction with the SANS measurements. These results also indicate that decreasing interface energy makes the capillary effect smaller which makes large particles more difficult to grow, so a finer precipitate size and slower precipitation are predicted. All volume fraction curves eventually reach the equilibrium value of 0.084% for aging at 700^{o}C. These calculation results of decreasing interface energy are qualitatively consistent with the experimental observations of deformation-induced nanosized Cu precipitation [222]. Increasing the truncating radius from 0.5nm to 0.7nm significantly delays the precipitation, although it has only minor influence on the calculated mean precipitate size, and only during the initial stage of precipitation.

The simulation results with the adjusted interface energy 0.3J/m^2 are compared with the normalized TEM measured particle size distribution / volume number frequency in ferrite at 300 minutes in Figure 3.16. The predicted mean radius of Nb precipitate particles of 1.93nm compares closely with the measured 1.82nm, and the particle size distributions also match reasonably. The simulated size distribution is missing the measured tail of large particles, however. This is likely due to easier nucleation and higher diffusion at the grain boundaries, segregated regions, or other locations in the steel microstructure, where larger precipitates can form locally in the real samples. In addition, the observed particles in TEM imaging have

irregular aspect ratio ~2.3 [220], which differs from the spherical assumption of the model, and suggests non-isotropic properties.

The calculated evolution of the size distribution of the Nb particles is depicted in Figure 3.17. Each curve has the same characteristic shape, which evolves with time. The number densities decrease with increasing particle size to a local minimum, increase to a peak, and finally decrease to zero. With increasing time, the number density of single (dissolved) pseudomolecules decreases from the large initial value, n_s, that contains all of the particles, to the small equilibrium value $n_{1,eq}$ at equilibrium. Very small particles in the first few size groups are unstable, as the chance of gaining pseudomolecules is less than that of losing pseudomolecules, owing to the high surface curvature. Thus, their number densities decrease with size, owing to the decreasing chance of a larger unstable embryo of pseudomolecules coming together due to the simulated process of random thermal diffusion. With increasing size above the critical size, pseudomolecule attachment increasingly exceeds dissolution, so these stable particles grow increasingly faster and become larger. Very large particles are rare simply due to insufficient growth time.

The entire size distribution grows larger with time. Except for the small unstable embryos which decrease in number, all other particle sizes increase in number during this period. The maximum particle radius increases from 1.4nm at 20s to 2.0nm at 330s, while the most common size (peak number density) increases from 0.4nm to 0.8nm.

After this initial growth stage, single pseudomolecules approach the equilibrium concentration. Smaller particles then decrease slowly in number due to dissolution, which provides single pseudomolecules for the slow growth of large particles. This is the particle coarsening or "Ostwald ripening" stage. This final precipitation stage is estimated to begin at ~330s, based on the maximum total number of particles larger than 0.7nm, shown in Figure 3.17. This time matches with the decrease in slope of precipitated volume fraction with time that is both predicted and measured in Figure 3.15(b). The precipitate size evolution after 100,000s roughly follows the law of $\overline{r_p} \propto t^{0.3}$ in Figure 3.15(a), which agrees with the value of 1/3 from classical LSW coarsening theory [173, 174]. As larger particles grow, and smaller particles shrink during coarsening, the total number of particles decreases. This corresponds with the evolution of critical radius, included in Figure 3.14. Starting smaller than the mean size, the

critical size increases with time to approach the mean, as supersaturation decreases towards 1 at equilibrium.

The model results also quantify and provide a new insight into the classical stages of precipitate nucleation, growth, and coarsening. For example, a critical radius, r_c, can be obtained by setting $\beta_i n_{1i}=\alpha_i A_i$, which means that the rate of particle growth due to diffusion of single pseudomolecules to the surface exactly matches the rate of particle shrinking due to dissociation, and from Eqs. (3.76)-(3.77), leads to:

$$r_c = \frac{2\sigma V_P}{R_g T \ln(n_1 / n_{1,eq})} \tag{3.115}$$

At this critical size, the surface concentration of pseudomolecules, n_{1i}, equals that at the far-field, n_1. Although this relation holds at any time, it is consistent with classical nucleation theory, which balances the decrease in volumetric free energy ΔG_V in forming a spherical nucleous with the energy increase to form the new interface, σ, when Δg_V for a single precipitate system is defined as:

$$\Delta g_V = \frac{R_g T}{V_P} \ln \Pi \tag{3.116}$$

where Π is the time-dependent supersaturation, which can be interpreted as $n_1/n_{1,eq}$ in the current model. The same trends of critical radius in Figure 3.18 are observed with classical precipitation models. The current PSG method is more general, however, as the precipitation evolves naturally according to the time-varying local concentration gradients and cooling conditions.

3.4.3 Precipitation-Temperature-Time (PTT) Diagram of Nb(C,N)

The third validation problem is to simulate the precipitation of Nb(C,N) in austenite containing 0.067%C, 1.23%Mn, 0.20%Si, 0.008%S, 0.008%P, 0.040%Nb, 0.02%Al and 0.006%N, to compare with the measured precipitation start and finish times in in Precipitation-Temperature-Time (PTT) diagram [164].

The isothermal precipitation behavior was determined using a computerized material testing system in vacuums. The cylindrical samples with 8mm long and 4mm in diameter, were reheated to the solution temperature of 1150^{o}C, held for 30 minutes, and then cooled down to test temperature between 850^{o}C and 950^{o}C at intervals of 25^{o}C. Each sample was held for 1 minute at the test temperature to stabilize, and 5% deformation was then executed using a constant strain

rate of 0.1s. The stress decreases with time was monitored, while the strain level after deformation was kept constant.

The stress vs time curves for this Nb-containing steel in the above stress relaxation tests are then recorded in Figure 3.19(a). Comparing with stress relaxation curves of reference plain carbon steel, the time dependence of the stress cannot be described by a logarithmically linear relationship anymore when precipitation occurs within sample, as shown in Figure 3.19(b) [25]. The precipitation causes a stress increment in addition to the basic logarithmic part, and the start and finish times are identified as the stress increment deviates from zero and reaches its maximum in stress relaxation curves [164]. These points are believed to correspond with the start point of the growth and coarsening stages of precipitation, separately.

The equilibrium precipitation calculation result for this steel composition in austenite is shown in Figure 3.20. MnS precipitates first at 1564^{o}C, then Nb(C,N) begins to precipitate at 1141^{o}C, and AlN occurs at 1021^{o}C finally. Figure 3.20(b) shows the molar fraction of niobium nitride and carbide in mixed Nb(C,N) evolving with time.

Isothermal precipitation simulations of 1000 second at each test temperature were run, neglecting the cooling histories before and after that. A constant $R_V=2$ and 30 size groups were used to cover particle radius up to ~100nm in simulation. The diffusion coefficient of Nb in austenite is taken as Table 3.2, molar volume of Nb(C,N) is 13.06×10^{-6}m^3/mol, which is assumed to be the average of NbN and $NbC_{0.87}$ [36], and independent of the composition and temperature, the effective interface energy is defined as $\sigma_{Nb(C,N)} = \xi(f_{NbC,eq}\sigma_{NbC} + f_{NbN,eq}\sigma_{NbN})$, where $f_{NbC,eq}$ and $f_{NbN,eq}$ are equilibrium molar fractions shown in Figure 3.20(b). σ_{NbC} and σ_{NbN} are calculated in Appendix A, and it shows that these interface energies slightly increase with lowing temperature.

By choosing a modified factor ξ=0.475 for accounting the deformation introduced in tests and a truncating radius of 0.8nm, the calculated precipitated fraction evolutions with time are shown in Figure 3.21(a). These precipitated fraction curves are normalized with a ratio of $Nb_0/(Nb_0-[Nb]_{eq})$, thus will tend to reach 1 finally. The slope transition points in these curves, labeled with circle symbols, are thought to stand for the precipitation start and finish times, which are determined as the slope transition points in stress-time curves in the stress relaxation tests, as shown in Figure 3.19(a).

The comparison of precipitation start and finish times between calculation and experiment is shown in Figure 3.21(b), and good matches for all five test temperatures are found by slope method. The curves of 1%, 5%, 10%, 50% and 90% precipitated fractions are also shown in the same figure. All curves show a classical "C" shape in PTT diagram. At high temperature just below the precipitation temperature 1130°C, the precipitation rate is slow because of a low supersaturation, although diffusion rate is high. At low temperature, the precipitation is also slow because of a low diffusion rate, although the supersaturation is high now. Thus a quickest precipitation rate is expected at a medium temperature range, around a nose temperature of 900°C.

3.5 Parameter Investigation

In order to understand the influence of different physical parameters on precipitation, the numerical investigation is applied for the Nb(C,N) case at T=900°C in section 3.4.3. Niobium is always assumed to control the diffusion rate of precipitate and determine the particle number densities Nb(C,N) due to its shortage. The reference state has the niobium concentration of 0.04 wt%, diffusion coefficient of 1.125×10^{-16}m^2/s, interface energy of 0.3J/m^2 and equilibrium niobium concentration of 0.004327 wt%, which are the properties at 900°C. The molar volume of Nb(C,N) is determined as $f_{NbC,eq}V_{NbC} + f_{NbN,eq}V_{NbN}$=$13.12\times10^{-6}$m^3/mol. Constant R_V=*2* and 30 size groups are used to reach the largest precipitate radius as ~100nm. Truncating radius is set as 0.5nm. The parameters of precipitation investigated include the diffusion coefficient, interface energy and equilibrium concentration.

A larger diffusion coefficient obviously increases both the precipitation rate and the precipitate size, as shown in Figure 3.22. The increase of precipitation rate is roughly proportional to the increase of diffusion coefficient. But the increase of precipitate size does not correspond with the relationship of $r \propto (D_M t)^{1/2}$ in growth or $r \propto (D_M t)^{1/3}$ in coarsening in classical precipitation theory because a larger diffusion coefficient also increases the nucleation rate, which generates more stable nuclei and so causes less increase in precipitate size. The diffusion coefficient on grain boundaries is believed to be ~1000-10000 times than that in matrix [14, 198], which could explain the observed presence of coarser precipitates on grain boundaries in most measurements.

The influence of interface energy on precipitation includes two sides. Smaller interface

energy decreases the nucleation barrier to form stable particles, so increases the precipitation rate at the beginning of precipitation. On the other hand, a decrease of interface energy causes a smaller capillary effect, and makes more fine precipitates and less coarse precipitates to form. The larger precipitates caused by the higher interface energy facilitate more complete precipitation at intermediate times (~1000s). These effects of interface energies of $0.25J/m^2$, $0.3J/m^2$ and $0.35J/m^2$ are compared and shown in Figure 3.23.

The last important parameter which can influence precipitation behavior is the equilibrium concentration. As shown in Figure 3.24, for the same initial concentration, an increase of equilibrium dissolved concentration of niobium, causes supersaturation of pseudomolecules of niobium precipitate to decrease. This will delay the precipitation rate due to a decrease of solutes in matrix that can precipitate out. At the same time, a lower supersaturation causes a smaller nucleation rate and less stable particles, thus a coarser size distribution of precipitate is expected. All of these findings from parameter investigation are identical with those numerical results predicted by the classical precipitation theory [223, 224].

The results presented in this chapter are only approximate, because homogeneous nucleation (it may include nucleation in matrix, on dislocations or grain boundaries, but only one type of precipitates is involved and no solid surface to aid nucleation) of only one type of precipitate was simulated, instead of the many different types of precipitates that actually form in steel, and only the physical properties of the matrix phase were adopted. These are not fundamental limitations of the method, however. Competition between the different precipitates for the alloy elements, such as different nitrides consuming nitrogen, causes inaccuracies that are addressed in Chapter 4 by generalizing the current model to handle multiple precipitates. Such an enhanced multiphase precipitate model is needed to account for previously formed precipitates which act as heterogeneous nucleation sites for new precipitates of different composition. Heterogeneous nucleation also needs consideration of grain-boundary and dislocation effects on the interfacial energy.

3.6 Tables and Figures

Table 3.1: Relationship between size group and size range for R_V=2 and R_V=3

R_V=2			R_V=3		
Size group	Number of pseudomolecules	Radius range	Size group	Number of pseudomolecules	Radius range
1	1	0.17nm	1	1	0.17nm
2	2	0.22nm	2	2-5	0.22-0.29nm
3	3-5	0.25-0.29nm	3	6-15	0.31-0.42nm
4	6-11	0.31-0.38nm	4	16-46	0.43-0.61nm
5	12-22	0.39-0.48nm	5	47-140	0.62-0.89nm
6	23-45	0.49-0.61nm	6	141-420	0.89-1.28nm
7	46-90	0.61-0.77nm	7	421-1262	1.28-1.84nm
8	91-181	0.77-0.97nm	8	1263-3787	1.84-2.66nm
9	182-362	0.97-1.22nm	9	3788-11363	2.66-3.84nm
10	363-724	1.22-1.53nm	10	11364-34091	3.84-5.53nm
11	725-1448	1.53-1.93nm	…	…	…
12	1449-2896	1.93-2.43nm	15	2.76×10^{6}-8.28×10^{6}	23.9-34.5nm
13	2897-5792	2.43-3.07nm	20	6.71×10^{8}-2.01×10^{9}	149-216nm
14	5793-11585	3.07-3.86nm	25	1.63×10^{11}-4.89×10^{11}	0.93-1.34μm
15	11586-23170	3.86-4.87nm	30	3.98×10^{13}-1.19×10^{14}	5.82-8.39μm
…	…	…	35	9.63×10^{15}-2.89×10^{16}	36.3-52.4μm
20	3.71×10^{5}-7.41×10^{5}	12.3-15.4nm	40	2.34×10^{18}-7.02×10^{18}	227-327μm
25	1.19×10^{7}-2.37×10^{7}	38.9-49.0nm			
30	3.80×10^{8}-7.59×10^{8}	124-156nm			
35	1.21×10^{10}-2.43×10^{10}	392-494nm			
40	3.89×10^{11}-7.77×10^{11}	1.25-1.57μm			
45	1.24×10^{13}-2.49×10^{13}	3.95-4.98μm			
50	3.98×10^{14}-7.96×10^{14}	12.6-15.8μm			
55	1.27×10^{16}-2.55×10^{16}	39.9-50.2μm			
60	4.08×10^{17}-8.15×10^{17}	127-159μm			

*The calculation of particle size is special based on AlN with $V_P=12.54\times10^{-6}m^3/mol$

Table 3.2: Diffusion Coefficients for elements in austenite and in ferrite [36, 197-202]

Element	In austenite ($m^2 \cdot s^{-1}$)	In ferrite ($m^2 \cdot s^{-1}$)
N	$0.91\times10^{-4}\exp(-168500/RT)$	$0.008\times10^{-4}\exp(-79100/RT)$
C	$0.0761\times10^{-4}\exp(-134600/RT)$	$0.0127\times10^{-4}\exp(-81400/RT)$
O	$1.3\times10^{-4}\exp(-166000/RT)$	$0.00291\times10^{-4}\exp(-89500/RT)$
S	$2.4\times10^{-4}\exp(-223400/RT)$	$4.56\times10^{-4}\exp(-214600/RT)$
Ti	$0.15\times10^{-4}\exp(-251200/RT)$	$3.15\times10^{-4}\exp(-248000/RT)$
Nb	$0.83\times10^{-4}\exp(-266500/RT)$	$50.2\times10^{-4}\exp(-252000/RT)$
V	$0.25\times10^{-4}\exp(-264200/RT)$	$0.61\times10^{-4}\exp(-267100/RT)$
Al	$2.51\times10^{-4}\exp(-253400/RT)$	$30\times10^{-4}\exp(-234500/RT)$
Mn	$0.055\times10^{-4}\exp(-249400/RT)$	$0.76\times10^{-4}\exp(-224400/RT)$

Table 3.3: Comparison of computational cost for test problems

	Collision ($t^*=1$)			Diffusion ($t^*=10000$)		
	Exact	PSG(R_V=2)	PSG(R_V=3)	Exact	PSG(R_V=2)	PSG(R_V=3)
Storage	i_M=12000	G_M=16	G_M=11	i_M=50000	G_M=18	G_M=13
Computational time	~225 hours	~0.8s	~0.4s	~27 hours	~560s	~390s

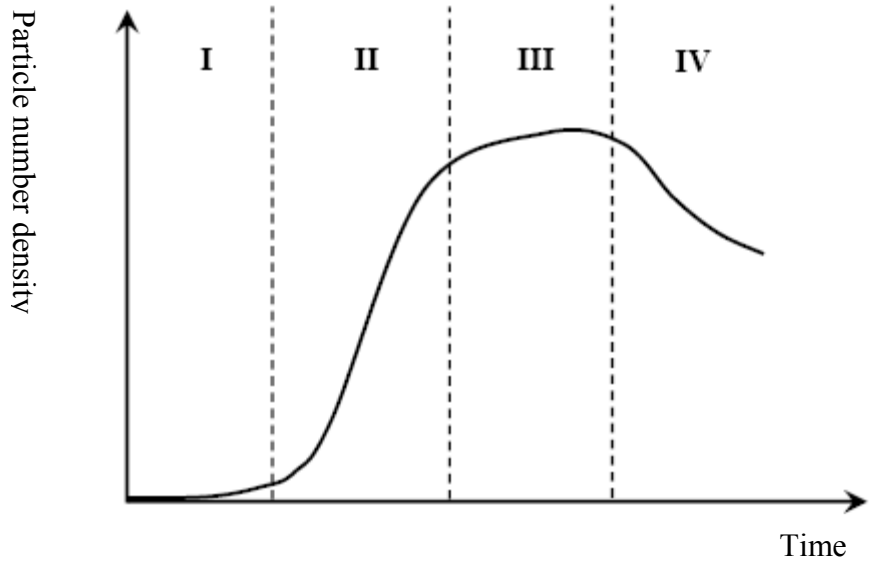

Figure 3.1: Schematic of particle number density vs time over preciptiation. The four regions are: I. Induction; II. Nucleation; III. Growth; IV. Coarsening

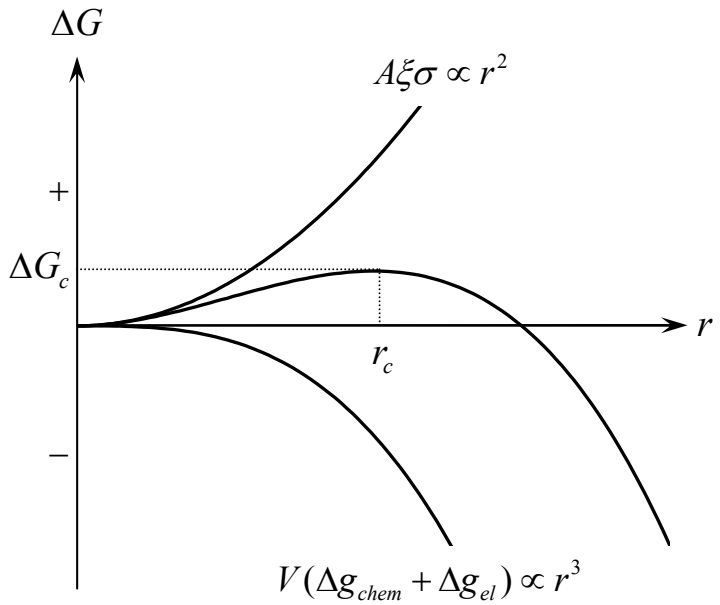

Figure 3.2: Schematic disgram of free energy change for the nucleation of a spherical nucleus as a function of its radius

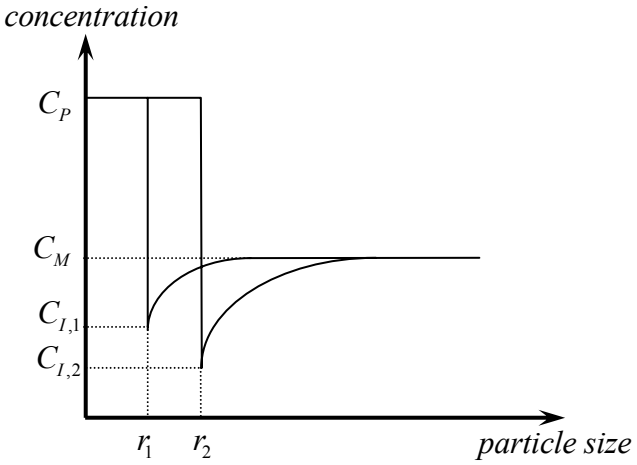

(a). Growth

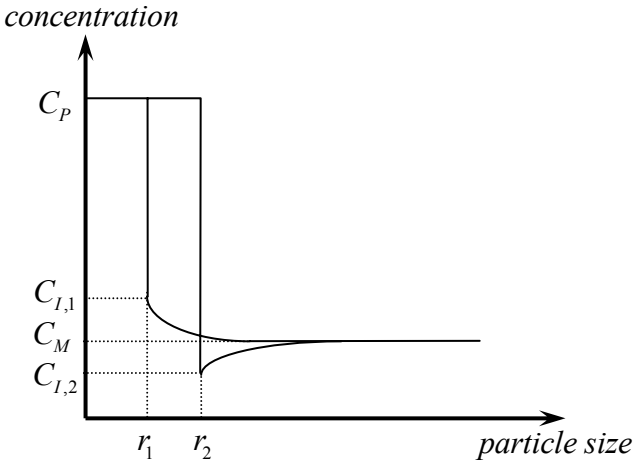

(b). Coarsening

Figure 3.3: Schematic of the solute concentration of different particles during the growth and coarsening stage

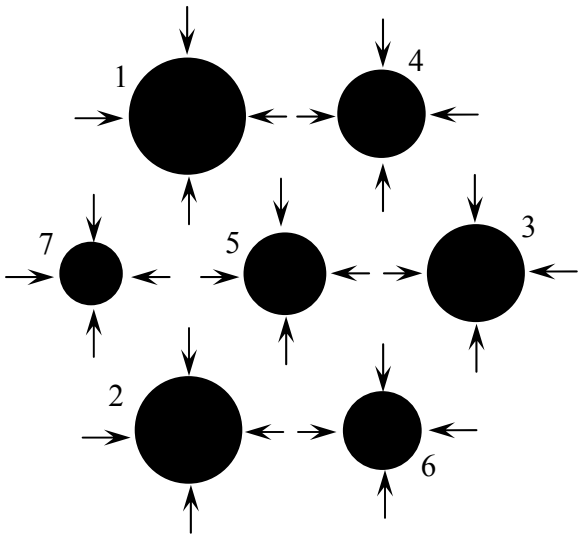

(a). Growth

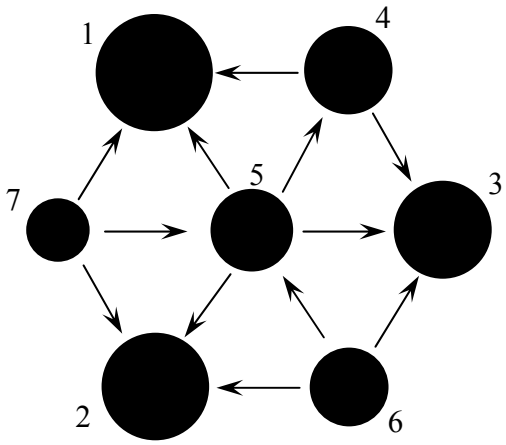

(b). Coarsening

Figure 3.4: Schematic of 2-D diffusion during the growth and coarsening stages

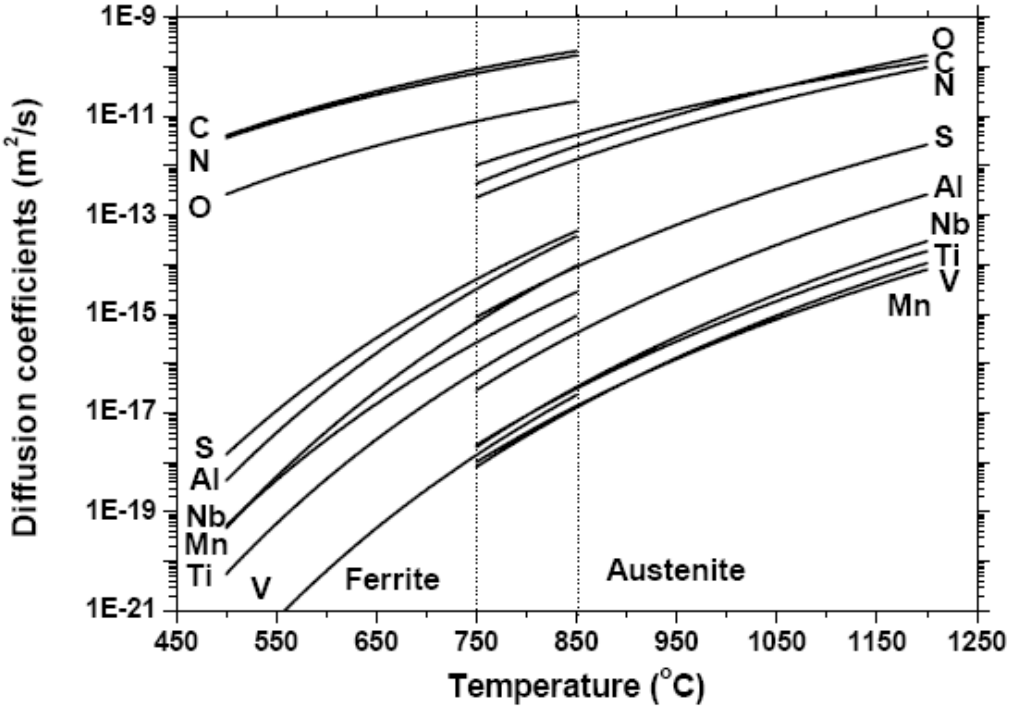

Figure 3.5: Diffusion coefficients of alloying elements in austenite and ferrite

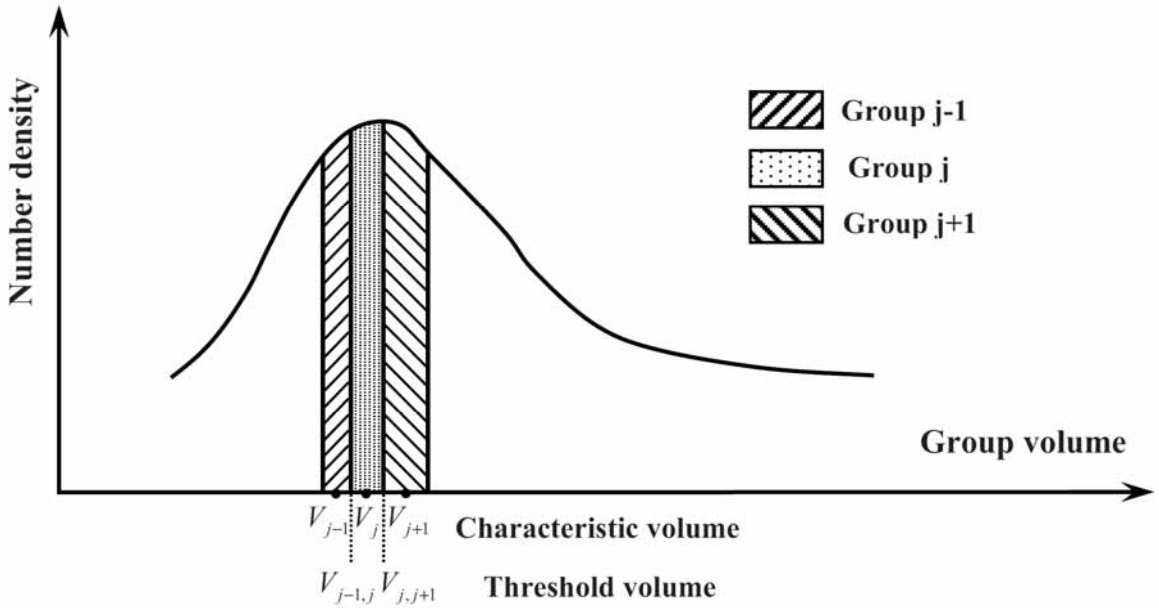

Figure 3.6: Schematic of particle size distribution in PSG method

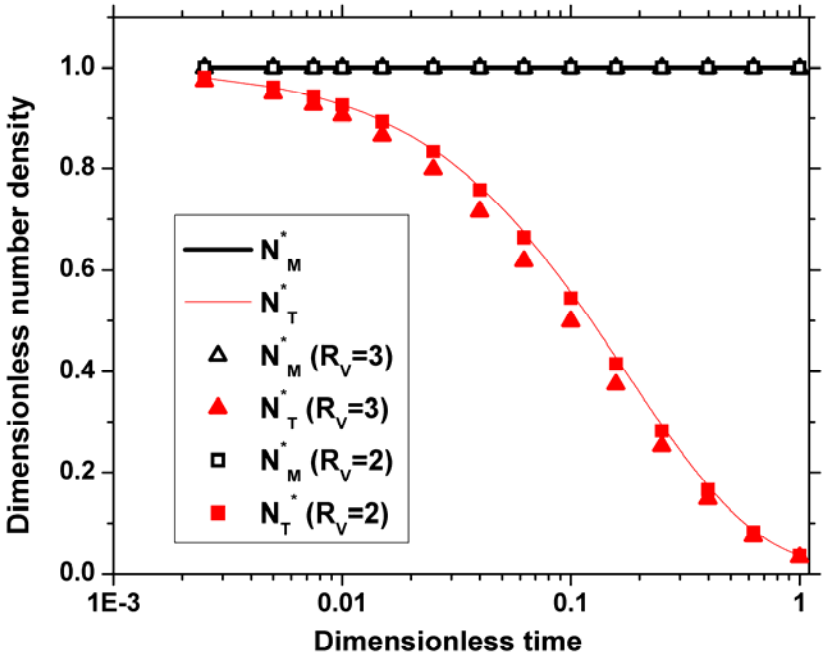

Figure 3.7: Comparison of collision curve calculated by PSG method with exact solution for different R_V

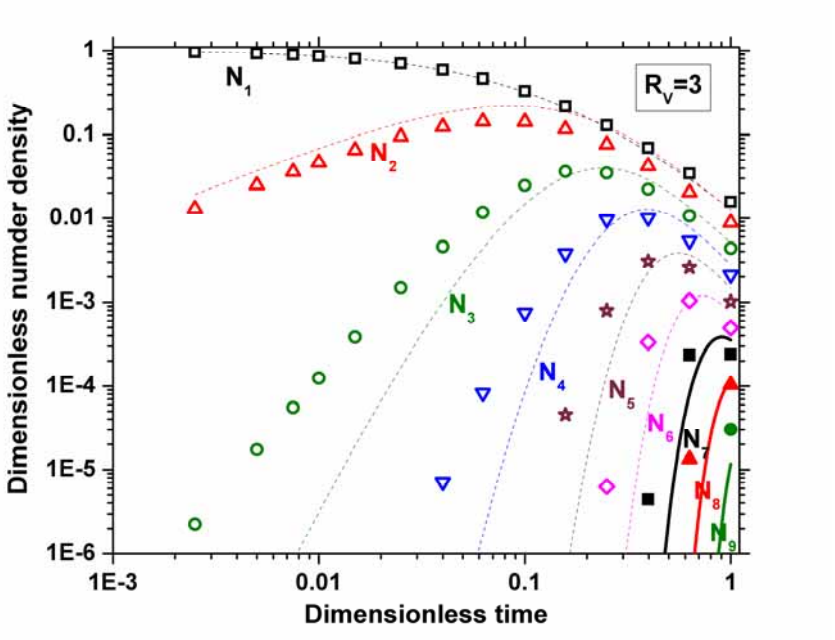

(a). R_V=3

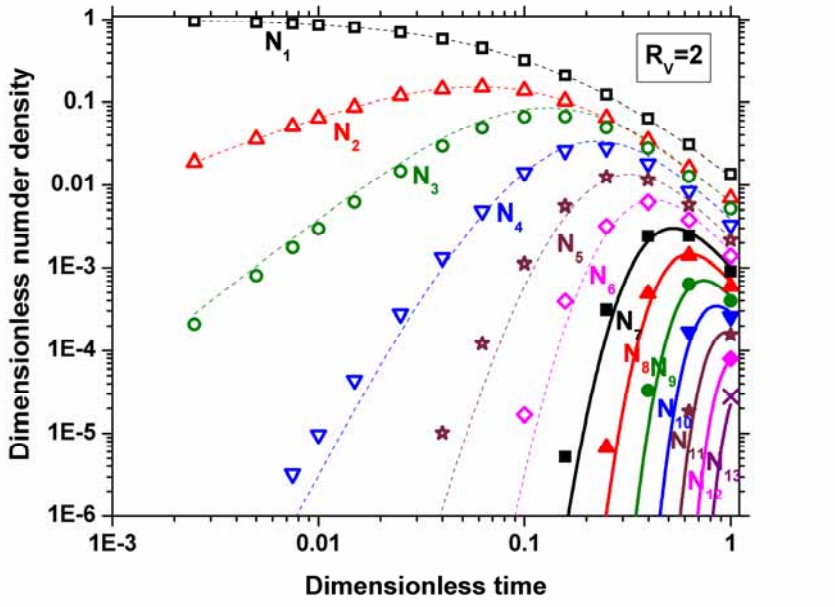

(b). R_V=2

Figure 3.8: Comparison of collision curve of each size group calculated by PSG method with exact solution for different R_V

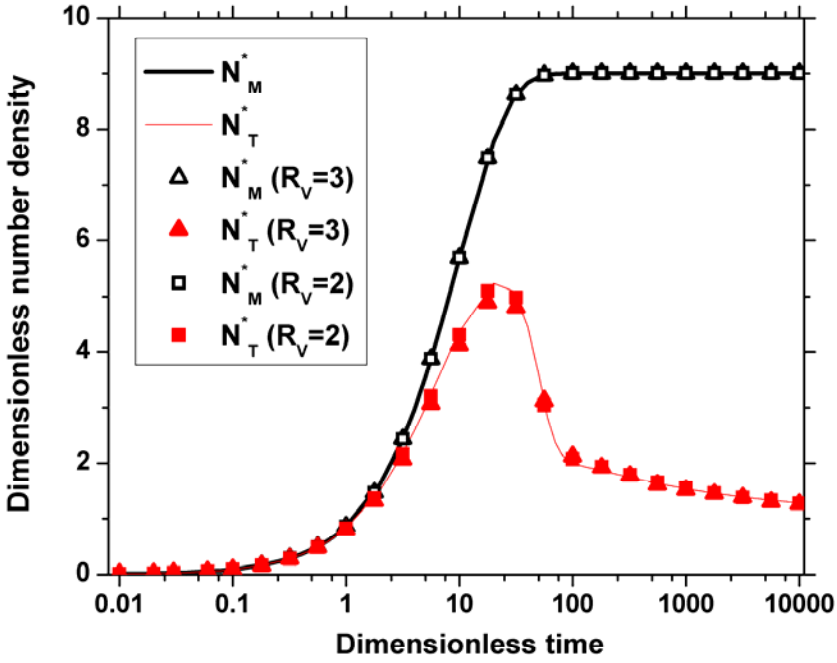

Figure 3.9: Comparison of diffusion curves calculated by PSG method with exact solution for different R_V

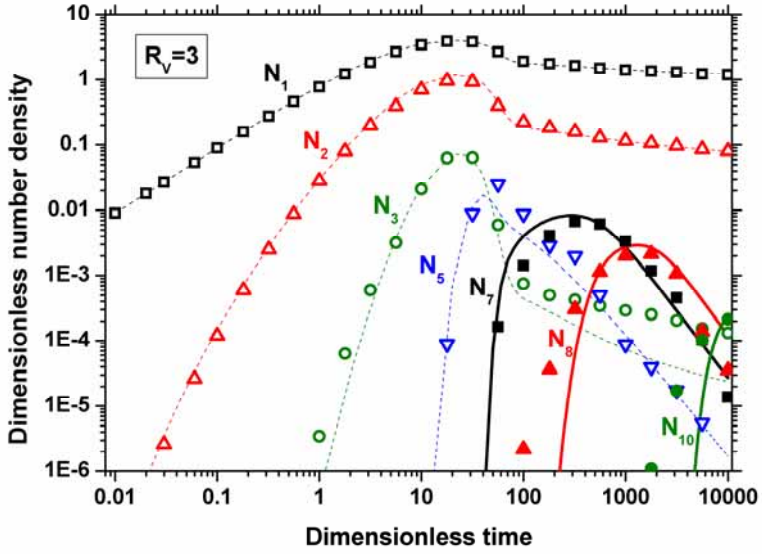

(a). R_V=3

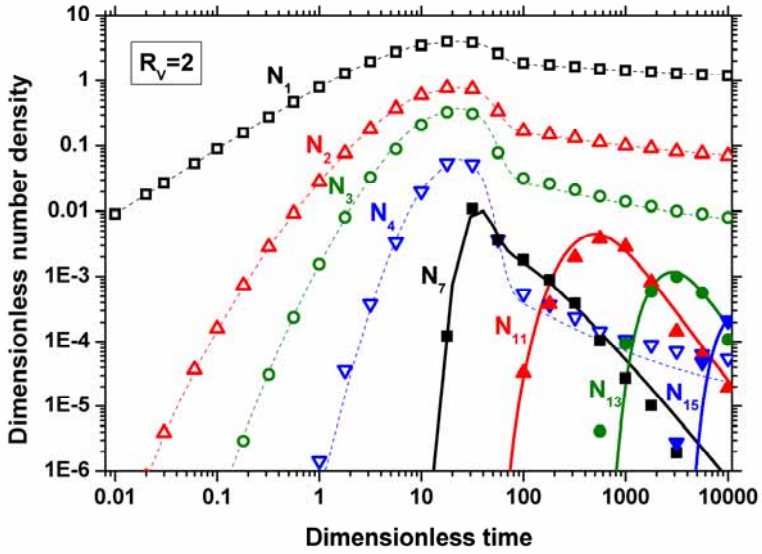

(b). R_V=2

Figure 3.10: Comparison of evolving numbers of each size group calculated by PSG diffusion method with exact solution for different R_V

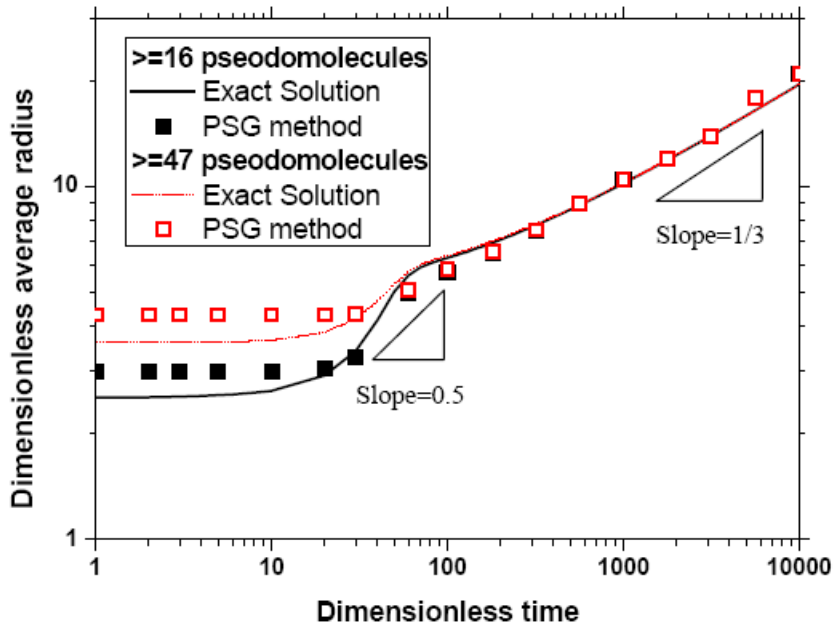

(a). R_V=3

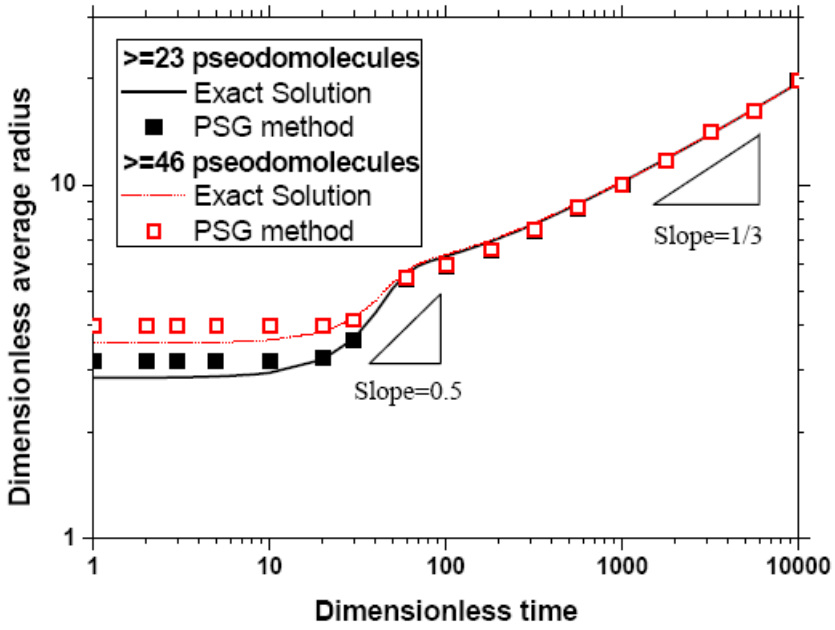

(b). R_V=2

Figure 3.11: Comparison of average particle radius between PSG method and exact solution for different R_V

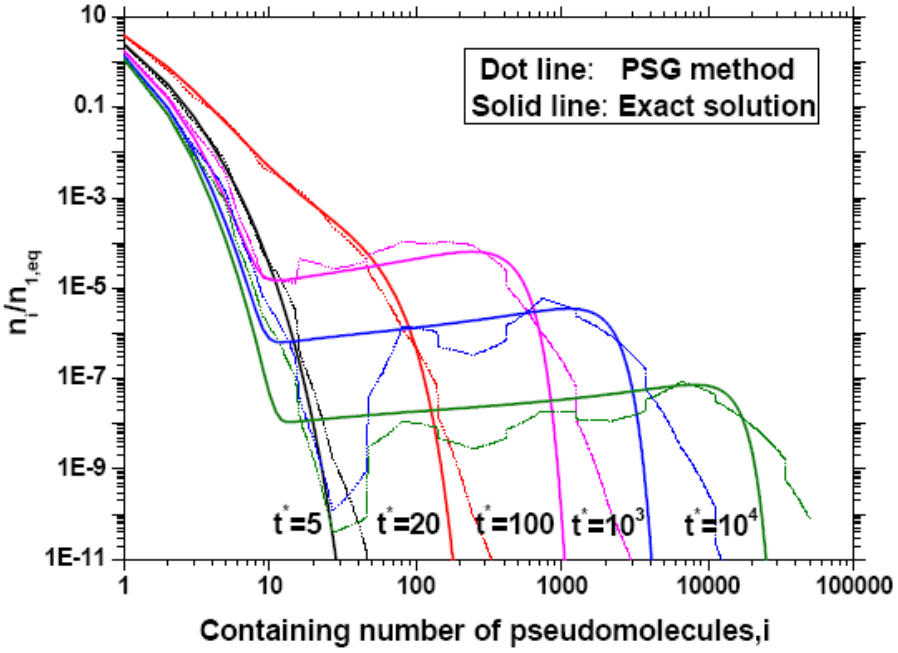

(a). R_V=3

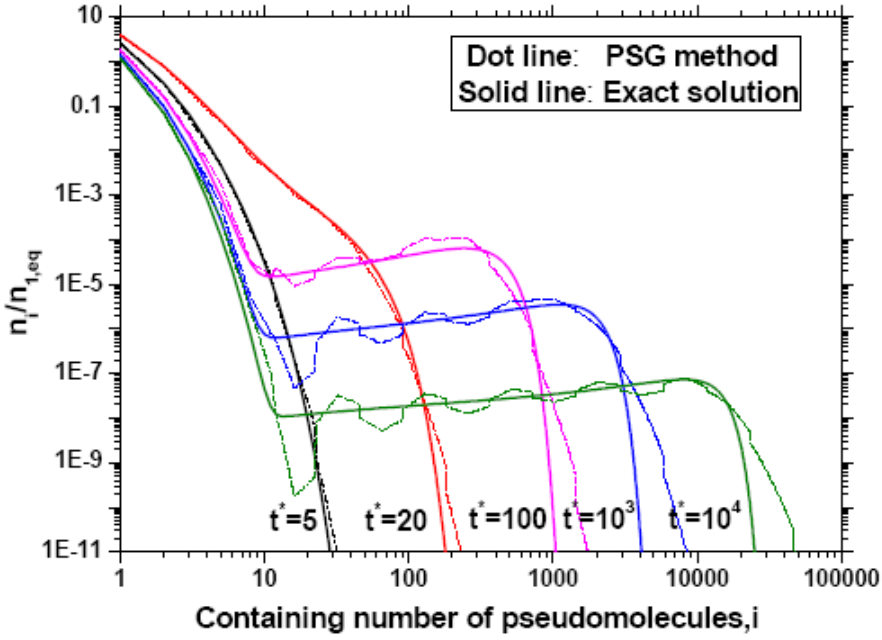

(b). R_V=2

Figure 3.12: Comparison of size distribution between PSG method and exact solution for different times and R_V

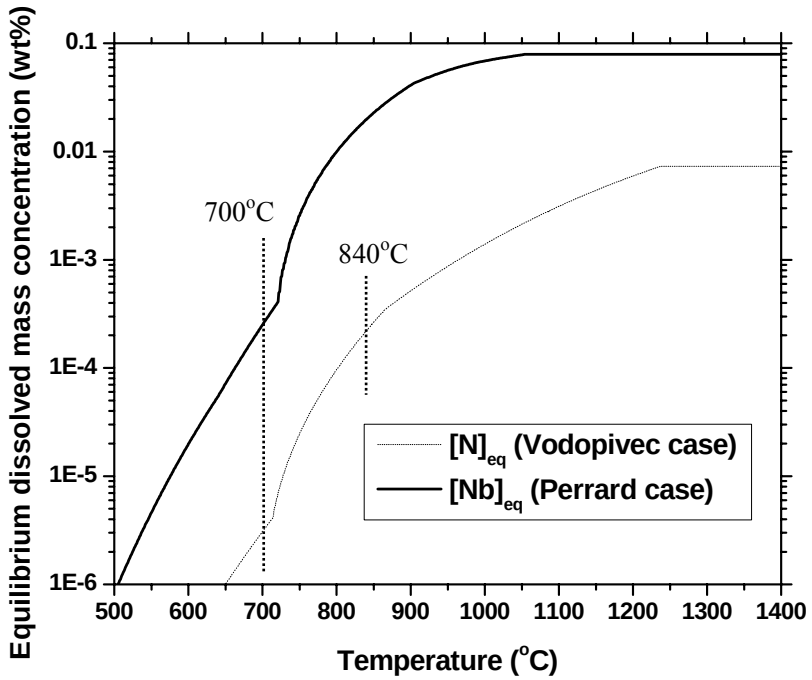

Figure 3.13: Calculated equilibrium dissolved mass concentration of N for Vodopivec case [138] and Nb for Perrard case [220] showing aging test temperatures

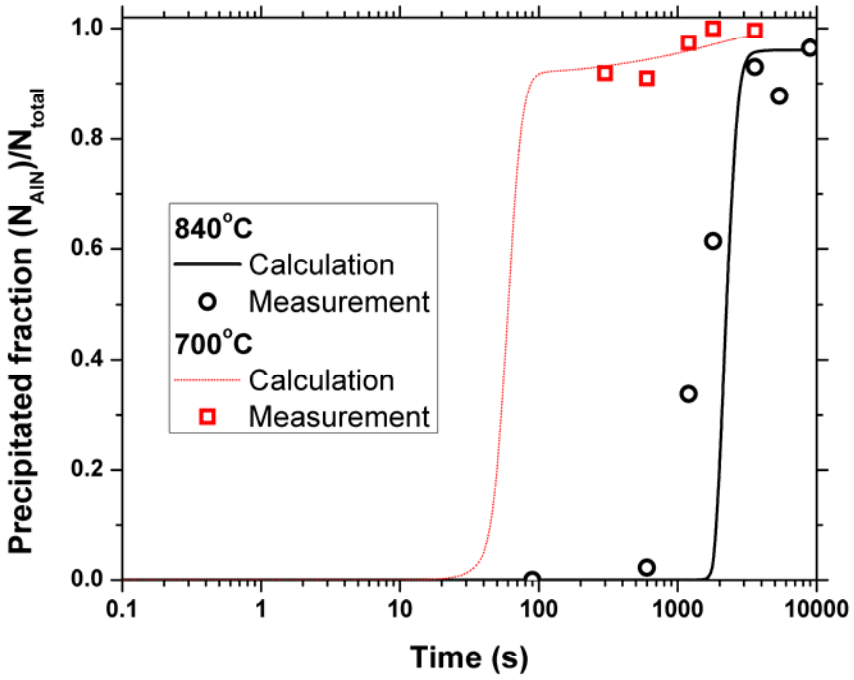

Figure 3.14: Calculated and measured precipitated fraction of AlN in 0.051wt%Al-0.0073wt%N steel during isothermal aging at 840°C and 700°C (experimental data from Vodopivec [138])

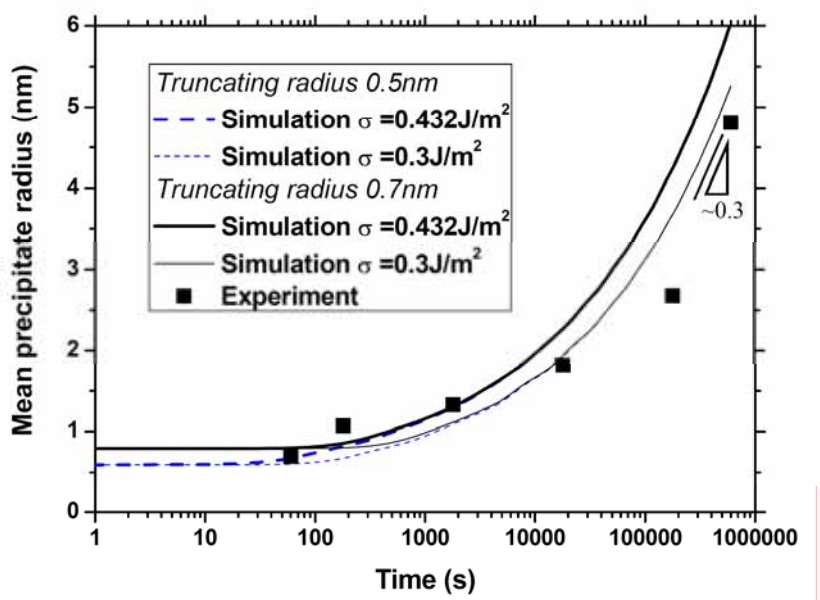

(a). Mean precipitate radius, $\overline{r}_P$

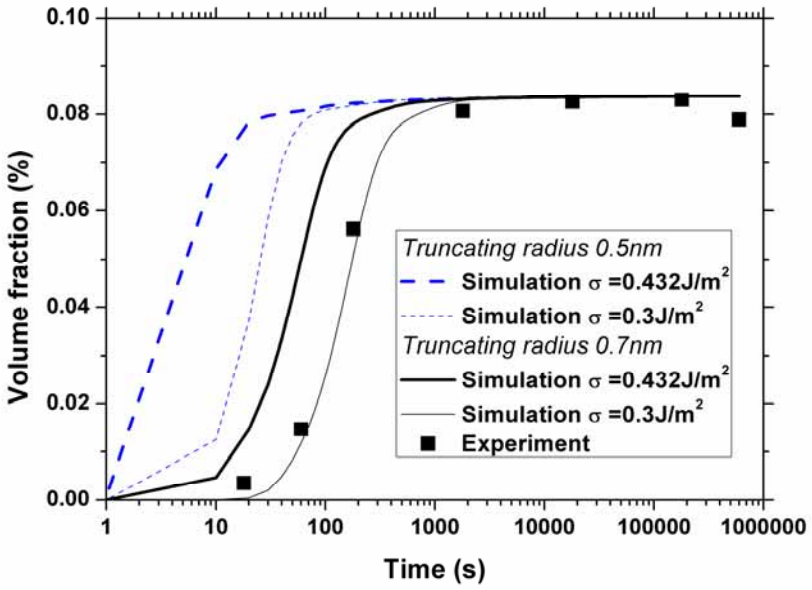

(b). Volume fraction precipitated, φ_P

Figure 3.15: Comparison of calculated and SANS measured niobium precipitation during isothermal aging at 973K (700°C) [220]

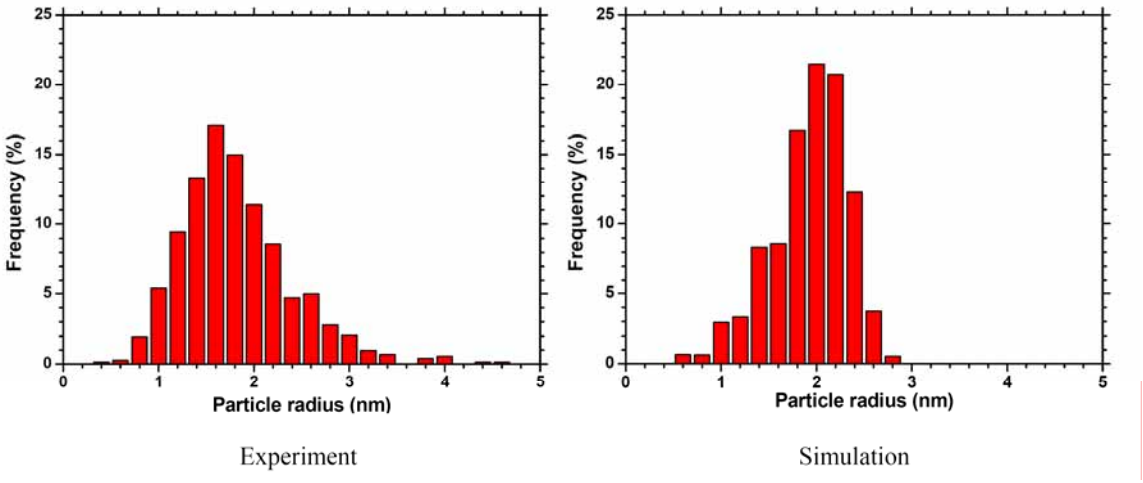

Figure 3.16: Normalized size distribution of niobium particles simulated compared with TEM measurements at 18,000s (300 minutes) [220]

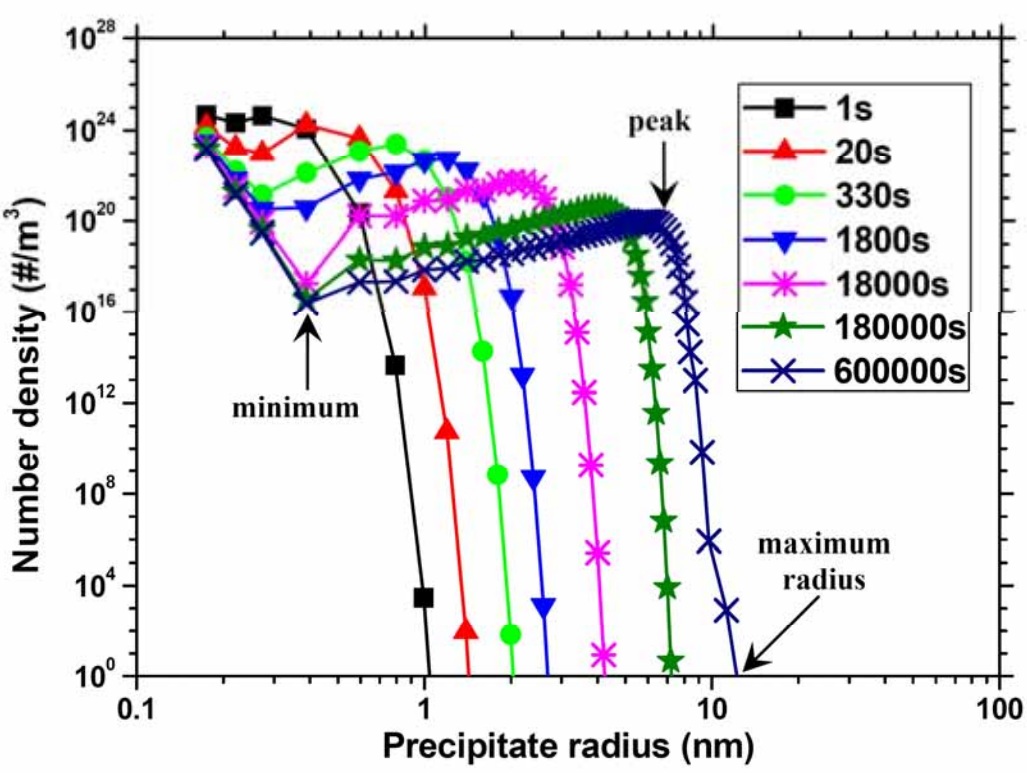

Figure 3.17: Calculated size distributions of niobium precipitate particles

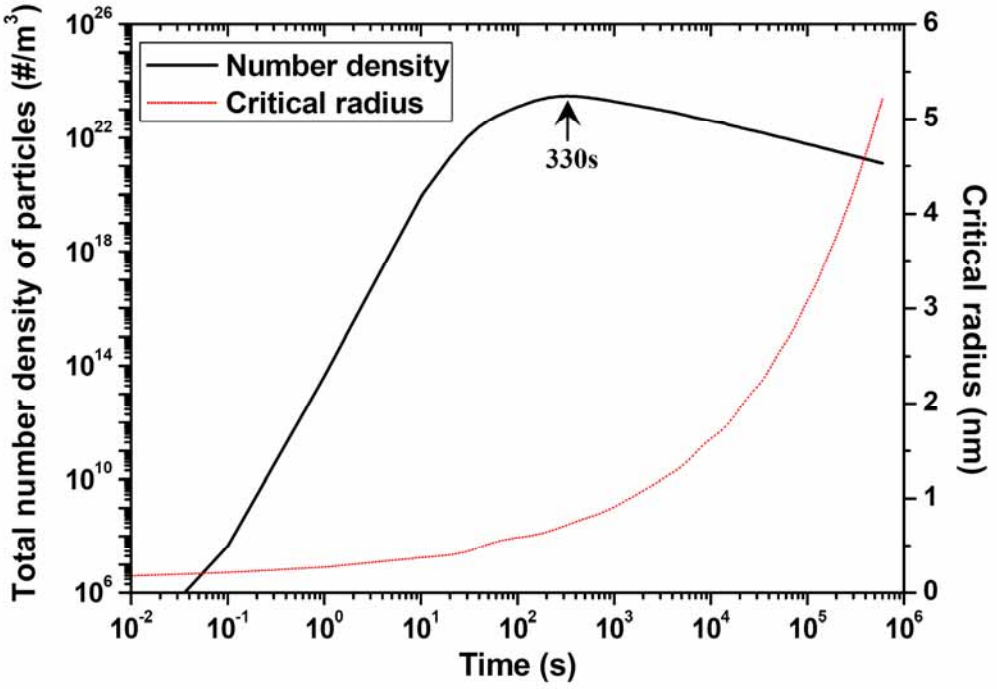

Figure 3.18: Calculated number density and critical radius of niobium precipitate particles

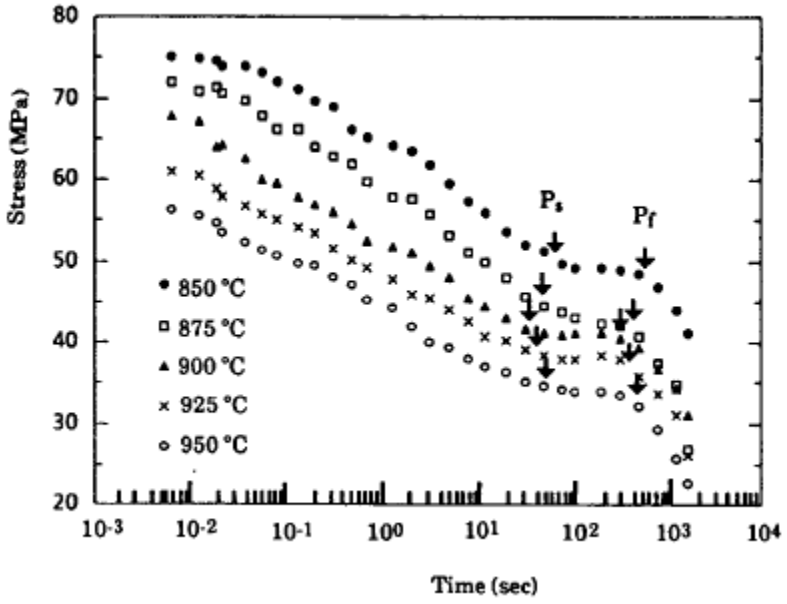

(a). For Nb-containing steel deformed 5% [164]

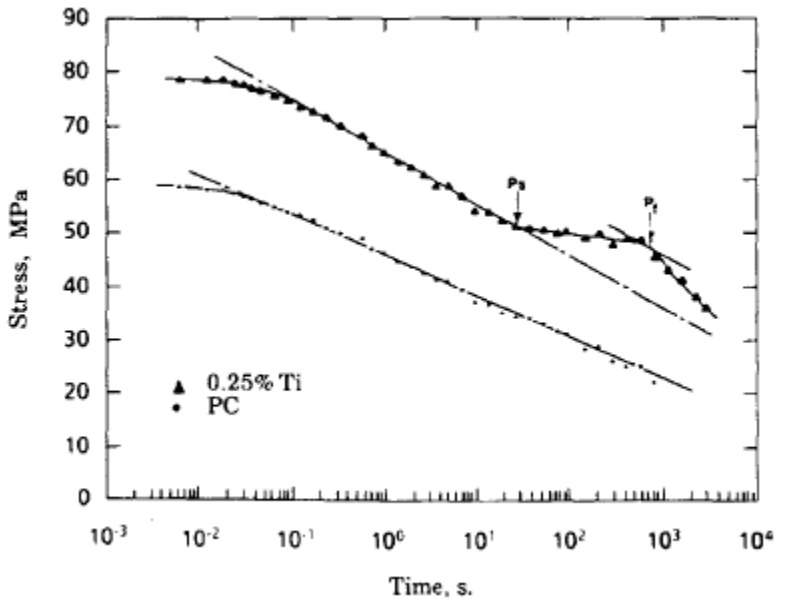

(b). For Ti-containing and reference plain carbon steels [25]

Figure 3.19: Stress relaxation curves in experiments

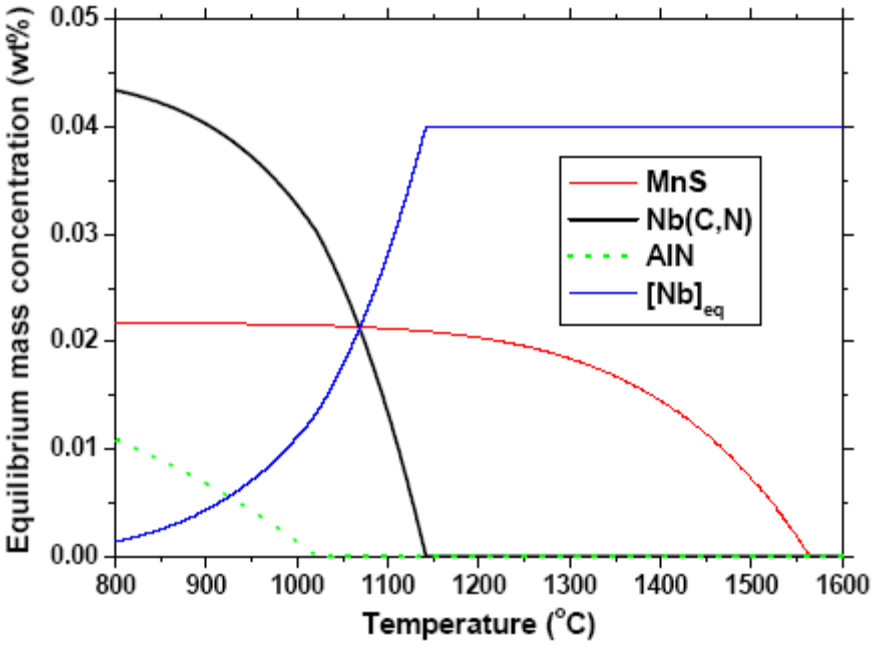

(a). Precipitate amount

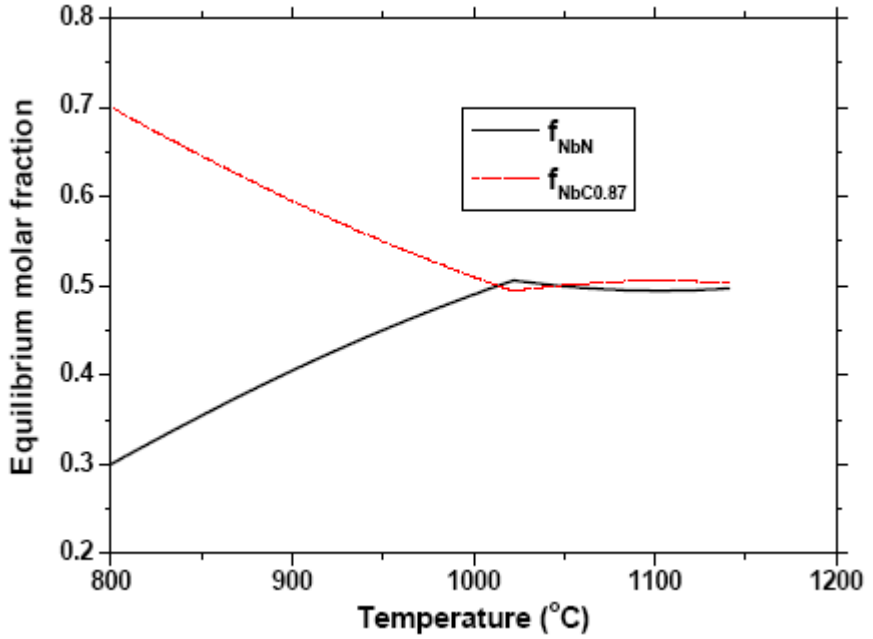

(b). Molar fraction of mixed Nb(C,N) precipitates

Figure 3.20: Equilibrium calculation of Nb-containing steel in austenite (0.067%C, 0.040%Nb and 0.006%N)

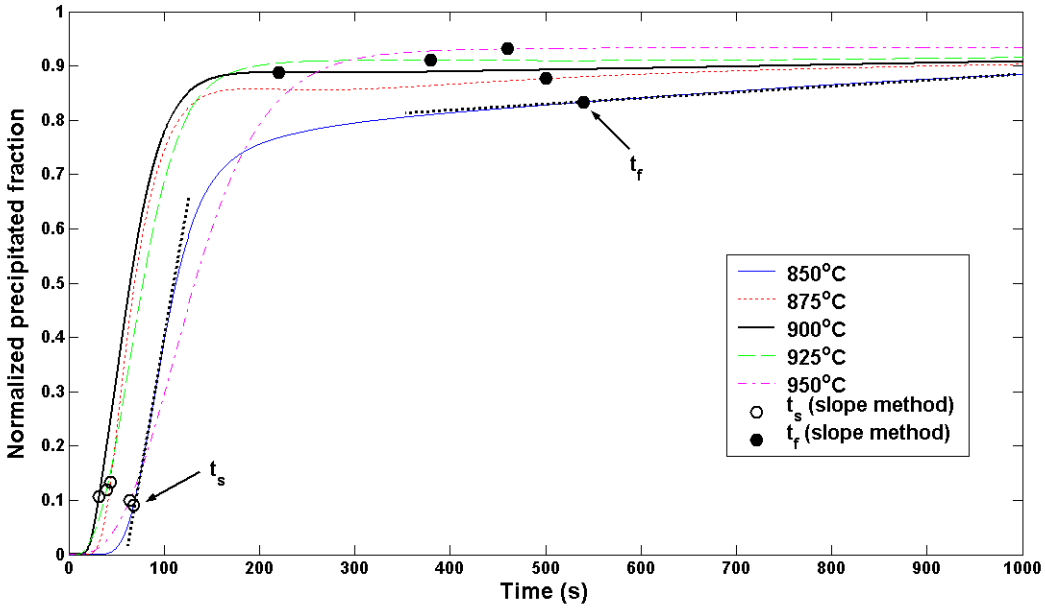

(a). Precipitated fraction and precipitation start and finish times determined by slope method

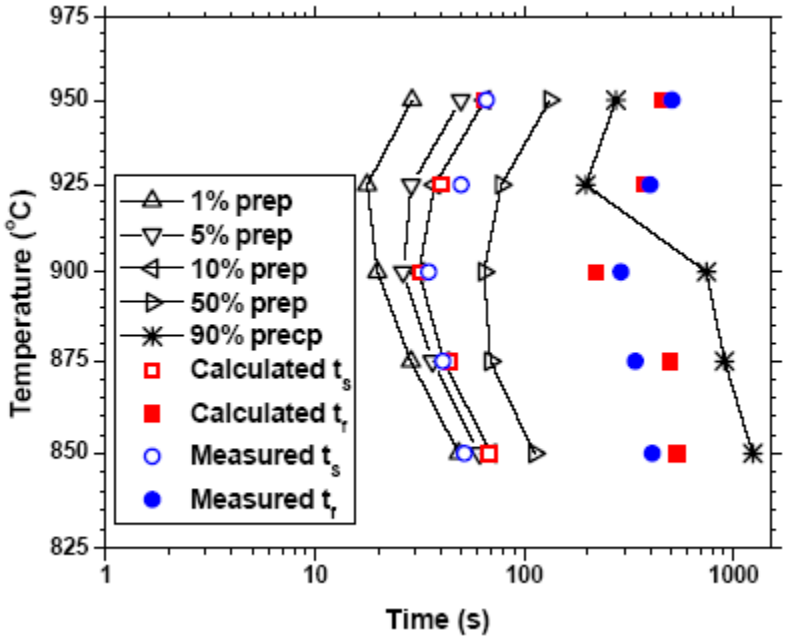

(b). Comparison of precipitation start and finish times with stress relaxation experiment [164]

Figure 3.21: Calculation and comparison of precipitation start and finish times of Nb-containing steel (0.067%C, 0.040%Nb and 0.006%N)

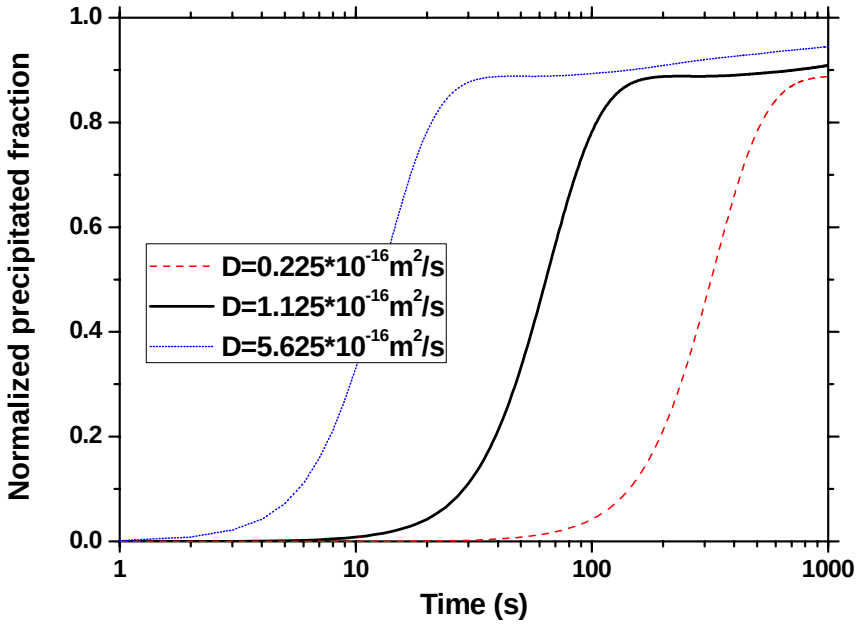

(a). Precipitated fraction

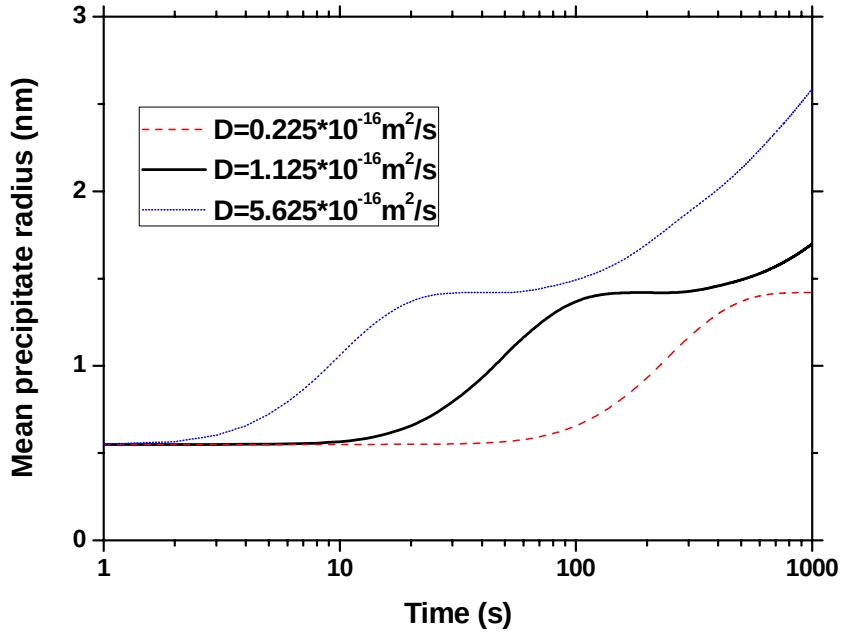

(b). Mean precipitate radius

Figure 3.22: Influence of diffusion coefficient on precipitation

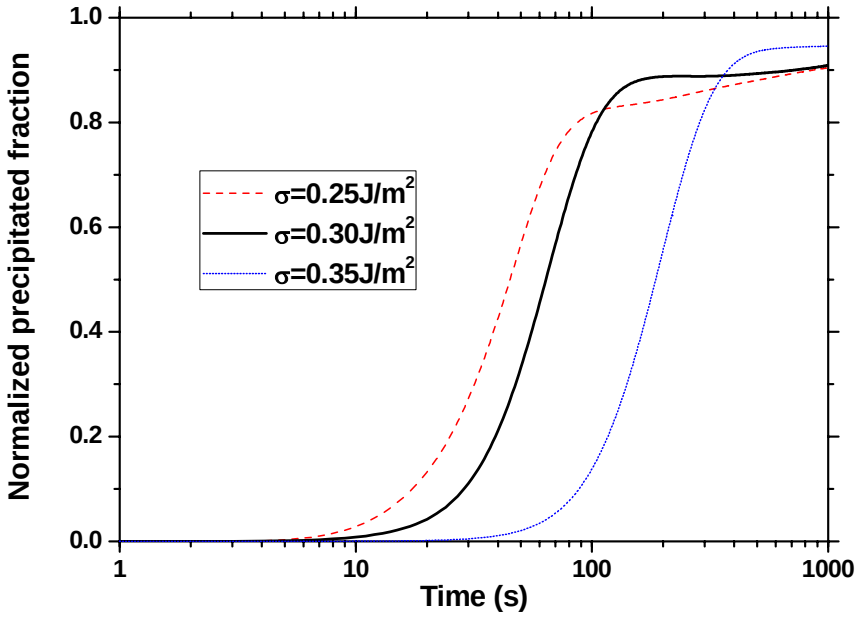

(a). Precipitated fraction

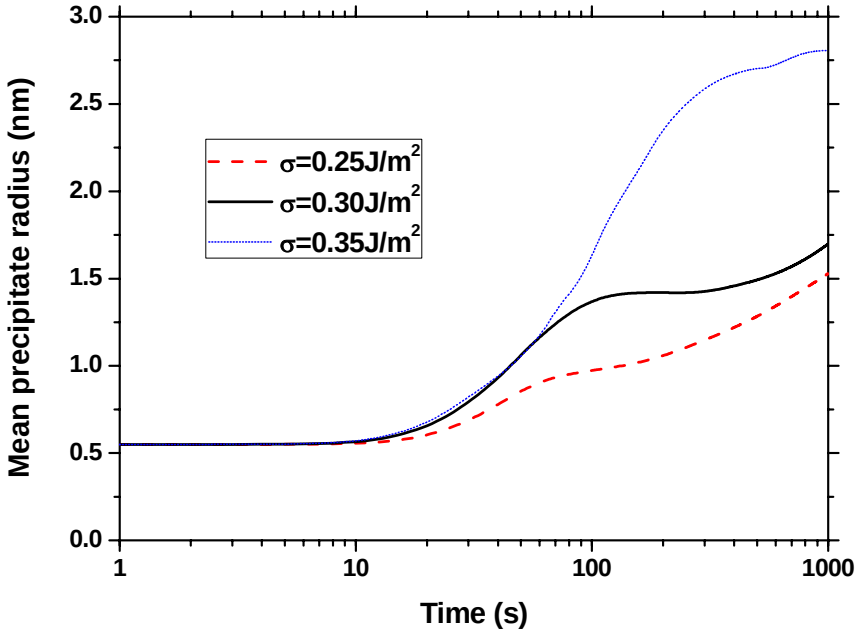

(b). Mean precipitate radius

Figure 3.23: Influence of interface energy on precipitation

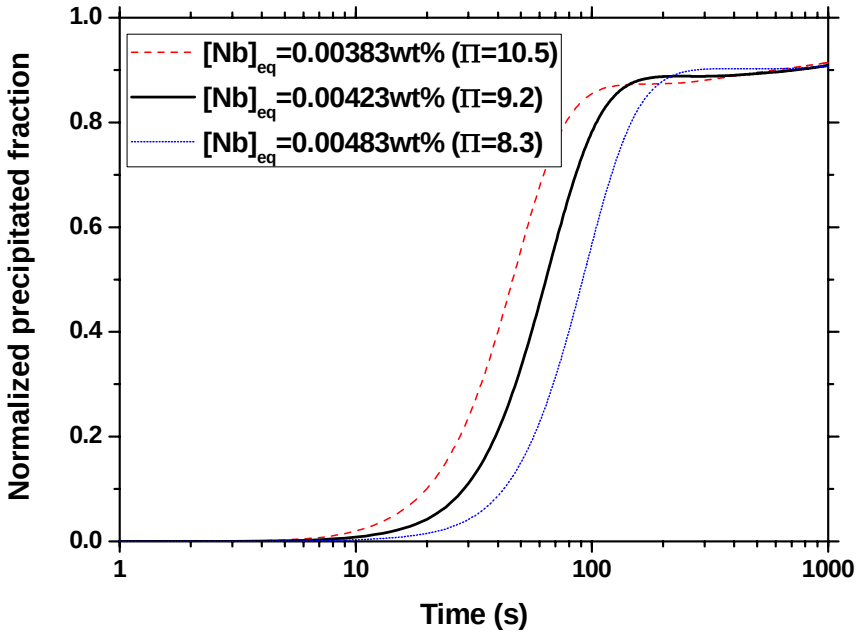

(a). Precipitated fraction

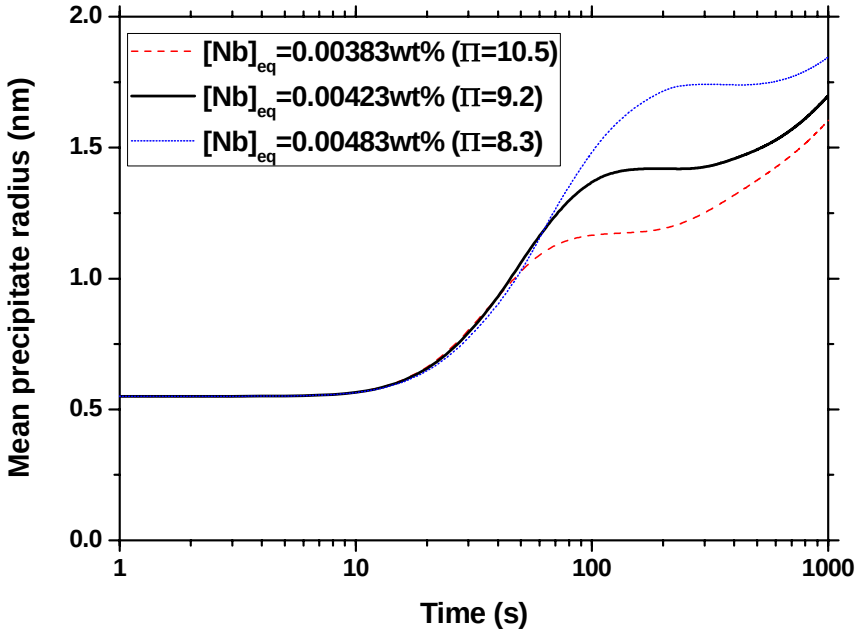

(b). Mean precipitate radius

Figure 3.24: Influence of supersaturation on precipitation

CHAPTER 4
MULTIPHASE PRECIPITATION MODEL

Because steel always contains dozens of alloying elements, the interactions almost always cause more than one type of precipitate to form. Some experimental micrographs of typical multiphase microalloy-based precipitates are shown in Figure 1.1. This figure shows that different kinds of precipitates can be mixed together to form larger coarse particles, instead of being separately distributed.

During thermal processing of real metal systems, competition always exists between alloying elements to form different precipitates, such as different nitrides attracting nitrogen in microalloyed steels. During cooling, more stable precipitates form generated first at high temperature. The formation of these precipitates changes the remaining concentrations of dissolved elements in the matrix, and thereby changes the later formation of other precipitates. The previously forming precipitates can also provide heterogeneous nucleation and growth cores for new precipitates of different composition, leading to mixed precipitates with complex structures. This makes new precipitates easier and faster to form and causes the size of the ultimate mixed precipitate to be coarser. Thus, consideration of multiphase precipitation leads to very different behavior than predicted by the modeling of homogeneous precipitation of a single precipitate phase in the matrix. All of these phenomena make a multiphase precipitation model important and necessary for realistic predictions of real systems.

4.1 Previous Work

The complex nature of the multiphase precipitation makes it very difficult to simulate. Recently, some promising attempts have been made to develop models of precipitation kinetics in multi-component and multi-phase systems.

The easiest way to model multiphase precipitation is maybe to revise and expand the classical precipitation theories of single precipitate to multiphase precipitate. Sourmail [225] and Perez [226] et al used this approach to model simultaneous two-phase precipitation in steels. Similarly, TC-PRISMA (PRecIpitation Simulations in MAterials) is a new software package for modeling multiphase precipitation that uses modified Langer-Schwartz theory [178,179] and Kampmann-Wagner numerical approach [49] as described in chapter 3. By expanding the

classical nucleation and growth theories to multi-component and multi-phase system, TC-PRISMA extends the functionality available through Thermo-Calc and DICTRA. Some description and applications of this software is given elsewhere [227, 228].

The "Multiphase-field" method is perhaps another possible way to model multiphase precipitation. Compared with conventional two-phase (e.g. matrix and precipitate phase) phase-field methods, more mobilities and order parameters for different alloying elements and precipitate phases must be included. The general theory of multiphase field method is given by Steinback and Pezzolla [229], and an application of concurrent precipitation of two intermetallic compounds in the Cu-Sn System is performed by Park et al [230].

Matcalc is maybe the most effective tool which has been developed for modeling multiphase precipitation until now. By properly adjusting the classical nucleation theory and applying the thermodynamic extreme principle, Matcalc describes the evolution of precipitate structure and the interaction of precipitates of different phases, of different chemical composition and of different sizes via diffusion inside both matrix and precipitate phases. The theory, numerical solution and application of Matcalc [44-46], and a simulation of competing precipitation of AlN and VN in steel [231] are given by Kozeschnik *et al*.

To the knowledge of the author, a molecule-based population-balance model for diffusion-controlled multiphase precipitation has never been attempted. In chapter 2, the equilibrium model has already considered the influence of a multi-composition system on the equilibrium concentrations of alloying elements, which is independent of kinetic model that will be used afterward. The purpose of this chapter is to expand the population balance and PSG equations of single-phase precipitation in chapter 3 to the multiphase precipitation. The new model must satisfy the mass balance of each precipitate phase, and be identical to the single-phase precipitation model when the number of precipitate phases is reduced to one. The results of the newly-developed multiphase models are first validated to match two rigorous extreme test problems of completely mutually-exclusive and mutually-soluble precipitation. Then a new PSG method for multiphase precipitation is developed and validated with the exact solution of the population balance equations.

4.2 Equations for Multiphase Population Balance

Following the population balance equations for single-phase precipitation in chapter 3, the growth or dissolution of all particles are also assumed to be only caused by the movement of pseudomolecules in the matrix in multiphase precipitation. The difference of multiphase precipitation kinetics is that the pseudomolecules of each precipitate phase can influence all aspects of particle nucleation, growth, and coarsening, and other precipitate phases, and must be carefully considered in theory.

For multiphase precipitation, in addition to the number density, the average composition of each precipitate phase containing in the particles of certain size also must be characterized. Thus for a size *i* particle containing *i* pseudomolecules, n_i is the number density, and p_i^z is the average molar fraction of precipitate phase z in size *i* particles, where the precipitate phase, z=1, 2, …, n_p. Since the pseudomolecules composing the particle may come from the different precipitate phases, the particle size is determined by the total number of pseudomolecules it contains, the molar volume and the average molar fraction of the precipitate phases, as follows

$$V_i = i\sum_{z=1}^{n_p} p_i^z V_1^z = i\sum_{z=1}^{n_p} p_i^z \frac{V_P^z}{N_A} = \frac{4}{3}\pi r_i^3 \tag{4.1}$$

Here V_P^z and V_1^z are the molar volume and the volume of the unit cell that contains one single pseudomolecule of precipitate phase z, n_p is the total number of precipitate phases in size *i* particles, and V_i is the volume of size *i* particles. The radius of size *i* particles, r_i, is thus computed as

$$r_i = \left(\frac{3V_i}{4\pi}\right)^{1/3} \tag{4.2}$$

Since the molar fractions of precipitate phases may vary with time for multiphase precipitation, the volume and radius of size *i* particles is also a function of time, instead of remaining constant as in single-phase model.

Similar to single-phase precipitation, the generation of a size *i* particle may come from a size *i*-1 particle that gains one single pseudomolecule or from a size *i*+1 particle that loses one single pseudomolecule. On the other hand, the loss of a size *i* particle could be caused by gaining one single pseudomolecule during diffusion growth or by losing one single pseudomolecule during dissolution of the size *i* particle itself. But these single pseudomolecules could come from any precipitate type that is thermodynamically stable. For multiphase precipitation, the free

pseudomolecules of each precipitate phase have an influence on diffusion growth of size *i* particles. Simultaneously, the size *i* particles are likely to dissolve pseudomolecules of any precipitate phase to the matrix. Thus the corresponding population-balance equation for the number density change of precipitate phase *z* in size *i* particles for multiphase precipitation is suggested as

$$\frac{d(p_i^z n_i)}{dt} = -\sum_{s=1}^{n_P} \beta_i^s n_1^s p_i^z n_i + \sum_{s=1}^{n_P} \beta_{i-1}^s n_1^s n_{i-1} \frac{(i-1)p_{i-1}^z + \delta_{s,z}}{i} - \sum_{s=1}^{n_P} \alpha_i^{s-z} A_i p_i^z n_i$$
$$+ \sum_{s=1}^{n_P} \alpha_{i+1}^{s-z} A_{i+1} n_{i+1} \frac{(i+1)p_{i+1}^z - \delta_{s,z}}{i} \quad (i \geq 2)\ (\mathrm{z}=1,2,...,\mathrm{n_p}) \qquad \textbf{(4.3)}$$

On the right side of the equation, the first term accounts for the loss of size *i* particles due to "diffusion growth", which means that adding one single pseudomolecule of any type can make a size *i* particle of precipitate phase z (number density is $p_i^z n_i$) grow into a size *i*+1 particle. The second term is for the increase of size *i* particles of phase z by adding one single pseudomolecule of any type into size *i*-1 particles. The third term represents the loss of size *i* particles, which can dissolve with dissociation rates of any precipitate phases s into the matrix under the influence of precipitate phase z, α_i^{s-z}., and the last term is for the increase of the size *i* particles by dissolution of size *i*+1 particles. The corresponding coefficients are inserted into each term in order to conserve mass.

The population equation for the single pseudomolecules of precipitate phase z is thus given analogously

$$\frac{dn_1^z}{dt} = -\beta_1^z n_1^z \sum_{s=1}^{n_p} n_1^s - n_1^z \sum_{s=1}^{n_p} \beta_1^s n_1^s - n_1^z \sum_{i=2}^{i_M} \beta_i^z n_i + 2\sum_{s=1}^{n_p} a_2^{s-z} A_2 p_2^z n_2 + \sum_{i=3}^{i_M} \alpha_i^{z-z} A_i n_i \qquad \textbf{(4.4)}$$

The positive and negative terms account for the generation and loss of single pseudomolecules of phase z separately, which are correspondingly caused by dissolution and diffusion growth terms. Each term can be explained similarly by a certain reaction in Eq. (4.3).

After the number densities of are calculated from Eqs. (4.3) and (4.4), one extra equation is needed to solve for all variables, $\mathrm{n_i}$ and p_i^z $(\mathrm{z}=1,2,...,\mathrm{n_p})$, which is given by the normalization condition of precipitate compositions for all particle sizes at all time:

$$\sum_{z=1}^{n_p} p_i^z = 1 \qquad \textbf{(4.5)}$$

Since the properties of each precipitate phase are different, the multiphase diffusion rates, β_i^z, and dissociation rates, α_i^{s-z}, are calculated as follows

$$\beta_i^z = 4\pi r_i D_M^z \quad (z=1,2,...,n_p) \tag{4.6}$$

$$\alpha_i^{z-s} = \frac{4\pi r_i D_M^z n_{1,eq}^z}{A_i} \exp\left(\frac{2\sigma^{z-s} V_P^z}{RTr_i}\right) \quad (z=1,2,...,n_p) \tag{4.7}$$

where i is the size of particle, s and z are the precipitate phases. D_M^z and $n_{1,eq}^z$ are the diffusion rate and equilibrium number density of precipitate phase z, and σ^{z-s} is the interface energy between precipitate phase z and matrix under the influence of precipitate phase s. The above equations (4.3)-(4.7) comprise the multiphase precipitation solution and give the exact solution for comparison.

Several important observations can be made from the above equations. Firstly, the loss of pseudomolecules z from size i particles by the first diffusion-growth term in Eq. (4.3) and from the single pseudomolecules by the third diffusion-growth term in Eq. (4.4) must equal the gain of pseudomolecules z for size i+1 particles by the second term of diffusion growth in Eq. (4.3). This is automatically ensured by substituting into the two terms and noting that:

$$-(-i\sum_{s=1}^{n_P}\beta_i^s n_1^s p_i^z n_i - \beta_i^z n_1^z n_i) = (i+1)\sum_{s=1}^{n_P}\beta_i^s n_1^s n_i \frac{ip_i^z + \delta_{z,s}}{i+1} \tag{4.8}$$

Similarly, the dissolution terms in Eqs. (4.3)-(4.4) satisfies the following relationship:

$$-(-i\sum_{s=1}^{n_P}\alpha_i^{s-z} A_i p_i^z n_i) = (i-1)\sum_{s=1}^{n_P}\alpha_i^{s-z} A_i n_i \frac{ip_i^z - \delta_{s,z}}{i-1} + \alpha_i^{z-z} A_i n_i \tag{4.9}$$

Thus the number of pseudomolecules of precipitate phase z containing in all size particles is must be conserved by satisfying the following equation:

$$\sum_{i=1}^{\infty} i\frac{d(p_i^z n_i)}{dt} = 0 \quad (z=1,2,...,n_p) \tag{4.10}$$

When n_p=1, these population balance equations for multiphase precipitation are simplified to be exactly the same as Eqs. (3.74)-(3.75) for single-phase precipitation.

The above model has been implemented into an explicit code in order to model two extreme special cases:

1). completely mutually-exclusive precipitates

For completely mutually exclusive precipitates, the interface energies between different precipitate phases are much higher than those between matrix and each precipitate phase. The high repulsive force between different precipitate phases enables single pseudomolecules of each phase to quickly dissolve into the matrix because of the presence of other precipitates. This large inter-precipitate dissociation rate makes "mixed precipitates" (individual particles containing different precipitate phases) impossible. The single pseudomolecules of each precipitate phase are assumed to react only with particles of the same phase, and the different types of precipitates form and evolve separately in the matrix, which causes $\alpha_i^{z-s} = \alpha_i^z$ (z=1,2,...,n_p). All terms involving mutual reactions vanish, and Eqs. (4.3) and (4.4) simplify to the following by setting s=z:

$$\frac{d(p_i^z n_i)}{dt} = -\beta_i^z n_1^z p_i^z n_i - \alpha_i^z A_i p_i^z n_i + \beta_{i-1}^z n_1^z p_{i-1}^z n_{i-1} + \alpha_{i+1}^z A_{i+1} p_{i+1}^z n_{i+1} \ (i \geq 2) \ (\text{z=1,2,...,n}_\text{p}) \tag{4.11}$$

$$\frac{d(n_1^z)}{dt} = -n_1^z \sum_{i=1}^{i_M} (1+\delta_{1,i}) \beta_i^z p_i^z n_i + \sum_{i=2}^{i_M} (1+\delta_{2,i}) \alpha_i^z A_i p_i^z n_i \quad (\text{z=1,2,...,n}_\text{p}) \tag{4.12}$$

These equations are similar to the single-phase model, except that the number density of each precipitate, $n_i p_i^z$ (z=1,2,...,n_p), is used instead of n_i.

2). completely mutually-soluble precipitates

For completely mutually-soluble precipitates, it is assumed that the dissociation rate of each precipitate phase is not influenced by other precipitate phases. Inserting $\alpha_i^{z-s} = \alpha_i^z$ (z=1,2,...,n_p) into Eqs. (4.3) and (4.4), and summing Eq. (4.3) over all precipitate phases, the number density of size i particles evolves as follows

$$\frac{dn_i}{dt} = -\sum_{s=1}^{n_p} \beta_i^s n_1^s n_i - \sum_{s=1}^{n_p} \alpha_i^s A_i n_i + \sum_{s=1}^{n_p} \beta_{i-1}^s n_1^s n_{i-1} + \sum_{s=1}^{n_p} \alpha_{i+1}^s A_{i+1} n_{i+1} \ (i \geq 2) \tag{4.13}$$

This equation is similar to the single-phase precipitation model, Eq. (3.74), except that a summation over all precipitate phases is required. Moreover, if all precipitates are assumed to have identical properties (interface energy, diffusion coefficient, molar volume, supersaturation), Eqs. (4.13) gives the same results as those of the single-phase model if we treat all single pseudomolecules just as one type and set $\alpha_i = \sum_{s=1}^{n_p} \alpha_i^s$. This relationship gives $n_{1,eq} = \sum_{s=1}^{n_p} n_{1,eq}^s$,

which seems reasonable to keep the sum of dissolved concentration in the matrix of the different precipitate phases with identical properties constant.

4.3 Test Problems with Mutually Exclusive and Soluble Precipitates

1). completely mutually-exclusive precipitates

Let us assume that two kinds of completely mutually-exclusive precipitates (e.g. AlN and NbN in steels) form separately in matrix, but have identical properties. Under this circumstance, the multiphase precipitation model should give exactly the same results as two separate runs of the single-phase model, where the total and equilibrium number density of each precipitate are simply input identically for both runs.

The single pseudomolecules for the two precipitates in the system are assumed to be generated by an isothermal first order reaction with time:

$$n_s^A(t^*) = \sum_{i=1}^{i_M} i \cdot p_i^A n_i = 9 n_{1,eq}^A [1 - \exp(-0.1 t^*)] \tag{4.14}$$

$$n_s^B(t^*) = \sum_{i=1}^{i_M} i \cdot p_i^B n_i = 9 n_{1,eq}^B [1 - \exp(-0.1 t^*)] \tag{4.15}$$

The dimensionless time in these expressions is defined as

$$t^* = 4\pi D r_1 n_{1,eq} t \tag{4.16}$$

where the equilibrium number densities are chosen as $n_{1,eq}^A = 3.6\times10^{23}\#/\text{m}^3$, $n_{1,eq}^B = 2.4\times10^{23}\#/\text{m}^3$, $n_{1,eq} = n_{1,eq}^A + n_{1,eq}^B = 6\times10^{23}\#/\text{m}^3$, and r_1=0.294nm, $D=10^{-9}\text{m}^2/\text{s}$, $\sigma=0.02\text{J/m}^2$, T=300K for both precipitate phases. Explicit forward Euler scheme with a time step size Δt^*=0.01, and i_M=6000 are used in all test problems in this chapter.

The results from 2 runs of the single-phase precipitation model and 1 run of the multiphase precipitation model are shown and compared in Figure 4.1, which shows that the two methods match exactly for this test problem. In Figure 4.1(b), it is also observed that the number densities of single pseudomolecules are decreasing towards their dimensionless equilibrium values of $n_{1,eq}^A / n_{1,eq} = 0.6$ and $n_{1,eq}^B / n_{1,eq} = 0.4$ respectively.

It is worth to mention that Eqs (4.3)-(4.4) do not work directly for the mutually-exclusive precipitates. The large interface energy between mutually-exclusive precipitates causes large dissociation rates for all particle sizes, which makes all mixed particles dissolve. This problem

cannot be solved by the assumption of one particle size distribution function in this work. Instead, Eqs. (4.11)-(4.12) should be used to model mutually-exclusive precipitates.

2). completely mutually-soluble precipitates

Completely mutually-soluble precipitates (such as $Al^{26}N$ and $Al^{27}N$ in steels, where the superscript is atomic weight) are considered for this test problem. The precipitates are assumed to have identical properties, and the kinetics should exactly match that of single-phase precipitation. The total and equilibrium number density used in the single-phase model simulation are simply the sum of the values for the two mutually-soluble precipitates. In order to validate the current multiphase model, the number densities of each precipitate are input.

The pseudomolecules are assumed to be released via the same relationship used in the first test problem in Eq. (4.14) and (4.15). The parameters are chosen to be the same as those in the mutually-excusive case, as well as $n_{1,eq} = n_{1,eq}^{A} + n_{1,eq}^{B} = 6\times10^{23}\#/\mathrm{m}^3$, are used in a single run of the single-phase model for comparison. The results from the single-phase model are multiplied by the ratios 3/5 and 2/5 to get the values of each individual precipitate phase, and compared with results of multiphase model. Exact matches of size distributions are shown in Figure 4.2. The number densities of single pseudomolecules again are approaching their equilibrium values $n_{1,eq}^{A}(0.6n_{1,eq})$ and $n_{1,eq}^{B}(0.4n_{1,eq})$ in Figure 4.2(b).

The influence of mutually exclusive and soluble properties of precipitates on kinetics can be compared because all input values are the same in two test problems. As shown number densities evolutions in Figure 4.3, it is no surprise that the mutually soluble precipitates give larger size, because the previous precipitates can be supported as the nucleation and growth sites to attract pseudomolecules of both precipitate phases. On the other hand, the existing precipitates can only accept the pseudomolecules of the same type for the mutually-exclusive precipitates, which makes the particle size to increase slowly.

By slightly changing the relative ratios of diffusion coefficients, interface energies of two mutually-soluble precipitates, some interesting observations are found. For a fixing time t^*=100, the influence of changing ratio of diffusion coefficients, D_B/D_A, on the molar fraction of all size particles for precipitate phase A, is shown in Figure 4.4. An increase of diffusion coefficient, D_A, will cause an increase of molar fraction of phase A in very large particles, and also will form more unstable very-small-size embryos of phase A. Mass balance requires a decrease in the

intermediate size range. The molar fraction of single pseudomolecules, stays at the equilibrium value of $n_{1,eq}^{a}/(n_{1,eq}^{a}+n_{1,eq}^{b})=0.6$. This behavior causes the molar fraction curves shape observed in Figure 4.4.

Figure 4.5(a), as well as a zoom-in Figure 4.5 (b) on y-axis, shows the influence of changing the ratio of interface energies, σ_B/σ_A, on the molar fraction of all size particles for precipitate phase A. An increase of interface energy, σ_A, causes a larger capillary effect, which increases molar fraction of phase A for very large particles. Larger interface energy also causes an increase of the nucleation barrier, so unstable "embryos" with very small size will stay in solution, which cannot nucleate to become stable. In order to satisfy mass balance, a decrease of molar fraction of phase A must increase for the intermediate size range, which makes the curves in Figure 4.5 show their distinctive shape of parabolic increase followed by parabolic decrease.

4.4 Multiphase PSG Method

For the PSG method of multiphase precipitation, size group *j* is defined to include those particles with any number of pseudomolecules between $m_{j-1,j}$ and $m_{j,j+1}$, with its center lying pseudomolecule number m_j. The number density and average molar fraction of size group *j* is thus defined as

$$N_j = \sum_{m_{j,j+1}>m>m_{j-1,j}} n(m) \tag{4.17}$$

$$P_j^s = \frac{\sum_{m_{j,j+1}>m>m_{j-1,j}} m\cdot n(m)\cdot p_m^s}{\sum_{m_{j,j+1}>m>m_{j-1,j}} m\cdot n(m)} \tag{4.18}$$

It is worth mentioning that the volume and radius of size group *j* particles are functions of precipitate phases, which can change with time.

Following the population balance equations of multiphase precipitation, Eq. (4.3), and PSG equations for single-phase precipitation, the corresponding equations for PSG method are given as

$$\frac{d(P_j^z N_j)}{dt} = \frac{m_1}{m_j}\beta_j^z N_1^z (N_j - n_j^R) - \frac{m_1}{m_j}\alpha_j^z A_j (N_j - n_j^L) + \sum_{s=1}^{n_P} (\beta_{j-1}^s)^R N_1^s n_{j-1}^R \frac{floor(m_{j-1,j})(P_{j-1}^z)^R + \delta_{s,z}}{m_j}$$

$$+\sum_{s=1}^{n_P}(\alpha_{j+1}^{s})^{L}A_{j+1}^{L}n_{j+1}^{L}\frac{ceil(m_{j,j+1})(P_{j+1}^{z})^{L}-\delta_{s,z}}{m_j}$$

$$-\frac{floor(m_{j,j+1})}{m_j}\sum_{s=1}^{n_P}(\beta_j^{s})^{R}N_1^{s}(P_j^{z})^{R}n_j^{R}$$

$$-\frac{ceil(m_{j-1,j})}{m_j}\sum_{s=1}^{n_P}(\alpha_j^{s})^{L}A_j^{L}(P_j^{z})^{L}n_j^{L}\quad (j\geq 2)\ (\text{z=1,2,...,n}_\text{p}) \tag{4.19}$$

where P_j^z stands for the molar fraction of precipitate phase z for the size group *j* particles. On the right hand of the equation, the first two terms account for the diffusion growth and dissolution of precipitate z inside size group *j*; the third and fourth terms are for the generation of precipitate s of size group *j* by the diffusion growth of size group *j*-1 and the dissociation of size group *j*+1; and the last two terms are for the loss of size group j particles by their own diffusion growth and dissolution; The corresponding coefficients are inserted into each term to conserve mass. Note that this equation simplifies to Eq. (3.91) for single phase, n_p=1.

According to Eqs. (4.4) and (4.19), the population balance for single pseudomolecules of precipitate z in the PSG method is given as

$$\frac{d(N_1^z)}{dt}=-\beta_1^z N_1^z\sum_{s=1}^{n_p}N_1^s-N_1^z\sum_{s=1}^{n_p}\beta_1^s N_1^s-N_1^z\sum_{k=2}^{G_M}\beta_k^z(N_k-n_k^R)+\sum_{k=2}^{G_M}\alpha_k^z A_k(N_k-n_k^{L.})$$

$$-N_1^z\sum_{k=2}^{G_M}(\beta_k^z)^{R}n_k^{R}+\sum_{k=3}^{G_M}(\alpha_k^z)^{L}A_k^{L}n_k^{L.}+2\sum_{s=1}^{n_p}(a_2^s)^{L}A_2^{L}(p_2^z)^{L}n_2^{L}\quad (\text{z=1,2,...,n}_\text{p}) \tag{4.20}$$

The total mass of each precipitate phase is proved to be conserved by satisfying the relationship

$$\sum_{j=1}^{\infty}m_j\frac{d(P_j^z N_j)}{dt}=0\quad (\text{z=1,2,...,n}_\text{p}) \tag{4.21}$$

The diffusion growth rate β_j^z, and dissociation rate α_j^z of size group *j* particles and precipitate phase z needed are calculated with Eqs. (4.6)-(4.7) using the characteristic (mean) radius given by the following equation:

$$r_j=\left[\frac{3}{4\pi}m_j\sum_{z=1}^{n_p}P_j^z\frac{V_P^z}{N_A}\right]^{1/3} \tag{4.22}$$

The radius, diffusion growth rates, and dissociation rates for the border-sized particles and precipitate phase z are given as

$$r_j^L = \left[\frac{3}{4\pi} ceil\left(m_{j-1,j}\right)\sum_{z=1}^{n_p}(P_j^z)^L \frac{V_P^z}{N_A}\right]^{1/3},\ r_j^R = \left[\frac{3}{4\pi} floor\left(m_{j,j+1}\right)\sum_{z=1}^{n_p}(P_j^z)^R \frac{V_P^z}{N_A}\right]^{1/3} \tag{4.23}$$

$$(\beta_j^z)^L = 4\pi D_M^z r_j^L,\ (\beta_j^z)^R = 4\pi D_M^z r_j^R \tag{4.24}$$

$$(\alpha_j^z)^L = \frac{(\beta_j^z)^L N_{1,eq}^z}{A_j^L}\exp\left(\frac{2\sigma^z V_P^z}{R_g T}\frac{1}{r_j^L}\right),\ (\alpha_j^z)^R = \frac{(\beta_j^z)^R N_{1,eq}^z}{A_j^L}\exp\left(\frac{2\sigma^z V_P^z}{R_g T}\frac{1}{r_j^L}\right) \tag{4.25}$$

These diffusion growth rates and dissociation rates are calculated for all involving precipitate phases z=1, 2, …, n_p. The particle number densities for the border sizes n_j^L and n_j^R are still estimated by Eqs. (3.98)-(3.102), and the molar fractions for the border sizes particle, $(P_j^z)^L$ and $(P_j^z)^R$, are estimated from a geometric progression by assuming that molar fraction is exactly P_j^z at the center of size *j* group:

$$(P_j^z)^L = P_{j-1}^z\left(\frac{P_j^z}{P_{j-1}^z}\right)^{\frac{ceil(m_{j-1,j})-m_{j-1}}{m_j-m_{j-1}}},\ (P_j^z)^R = P_j^z\left(\frac{P_{j+1}^z}{P_j^z}\right)^{\frac{floor(m_{j,j+1})-m_j}{m_{j+1}-m_j}} \tag{4.26}$$

In order to propagate particle growth, if $P_j^s \neq 0$ and $P_{j+1}^s = 0$, $(P_j^s)^R$ is calculated by

$$(P_j^z)^R = (P_j^z)^L\left[\frac{P_j^z}{(P_j^z)^L}\right]^{\frac{floor(m_{j,j+1})-ceil(m_{j-1,j})}{m_j-ceil(m_{j-1,j})}} \tag{4.27}$$

These calculations of molar fractions are done for z=1, 2, …, n_p. It is worth to notice that these definitions are not necessary to guarantee the sum of molar fractions for the border-sized particles to be unit. Thus a normalization of molar fractions is suggested after calculation, as follows

$$(P_j^z)^L = \frac{(P_j^z)^L}{\sum_{z=1}^{n_p}(P_j^z)^L},\ (P_j^z)^R = \frac{(P_j^z)^R}{\sum_{z=1}^{n_p}(P_j^z)^R} \tag{4.28}$$

The Eqs. (4.19)-(4.27), (3.98)-(3.102) comprise the PSG method for multiphase precipitation. Comparing with other software, such as Matcalc and PRISMA, the current model does not require a classical nucleation theory, which has some assumptions and uncertainties and itself. But the diffusion inside the precipitate phases is not considered in the current model.

The total dimensionless number density of pseudomolecules of each precipitate phase, and that of particles are defined as

$$N_M^{*z} = \sum_{i=1}^{i_M} i \cdot n_i^* * p_i^z \,,\; N_T^* = \sum_{i=1}^{i_M} n_i^* \text{ for exact solution}$$

$$N_M^{*z} = \sum_{j=1}^{G_M} m_j \cdot N_j^* * P_j^z \;\;,\; N_T^* = \sum_{i=1}^{i_M} N_j^* \text{ for PSG method} \qquad \textbf{(4.29)}$$

The mass balance requires N_M^{*z} to exactly match the generation function, as Eq. (4.14) or (4.15) throughout the entire calculation.

4.5 Validation with Exact Solution

To test the multiphase PSG model by comparison with the exact population-balance model equations, a test problem was made by increasing the diffusion coefficient of phase B via setting the ratio D_B/D_A=1.1 and keeping other parameters unchanged as in test problem of section 4.3. The results of the PSG method and exact solution for this problem of multiphase precipitation are shown in Figure 4.6 and 4.7. As shown in Figure 4.6, the total volume of each precipitate predicted with the PSG method (i.e. the dimensionless number density of pseudomolecules) matches the exact population-balance solution and furthermore conserves mass by matching the input function (after scaling with n_1,eq to make dimensionless), which increases with time according to Eqs. (4.14)-(4.15). In addition, a good agreement for the total particle number density, N_T^*, is also found, which decreases with time once precipitation starts.

The histories of number density and molar fraction from both methods are compared in Figure 4.7. The particle size distribution evolves in a similar manner to that of single precipitates in Figure 3.10, and the number density of pseudomolecules of each precipitate phase evolves with time with similar values for both methods.

Because the logarithmic distribution of molar fraction with each size group, defined in Eq. (4.26), was causing instability, the molar fractions were simply fixed to have the center value throughout the size group. This solved the stability, but likely caused the accuracy problem with matching the molar fractions in Fig. 4.7(b). The trends of smaller fractions at small-size and large-size and larger fractions for intermediate size of phase A are observed in both methods, but PSG method underestimates the values at peaks and bottoms, which is caused by a bad choice of "border molar fractions" here. A good agreement is expected to be available from implicit scheme to avoid stability, and better estimations of border molar fractions In future.

4.6 Solution Details

In order to avoid stability problems due to dissociation exceeding diffusion growth, and to improve the time-efficiency of the calculation, the implicit Euler schemes are always adopted here to integrate these differentiate equations through time. Because mass conservation has been validated with test problems, the number density of single pseudomolecules of each precipitate phase is then computed with Eq. (4.28), instead of the more time-consuming Eq. (4.20) used previously:

$$N_1^z = n_s^z - \sum_{j=2}^{G_M} m_j P_j^z N_j \tag{4.30}$$

The ordinary differential equations (4.18) are discretized using implicit backward Euler scheme, which gives the similar results with Eq. (3.109) for each precipitate phase. Starting from known values at time step i, Gauss-Seidel method is used to calculate the number densities of a certain precipitate phase at time step i+1 from the smallest size group to largest size group. The same calculation will be done after moving to the next precipitate phase, and continues until all phases are calculated. The positive number density and molar fractions are always predicted now.

The suggested multiphase PSG model is most suitable for mutually-soluble precipitates. All precipitates can be divided into several groups of completely mutually-exclusive precipitates. The precipitation of different groups can be modeled as a mutually-exclusive extreme case by Eqs. (4.11)-(4.12). Inside each group, the precipitates are mutually soluble, which can be modeled by the suggested new multiphase PSG model. Thus the models described in this chapter can give a simplified approach to estimate the complete multiphase precipitation behaviors in alloys.

Whether the precipitates are mutually exclusive and soluble can be determined by difference of the crystal structures and lattice parameters of precipitate phases as in chapter 2. The underlying physics of this criterion is to compare the interface energies between matrix and difference precipitates, and between precipitates of different phases. If the interface energies between precipitates are much larger, it will cause the different precipitate phases to occur separately and goes to mutually-exclusive extreme. On the other hand, the precipitates of different phases tend to nucleate and grow on each other, if the interface energies between precipitates are much smaller. This causes heterogeneous precipitation, which is the mutually-

soluble extreme. In fact, a real precipitation happens between these two extremes, and each precipitate has a certain potential to attract or repel other precipitates. A true simulation of this requires arranging a size distribution of each precipitate phase, which can interact with precipitates of all phases.

4.7 Tables and Figures

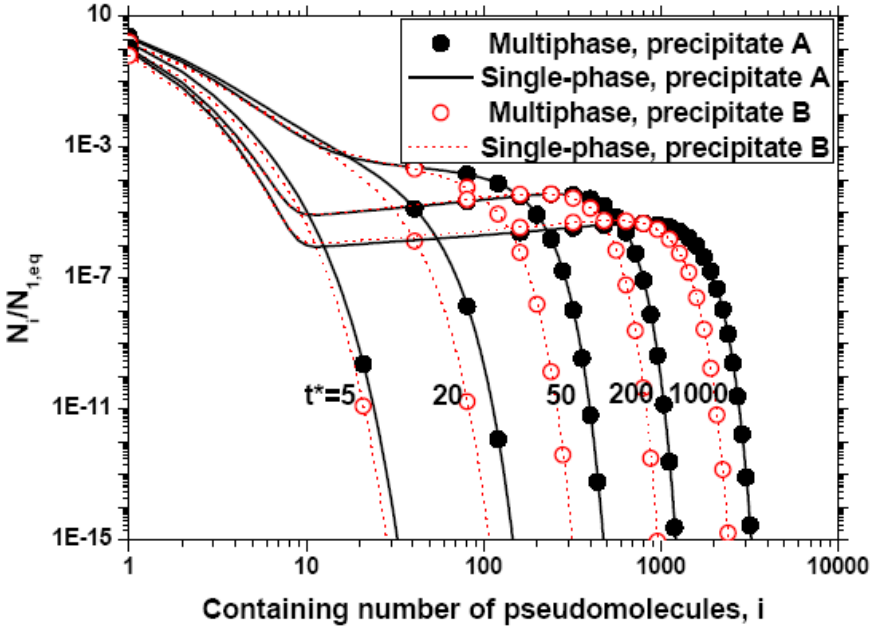

(a). Particle size distributions

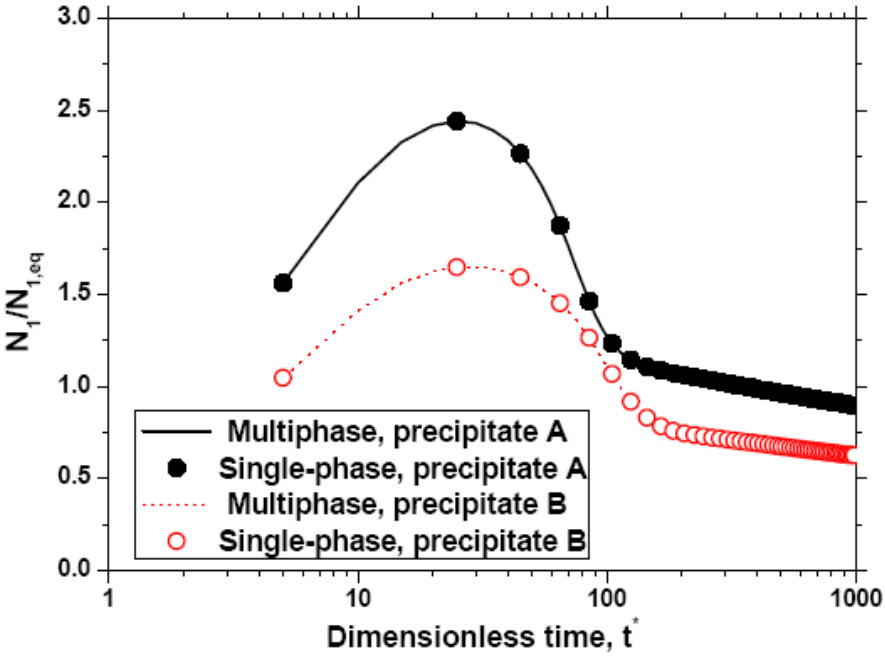

(b). Number densities of single pseudomolecules

Figure 4.1: Comparison for the mutually-exclusive precipitates at different time by multiphase and single-phase precipitation models

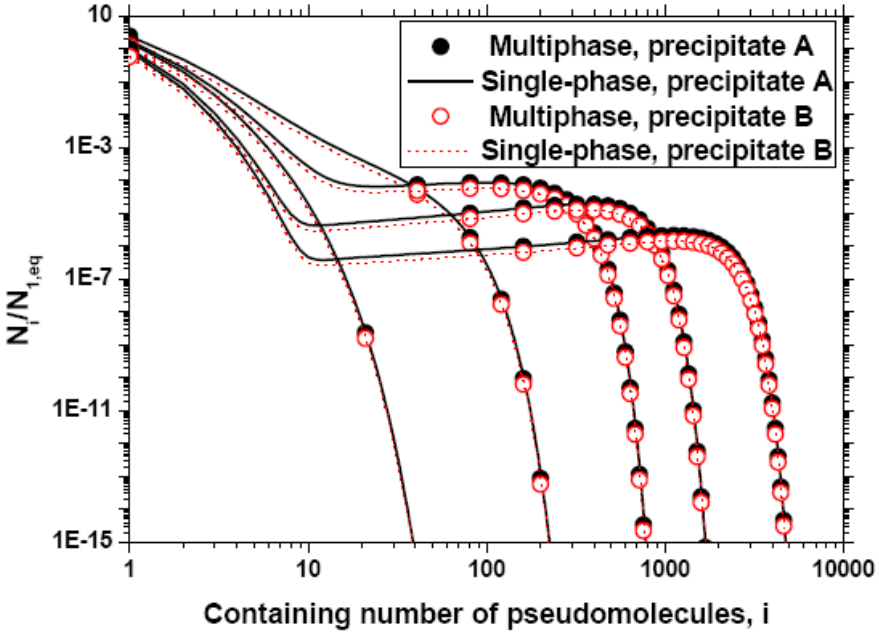

(a). Particle size distributions

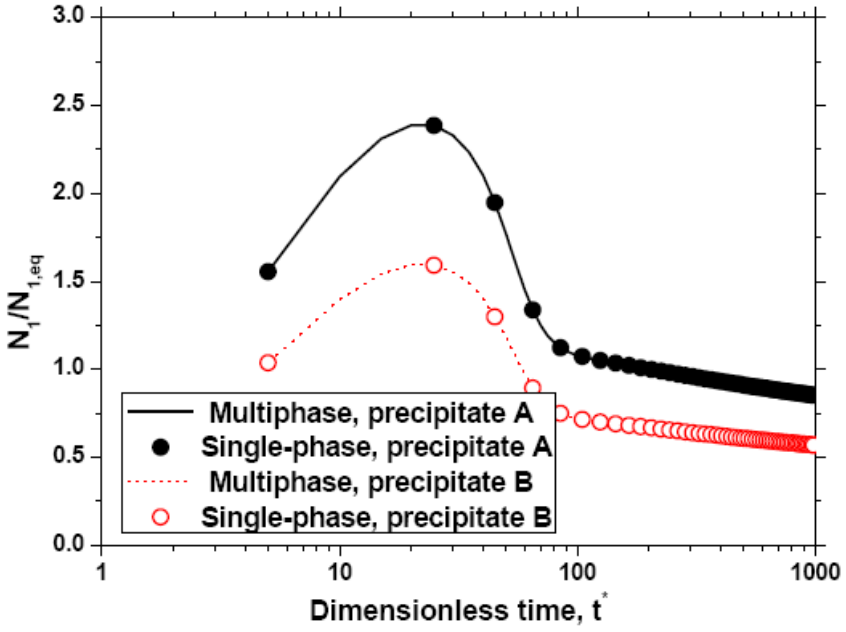

(b). Number densities of single pseudomolecules

Figure 4.2: Comparison for the mutually-soluble precipitates at different time by multiphase and single-phase precipitation models

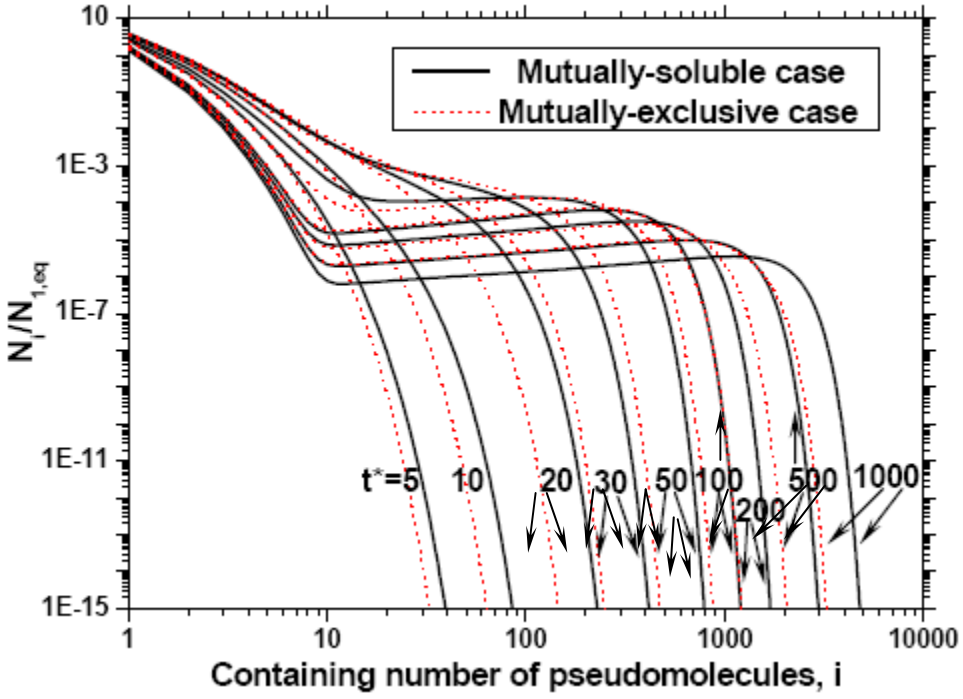

Figure 4.3: Comparison of total particle size distributions for the mutually-exclusive and mutually-soluble precipitates at different time

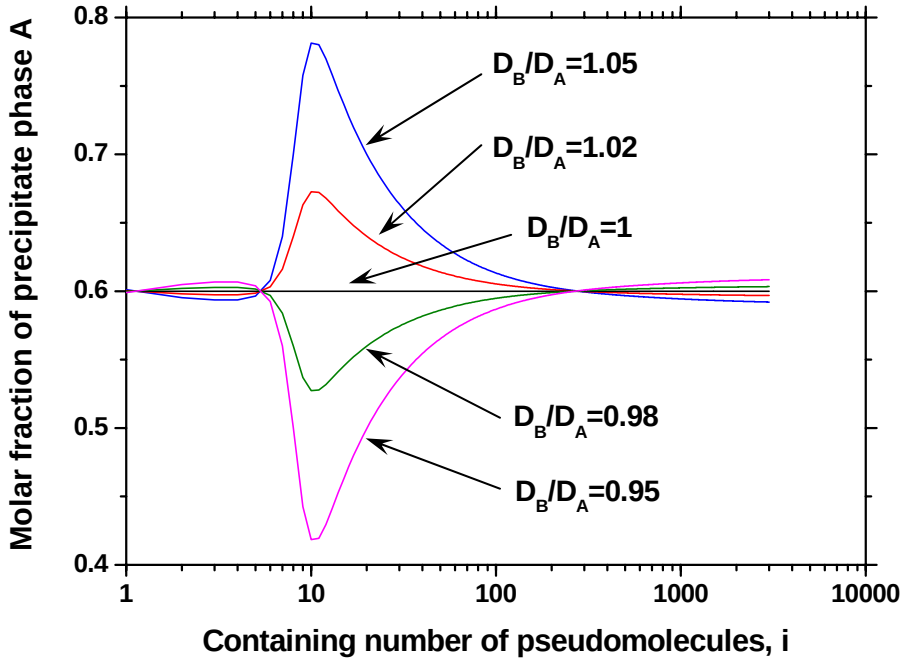

Figure 4.4: Influence of changing ratios of diffusion coefficients on molar fractions of phase A for mutually-soluble precipitates at t^{*}=100

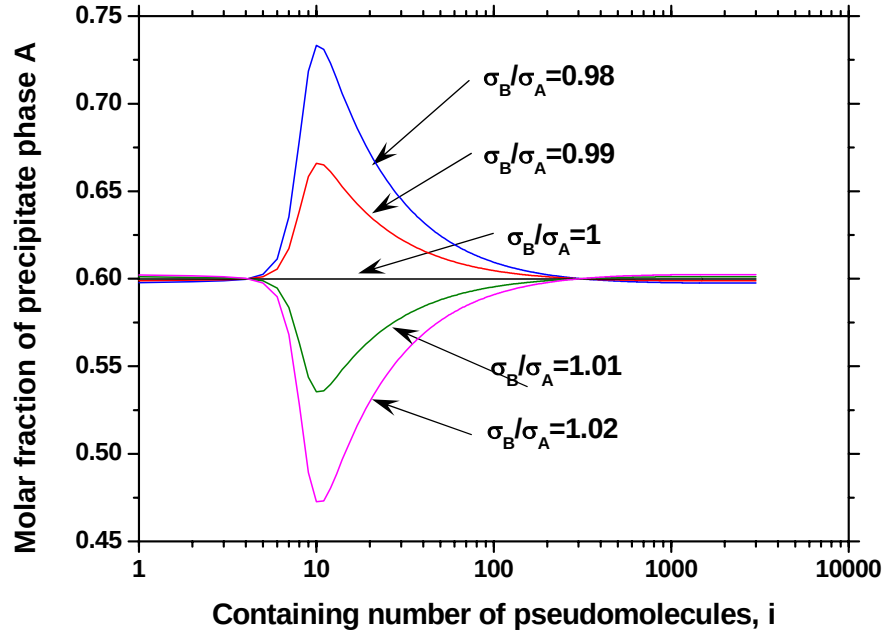

(a). Global picture

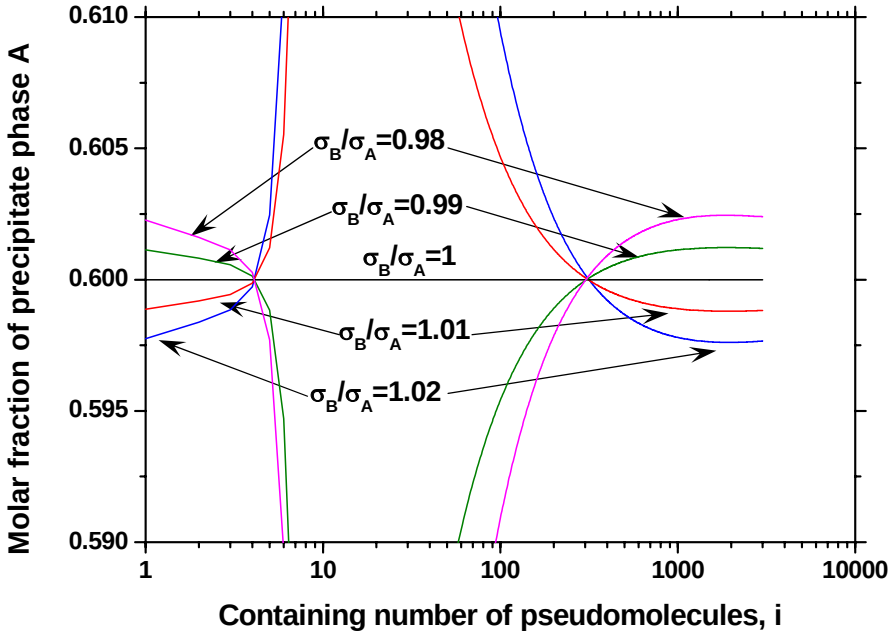

(b). Zoom-in picture

Figure 4.5: Influence of changing ratios of interface energies on molar fractions of phase A for mutually-soluble precipitates at t^{*}=100

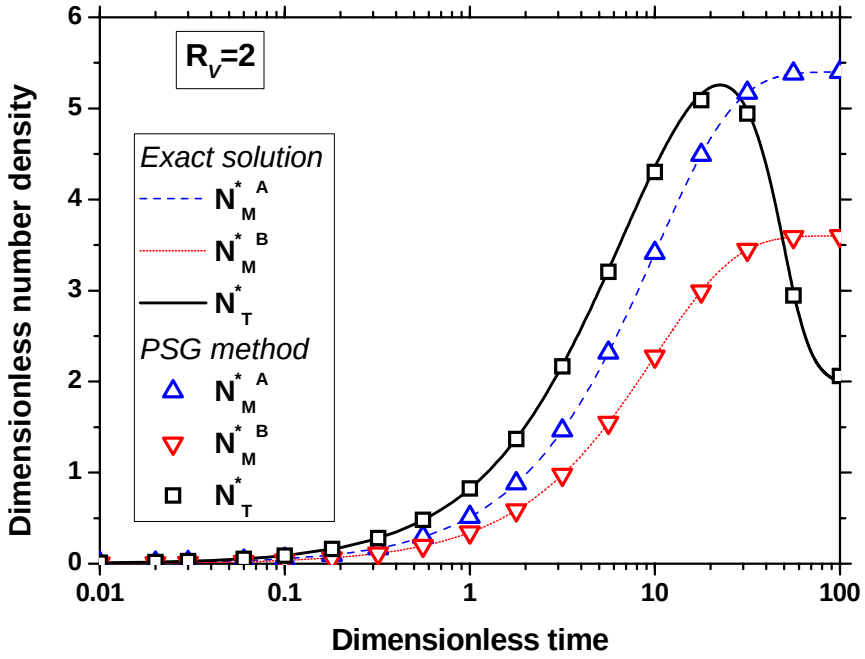

Figure 4.6: Comparison of multiphase diffusion curves calculated by PSG method with exact solution for R_V=2

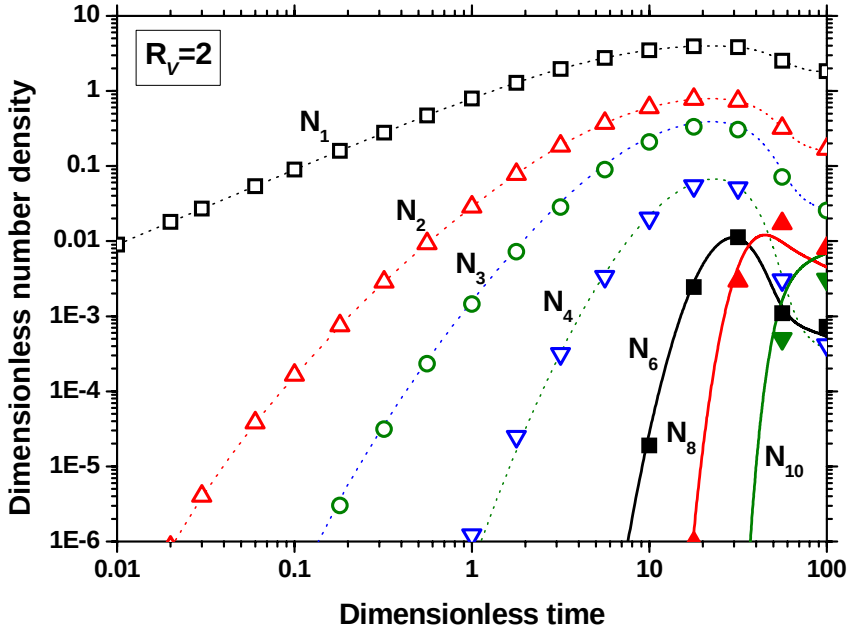

(a). Total number densities

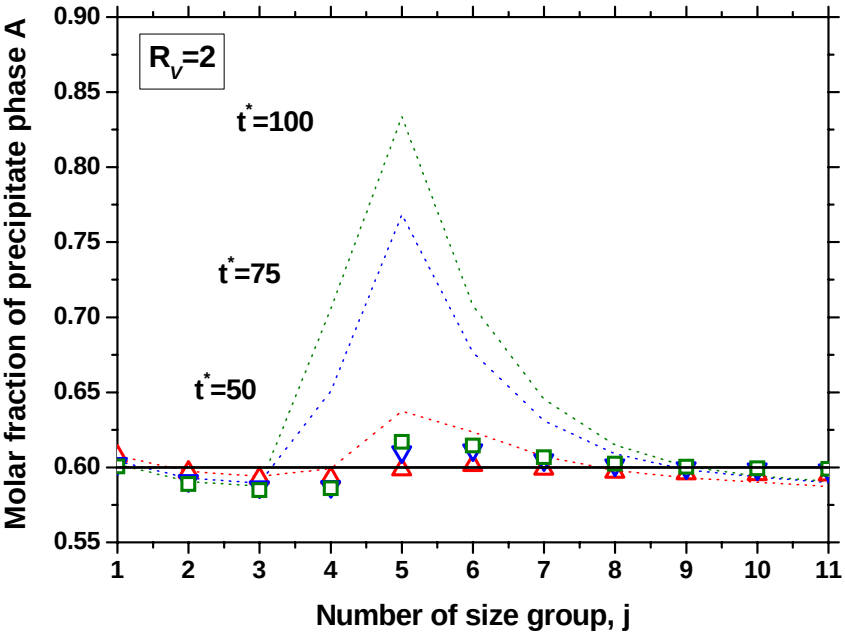

(b). Molar fraction of precipitate phase A

Figure 4.7: Comparison of multiphase diffusion curves of each size group calculated by PSG method with exact solution for R_V=2

CHAPTER 5
GRAIN GROWTH MODEL IN THE PRESENCE OF PRECIPITATES

Grain size is a very important factor to determine the microstructure and mechanical properties of materials, such as strength, ductility and toughness. Since the grain boundaries are open and disordered crystal regions of high energy, the thermodynamic driving force of grain growth is to decrease the total area of grain boundaries. If the grain size increases, accompanied by a reduction in the actual number of grains, the total area of boundary will be reduced. Thus, an inherent distribution of grain size within a given structure arises from achieving a minimum total free energy of the system and meeting the above requirements. It is the size differences between neighboring grains which provide a driving force for grain growth. Those grains with a size advantage over their neighbors would experience significant growth. Larger grains would grow at the expense of smaller grains, leading to an overall increase in grain size.

The precipitates are able to constrain grain boundary movement, and thus inhibit grain growth and refine grain size. This could result in an improvement of the ductility, which can reduce the occurrence frequency of transverse cracks. Both facts make a grain refinement and a kinetic model of grain growth important.

5.1 Previous Work

The grain growth is generally divided as two types: so-called “normal” and “abnormal” growth. The normal grain growth is referred to a self-similar coarsening process that the grain size distribution remains essentially quasi-stationary while the average grain size increases [232]. Alternatively, abnormal grain growth is a process in which a non-uniform grain size distribution develops by a selected number of grains growing more rapidly at the expense of others to achieve recrystallization. In order for this to occur, the subset of grains must possess some advantage over their competitors such as anisotropy of grain boundary energy or mobility, favorable texture, or non-uniform spatial distribution of precipitates. The details of abnormal grain growth are beyond this work, and are encouraged to be found elsewhere [233].

A necessary condition for the occurrence of abnormal grain growth is that normal grain growth is inhibited. There are several ways to retard the grain growth, but the only well-known method of completely inhibiting grain growth in bulk materials is by the introduction of second

phase particles [6]. If a single boundary intersects a spherical particle, a small area of grain boundary disappears, thus the total boundary area arising from the location of particle is less than that which arises if the particle is situated elsewhere in the matrix phase. Consequently, grain boundary migration will occur only if the driving force for grain growth exceeds the pinning force exerted by particles on the boundary. Otherwise, the grain growth will be inhibited completely.

In continuous casting process, the austenite grain growth is the dominant microstructural phenomena in casting, reheating and between rolling strands after completion of recrystallization. The austenite microstructure also determines the final ferrite grain size. Thus it plays a key role to determine the final mechanical properties of the steel product, and attempted to b modeled.

5.1.1 Normal Grain Growth

The driving force of grain growth is the reduction of grain boundaries area, and the driving pressures is given by the combination of surface tension and the curvature of the grain boundary, as follows [234]

$$P_G = \sigma / \rho_c \tag{5.1}$$

where grain boundary curvature radius $\rho_c = \overline{R} = \overline{D}/2$ for a spherical grain, substituting this into equation fields

$$P_G = \sigma / \overline{R} = 2\sigma / \overline{D} \tag{5.2}$$

The numerical constant in this equation can vary by several times, depending on the assumptions of the models. A better description is given by a heterogeneity factor, which is the ratio of the radii of growing grains to matrix grains suggested by Gladman [36], as follows

$$P_G = K_1 \sigma / \overline{D} \tag{5.3}$$

The grain boundary migration rate is related to the effective driving force through the following equation

$$V = \frac{d\overline{R}}{dt} = \frac{1}{2}\frac{d\overline{D}}{dt} = M\left(\Delta P_G\right)^{(1/n-1)} \tag{5.4}$$

where M is grain boundary mobility, which is often expressed by an Arrhenius function $M = M_0 \exp(-Q_{app}/RT)$. Q_{app} is the temperature-independent activation energy for grain boundary migration, and n is the time exponent in grain growth equation, which approaches a

constant value of 0.5 for the ideal case of ultrapure metals annealed at high temperature [235]. However, experimentally determined values of n vary considerably and are frequently less than the theoretical value, which may be influenced by the presence of solute atoms, solute segregation, second phase particles and texture effects and widely accepted as reasons of grain growth inhibition [236, 237].

5.1.2 Grain Size Inhibition by the Precipitates

The addition of second phase precipitates is believed to be an efficient tool to control or refine the grain size. The well-known work by Zener, gives the first analysis of forces balance between particles and grain boundaries [6]. For a single boundary intersecting a spherical particle, a small area of grain boundary disappears and the local curvature of the boundary is altered as shown in Figure 5.1. Unpinning requires an additional energy by the driving force for grain boundary movement.

The pinning force exerted by as single second phase particle on the grain boundary is written as the product of the component of interface tension of grain boundary in the direction of its movement, $\sigma\sin\theta$, and the linear length of contact area, $2\pi r\cos\theta$, as follows

$$F_Z = 2\pi r\sigma \sin\theta\cos\theta \tag{5.5}$$

For maximum pull, $\theta=45^o$ gives $F_Z^{\max} = \pi r\sigma$

The surface density of particles on the grain boundary can be written as their volume density multiplying the precipitate radius r:

$$N_s = N_V \cdot r = \frac{\varphi_V}{4\pi r^3/3}\cdot r = \frac{3\varphi_V}{4\pi r^2} \tag{5.6}$$

The maximum pinning pressure due to all particles on the unit grain boundary is thus given as

$$P_Z = N_s \cdot F_z^{\max} = \frac{3\varphi_V\sigma}{4r} \tag{5.7}$$

On the other hand, the driving pressure for grain growth is still given by Eq. (5.2). When the system is at equilibrium, $P_g = P_Z$, the grain radius is the Zener limit, which is the critical grain radius under the balance of driving and pinning pressures, as follows

$$R_c = \frac{4r}{3\varphi_V} \tag{5.8}$$

This work demonstrated for the first time, both qualitatively and quantitatively that, for a given particle-containing material, an increase in the volume fraction, or a decrease in particle size will cause a decrease of pinning grain size. It suggests an important method to achieve a fine size for particle-containing materials. However, the coarsening or dissolution of the precipitates may adversely initiate abnormal grain growth of some unpinning grains.

The precipitate particles are always distributed with a size range, and it will have the different pinning effect with the uniform distribution of its own mean size, or other size distributions with the same mean size on restricting the grain growth. Fullman [238] suggested to rewritten the Eq. (5.8) of critical grain radius as

$$R_c = \frac{4}{3} / \sum_i \frac{\varphi_V(r_i)}{r_i} \tag{5.9}$$

After Zener equation was developed, many researchers tried to introduce less assumptions in derivation and improve accuracy and applicability to more realistic situations. Hillert pointed out that for Zener limit of grain growth inhibition, the lower limit is 0.44r/f and the upper limit is $0.67r/\varphi_V$ [232]. Clearly, the initial Zener limit is beyond this range by a factor of 2-3. But if following Gladman's suggestion [239], the way to judge whether the particles is in contact with a grain boundary is when the center of the particle within ±r of the boundary, and the contacting distance should be 2r, instead of r in Zener's initial work. This idea gives the Zener limit exactly as the upper limit suggested by Hillert.

According to many modifications, a more general form of critical grain radius could be expressed as [240]

$$R_c = \frac{K_1}{2K_2} \frac{r}{\varphi_V^m} \tag{5.10}$$

It shows that the critical grain radius increases as mean precipitates size increases and the particle volume fraction decreases, but the numerical constants may vary. The exponent m can vary from 0.33 to 1, which is directly related to apparent volume fraction of particles located near the grain boundaries, rather than the true volume fraction through the materials [241]. For an isothermal process, the limiting grain size continues to decrease first after precipitates begin to form, until the grain growth is completely inhibited. After the equilibrium state is approached, the volume fraction of precipitates is kept as constant and the particle size increases with time by

coarsening. This may cause the limiting size to increase again. More details of Zener equation development are encouraged to be found in the work of Manohar *et al* [240].

5. 1. 3 Grain Growth in the Presence of Precipitates

By coupling the Zener pinning force, a general equation to describe the grain growth in the presence of precipitates is thus suggested as [242]

$$V = \frac{d\bar{R}}{dt} = \frac{1}{2}\frac{d\bar{D}}{dt} = M\left(P_G - P_Z\right)^{(1/n-1)} \tag{5.11}$$

According to Eq. (5.10), the general form of the pinning force, P_Z, is given as

$$P_Z = K_2\sigma\frac{\varphi_V^m}{r} \tag{5.12}$$

Inserting the general forms of driving force P_G and pinning force P_Z, Eq. (5.3) and (5.12), the above equation is rewritten as

$$\frac{d\bar{D}}{dt} = 2M_0\exp\left(-\frac{Q}{RT}\right)(K_1\sigma)^{(1/n-1)}\left(\frac{1}{\bar{D}} - \frac{K_2}{K_1}\frac{\varphi_V^m}{r}\right)^{(1/n-1)} \tag{5.13}$$

Setting $A=2M_0(K_1\sigma)^{(1/n-1)}$ and $B=K_1/K_2$, the equation is simplifies as follows

$$\frac{d\bar{D}}{dt} = A\exp\left(-\frac{Q}{RT}\right)\left(\frac{1}{\bar{D}} - \frac{1}{B}\frac{\varphi_V^m}{r}\right)^{(1/n-1)} \tag{5.14}$$

The parameter A and B are related to the grain boundary mobility and the pinning efficiency of the precipitates, respectively. The grain growth will stop when $d\bar{D}/dt=0$, which given the limiting grain diameter as

$$\bar{D}_{\lim} = B\frac{r}{\varphi_V^m} \tag{5.15}$$

The parameter B is coefficient related to the pinning efficiency of the precipitates, which is equal to 8/3 in the original Zener's model, but can vary by over one order of magnitude in other models [240]. Under precipitate pinning, the grain growth will be completely inhibited if grain size is already larger than this limiting size, which states that the pinning force of precipitates is larger than the driving force of grain growth. Otherwise, the precipitate pinning decreases the rate of grain growth, which is calculated by Eq. (5.14).

If a grain size distribution is modeled, instead of the mean size in the above model, the driving force for grain growth is believed to be the curvature difference of neighboring grains.

Eq. (5.11) will be applied to compute the growth rate of each individual grain under the influence of all of its neighboring grains. Only grains with size advantage over their neighbors can grow, and others will shrink. The grain boundary energies are always required to be different for some grains to induce an initial uniform grain size to develop. These kinds of work are well developed by Abbruzzese et al [243, 244]. But these calculations are highly limited by the number of grains in simulation, and are not considered in this work.

5.2 Implications of Model

The austenite grain growth equation (5.14) in the presence of precipitates suggested by Anderson and Ø. Grong [242] is used in this thesis. The initial austenite diameter at the beginning of calculation is assumed to equal to the primary dendrite arm spacing (PDAS) at the highest temperature of a totally austenite structure. The PDAS is estimated as function of cooling rate and carbon content as [245]

$$\lambda_1 = \begin{cases} 278.748(C_R)^{-0.2063}(C_0)^{-0.3162+2.0325C_0} & 0 \le C_0 \le 0.15 \\ 278.748(C_R)^{-0.2063}(C_0)^{-0.0189-0.4917C_0} & 0.15 \le C_0 \le 1.0 \end{cases} \quad \textbf{(5.16)}$$

where C_R is cooling rate during solidification, which is predicted by the difference and cooling time between solidus and liquidus temperatures. C_0 is carbon content with the unit of wt%.

For austenite grain growth, apparent activation energy is always assumed to equal to the activation energy for diffusion of iron in austenite, but it may depend on the chemical composition of microalloy and segregation. Bernhard *et al* suggested the values of parameters for austenite grain growth model, which give a good match with experimental for a wide range of steel composition. The kinetic constant A is assumed to be 4×10^{-3} m^2s^{-1} and time exponent n is taken as 0.5. The equivalent carbon content C_P and apparent activation energy Q_{app} for grain growth above 0.1wt% of equivalent carbon content are given as [53, 246]

$$wt\%C_P = wt\%C - 0.14wt\%Si + 0.04wt\%Mn \quad \textbf{(5.17)}$$

$$Q_{app} = 167686 + 40562 \cdot wt\%C_P \quad \textbf{(5.18)}$$

The calculation shows a maximum grain size bewteen the equivalent carbon mass content of 0.15% to 0.17% [53, 246], which corresponds with the highest frequency of transverse cracks index in literature.

The calculation of austenite grain size is carried out as the following procedure: the temperature and steel phase histories are first given by the experimental measurements or numerical modeling. The cooling rate for calculating PDAS in Eq (5.16), is the average rate during solidification. After the PDAS is determined and taken as the initial austenite grains size, the simulation of austenite grain growth starts from the temperature of totally austenite and continues with the given temperature history.

5.3 Validation with Experimental Measurements

A simple case is run to check the effectiveness of the model. The number and area of austenite grains near the surface of cast slabs with a wide range of chemical compositions are determined from micrograph, and parameters for the distribution and average value of grains are calculated by statistics software [246].

The simulations start from the highest temperature of a totally austenite structure, which is calculated and given in the initial work [246]. The initial austenite grain size is assumed to be ~100μm, which is due to the rapid cooling near slab surfaces. Since only one measured temperature curve by thermocouple is available, an average cooling rate is roughly estimated to be ~ 5^{o}C/s for temperatures above 1000^{o}C as shown in Figure 5.2 [246], which is believed to be the decisive temperature range for austenite grain growth. This cooling rate is then approximately used in simulations of all steel compositions. The calculation is run until 900^{o}C when austenite starts to transform, and the influence of precipitates is ignored due to the rapid cooling in tests.

The comparison of calculated results with experiments is shown in Figure 5.3. A reasonable agreement is observed for all steel compositions (slope=1.061). It is logic that the simulation will produce a little large austenite size, because an average cooling rate of 5^{o}C/s overestimates the real rate at high temperature, as shown in Figure 5.2, which is believed to be most important for grain growth under kinetic consideration. More validations of this model with the presence of precipitates in continuous casting are given elsewhere [53].

5.4 Tables and Figures

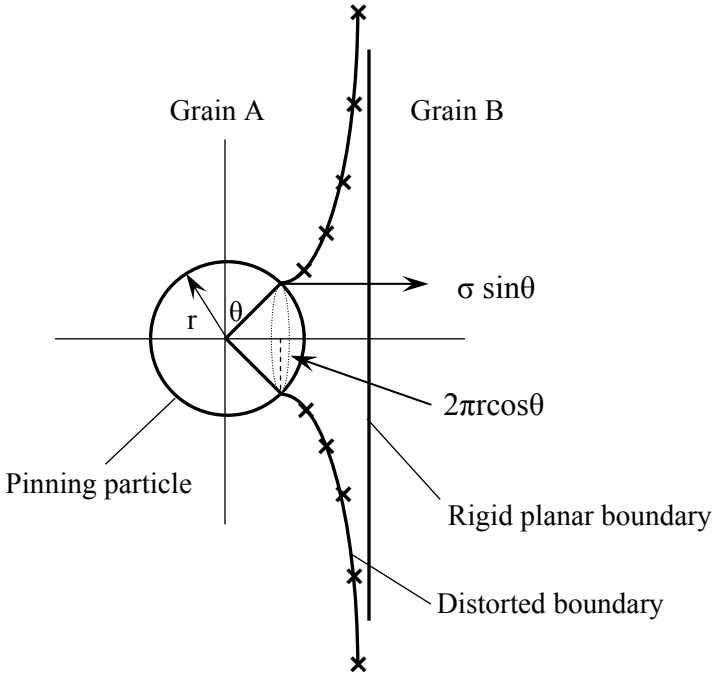

Figure 5.1: Schematic of the interaction of a spherical particle with a grain boundary

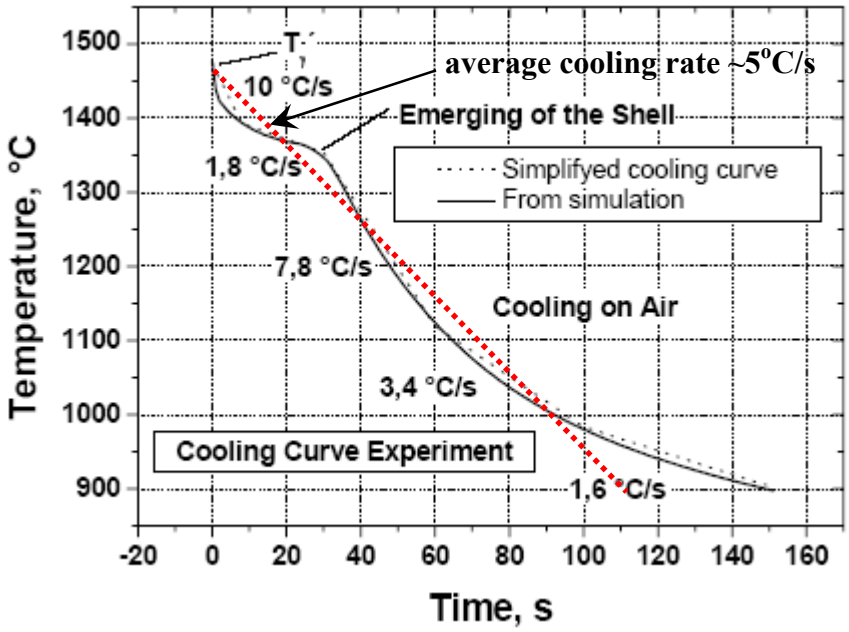

Figure 5.2: Estimation of an average cooling rate from measured temperature of shell surface [246]

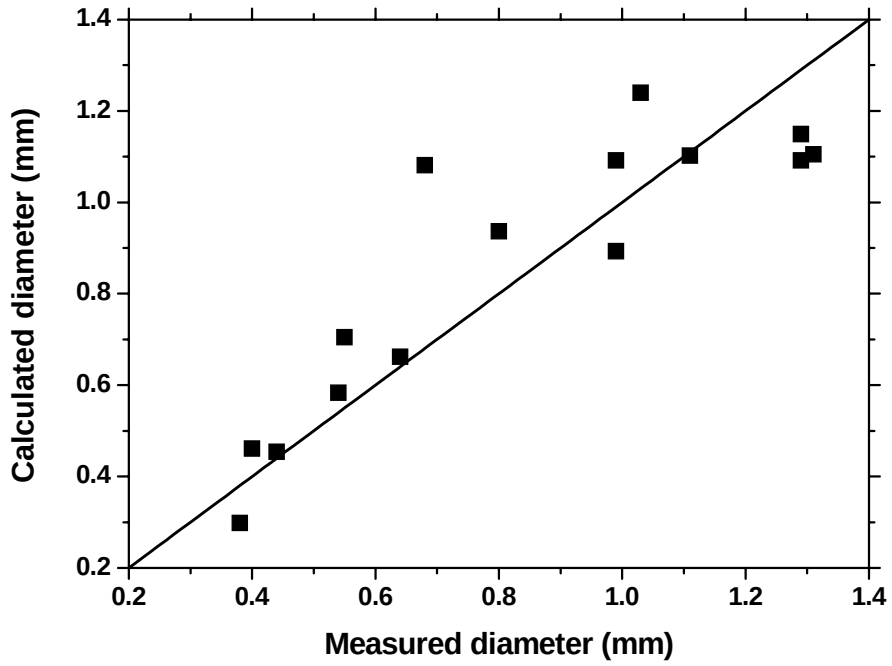

Figure 5.3: Comparison of calculated and measured austenite grain size [246]

CHAPTER 6
CALCULATION FOR PRACTICAL STEEL GRADE IN CONTINUOUS CASTING

The suggested models in the previous chapters are combined together to simulate precipitate formation and grain growth for practical steel grade in continuous casting process. Instead of isothermal holding for most previous validation cases, a heat transfer model, CON1D, is first applied to calculate the histories of temperature and steel phases across the entire slab region in the process. Then the equilibrium model in chapter 2 and kinetics models in chapter 3-4 are applied to simulate the evolution of precipitate fraction and size distribution, and finally austenite grain growth model in chapter 5 is applied to calculate the grain size evolution under the presence of precipitates for the chosen positions of the slab.

After exiting the mold, the continuous casting slab usually passes through a secondary cooling region, with nozzles that continuously spray water against the solid steel shell between the rolls. This often causes a heavy temperature oscillation for the slab surface. The surface temperature may drop to a favorable temperature range of precipitation on PTT diagram, and even below the transformation temperature of austenite to ferrite to cause a quick precipitation. On the other hand, the interior of slab does not account this kind of temperature oscillation or undercooling, which makes the precipitation and grains quite different compared with slab surface. A simulation of these phenomena across the slab is important to understand the effects of continuous casting process, and to explain the possible formation of transverse surface cracks.

6.1 Introduction of Continuous Casting Process

After it became commercially feasible in 1960, the continuous casting quickly became popular and widespread in steel industry. Comparing with the conventional ingot making, the continuous casting process casts molten steel directly into the different semi-finished shapes as possible to end products, such as round solid billets, round hollow billets and beam blanks, bypassing the steps of soaking or blooming, on a continuous basis. It thus improves product yield and resource conservation by reducing equipment, labor, energy and time requirements, and promotes the progress of the steel industry as a modern manufacturing industry. Today, continuous casting is the most common process in steel production, and accounts for more than 90% of the world's output, including almost all varieties of steel grades.

During its development, continuous casting of steels had encountered several breakthroughs to resolve several major technical difficulties and reach the modern process. In 1934, Junghans suggested a vertical mold oscillation to prevent the solidified shell from sticking to the mold and causing breakout of molten steel. A curved circular-arc-type machine was introduced by June in 1963, instead of an initial vertical machine. It overcame the required long time for the complete solidification of steels and achieved a much higher productivity. A historical overview of continuous casting development is given elsewhere [247].

The schematic of a modern continuous casting process is shown in Figure 6.1 [248]. Fluid flow in continuous casting process is driven by gravity. The purified liquid steel was first poured in a large ladle, which is placed above the casting machine. The steel flows out from the open bottom of the ladle into a reservoir called as tundish, which acts as a buffer between ladle changes to make the process continuous without interruption. The liquid steel next flows through a refractory submerged entry nozzle into a bottomless, water-cooled and oscillating copper mold. The flow out of the tundish is controlled by either a stopper rod within the tundish or a slide-gate mechanism within the entry nozzle.

The steel solidifies soon after contacting with the mold walls, forming a thin shell of solid steel, which is withdrawn continuously with a rate of so-called casting speed. After exiting the mold, the steel travels through a region known as secondary cooling, which consists of several zones of nozzles that continuously spray water against the steel shell between the driving rolls that lead the steel strand from a vertical to a horizontal configuration. Once the steel strand is completely solidified at a distance below meniscus, called as metallurgical length, a torch cuts the steel strand into separate slabs of desired length. The section of steel continues to further processing, such as reheating, homogenization, hot-rolling, coiling or other required processes to get the final product.

A recent new technology of continuous casting is the Compact Strip Production (CSP), which is characterized by casting a slab of around ~50mm at a speed of 5m/min or higher. Because of a reduction of slab thickness, shorter spray zones, fast solidification rate, less segregation and finer as-cast grain size are expected. Combined with higher thermal strains and strain rates, the process greatly changes the metallurgical behavior, such as strain-induced precipitation, grain growth, grain boundary embrittlement and susceptibility to transverse cracks

[249]. There is a strong need for accurate predictive tools to help design cooling practices to avoid cracks and to maximize surface quality.

The purpose of this chapter is to integrate all available models together to simulate the precipitate formation and grain growth for an industrial steel grade in a practical continuous casting process. The calculated results are then compared with available experimental measurements.

6.2 Experimental Measurements

Recenly, Dyer *et al* measured the precipitated fractions and size distribution to find the effect of microalloy precipitation and dissolution during direct slab production relative to the position within slab and alloy composition. Three steel compositions of different niobium addition and the surface, columnar and centerline of slab are explored to incorporate the influence of different temperature histories, solidification rates and alloy segregations [250, 251].

A 1200mm×50mm thin slab of HSLA steel was continuously cast at Nucor-Steel-Hickman at a speed of 5.0m/min. This "high-Nb" steel (as designated in the prior publication [251]) had weight composition of 0.031% C, 1.039% Mn, 0.194% Si, 0.031% Ni, 0.032% Cr, 0.01% Mo, 0.003% Ti, 0.046% Nb, 0.001%V, 0.031% Al, 0.006% N, 0.003% S, 0.012% P. The mold working length was 850mm, and the water spray cooling zones spanned from mold exit to 6m below the meniscus. The typical recorded slab surface temperature was 900^{o}C at exit from the last support roll in the spray zone. The slab then travels a few meters past a cutoff shear, and was hot charged at 900-1100^{o}C surface temperature into a several-hundred-meter-long reheating furnace with an internal temperature of 1150^{o}C.

The slab samples were full-width crops of ~700mm length taken either at the shear or prior to the hot-rolling mill. Each cropped steel sample was rapidly quenched in agitated water to room temperature, and cut into small pieces, 300mmx125mmx50mm. The samples were first dissolved in two stages to separate and measure the precipitated Nb from the Nb in solution by electrochemical extraction. Then, the precipitates were counted in selected sections and compositions were measured to determine the size distributions of Nb-bearing precipitates on TEM micrographs of carbon replicas.

Electrochemical extraction and inductively coupled plasma atomic emission spectrometry (ICP-AES) techniques were used to quantify the amounts of niobium in solution and precipitate

form. Three different volumes were cut from each slab sample and identified as chill zone near the slab surface/edge (S), columnar zone at medium depth (M), and equiaxed zone near the slab center (C), as shown in Figure 6.2. Three different trial heats were tested, containing low, medium, or high niobium additions, and with similar levels of carbon, manganese, silicon, aluminum and nitrogen. Each steel specimen was dissolved in an aqueous solution of 5% hydrochloric acid and 3% tartaric acid and filtered to separate the dissolved steel matrix from the alloy precipitate. The precipitate residue and filter papers were then dissolved in a second solution prior to chemical analysis. After chemical extraction and precipitate dissolution, each solution was diluted with deionized water prior to ICP-AES. The sum of the two niobium amounts (in solution and precipitate form) gives the total niobium measured. Good reproducibility was found to demonstrate accuracy of the experiments [250].

The precipitate size distributions and compositions were then measured by TEM and EDS on carbon extraction replicas from selected samples. A typical precipitate particle distribution for the high-Nb steel at the furnace exit that is measured and modeled in this work is shown in Figure 6.3. The length and width of each precipitate particle are found using an arbitrary line measurement function of imaging pictures to calculate its area. Five carbon replicas were made for each specimen, and analyses of at least three replicas, were completed to ensure a general observation for each alloy, process location and solidificaiton region. Approximately 200 particles were counted from ten fields of view per condition, to obtain particle size distributions. At least ten precipitates were analyzed using EDS analysis for each processing considiton and solidification region. The cross-sectional area of the each precipitate was used to calculate its "equivalent diameter", by assuming that the particle is perfectly circular [251].

The measurements show that the extent of precipitation increased with increasing niobium addition. The most niobium precipitation occurred at the slab surface along the edges of the thin slab, where dissolution subsequently occurs during reheating and equalization in the tunnel furnace. The columnar region comprised the bulk of the slab volume, and exhibited minimal alloy segregation and the lowest amount of precipitated niobium. The slab edge exhibited relatively small (10-30nm) irregular-cuboidal and cuboidal precipitates, and the columnar and centerline regions contained larger irregular-cuboidal and cuboidal precipitates. Further details of these experiments are provided elsewhere [250, 251].

6.3 Simulation Results

The model is applied here to predict temperature, precipitation, and grain size for the processing conditions of the reheated and quenched high-Nb steel samples for which measurements were available. The surface/edge (S), middle/columnar (M) and center (C) locations in the experiments are chosen as 0mm, 12.5mm and 25mm from the slab surface in the simulation. The modeling procedure follows the flow chart presented in Figure 1.7.

6.3.1 Heat Transfer

In this work, the transient heat conduction equation is solved in the mold, spray regions, reheating furnace and quenching water of a continuous steel slab caster using the CON1D program [252]. This finite-difference model calculates one-dimensional heat transfer within the solidifying steel shell coupled with two-dimensional steady-state heat transfer in the mold and a careful treatment of the interfacial gap between the shell and mold. Below the mold, the model includes the temperature and spatially-dependent heat transfer coefficients of each spray nozzle, according to the local water flow rates, and the heat extraction into each support roll. After exiting the last spray zone, subsequent reheating or quenching stages can be added by restarting the simulation using an "initial" temperature profile from any desired previously-calculated time. A non-equilibrium microsegregation model, based on an analytical Clyne-Kurz equation developed by Won and Thomas [253], was applied to compute the liquidus temperature, solidus temperature and steel phase fractions. Complete details of CON1D are provided elsewhere [252].

The pouring temperature is assumed to be 1553^{o}C. Starting with the heat transfer coefficient boundary conditions of [254], The water spray heat transfer rates are adjusted in order to match the recorded caster exit temperature of 900^{o}C and tunnel furnace entry temperature of 900-1100^{o}C. The casting speed is changed to 11.2m/s to match the time of 20 minutes in 225m-long reheating furnace. A "restart run" is performed to continue reheating of the sample in the tunnel furnace and quenching in agitated water, by taking the initial condition from the final results at the end of last stage. Natural convection with air is taken as 8.7W$\cdot$m$^{-2}\cdot$K^{-1}, and the heat transfer coefficient for the agitated water is 2000W$\cdot$m$^{-2}\cdot$K^{-1}.

Figure 6.4 shows the calculated equilibrium steel phase evolution with temperature, and it follows as liquid$\rightarrow$ δ ferrite$\rightarrow$ austenite$\rightarrow$ α ferrite (and Fe_3C) with decreasing temperature. The

liquidus and solidus temperatures are calculated as 1525.4^{o}C and 1504.8^{o}C, and the δ-ferrite is completely transformed to austenite at temperature of 1381.8^{o}C.

The predicted temperature histories inside the slab are shown in Figure 6.5. At the slab surface, the temperature decreases quickly in the mold and oscillates in water spray cooling zones. Surface temperature increases after exiting the caster due to heat supplied from the slab interior, which tends to equilibrate the temperature distribution. Temperature decreases again slightly due to air cooling, prior to entering the reheating furnace. After an initial increase, temperature stays constant through most of the reheating furnace, and sharply decreases when the cropped sample is water quenched. In the slab interior, as half thickness and center, the temperature decreases slowly in the mold and water spray cooling zone, and continues to decrease due to air cooling after the caster. Like the surface, internal temperature slightly increases to a constant in the reheating furnace, and finally sharply decreases by water quenching.

6.3.2 Equilibrium Precipitation

The equilibrium precipitation model is used to predict equilibrium phases as a function of temperature, based on the given steel composition and the matrix phases corresponding with the temperatures and predicted using CON1D. The results are graphed in Figure 6.6 for the steel phase fractions in Figure 6.4. Solubility products and Wagner interaction coefficients for the liquid, ferrite and austenite are tabulated elsewhere [87], and the effect of the small amount of Fe_3C (<0.4%) is ignored.

For this steel, MnS starts to precipitate at 1508^{o}C in δ-ferrite, and then partly dissolves during the δ-ferrite to austenite transformation because of a higher solubility limit of MnS in austenite. This is consistent with experimental observations of large sulfide precipitates, which were not included in the size distributions counted in experiments [251]. With decreasing temperature, (Ti,Nb,V)(C,N) precipitates from 1288^{o}C and AlN precipitates from 1038^{o}C in austenite as shown in Figure 6.6(a). The precipitation of AlN is delayed by the formation of (Ti,Nb,V)(C,N) because part of its required nitrogen has been consumed. The equilibrium dissolved mass concentrations of niobium and titanium, which is represented as $[Nb]_{eq}$ and $[Ti]_{eq}$ are also shown in the same figure. These data are input into the transient precipitation model to compute equilibrium number density of single pseudomolecules in Eq. (3.109).

Figure 6.6(b) shows the composition changes expected in the mixed (Ti,Nb,V)(C,N) precipitates. At high temperature, TiN is the most thermodynamically stable compound, so the mixed precipitates are mainly TiN according to the thermodynamic model employed for these calculations. With decreasing temperature, more carbides form as they become stable and there is much more carbon than nitrogen in steel. Interestingly, the NbN fraction increases, then decreases, with decreasing temperature, and reaches a maximum at ~1050^{o}C. Below 650^{o}C, $NbC_{0.87}$ comprises over 86% of the (Ti,Nb,V)(C,N). The fractions of TiC, VN and V_4C_3 are always small because these compounds are relatively less stable, which can be often ignored in kinetic precipitation simulation.

6.3.3 Transient Precipitation

Results from the heat transfer and equilibrium models are used in the transient precipitation model to predict the evolving size distributions of precipitates in the measured samples. Titanium, niobium and vanadium are found to be in shortage, so limit the formation of (Ti,Nb,V)(C,N) precipitates, and thus the calculation of the number densities of precipitate particles is based on these metal elements for this given steel composition. Because the fraction of vanadium precipitates is found to be small by the equilibrium model, this complex precipitate system will be treated as two mutually-soluble phases, Ti(C,N) and Nb(C,N), by the multiphase kinetic model. The diffusion coefficients are based on the steel-matrix phase fractions according to a crude mixture rule, $D=f_\gamma D_\gamma+f_\alpha D_\alpha$, and those diffusion coefficients in austenite, D_γ, and in ferrite, D_α, are given in Table 3.2. While this assumption is crude, it only has an influence in the small temperature range where the matrix is undergoing transformation. The interfacial energies between Nb(C,N) or Ti(C,N) and the steel matrix are taken to be constant 0.5J·m^{-2} and 0.8J·m^{-2} as a first approximation of the results in appendix A. A constant $R_V=2$ and 35 size groups were always used to cover particle radius up to ~300nm in the simulation.

A first calculation is run for a Nb(C,N) precipitate using the single-phase precipitation model. The calculated particle size distributions just prior to entering the reheating furnace, at the end of the reheating furnace, and after quenching are shown in Figure 6.7. During casting, the precipitates are not stable, so their number density is a maximum for (dissolved) single pseudomolecules (~0.35nm in diameter) and decreases exponentially with increasing diameter. At the slab surface, large particles continue to grow and small particles begin to dissolve during

the reheating stage, which clearly shows the effect of coarsening. In the slab interior, the precipitate particles are not predicted to grow much until the quenching stage, where a sharp increase of precipitate size is observed and explained by the austenite to ferrite transformation. With much higher diffusion rate and lower solubility limit, the precipitation of Nb(C,N) is expected to be greatly accelerated during this phase transformation. The final precipitate size in the centerline region is a little larger than that of the columnar region because the slower cooling rate there provides more time for precipitation.

The size distributions from the calculated Nb(C,N) results from the single-phase model are compared with the measurements in Figure 6.8. The prediction comes closest at the surface (edge), where the mean predicated particle size of 14nm compares with the measured mean of 24nm, and the distribution shape is similar. The measurements show that particle size consistently increases with distance from the surface (edge), to middle (columnar) to centerline regions. The calculation fails to show this trend. The calculated precipitate sizes are only ~3nm, which is clearly much smaller than the measurements for the slab interior, which are 72nm for columnar region and 91nm for centerline.

The very small precipitate size of Nb(C,N) in slab interior predicted by the single-phase model suggests that the low supersaturation cannot provide enough driving force for niobium to precipitate before quenching. An underestimation of the measured size distribution is maybe explained by the mutual solubility of Nb(C,N) with much more stable TiN, which promotes precipitation in the reheating furnace or even before reheating at a much higher temperature in austenite. Newly formed Nb(C,N) can precipitate on the surface of large Ti-bearing precipitates to further form coarsened particles. This is consistent with the EDS detection of titanium in most of the larger precipitates in the experiments [251].

The calculated particle size distributions assuming two different precipitate phases, Ti(C,N) and Nb(C,N), which are mutually soluble, by the multiphase model are shown in Figure 6.9. During casting, some fine precipitates have been found. The slab surface contains the smallest size precipitates because of its lower temperature and corresponding higher supersaturation. Significant particle coarsening is observed at all locations during reheating, where large particles grow, while the small ones shrink. During quenching, there is not enough time for coarsening of large particles, but more fine particles form due to a further precipitation of the remaining solutes in the matrix. The slab surface always shows smaller precipitate size

than that of slab interior, because the lower temperatures before reheating have caused a high supersaturation to generate more fine precipitates at surface. In conclusion, a small addition of 0.003% Ti causes an important change of precipitate behaviors, which agrees with the EDS results showing that Ti always exists in the precipitate particles measured [251].

A comparison of the measured size distributions with the calculated (Ti,Nb)(C,N) results from the multiphase model are shown in Figure 6.10. The multiphase precipitation model greatly increases the calculated precipitate size and gives a much closer match with the measurements. The calculated precipitate diameter has a magnitude of around 20-50nm, which matches reasonably with the measurements at slab surface, but still underpredicts the measurements at the slab interior. The trend of increasing size from surface to middle to center agrees with the measurements.

The final molar fractions of Ti/(Nb+Ti) contained in all of the different-sized particles is shown in Figure 6.11. This fraction is only larger than 0.5, indicating Ti-enrichment, for very large particles. For very small size, it is close to zero, which means that niobium precipitates are dominant in the small size range. A peak at the intermediate size range of 10-20nm is likely caused by secondary precipitation during the final quenching stage for sample acquisition, when enough supersaturation is sharply provided that precipitate nucleation occurs without difficulty. The values of these peaks can be compared with the molar fraction of 0.112 in the recorded steel composition.

The calculated amounts of precipitated niobium during casting, transfer, reheating, and quenching of the thin-slab samples is shown in Figure 6.12. The predictions are compared with experimental measurements in the final quenched samples. The precipitate diameter used to define the size distributions is truncated at 4nm, according to the estimated resolution limit of the electrochemical extraction experiment. At the slab surface, Nb starts to precipitate during the casting stage and reaches a maximum at the end of spray cooling. This precipitated Nb then mainly redissolves during the transfer stage due to reheating from the slab interior. A tiny peak is observed near the end of the transfer stage, owing to a slight cooling of the surface prior to entering the reheat furnace. In the reheating furnace, Nb precipitates continue to dissolve due to the increasing temperature, as expected, which causes the precipitated Nb to continue to decrease slightly during reheating. In the slab interior, Nb starts to precipitate in the spray cooling zones when the solubility of (Ti,Nb)(C,N) is exceeded, and a minor dissolution of Nb is found to occur

during reheating. The precipitated amount of Nb is observed to sharply increase during quenching, due to the austenite to α-ferrite transformation. Because the slab interior is cooled slower than the slab surface during quenching, more niobium precipitated in the slab interior. The calculations match closely with the fractions measured at slab surface, but predict higher values at the slab interior. The predicted fraction increase from the surface to the centerline is just opposite to the measurements.

The mismatches with size measurements may arise for many different reasons. Segregation likely causes local enrichment of the solute concentration field during solidification, which is greater towards the slab interior, when macrosegregation is considered. A calculation for similar temperature profiles has been done, and the precipitate size in the slab interior is shown to increase due to segregation [255]. In addition, diffusion is much faster along the grain boundaries than in the steel matrix, which could cause a larger precipitate size than predicted, but is not considered in the current work. MnS is likely to form in liquid during solidification due to heavy segregation of sulfur, leaving large MnS particles to act as cores for heterogeneous nucleation and leading to larger precipitates.

The mismatch may be also caused by inaccurate temperature predictions since no reliable measurement is available, and the heat transfer model CON1D has not been validated for this caster. The predicted temperature might be a little low, leading to overprediction of the precipitated amount. The experiments perhaps have uncertainties themselves. Small particles could easily flow through the filter and escape, so that the precipitated amount could be underestimated. Indeed, it is likely that particle agglomeration is needed to explain why the measurement is as large as it is. The center may be quenched slow, as predicted in calculation. But the center and surface sample regions may alternatively have been taken from the exposed surface, and thus experienced similar rapid cooling rates.

Although water quenching is generally thought to be an effective tool to “lock-in” the precipitate properties at high temperature, the current simulation suggests that this may not always be true, especially for the inside of thick samples. This is because precipitation is greatly accelerated during the γ→α phase transformation due to the much lower solubility limits and the much higher diffusion rates in ferrite [149, 150]. This agrees with the findings of Simoneau *et al* , who pointed out that a significant fraction of the remaining niobium will precipitate during the γ→α transformation, even for cooling rates as high as 100^{o}C/s [21]. Thus, it is important that

minimum-sized samples be taken from an exposed surface of a cropped sample, and that the actual sample location and cooling conditions are recorded and taken into account via modeling during the analysis phase.

6.3.4 Grain Growth

The austenite grain growth model in chapter 5 is applied to calculate the evolution of grain size. The PDAS for surface, columnar and centerline regions are determined as 192μm, 470μm and 585μm separately according to Eq. (5.16) and cooling rates of 470^{o}C/s, 5.66^{o}C/s and 1.96^{o}C/s from CON1D results. The calculations start from the temperature of 1381.8^{o}C when austenite is completely transformed.

The calculated histories of austenite grain size at different locations are shown in Figure 6.12. The smallest grain size is found in the slab surface due to its much higher cooling rate and lower temperature relative to elsewhere in the casting. The grain size of the columnar region is predicted to be higher than that of the centerline because it transforms to austenite earlier and has more time to grow. Without consideration of precipitates, the grains sizes from the surface to the centerline are approximately 0.58mm, 1.09mm and 0.96nm before entering the tunnel furnace. The grains at all locations experience enough time to grow in size considerably during reheating, and have similar kinetics as temperature within the slabs equilibrates. The grains stop growing shortly after quenching because of the quickly decreasing mobility of grain boundaries with lowing temperature. All of the austenite grains have a final size of ~ 2.5mm after reheating and quenching at all 3 locations. In the presence of precipitates, grain growth is completely inhibited once the grain becomes larger than the critical size for precipitate pinning, which is predicted by Eq. (5.9) for the calculated size distributions of (Ti,Nb)(C,N) from the multiphase model. By safely assuming that precipitates with radius larger than 2nm can exert pinning effect, the calculations clearly show that the precipitates are effective to inhibit the grain growth at all 3 locations during reheating, with final predicted sizes of 0.445mm, 1.013mm, 0.905mm for the slab surface, middle, and center. The limiting grain sizes predicted by Eq. (5.9) are also plotted in Figure 6.12. They sharply decrease once precipitates start to form, and slightly increase during reheating as coarsening of the precipitates lowers their effectiveness. A decrease of the limiting size is observed at the beginning of quenching because of the formation of some new fine precipitates, which are most effective to inhibit grain growth. Since the limiting grain sizes are

smaller than their real sizes, grain growth stops, and the calculated grain sizes are all kept constant during reheating and quenching. These grain-size refinements due to precipitate pinning are generally beneficial to improve properties of the final product after rolling.

From these results of precipitation and grain growth, the ductility can be determined by empirical formulae from experiments. For high Mn (1-1.4%) steels with S levels larger than 0.005%, Mintz suggested that RA is a function of grain size, interparticle spacing, precipitate size and strain rate [59], as follows

$$\text{Min. RA\%} = 700D^{-1/2}(1-4.3s^{-1/2}) + 20(\log\dot{\varepsilon} + 2.5) \quad \textbf{(6.1)}$$

where D is grain diameter in μm, s is the sum of interparticle spacing and particle diameter of precipitate in nm, and $\dot{\varepsilon}$ is the strain rate in s^{-1}. An increase of precipitated amount or a decrease of precipitate size both causes the value of s to decrease, thus a lower value of RA is predicted. Other relationships between RA and steel composition were also given in previous work [57].

The strain to fracture, or the critical strain is related to the RA values (%) by the following equation [256]

$$\varepsilon_c = \ln\left(\frac{100}{100 - RA}\right) \quad \textbf{(6.2)}$$

The strain and strain rate on the slab surface are reported to be roughly 2% and 10^{-3}-10^{-4}/s in conventional continuous casting [257]. For this range of strain rate and a austenite diameter of 500μm, the minimum RA predicted by Eq. (6.1) is always smaller than 20% for any amount and size of precipitates. Transverse cracks might form with such a low docility.

A better prediction of crack formation requires a complete thermal-stress analysis. The susceptibility to transverse cracks could be determined by checking whether the strain is larger than the critical value at locations of interest. This could offer a framework for the development of better quality control for steel processes in the future. In practical continuous casting processes, the straightening temperature should be chosen to be outside the region of low ductility, which is greatly affected by precipitate formation.

6.4 Tables and Figures

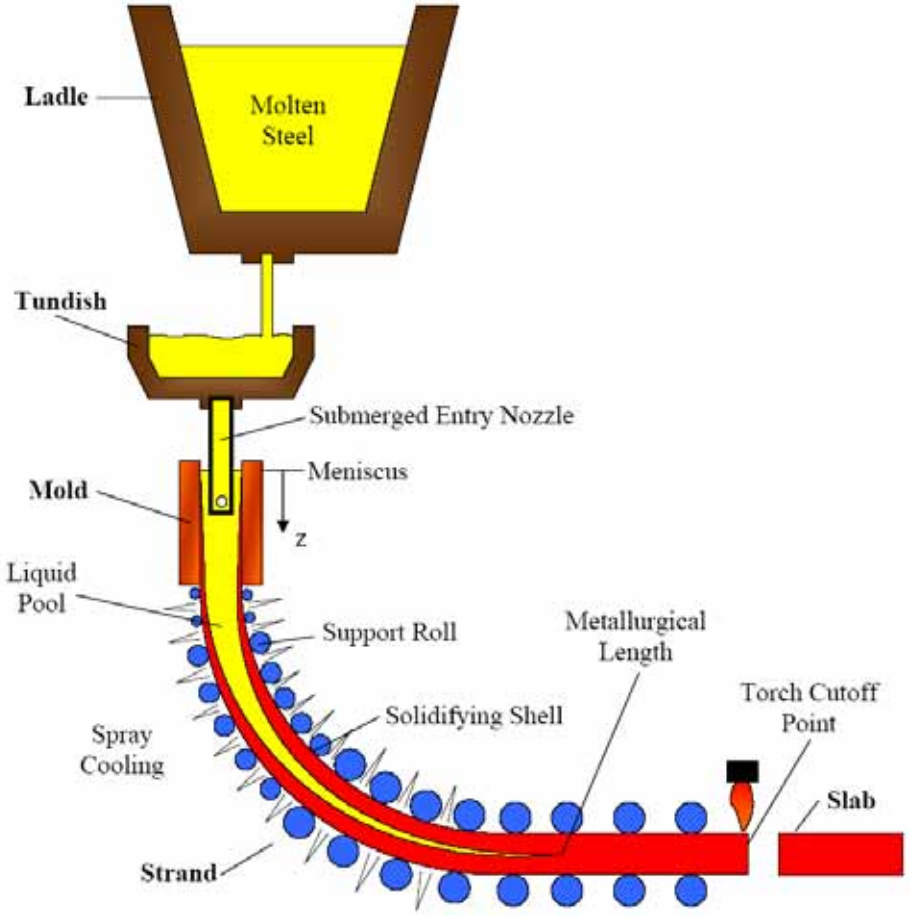

Figure 6.1: Schematic of continuous casting process

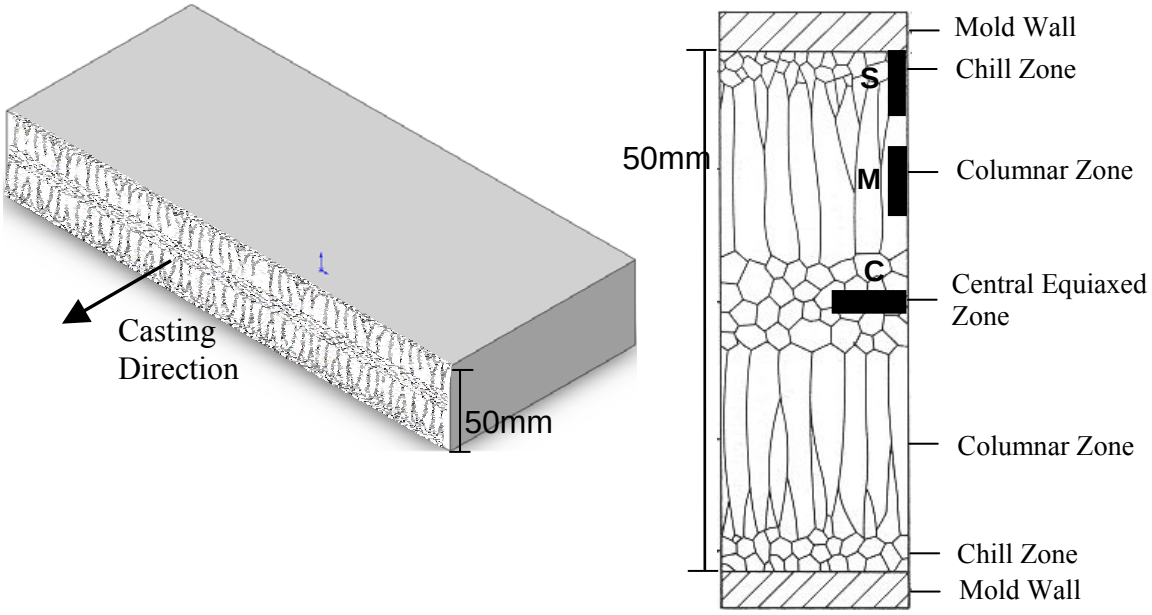

Figure 6.2: Solidification regions and sample orientations within cast slab [250, 251]

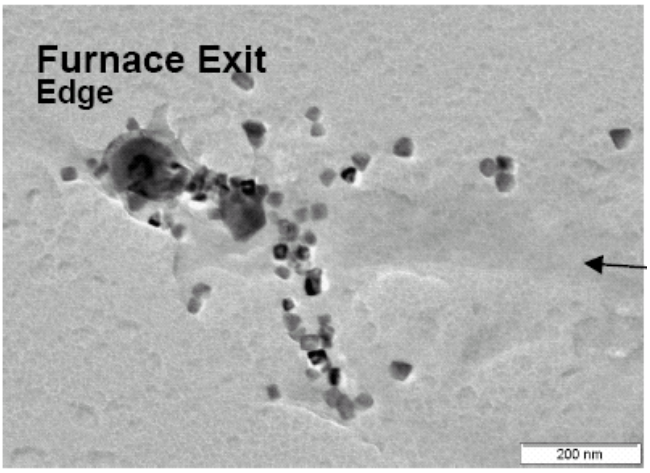

Figure 6.3: TEM analysis of precipitates in the slab edge/surface sample quenched after reheat furnace exit [251]

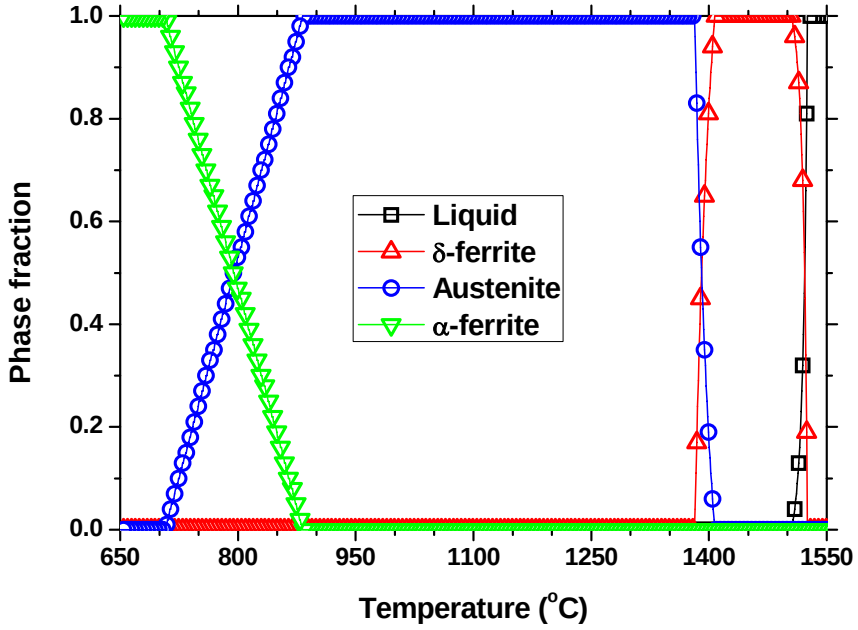

Figure 6.4: Evolution of phase fractions with temperature for experimental steel

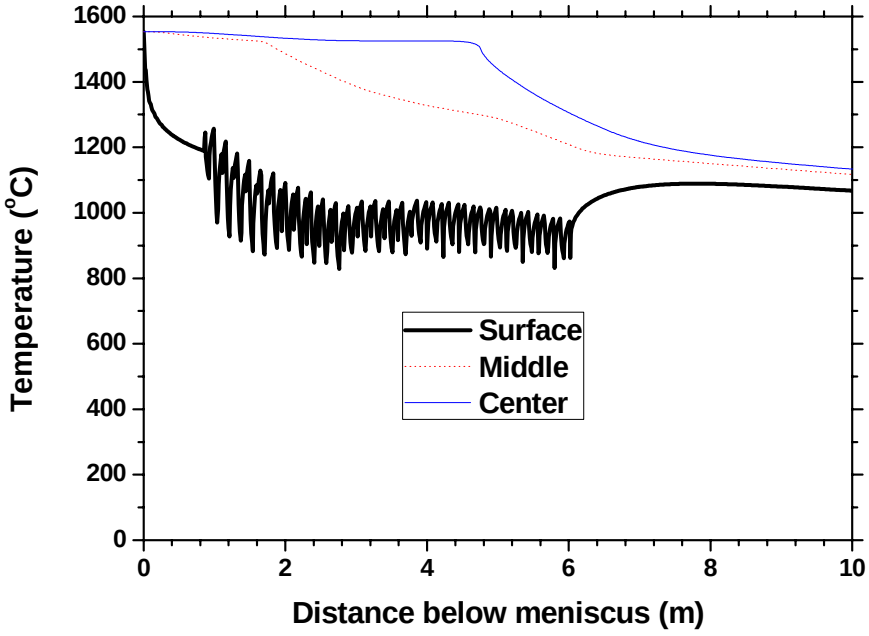

(a). In caster region

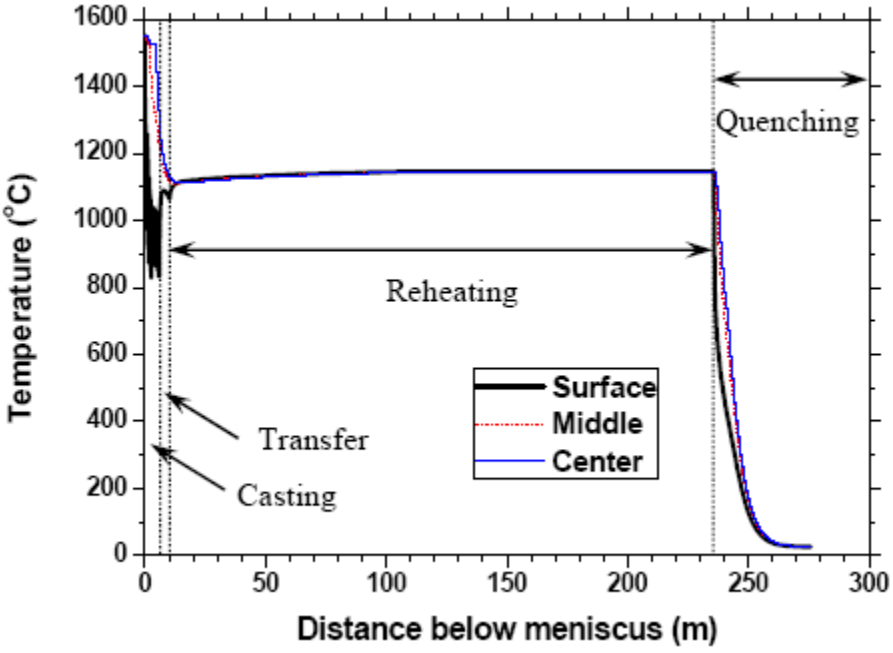

(b). In reheating furnace

Figure 6.5: Calculated temperature history in continuous casting

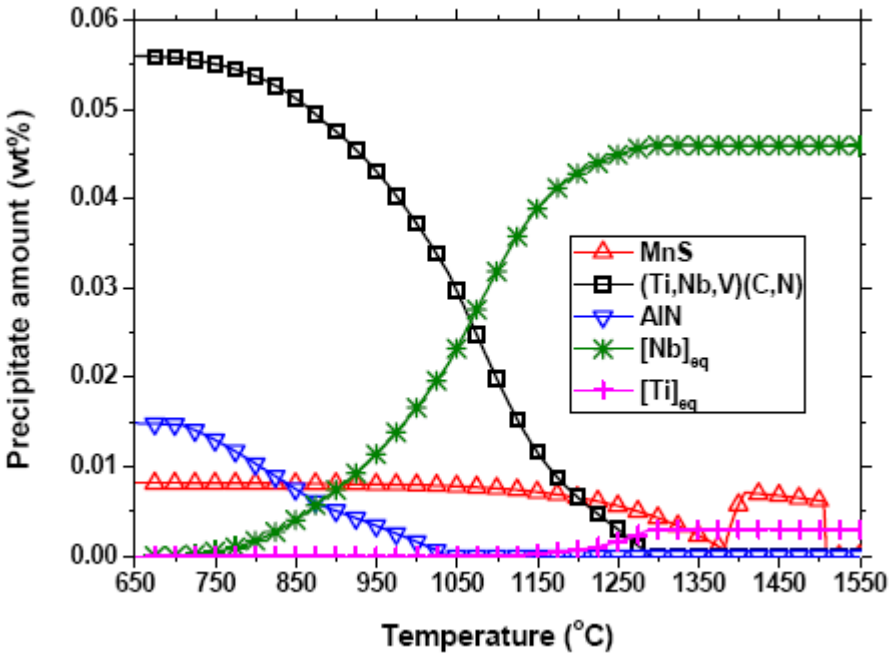

(a). Precipitate phases and amounts

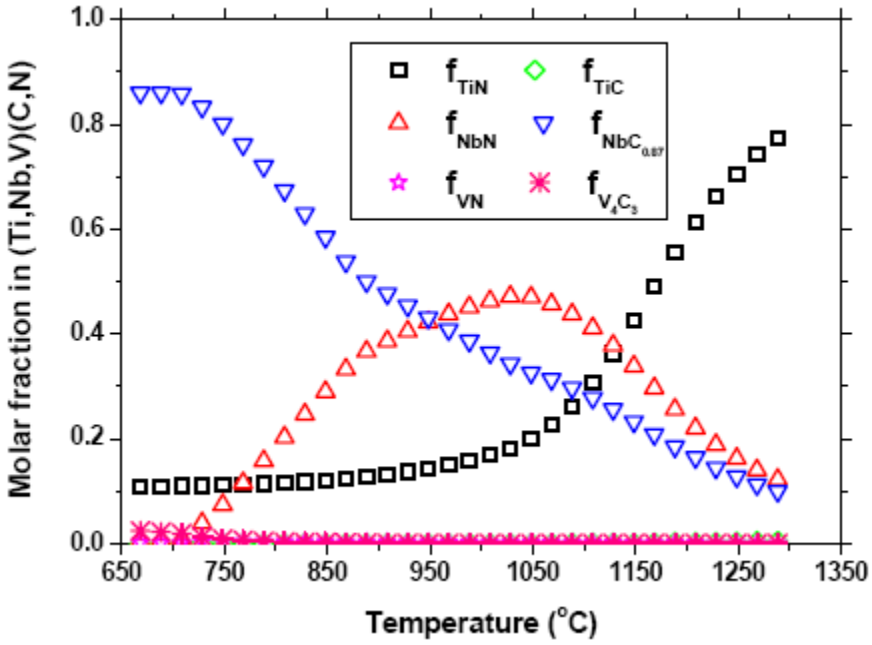

(b). Molar fractions in mixed (Ti,Nb,V)(C,N) precipitates

Figure 6.6: Equilibrium calculation of high Nb steel

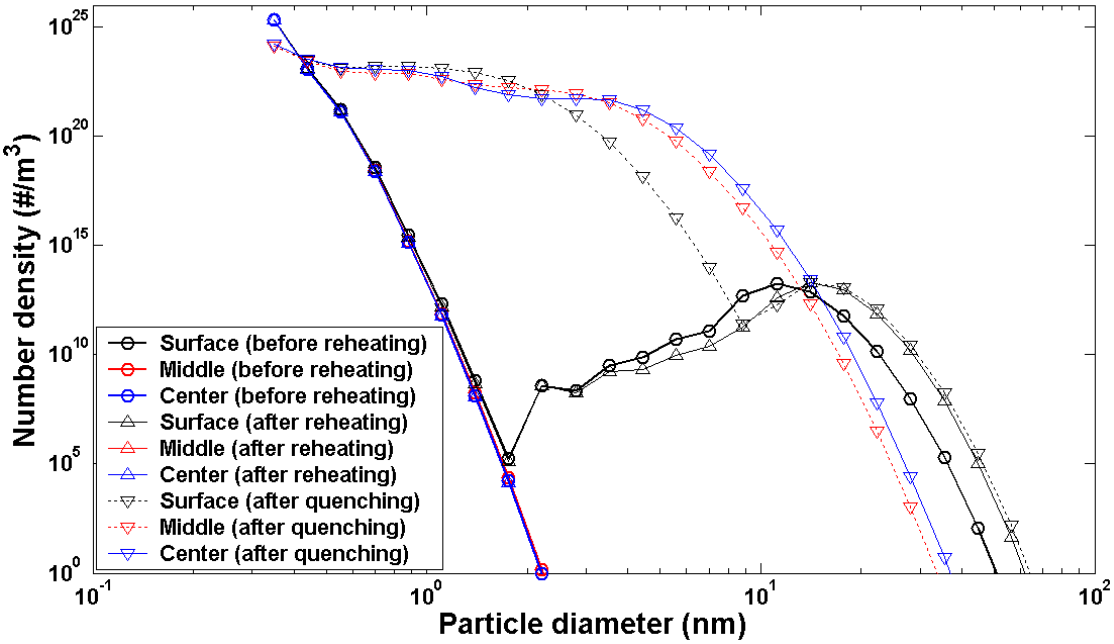

Figure 6.7: Calculated particle size distribution evolution of Nb(C,N) during processing by single-phase model

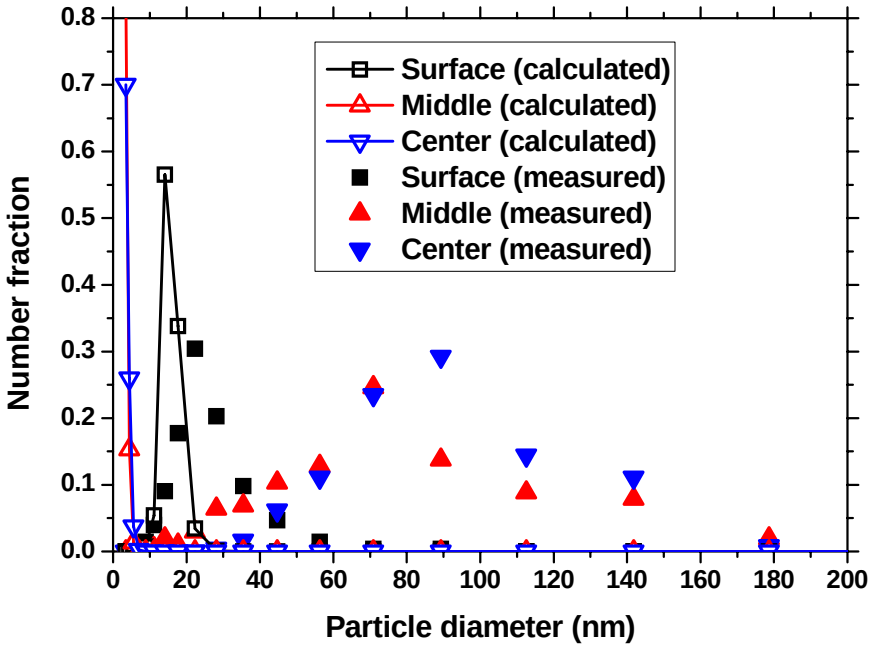

Figure 6.8: Comparison of size distributions from measurement and calculated Nb(C,N) results by single-phase model

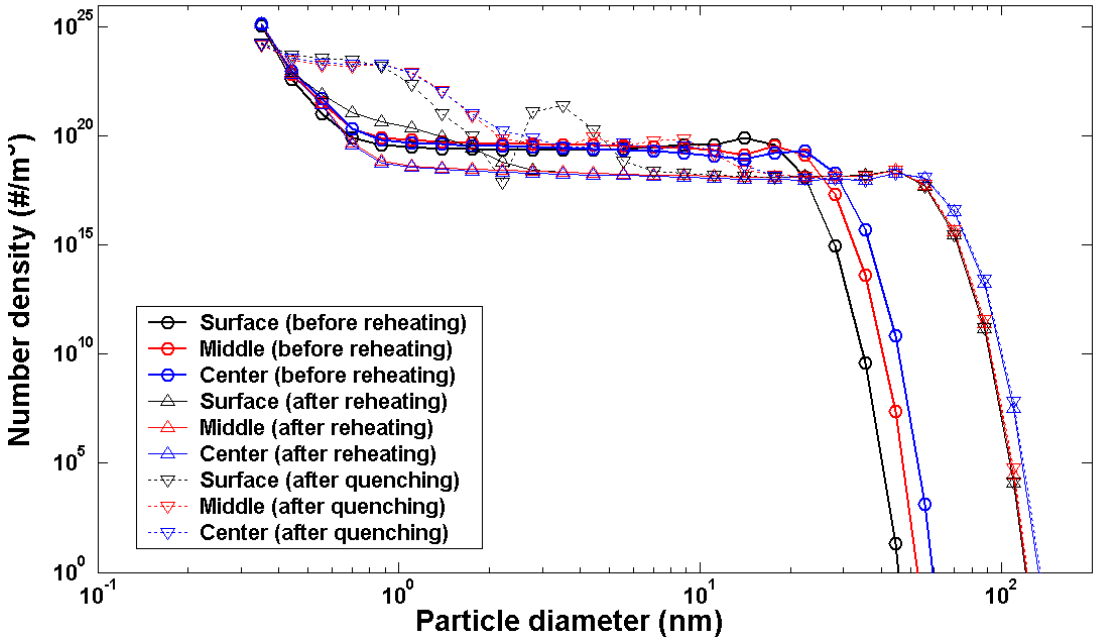

Figure 6.9: Calculated particle size distribution evolution of (Ti,Nb)(C,N) during processing by multiphase model

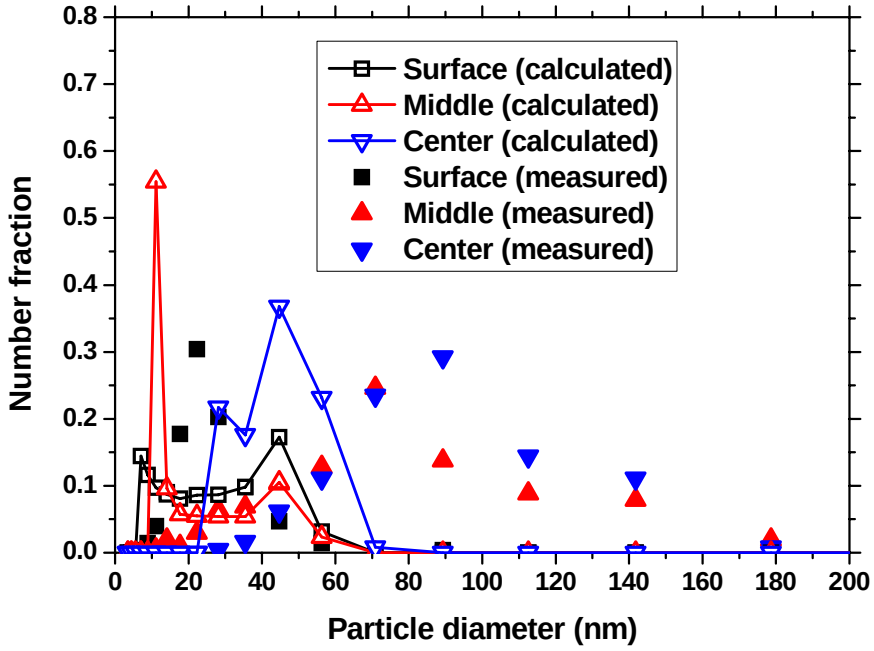

Figure 6.10: Comparison of size distributions from measurement and calculated (Ti,Nb)(C,N) results by multiphase model

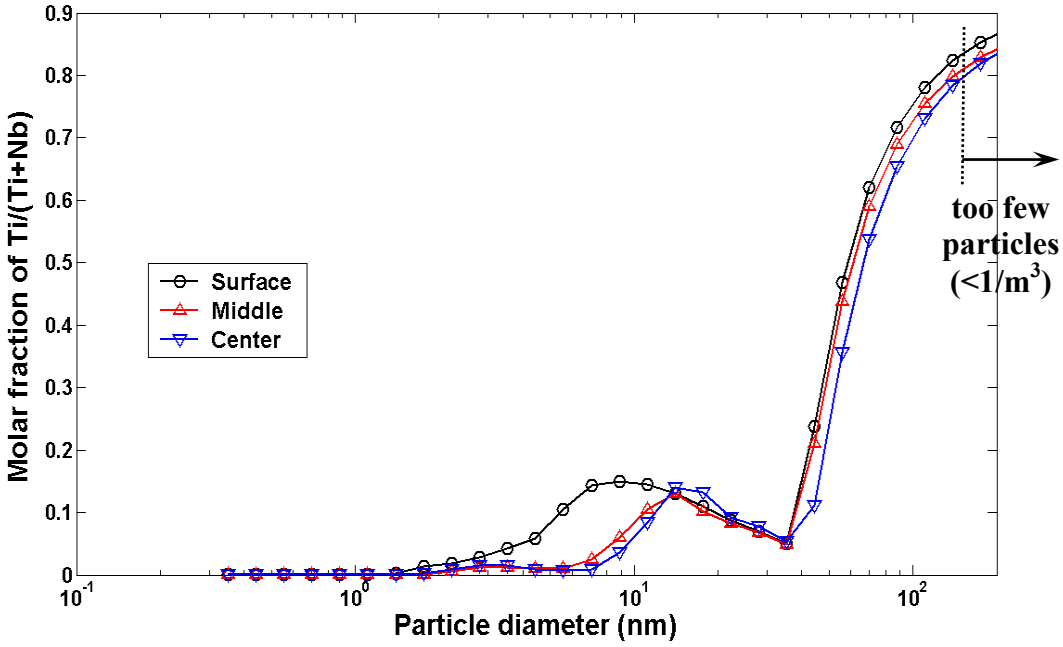

Figure 6.11: Calculated molar fraction of Ti/(Ti+Nb) for different size of (Ti,Nb)(C,N) particles by multiphase model after reheating and quenching

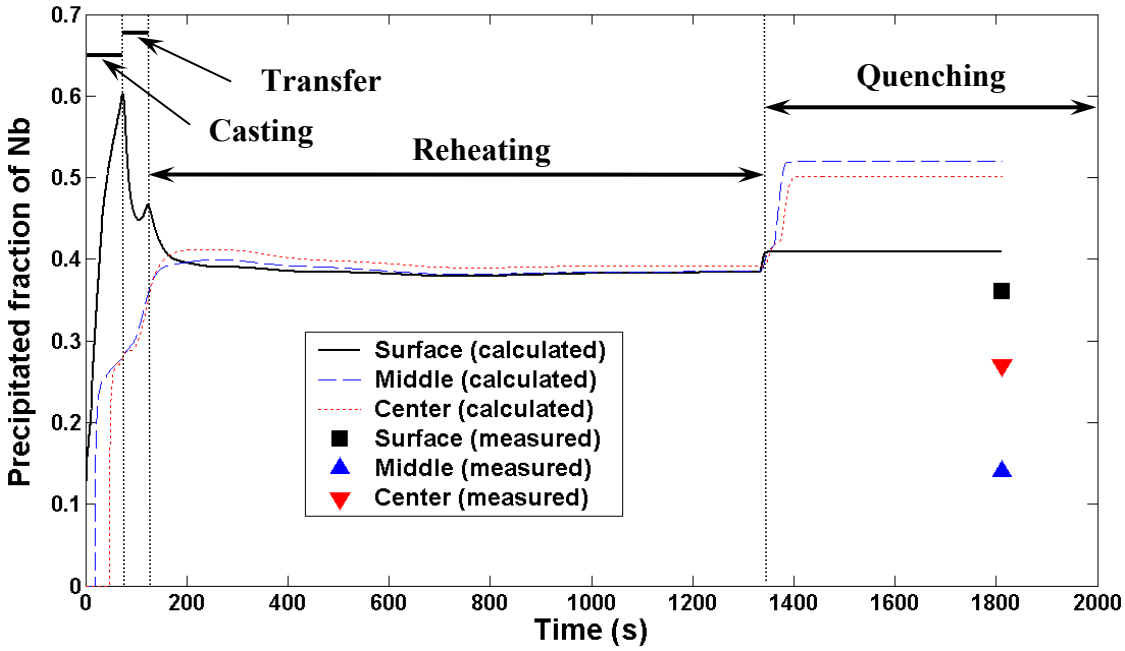

Figure 6.12: Calculated and measured precipitated fraction of Nb of slab

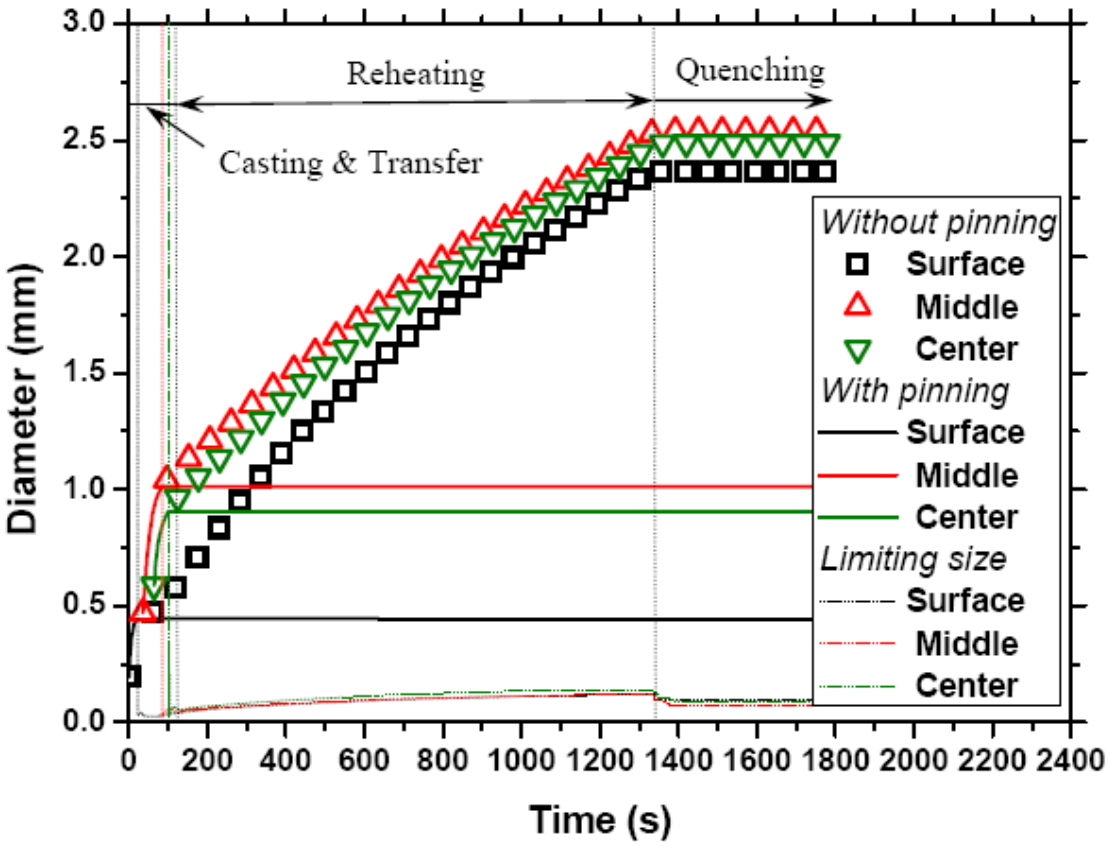

Figure 6.13: Grain size prediction showing the effectg of precipitates

CHAPTER 7
SUMMARY AND FUTURE WORK

A comprehensive set of models has been developed to determine precipitate formation during steel processing for the given compositions and cooling practice, based on a quantitative prediction of the microstructure evolution. They include an equilibrium precipitation model to predict the amounts and compositions of the precipitates at equilibrium, and kinetic models for single-phase and multiphase precipitation based on a PSG method to predict the amount and size distribution evolution of the precipitates.

The thermodynamic solubility-product-based equilibrium model has been first applied to predict equilibrium precipitation behavior in microalloyed steels. This model calculates the solubility limits of 18 common precipitates, including the Wagner interaction effect, mutual solubility effect, and complete mass conservation of all 13 alloying elements during precipitation. The model is validated by matching with analytical solutions, the commercial package JMatPro, and experimental measurements of precipitate amounts, types and compositions.

The equilibrium precipitation model demonstrates the impact of mutual solubility. For mutually exclusive precipitates, the formation of a precipitate phase may delay the formation and decrease the equilibrium amount of other precipitates when they share some alloying elements. However, this result tends to reverse for mutually soluble precipitates, which experience decreased equilibrium activities.

For modeling kinetic behavior, a new, efficient PSG population-balance method for diffusion-controlled single-phase precipitation has been developed. The method features geometrically-based thresholds between each size group, reasonable estimates of border values in order to accurately include intra-group and inter-group diffusion, and an efficient implicit solution method to integrate the equations. The accuracy and exponentially tremendous computational time-efficiency of this method have been validated by comparing with exact solutions of the original population balance equations. It enables accurate and realistic modeling of non-equilibrium precipitation processes at reasonable computational cost.

The new PSG method can simulate incubation, nucleation, growth, and coarsening as one continuous and competing process over a wide size range, with no explicit laws or fitting parameters required. This method is applied to compute the precipitated fraction, size

distribution and PTT diagram, and show encouraging agreement with previous experimental measurements. Precipitation in ferrite is found to be greatly accelerated due to the lower solubility limit and higher diffusion rate in ferrite. The predicted time evolution of the precipitate size distribution results exhibit trends of critical size, number, and slope that are consistent with classical nucleation, growth, and coarsening theories.

The kinetic model of single-phase precipitation is generalized to predict multiphase precipitation to incorporate more realistic heterogeneous complex/mixed precipitates. The corresponding population balance and PSG equations are developed, including mutually-exclusive precipitates and mutually-soluble precipitates. The movement of each precipitate is tracked to conserve its mass. The models are validated with extreme cases, and by matching with exact solutions of the population balance equations.

From the result of the previous precipitation model, a kinetic model for austenite grain growth is applied to predict the evolution of austenite grain size in the presence of precipitates, and the inhibiting effect of the precipitates on grain growth. This model starts when austenite first forms, assuming that initial grain size equals the primary dendrite arm spacing, and calculates the evolution of average austenite grain size with grain boundary pinning according to the precipitate size distribution.

Combined with a transient macroscopic heat transfer model, CON1D, which is applied to calculate the histories of temperature and steel phases within the entire slab for commercial steel grades and practical casting processes, the models developed in this work are applied together to simulate the evolution of precipitate composition, size distribution and grain size. The predictions compare with experimental measurements in samples from the continuous cast product. The calculation results of (Ti,Nb)(C,N) by multiphase model shows that more stable TiN phases precipitate first at high temperature, and acts as heterogeneous nucleation and growth sites for the further precipitation of niobium. Compared with results of the single-phase model for Nb(C,N), the calculated multiphase precipitate size distribution is much larger. This calculated precipitate size distribution matches the increasing trend of precipitate size from the slab surface to the center, and are much closer to experimental measurements. The precipitates are predicted to inhibit austenite grain growth in the reheating furnace, which may be beneficial to rolled product. The potential importance of precipitation during specimen acquisition (associated with quenching) is highlighted by the model predictions.

This powerful methodology has a broad range of potential applications in predicting precipitate formation and grain growth during thermal processing of metal alloys. By further incorporation of segregation models, stress analysis, empirical formulae of ductility and failure, the models in this work would take another step towards the fundamental prediction and prevention of important practical problems such as the formation of transverse cracks in microalloyed steel.

In summary, new fundamental models of equilibrium and non-equilibrium precipitation have been developed and extensively validated. These models, combined together with heat transfer, grain growth, and other models, are successfully applied to predict precipitation and grain size evolution during thermal processing of microalloyed steel. This work is a first step to quantitatively predict microstructure, material properties such as ductility, and crack formation during materials processing. To achieve this, more improvements and further validation of the models of this work are still necessary.

Future work to improve the model is suggested to include:

1). Microsegregation may be important, which could cause more precipitation to occur in the area of highly enriched solutes both during and after solidification. The precipitate growth under this circumstance is greatly enhanced by rapid liquid-phase diffusion, and perhaps also by collision, so a much larger precipitate size should be obtained. The collision PSG model suggested in section 3.2.1 is reasonable to be added into the set of models. The remaining concentrations of elements in solid are also reduced after precipitation, which should be tracked and input to calculate the diffusion-controlled precipitation in the solid.

2). At grain boundaries, many different phenomena cause different precipitation behavior. Microsegregation, increased vacancy concentration and higher diffusion rates all cause the easy formation of much coarsened particles. The interface energy on grain boundaries is likely very different from the precipitate/matrix values in this work, and the curvature effect on nearby concentration in the Gibbs-Thomson equation is maybe proportional to the grain size, instead of particle size. Both fast short-circuit diffusion along grain boundaries and the slow bulk diffusion of atoms from the grain interior to the grain boundaries happens simultaneously, which may contribute to a much larger precipitate size often observed at grain boundaries. All of these make precipitation models at grain boundaries necessary.

3). The thermodynamic models in this work are encouraged to be combined with stress analysis, which would calculate the strain rate, strain and stress during the thermal processing. The ductility could be determined from the results of precipitate formation, grain growth and stress analysis by empirical formula applied at different locations. The stress/strain could be compared to check whether a critical value is exceeded for the calculated low ductility, to provide quantitative clues to prevent transverse cracks of steel slabs.

4). Transverse cracks are mostly likely to occur under oscillation marks or near corners of slabs. The higher temperature due to heat flow resistance across gap there will result in a faster grain growth rate and a lack of precipitate pinning effect. This may cause local "recrystallization" or abnormal grain growth to form a large grain size and get a poor ductility. When the slabs are in unbending, transverse cracks may form with an overcritical tensile stress and strain. The calculations of temperature profile, precipitation formation and grain size under these sensitive locations are required to better explain this phenomenon.

5). The methods developed in this work can be easily extended to many other material systems and problems. For example, the border value estimation of PSG method can be moved to cluster dynamics to cover a much larger size range with reasonable computation cost. Although this work has mainly been applied to microalloyed steel, there are no doubt that these methods can be applied to simulate precipitation in other systems, such as Al_3Zr and Al_3Sc in aluminum alloys.

APPENDIX A: CALCULATION OF INTERFACIAL ENERGY

The experimental measurements of temperature and orientation dependent interface energy between precipitate and matrix are difficult and rare. The energy of an interphase boundary depends on many parameters, such as the atomic bonding and interfacial misfit within the phases, etc.

According to Turnbull [258] and Jonas [161], the interfacial energy consists of two parts: a chemical part (σ_c) and a structural part (σ_{st}), so that

$$\sigma = \sigma_c + \sigma_{st} \quad \textbf{(A1)}$$

The chemical interfacial energy is estimated from the difference between the energies of bonds broken in the separation process and of bonds made in forming the interface, with only the nearest neighbors considered. As given by Russell [37]

$$\sigma_c = \frac{\Delta E_0 N_s Z_s}{N_A Z_l}(X_P - X_M)^2 \quad \textbf{(A2)}$$

where ΔE_0 is the heat of solution of precipitates in a dilute solution in the matrix, N_s is the number of atoms per unit area across the interface, Z_s is the number of bonds per atom across the interface, Z_l is the coordinate number of nearest neighbors within the precipitate crystal lattice, and X_P and X_M are the molar concentrations of the precipitate-forming element in the precipitate (P) and matrix (M) phase respectively. ΔE_0 is estimated to equal $-\Delta H$, the heat of formation of the precipitate. X_P=0.5 and $X_P >> X_M$.

Merwe [259] presented a calculation of structural energy for a planar interface. When the two phases have the same structure and orientation, but different lattice spacing, the mismatch may be accommodated by a planar array of edge dislocations. Including the strain energy in both crystals, σ_{st} is given as

$$\sigma_{st} = \frac{\mu_I \bar{c}}{4\pi^2}\left\{1+\beta-(1+\beta^2)^{1/2}-\beta\ln\left[2\beta(1+\beta^2)^{1/2}-2\beta^2\right]\right\} \quad \textbf{[A3]}$$

with $\frac{2}{\bar{c}} = \frac{1}{c_M^e} + \frac{1}{c_P^e}$, $\beta = 2\pi\delta\frac{\lambda_+}{\mu_I}$, $\frac{2}{\mu_I} = \frac{1}{\mu_M} + \frac{1}{\mu_P}$,

$$\delta = \frac{2\left|c_M^e - c_P^e\right|}{c_M^e + c_P^e}, \quad \frac{1}{\lambda_+} = \frac{1-\nu_M}{\mu_M} + \frac{1-\nu_P}{\mu_P} \quad \textbf{[A4]}$$

where c_M^e and c_P^e are the nearest-neighbor distance across the interface, which are estimated from the lattice parameters c_M, c_P and interface orientations, $\overline{c}$ is the spacing of a reference lattice across the matrix/precipitate interface. μ_M, μ_P and μ_I are shear moduli in the matrix (M), precipitate (P) and interface (I) respectively; ν_M and ν_P are Poisson's ratios. δ is the lattice misfit across the interface.

The crystallographic relationships between the f.c.c. (TiN, TiC, NbN, NbC, VN, VC, MnS) and h.c.p. (AlN) precipitate, and steel matrix austenite phase (f.c.c.) or ferrite phase (b.c.c.) are chosen as

Highest planar density orientation: $(111)_{f.c.c.}//(111)_{\gamma-Fe}$ [37, 161]

Baker-Nutting orientation: $(100)_{f.c.c.}//(100)_{\alpha-Fe}$ [260]

Shoji–Nishiyama orientation: $(0001)_{h.c.p.}//(111)_{\gamma-Fe}$ [261, 262]

Burgers orientation: $(0001)_{h.c.p.}//(110)_{\alpha-Fe}$ [263]

For γ-Fe (111) plane, $Z_s^{\gamma-Fe}=3$ and $N_s^{\gamma-Fe}=4/(\sqrt{3}c_{\gamma-Fe}^2)$. For α-Fe, (100) plane $Z_s^{\alpha-Fe}=4$, $N_s^{\alpha-Fe}=1/c_{\alpha-Fe}^2$, and (110) plane $Z_s^{\alpha-Fe}=4$, $N_s^{\alpha-Fe}=\sqrt{2}/c_{\alpha-Fe}^2$. For both f.c.c. and h.c.p. precipitate structures, $Z_l=12$. The elastic properties and heat of formation of iron and various precipitates are listed in Table A1 and A2. The lattice parameters of austenite and ferrite are $c_{\gamma-Fe}(nm)=0.357$ and $c_{\alpha-Fe}(nm)=0.286$ [36], and of various precipitates are listed in Table 2.1.

The calculated interfacial energies between different precipitates and steel matrix are shown in Figure A1. It shows that interfacial energy decreases slightly as temperature increases because of lower heat of formation and shear modulus.

Some errors are introduced by this model itself. For example, complete interactions between chemical bonds of iron, metal and interstitial element of precipitate phase are not considered. Only bonds of nearest neighbors are counted, which ignores the influence of second nearest neighbors and others with longer distance. The dislocation may relax lattice mismatch, and reduce the structural part of interface energy, which is not expressed in this model. But the result of this model still gives a reasonably first approximation when the available measurements are not available.

Table A1: Elastic properties of iron and various precipitates

Parameters	Values	Ref.
$\mu_{\gamma\text{-Fe}}$ (Mpa)	$8.1\times10^4\left[1-0.91(T-300)/1810\right]$	[264]
$\mu_{\alpha\text{-Fe}}$ (Mpa)	$6.92\times10^4\left[1-1.31(T-300)/1810\right]$	[264]
μ_{TiN} (Mpa)	21.3×10^4	[265]
μ_{TiC} (Mpa)	$19.3\times10^4\left[1-0.18(T-300)/3523\right]$	[264]
μ_{NbN} (Mpa)	15.6×10^4	[266]
μ_{NbC} (Mpa)	$13.4\times10^4\left[1-0.18(T-300)/3613\right]$	[264]
μ_{VN} (Mpa)	15.9×10^4	[266]
μ_{VC} (Mpa)	$12.7\times10^4\left[1-0.27(T-300)/2921\right]$	[264]
μ_{MnS} (Mpa)	4.5×10^4	[269]
μ_{AlN} (Mpa)	12.7×10^4	[265]
$\nu_{\gamma\text{-Fe}}$	0.29	[168]
$\nu_{\alpha\text{-Fe}}$	0.29	[168]
ν_{TiN}	0.21	[265]
ν_{TiC}	0.204	[268]
ν_{NbN}	0.27	[266]
ν_{NbC}	0.194	[268]
ν_{VN}	0.25	[266]
ν_{VC}	0.26	[268]
ν_{MnS}	0.30	[267]
ν_{AlN}	0.23	[265]

Table A2: Heat of formation of various precipitates

Precipitate	$-\Delta H$ (KJ·mol^{-1})	Ref.
TiN	$356.77 - 5.04\times10^{-2}T - 2.98\times10^{-7}T^2 - 1210/T$	[269]
TiC	$206.77 - 5.57\times10^{-2}T + 4.07\times10^{-6}T^2$	[268]
NbN	$235.1 - 3.90\times10^{-2}(T - 298.15)$	[270]
NbC	$157.76 - 4.54\times10^{-2}T - 3.84\times10^{-6}T^2$	[268]
VN	$233.49 - 4.39\times10^{-2}T - 5.61\times10^{-6}T^2 - 815.7/T$	[269]
VC	$116.50 - 3.84\times10^{-2}T - 6.90\times10^{-6}T^2 - 815.7/T$	[271]
MnS	$203.4 + 1.114\times10^{-2}T - 1.73\times10^{-5}T^2$	[272]
AlN	$341.32 - 4.98\times10^{-2}T - 1.12\times10^{-6}T^2 - 2813/T$	[268]

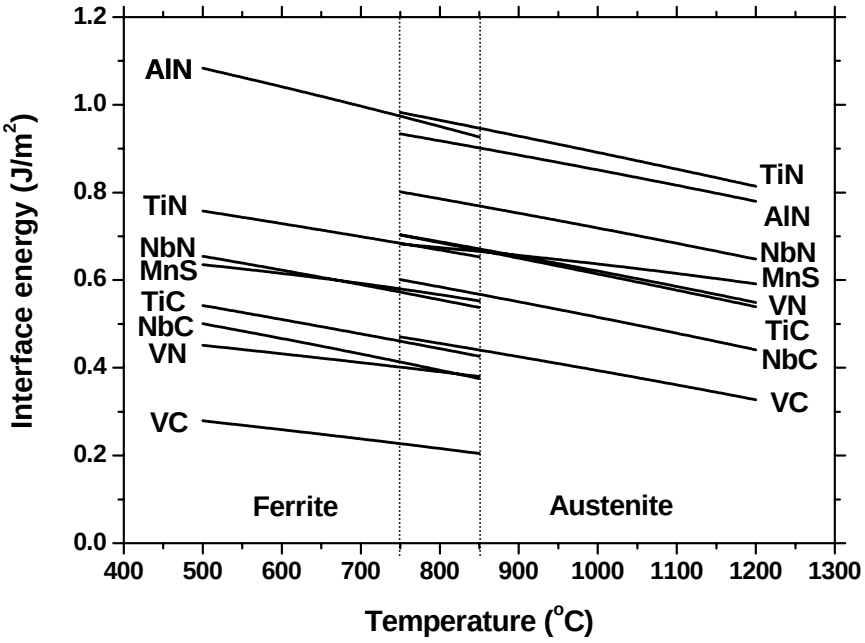

Figure A1: Calculated interfacial energies associated with various precipitates

REFERENCES

1. S. C. Park, I. H. Jung, K. S. OH and H. G. LEE, "Effect of Al on the Evolution of Non-Metallic Inclusions in the Mn-Si-Ti-Mg Deoxidized Steel during Solidification: Experiments and Thermodynamic Calculations", *ISIJ International*, 2004, vol. 44, pp. 1016-1023.

2. J. A. Garrison, J. G. Speer, D. K. Matlock and K. P. Williams, "Aluminum Nitride Precipitation Behavior in Thin Slab Material", *AIST 2005 Proceeding*, volume II, June 2005, pp. 107-116.

3. Y. Li, J. A. Wilson, D. N. Crowther, P. S. Mitchell, A. J. Craven and T. N. Baker, "The Effects of Vanadium, Niobium, Titanium and Zirconium on the Microstructure and Mechanical Properties of Thin Slab Cast Steels", *ISIJ International*, 2004, vol. 44, pp. 1093-1102.

4. M. Charleux, W. J. Poole, M. Militzer and A. Deschamps, "Precipitation Behavior and Its Effect on Strengthening of an HSLA-Nb/Ti Steel", *Metallurgical and Materials Transactions A*, 2001, vol. 32A, pp. 1635-1647.

5. F. Perrard, P. Nonnadieu, A. Deschamps, P. Barges, "TEM Study of NbC Heterogeneous Precipitation in Ferrite", *Philosophical Magazine*, 2006, vol. 86, pp. 4271-4284.

6. C. Zener (quoted by C.S. Smith), "Grain, Phases, and Interfaces: an Interpretation of Microstructure," *Transaction of the American Institute Mining and Metallurgical Engineerings*, 1948, vol. 175, pp. 15-51.

7. B. G. Thomas, J. K. Brimacombe and I. V. Samarasekera, "The Formation of Panel Cracks in Steel Ingots: a State-of-the-art Review, I. Hot Ductility of Steel," *ISS Transactions*, 1986, vol.7, pp. 7-20.

8. E. S. Szekeres, "A Review of Strand Casting Factors Affecting Transverse Cracking", *Proceedings of 6th International Conference on Clean Steel*, Balatonfüred, Hungary, June 2002, pp. 324-338.

9. L. Zhang and B. G. Thomas, "State of the Art in the Control of Inclusions during Steel Ingot Casting", *Metallurgical and Materials Transactions B*, 2006, vol. 37, pp. 733-761.

10. Z. Hu and Z. Yang, "Identification of the Precipitates by TEM and EDS in X20CrMoV12.1 after long-Term Service at Elevated Temperature", *Journal of Materials Engineering and Performance*, 2003, vol. 12, pp. 106-111.

11. N. E. V. Díaz, S. S. Hosmani, R. E. Schacherl and E. J. Mittemeijer, "Nitride Precipitation and Coarsening in Fe-2.23at.% V Alloys: XRD and (HR)TEM Study of Coherent and Incoherent

Diffraction Effects Caused by Misfitting Nitride Precipitates in a Ferrite Matrix", *Acta Materialia*, 2008, vol. 56, pp. 4137-4149.

12. H. F. Beeghly, "Determination of Aluminum Nitride Nitrogen in Steel", *Analytical Chemistry*, 1949, vol. 21, pp. 1513-1519.

13. A. L. Rivas, D. K. Matlock and J. G. Speer, "Quantitative Analysis of Nb in Solution in a Microalloyed Carburizing Steel by Electrochemical Etching", *Materials Characterization*, 2008, vol. 59, pp. 571-577.

14. M. Takeda, N. Suzuki, G. Shinohara, T. Endo and J. Van Landuyt, "TEM Study on Precipitation Behavior in Cu-Co Alloys", *Physica Status Solidi A*, 1998, vol. 168, pp. 27-35.

15. O. Sariano-Vargas, M. L. Saucedo-Muñoz, V. M. Lopez-Hirata and A. D. Paniagua-Mercadi, "Coarsening of β' Precipitates in an Isothermally-Aged Fe_{75}-Ni_{10}-Al_{15} Alloy", *Materials Transactions*, 2010, vol. 51, pp. 442-446.

16. R. Uemori, R. Chijiiwa, H. Tamehiro and H. Morikawa, "AP-FIM Study on the Effect of Mo Addition on Microstructure in Ti-Nb Steel", *Applied Surface Science*, pp. 255-260.

17. K. A. Pischow, A. K. Haraldsen and A. S. Korhonen, "Scanning Tunneling Microscopy Study of Precipitates in a Microalloyed Steel", *Materials Characterization*, 1993, vol. 31, pp. 69-75.

18. M. De La Garzam T. R. Yáñez, R. Colás and Y. Houbaert, "Study of Precipitates Formed in a Wrought Aluminum Alloy by Means of Atomic Force Microscopy", *Materials Characterization*, 2001, vol. 47, pp. 397-400.

18. W. R. Bandi and G. Krapt, "Differential Thermal Analysis – Evolved Gas Analysis for the Determination of Carbide and Nitride Phases in Steel", *Analytical Chemistry*, 1977, vol. 49, pp. 649-654.

19. A. K. Jena, A. K. Gupta and M. C. Chaturved, "A Differential Scanning Calorimetric Investigation of Precipitation Kinetics in the Al-1.53wt% Cu-0.79wt% Mg Alloy", *Acta Metallurgica*, 1989, vol. 37, pp. 885-895.

20. A. Brahmi and R. Borrelly, "Study of Aluminum Nitride Precipitation in Pure Fe-Al-N Alloy by Thermoelectric Power Measurements", *Acta Materialia*, 1997, vol. 45, pp. 1889-1897.

21. R. Simoneau, G. Bégin and A. H. Marquis, "Progress of NbCN precipitation in HSLA steels as determined by electrical resistivity measurements", *Metal Science*, 1978, pp. 381-386.

22. S. Celotto and T. J. Bastow, “Study of Precipitation in Aged Binary Mg-Al and Ternary Mg-Al-Zn Alloys Using ^{27}Al NMR Spectroscopy”, *Acta Materialia*, 2001, vol. 49, pp. 41-51.
23. R. Schaller and W. Benoit, “Internal Friciton Associated with Precipitation and Recrystallization”, *Journal de Physique Colloques*, 1983, vol. 44, C9-17-C9-27.
24. 1. I. Weiss and J. J. Jonas, “Interaction between Recrystallization and Precipitation during the High Temperature Deformation of HSLA Steels”, *Metallurgical Transactions A*, 1979, vol. 10A, pp. 831-840.
25. W. J. Liu and J. J. Jonas, “A Stress Relaxation Method for Following Carbonitride Precipitation in Austenite at Hot Working Temperature”, *Metallurgical Transactions A*, 1988, vol. 19A, pp. 1403-1413.
26. W. P. Sun, W. J. Liu and J. J. Jonas, “A Creep Technique for Monitoring MnS Precipitation in Si Steels”, *Metallurgical Transactions A*, 1989, vol. 20A, pp. 2707-2715.
27. B. S. Seong, E. Shin, S. H. Choi, Y. Choi, Y. S. Han, K. H. Lee and Y. Tomota, “Quantitative Analysis of Fine Nano-Sized Precipitates in Low-Carbon Steels by Small Angle Neutron Scattering”, *Applied Physics A*, 2010, vol. 99. Pp. 613-620.
28. A. Deschamps, L. David, M. Nicolas, F. Bley, F. Livet, R. Seguela, J. P. Simon, G. Vigier and J. C. Werenskiold, “Recent Developments in Small-Angle X-ray Scattering for the Study of Metals and Polymers”, *Advanced Engineering Materials*, 2001, vol. 3, pp. 579-586.
29. Abaqus (Finite Element Analysis Software, Version 6.11), Simulia Corp., Providence, Rhode Island, USA, 2011.
30. Ansys (Engineering Simulation Software, Version 14.0), Ansys Inc., Canonsburg, Pennsylvania, USA, 2011.
31. N. Yoshinaga, K. Ushioda, S. Akamatsu and O. Akisue, “Precipitation Behavior of Sulfides in Ti-Added Ultra Low-Carbon Steels in Austenite, *ISIJ International*, 1994, vol. 34, pp. 24-32.
32. E. E. Kashif, K. Asakura, T. Koseki and K. Shibata, “Effect of Boron, Niobium and Titanium on Grain Growth in Ultra High Purity 18% Cr Ferritic Stainless Steel”, *ISIJ International*, 2004, vol. 44, pp. 1568-1575.
33. S. C. Park, I. H. Jung, K. S. OH and H. G. Lee, “Effect of Al on the Evolution of Non-Metallic Inclusions in the Mn-Si-Ti-Mg Deoxidized Steel during Solidification: Experiments and Thermodynamic Calculations”, *ISIJ international*, 2004, vol. 44, pp. 1016-1023.
34. Y. Li, J. A. Wilson, D. N. Crowther, P. S. Mitchell, A. J. Craven and T. N. Baker, “The Effect

of Vanadium, Niobium, Titanium and Zirconium on the Microstructure and Mechanical Properties of Thin Slab Cast Steels", *ISIJ International*, 2004, vol. 44, pp. 1093-1102.

35. R. L. Klueh, K. Shiba and M. A. Sokolov, "Embrittlement of Irradiated Ferritic/Martensitic Steels in the Absence of Irradiation Hardening", *Journal of Nuclear Materials*, 2008, vol. 377, pp. 427-437.

36. T. Gladman, "*The Physical Metallurgy of Microalloyed Steels*", The Institute of Materials, London, England, 1997.

37. K. C. Russell, "Nucleation in Solid: the Induction and Steady State Effects", *Advances in Colloid and Interface Science*, 1980, vol.13, pp. 205-318.

38. H. I. Aaronson, C. Laird, K. R. Kinsman, *Phase Transformation*, Edited by H. I. Aaronson, Metals Park, Ohio, American Society of Metals, pp. 313-396.

39. M. Kahlweit, "Ostwald Ripening of Precipitates", *Advances in Colloid and Interface Science*, 1975, vol. 5, pp. 1-35.

40. W. M. Young and E. W. Elcock, "Monte Carlo Studies of Vacancy Migration in Binary Ordered Alloys", *Proceedings of the Physical Society*, 1966, vol. 89, pp. 735-746.

41. E. Clouet, M. Nastar and C. Sigli, "Nucleation of Al_3Zr and Al_3Sc in Aluminum Alloys: from Kinetic Monte Carlo Simulations to Classical Theory", *Physical Review B*, 2004, vol. 69, 064109.

42. C. Hin, B. D. Wirth and J. B. Neaton, "Formation of Y_2O_3 Nanoclusters in Nanostructured Ferritic Alloys during Isothermal and Anisothermal Heat Treatment: A Kinetic Monte Carlo Study", *Physical Review B*, 2009, vol. 80, 134118.

43. R. Mukherjee, T. A. Abinandanan and M. P. Gururajan, "Phase Field Study of Precipitate Growth: Effect of Misfit Strain and Interface Curvature", *Acta Materialia*, 2009, vol. 57, pp. 3947-3954.

44. R. Mukherjee, T. A. Abinandanan and M. P. Gururajan, "Precipitate Growth with Composition-Dependent Diffusivity: Comparison between Theory and Phase Field Simulations", *Scripta Materialia*, 2010, vol. 62, pp. 85-88.

45. Y. Tsukada, A. Shiraki, Y. Murata, S. Takaya, T. Koyama and M. Morinaga, "Phase-Field Simulation of Nucleation and Growth of $M_{23}C_6$ Carbide and Ferromagnetic Phases during Creep Deformation in Type 304 Steel", *Journal of Nuclear Materials*, 2010, vol. 401, pp. 154-158.

46. J. Svoboda, F. D. Fischer, P. Fratzl and E. Kozeschnik, "Modeling of Kinetics in Multi-Component Multi-Phase Systems with Spherical Precipitates I: Theory", *Materials Science and Engineering A*, 2004, vol. 385, pp. 166-174.

47. E. Hozeschnik, J. Svoboda, P. Fratzl and F. D. Fischer, "Modeling of Kinetics in Multi-Component Multi-Phase Systems with Spherical Precipitates II: Numerical Solution and Application", *Materials Science and Engineering A*, 2004, vol. 385, pp. 157-165.

48. E. Kozeschnik, J. Svoboda, R. Radis and F. D. Fischer, "Mean-Field Model for the Growth and Coarsening of Stoichiometric Precipitates at Grain Boundaries", *Modelling and Simulation in Materials Science and Engineering*, 2010, vol. 18, 015011.

49. E. Clouet, A. Barbu, L. Laé and G. Martin, "Precipitation Kinetics of Al_3Zr and Al_3Sc in Aluminum Alloys Modeled with Cluster Dynamics", *Acta Materials*, 2005, vol. 52, pp. 2313-2325.

50. J. Lepinoux, "Modeling Precipitation in Binary Alloys by Cluster Dynamics", *Acta Materials*, 2009, vol. 57, pp. 1086-1094.

51. J. Lepinoux, "Comparing Kinetic Monte Carlo Simulations with Cluster Dynamics: What Can We Learn about Precipitation? Application to AlZr Alloys", *Philosophical Magazine*, 2010, vol. 90, pp. 3261-3280.

52. I. Andersen and Ø. Grong, "Analytical Modeling of Grain Growth in Metals and Alloys in the Presence of Growing and Dissolving Precipitates –I. Normal Grain Growth", *Acta Metallurgica Materialia*, 1995, vol. 43, pp. 2673-2688.

53. C. Bernhard, J. Reiter and H Presslinger, "A model for Predicting the Austenite Grain size at the Surface of Continuously-Cast Slabs", *Metallurgical and Materials Transactions,* 2008, vol. 39B, pp. 885-895.

54. J. K. Brimacombe and K. Sorimachi, "Crack Formation in the Continuous Casting of Steel", *Metallurgical Transactions B*, 1977, vol. 8B, pp. 489-505.

55. B. G. Thomas, J. K. Brimacombe and I. V. Samarasekera, "The Formation of Panel Cracks in Steel Ingots: A stage-of-the-Art Review", *ISS Transactions*, 1986, vol. 7, pp. 7-20.

56. Y. Maehara, K. Yasumoto, H. Tomono, T. Nagamichi and Y. Ohmori, "Surface Cracking Mechanism of Continuously Cast Low Carbon Low Alloy Steel Slabs", *Materials Science and Technology*, 1990, vol. 6, pp. 793-806.

57. B. Mintz, “The Influence of Composition on the Hot Ductility of Steels and to the Problem of Transverse Cracking”, *ISIJ International*, 1999, vpl. 39, pp. 833-855.
58. B. Mintz and R. Abushosa, “Influence of Vanadium on Hot Ductility of Steel”, *Ironmaking and Steelmaking*, 1993, vol. 20, pp. 445-452.
59. D. N. Crowther and B. Mintz, “Influence of Grain Size on Hot Ductility of Plain C-Mn Steels”, *Materials Science and Technology*, 1986, vol. 2, pp. 951-955.
60. B. Mintz, S. Yue and J. J. Jonas, “Hot Ductility of Steels and Its Relationship to the Problem of Transverse Cracking during Continuous Casting”, *International Materials Reviews*, 1991, vol. 36, pp. 187-217.
61. H. G. Suzuki, S. Nishimura, J. Imamura and Y. Nakamura, “Embrittlement of Steels Occurring in the Temperature Range from 1000 to 600^{o}C”, *Transactions of the Iron and Steel Institute of Japan*, 1984, vol. 24, pp. 169-177.
62. Y. Maehara, K. Nakai, K. Yasumoto and T. Mishima, “Hot Cracking of Low Alloy Steels in Simulated Continuous Casting – Direct Rolling Process”, *Transactions of the Iron and Steel Institute of Japan*, 1988, vol. 28, pp. 1021-1027.
63. M. G. Akben, I. Weiss and J. J. Jonas, “Dynamic Precipitation and Solute Hardening in a V Microalloyed Steel and Two Nb Steels Containing High Level of Mn”, *Acta Metallurgica*, 1981, vol. 29, pp. 111-121.
64. M. G. Akben, T. Chandra, P. Plassiard and J. J. Jonas, “Dynamic Precipitation and Solute Hardening in a Titanium Microalloyed Steel Containing Three Level of Manganese”, *Acta Metallurgica*, 1984, vol. 32, pp. 591-601.
65. B. Mintz and J. M. Arrowsmith, “Hot-Ductility Behavior of C-Mn-Nb-Al Steels and Its Relationship to Crack Propagation during the Straightening of Continuously Cast Strand”, *Metals Technology*, 1979, vol. 6, pp. 24-32.
66. T. H. Coleman and J. R. Wilcox, “Transverse Cracking in Continuously Cast HSLA Slabs – Influence of Composition”, *Materials Science and Technology*, 1985, vol. 1, pp. 80-83.
67. Z. Mahamed, “Hot Ductility Behavior of Vanadium Containing Steels”, *Materials Science and Engineering A*, 2002, vol. 326, pp. 255-260.
68. K. Suzuki, S. Mitagawa, Y. Saito and K. Shiotani, “Effect of Microalloyed Nitride Forming Elements on Precipitation of Carbonitride and High Temperature Ductility of Continuously Cast Low Carbon Nb Containing Steel Slab”, *ISIJ International*, 1995, vol. 35, pp. 34-41.

69. E. Takeuchi and J. K. Brimacombe, “Effect of Oscillation-Mark Formation on the Surface Quality of Continuously Cast Steel Slabs”, *Metallurgical Transactions B*, 1985, vol. 16B, pp. 605-625.

70. M. Hidayat and D. Sutrandi, “Improvement of Surface Quality of Continuously Cast Slab of Medium Carbon”, *South East Asia Iron and Steel Institute Quarterly*, 2004, vol. 33, pp. 26-31.

71. J. H. Hildebrand, “Solubility. XIII. Regular Solutions”, *Journal of the American Chemical Society*, 1929, vol. 51, pp. 66-80.

72. O. Redlich and A. T. Kister, “Algebraic Representation of Thermodynamic Properties and Classification of Solutions”, *Industrial and Engineering Chemistry*, 1948, vol. 40, pp. 345-348.

73. Y. M. Muggianu, M. Gambino and L. P. Bros, “Enthalpies of Formation of Liquid Alloy Bismuth-Gallium-Tin at 723K: Choice of an Analytical Representation of Integral and Partial Excess Functions of Mixing”, *Journal de Chimie Physique et de Physico-Chimie Biologique*, 1975, vol. 72, pp. 83-88.

75. M. Hillert and L. I. Staffanson, “The Regular Solution Model for Stoichiometric Phases and Ionic Melts”, *Acta Chemica Scandinavica*, 1970, vol. 24, pp. 3618-3626.

75. B. Sundman and J. Ågren, “A Regular Solution Model for Phases with Several Components and Sublattices, Suitable for Computer Applications”, *Journal of Physics and Chemistry of Solids*, 1981, vol. 42, pp. 297-301.

76. M. Hillert, B. Jansson, B. Sundman and J. Ågren, “ A Two-Sublattice Model for Molten Solutions with Different Tendency for Ionization”, *Metallurgical Transaction A*, 1985, vol.16A, pp. 261-266.

77. J. Y. Choi, B. S. Seong, S. C. Baik and H. C. Lee, “Precipitation and Recrystallization Behavior in Extra Low Carbon Steels”, *ISIJ International*, 2002, vol. 42, pp. 889-893.

78. B. J. Lee, “Thermodynamic Assessment of the Fe-Nb-Ti-C-N System”, *Metallurgical and Materials Transactions A*, 2001, vol. 32, pp. 2423-2439.

79. Y. Sun and T. Bell, “A Numerical Model of Plasma Nitriding of Low Alloy Steels”, *Materials Science and Engineering A*, 1997, vol. 224, pp. 33-47.

80. H. Le Chatelier, “Experimental and Theoretical Research on Chemical Equilibria”, *Annales des Mines et des Carburants*, 1888, vol. 13, pp. 157-382.

81. R. C. Hudd, A. Jones and M. N. Kale, “A Method for Calculating the Solubility and Composition of Carbonitride Precipitates in Steel with Particular Reference to Niobium Carbonitride”, *The Journal of the Iron and Steel Institute*, 1971, vol. 209, pp. 121-125.

82. W. J. Liu and J. J. Jonas, “Calculation of the $Ti(C_yN_{1-y})$-$Ti_4C_2S_2$-MnS-Austenite Equilibrium in Ti-bearing Steels”, *Metallurgical Transactions A*, 1989, vol. 20A, pp. 1361-1374.

83. N. Gao and T. N. Baker, “Influence of AlN Precipitation on Thermodynamic Parameters in C-Al-V-N Microalloyed Steels”, *ISIJ International*, 1997, vol. 37, pp. 596-604.

84. H. Adrian, “Thermodynamic Model for Precipitation of Carbonitrides in High Strength Low Alloy Steels Containing up to Three Microalloying Elements with or without Additions of Aluminium”, *Materials Science and Technology*, 1992, vol. 8, pp. 406-420.

85. P. R. Rios, “Effect of Aluminium on the Equilibrium Precipitation of a Multicomponent F.C.C. Carbonitride in Microalloyed Steels, *Materials Science and engineering A*, 1992, vol. 156, pp. L5-L8.

86. J. Y. Park, J. K. Park and W. Y. Choo, “Effect of Ti Addition on the Potency of MnS for Ferrite Nucleation in C-Mn-V Steels”, *ISIJ International*, 2000, vol. 40, pp. 1253-1259.

87. K. Xu, B. G. Thomas and R. O’Malley, “Equilibrium Model of Precipitation in Microalloyed Steels”, *Metallurgical and Materials Transactions A*, 2011, vol. 42A, pp. 524-539.

88. G. V. Pervushin and H. Suito, “Effect of Primary Deoxidation Products of Al_2O_3, ZrO_2, Ce_2O_3 and MgO on TiN Precipitation in Fe-10mass%Ni Alloy”, *ISIJ International*, 2001, vol. 41, pp. 748-756.

89. K. Nakajima, H. Hasegawa, S. Khumkoa and S. Mizoguchi, “Effect of a Catalyst on Heterogeneous Nucleation in Pure Fe and Fe-Ni Alloys”, *Metallurgical and Materials Transactions B*, 2003, vol. 34B, pp. 539-547.

90. R. L. Clendenen and H. G. Drickamer, “Lattice Parameters of Nine Oxides and Sulfides as a Function of Pressure”, *The Journal of Chemical Physics*, 1966, vol. 44, pp. 4223-4228.

91. J. C. Brick, “The Lattice Constants of a-Quartz”, *Journal of Materials Science*, 1980, vol. 15, pp. 161-167.

92. S. P. Farrell, M. E. Fleet, I. E. Stekhin, A. Kravtsova, A. V. Soldatov and X. Liu, “Evolution of Local Electronic Structure in Alabandite and Niningerite Solid Solutions [(Mn,Fe)S, (Mg,Mn)S, (Mg,Fe)S] Using Sulfur *K*- and *L*-edge XANES Spectroscopy”, *American Mineralogist*, 2002, vol. 87, pp. 1321-1332.

93. M. Hua, C. I. Garcia and A.J. DeArdo, “Multi-Phase Precipitates in Interstitial-Free Steels”, *Scripta Metallurgica et Materialia*, 1993, vol. 28, pp. 973-978.
94. A. V. Kurdyumov, V. L. Solozhenko and W. B. Zelyavski, “Lattice Parameters of Boron Nitride Polymorphous Modifications as a Function of Their Crystal-Structure Perfection”, *Journal of Applied Crystallography*, 1995, vol. 28, pp. 540-545.
95. D. Sundararaman, P. Shankar and V. S. Raghunathan, “Electron Microscopic Study of Cr_2N Formation in Thermally Aged 316LN Austenite Stainless Steels”, *Metallurgical and Materials Transactions A*, 1996, vol. 27A, pp. 1175-1186.
96. “*Steelmaking Data Sourcebook”*, The Japanese Society for the Promotion of Science, The 19th committee on Steelmaking (revised edition), Gordon and Breach Science Publishers, Now York, 1988.
97. T. Binran, “*Iron and Steel Handbook”*, 3rd edition, Edited by ISIJ, Maruzen Co. Ltd., Tokyo, 1981.
98. H. Itoh, M. Hino and S. Ban-ya, “Deoxidation Equilibrium of Magnesium in Liquid Iron”, *ISIJ*, 1997, vol. 83, pp. 623-628.
99. S. Dimitov, A. Weyl and D. Janke, “Control of the Manganese-Oxygen Reaction in Pure Iron Melts”, *Steel Research*, 1995, vol. 66, pp. 87-92.
100. E. T. Turkdogan, “*Fundamental of Steelmaking”*, The institute of Materials, London, England, 1996.
101. K. Inonu, I. Ohnuma, H. Ohtani, K. Ishida and T. Nishizawa, “Solubility Product of TiN in Austenite”, *ISIJ International*, 1998, vol. 38, pp. 991-997.
102. E. T. Turkdogan, S. Ignatowicz and J. Pearson, “The Solubility of Sulphur in Iron and Iron-Manganese Alloys”, *Journal of the Iron and Steel Institute*, 1955, vol. 180, pp. 349-354.
103. J. Yang, K. Okumura, M. Kuwabara and M. Sano, “Behavior of Magnesium in the Desulfurization Process of Molten Iron with Magnesium Vapor Produced in-situ by Aluminothermic Reduction of Magnesium Oxide”, *ISIJ International*, 2002, vol. 42, pp. 685-693.
104. X. Yang, D. Vanderschueren, J. Dilewijns, C. Standaert and Y. Houbaert, “Solubility Products of Titanium Sulphide and Carbosulphide in Ultra-Low Carbon Steels”, *ISIJ International*, 1996, vol. 36, pp. 1286-1294.
105. V. Beta, E. V. Pereloma, “Reply to Comment on “an Alternative Physical Explanation of the Hall-Petch Relation””, *Script Materialia*, 2005, vol. 53, pp. 141-143.

106. M. Hillert and M. Jarl, “A Thermodynamic Analysis of the Iron-Nitrogen System”, *Metallurgical Transactions A*, 1975, vol. 6A, pp. 553-559.

107. S. Ban-ya, J. F. Elliott and J. Chipman, “Thermodynamics of Austenitic Fe-C Alloys”, *Metallurgical Transactions A*, 1970, vol. 1, pp. 1313-1320.

108. W. J. Liu, J. J. Jonas, D. Bouchard and C. W. Bale, “Gibbs Energy of Formation of TiS and $Ti_4C_2S_2$ in Austenite”, *ISIJ International*, 1990, vol. 30, pp. 985-990.

109. V. K. Lakshmanan, “Thermodynamics of the Interstitial Phases of Niobium in Iron Austenite”, *Master Thesis*, McMaster University, Hamilton, 1977.

110. Z. Morita and K. Kunisada, “Solubility of Nitrogen and Equilibrium of Titanium Nitride Forming Reaction in Liquid Fe-Ti Alloys”, *ISIJ*, 1977, vol. 63, pp. 1663-1671.

111. Y. M. Pomarin, G. M. Grigorenko and V. I. Lakomakii, “Solubility of Nitrogen in Liquid Iron Alloys with Vanadium or Niobium”, *Russian Metallurgy*, 1975, no. 5, pp. 61-65.

112. D. B. Evans and R.D. Pehlke, “Equilibria of Nitrogen with Refractory Metals Titanium Zirconium Columbium Vanadium and Tantalum in Liquid Iron”, *Transactions of the TMS of AIME*, 1965, vol. 233, pp. 1620-1624.

113. G. K. Sigworth and J. F. Elliott, “The Thermodynamics of Liquid Dilute Iron Alloys”, *Metal Science*, 1974, vol. 8, pp. 298-310.

114. M. Jarl, “A Thermodynamic Analysis of the Interaction between Nitrogen and Other Alloying Elements in Ferrite and Austenite”, *Scandinavian Journal of Metallurgy*, 1978, vol. 7, pp. 93-101.

115. J. Pak, J. Yoo, Y. Jeong, S. Tae, S. Seo, D. Kim and Y. Lee, “Thermodynamic of Titanium and Nitrogen in Fe-Ni Melt”, *ISIJ International*, 2005, vol. 45, pp. 23-29.

116. D. B. Evans and R.D. Pehlke: “Boron-Nitrogen Equilibrium in Liquid Iron”, *Transactions of the TMS of AIME*, 1964, vol. 230, pp. 1657-1662.

117. R. C. Sharma, V. K. Lakshmanan and J. S. Kirkaldy, “Solubility of Niobium Carbide and Niobium Carbonitride in Alloyed Austenite and Ferrite, *Metallurgical Transactions A*, 1984, vol. 15A, pp. 545-553.

118. T. Wada, H. Wada, J. F. Elliott and J. Chipman, “Thermodynamics of the FCC Fe-Mn-C and Fe-Si-C Alloys”, *Metallurgical Transaction*, 1972, vol. 3, pp. 1657-1667.

119. T. Wada, H. Wada, J. F. Elliott and J. Chipman, “Activity of Carbon and Solubility of Carbides in the FCC Fe-Mo-C, Fe-Cr-C, and Fe-V-C Alloys”, *Metallurgical Transaction*, 1972,

vol. 3, pp. 2865-2872.

120. M. Kishi, R. Inoue and H. Suito, "Thermodynamics of Oxygen and Nitrogen in Liquid Fe-20mass%Cr Alloy Equilibrated with Titanium-based Slags", *ISIJ international*, 1994, vol. 34, pp. 859-867.

121. Y. Guo and C. Wang, "Interaction Coefficients in Fe-C-Ti-i (i=Si, Cr, Al, Ni) Systems", *Metallurgical Transactions B*, 1990, vol. 21B, pp. 543-547

122. Q. Han, *Proc. of 6th International Iron Steel Congress*, vol. 1, *ISIJ*, Tokyo, 1990, pp. 166.

123. Z, Morita, T. Tanaka and T. Yanai, "Equilibria of Nitride Forming Reactions in Liquid Iron Alloys", *Metallurgical and Materials Transactions B*, 1987, vol. 18B, pp. 195-202.

124. Z. Hong, X. Wu and C. Kun, *Steel Research*, 1995, vol. 66, pp. 72-76.

125. S. Jo, B. Song and S. Kim, "Thermodynamics on the Formation of Spinel ($MgO{\cdot}Al_2O_3$) Inclusion in Liquid Iron Containing Chromium", *Metallurgical and Materials Transactions B*, 2002, vol. 33B, pp. 703-709.

126. S. Abraham, R. Klein, R. Bodnar and O. Dremailova, "Formation of Coarse Particles in Steel as Related to Ferroalloy Dissolution Thermodynamics Part II: Crystallographic Study of Ferroalloys and Coarse Particles", *Material Science and Technology (MS&T) Conference*, TMS, Warrendale, PA, 2006, pp. 109-122.

127. R. C. Nunnington and N. Sutcliffe, "The Steelmaking and Casting of Ti Stabilized Stainless Steels", *59th Electric Furnace Conference*, Phoenix, Arizona, 2001.

128. C. Wagner: "*Thermodynamics of Alloys*", Addison-Wesley Publishing Company, Cambridge, MA, 1952, pp. 51-53.

128. J. Chipman, "Thermodynamics of alloy system", *The Journal of the Iron and Steel Institute*, 1955, vol. 180, pp. 97-103.

130. C. H. P. Lupis and J. F. Elliott, "The Microdynamics Behavior of Aluminum Alloys", *Acta Metallurgica*, 1966, vol. 14, pp. 526-531.

131. J. G. Speer, J. R. Michael and S. S. Hansen, "Carbonitride Precipitation in Niobium/Vanadium Microalloyed Steels", *Metallurgical Transaction A*, 1987, vol. 18, pp. 211-222.

132. J. Strid and K. E. Easterling, "On the Solubility and Stability of Complex Carbides and Nitrides in Microalloyed Steels", *Acta Metallurgica*, 1985, vol. 33, pp. 2057-2074.

133. A. J. Craven, K. He. L. A. J. Craven and T. N. Baker, "Complex Heterogeneous

Precipitation in Titanium-Niobium Microalloyed Al-Killed HSLA Steels-I. (Ti,Nb)(C,N) Particles", *Acta Materialia*, 2000, vol. 48, pp. 3857-3868.

134. JMatPro (Materials Property Simulation Package Public Release Version 5.0), Sente Software, Guildford, UK, 2010.

135. S. Zajac and B. Jansson, "Thermodynamics of the Fe-Nb-C-N System and the Solubility of Niobium Carbonitrides in Austenite", *Metallurgical and Materials Transactions B*, 1998, vol. 29B, pp. 163-176.

136. A. O. Kluken and Ø. Grong, "Mechanisms of Inclusion Formation in Al-Ti-Si-Mn Deoxidized Steel Weld Metals", *Metallurgical Transactions A*, 1989, vol. 20A, pp. 1335-1349.

137. K. C. Hsieh, S. S. Babu, J. M. Vitek and S.A. David, "Calculation of Inclusion Formation in Low-Alloy-Steel Weld", *Material Science and Engineering A*, 1996, vol. 215, pp. 84-91.

138. F. Vodopivec, "Technical note: On the Influence of Hot Deformation of Low-Carbon Steel by Rolling on the Precipitation of Aluminium Nitride", *Journal of The Iron and Steel Institute*, 1973, pp. 664-665.

139. J. P. Michel and J. J. Jonas, "Precipitation Kinetics and Solute Strengthening in High Temperature Austenite Containing Al and N", *Acta Metallurgica*, 1981, vol. 29, pp. 513-526.

140. J. S Park, Y. S. Ha, S. J. Lee and Y. K. Lee, "Dissolution and Precipitation Kinetics of Nb(C,N) in Austenite of a Low-Carbon Nb-microalloyed Steel", *Metallurgical and Materials Transactions A*, 2009, vol. 40A, pp. 560-568.

141. W. J. Liu and J. J. Jonas, "Ti(CN) Precipitation in Microalloyed Austenite during Stress Relaxation", *Metallurgical Transactions A*, 1988, vol. 19A, pp. 1415-1424.

142. W. P. Sun, M. Militzer and J. J .Jonas, "Diffusion-Controlled Growth and Coarsening of MnS during Hot Deformation", *Metallurgical Transactions A*, 1992, vol. 23A, pp. 3013-3023.

143. H. C. Kand, S. H. Lee, D. H. Shin, K. J. Leem S. J. Kim and K. S. Lee, "Quantitative Analysis of Precipitation Behavior in Ferrite of V Added Microalloyed Steel", *Material Science Forum*, vols. 449-452, pp. 49-52.

144. H. J. Jun, K. B. Kang and C. G. Park, "Effects of Cooling Rate and Isothermal Holding on the Precipitation Behavior during Continuous Casting of Nb-Ti Bearing HSLA Steels", *Scripta Materials*, 2003, vol. 49, pp. 1081-1086.

145. M. Tsai and Y. Hwang, "Microstructure of Annealed Hot Band in Electrical Steels", *AISTech 2009 Proceeding*, Volume II, pp. 721-728.

146. S. S. Hansen, J. B. V. Sande and M. Cohen, "Niobium Carbonitride Precipitation and Austenite Recrystallization in Hot-Rolled Microalloyed Steels", *Metallurgical Transactions A*, 1980, vol. 11A, pp. 387-402.

147. A. Le Bon, J. R. Venis and C. Rossard, "Recrystallization and Precipitation during Hot working of a Nb-bearing HSLA Steel", *Metal Science*, 1975, vol. 9, pp. 36-40.

148.Y. J. Wang and H. S. Zurob, "The Precipitation of NbC on Dislocations in Austenite", *Applied Physics A*, 2002, vol. 74, pp. S1213-S1215.

149. A. R. Jones, P. R. Howell, B. Ralph, "Quantitative Aspects of Precipitation at Grain Boundaries in an Austenite Stainless Steel", *Journal of Materials Science*, 1976, vol. 11, pp. 1600-1606.

150. M. Mayrhofer, "Dissolution and Separation Kinetics of Aluminum Nitride in Aluminum Killed Steel," *BHM Berg- und Hüttenmännische Monatshefte*, 1975, vol. 120, pp. 312-321.

151. F. A. Khalid and D. V. Edmonds, "Interphase Precipitation on Microalloyed Engineering Steels and Model Alloys", *Material Science and Technology*, 1993, vol. 9, pp. 384-396.

152. A. N. Kolmogorov, "On the Static Theory of Recrystallization of Metals", *Izvestiya Akademii Nauk SSSR, Seriya Fizicheskaya*, 1937, vol. 1, pp. 335-338.

153. W. A. Johnson and R. F. Mehl, "Reaction Kinetics in Progresses of Nucleation and Growth", *Transactions of AIME*, 1939, 135, pp. 416-442.

154. M. Avrami, *Journal of Chemical Physics*, Kinetics of Phase Change I. General Theory 1939, vol.7, pp. 1103-1112; Kinetic of phase change II. Transformation-time Relation for Random Distribution for Nuclei, 1940, vol.8, pp. 212-224; Kinetics of phase change III. Granulation, Phase Change and Microstructure, 1941, 9, pp. 177-183.

155. J. W. Christian, *The Theory of Transformation in Metals and Alloys*, Part I, Pergamon Press, Oxford, 1975, Chapter 12.

156. G. A. Duit, T. M. Hoogendoom et al., Thermec-88, Tokyo, Japan, 1988, vol. 1, pp. 114.

157. D. Crespo and T. Pradell, "Evaluation of Time-Dependent Grain-Size Populations for Nucleation and Growth Kinetics", *Physics Review B*, 1996, vol. 54, pp. 3101-3109.

158. M. Volmer and A. Weber, "Keimbildung in Übersättigten Gebilden", Zeitschrift für Physikalische Chemie, 1926, vol. 119, pp. 277-301 (in Germany).

159. R. Becker, W. Döring, "Kinetische Behandlung der Keimbildung in Übersättigten Dämpfen", Annalen der Physik, 1935, vol. 24, pp. 719-752 (in Germany).

160. Y. B. Zeldovich, “Theory of Formation of a New Phase: Cavitation”, *Journal of Experimental and Theoretical Physics*, 1942, vol. 12, pp.525-538 (in Russian).

161. W. J. Liu and J. J. Jonas, “Characterization of Critical Nucleus/Matrix Interface: Application to Cu-Co Alloys and Microalloyed Austenite”, Materials Science and Technology, 1988, vol. 5, pp. 8-12.

162. J. D. Eshelby, “The Determination of the Elastic Field of an Ellipsoidal Inclusion, and Related Problems”, Proceedings of the Royal Society of London. Series A, *Mathematical and Physical Sciences*, 1957, vol. 241, pp. 376-396.

163. W. J. Liu and J. J. Jonas, “Nucleation Kinetics of Ti Carbonitride in Microalloyed Austenite”, *Metallurgical Transaction A*, 1989, vol. 20A, pp. 689-697.

164. S. H. Park, S. Yue and J. J. Jonas, “Continuous-Cooling-Precipitation Kinetics of Nb(CN) in High-Strength Low-Alloy Steels”, *Metallurgical Transactions A*, 1992, vol. 23A, pp. 1641-1651.

165. B. Dutta and C. M. Sellars, “Effect of Composition and Process Variables on Nb(C,N) Precipitation in Niobium Microalloyed Austenite”, *Materials Science and Technology*, 1987, vol.3, pp. 197-206.

166. C. Zener and J. H. Hollomon, “Effect of Strain Rate upon Plastic Flow of Steel”, *Journal of Applied Physics*, 1944, vol. 15, pp. 22-32.

167. M. J. Whelan, “On the Kinetics of Particles Dissolution”, *Metal Science Journal*, 1969, pp. 95-97.

168. L. M. Cheng, E. B. Hawbolt and T. R. Meadowcroft, “Modeling of Dissolution, Growth and Coarsening of Aluminum Nitride in Low-Carbon Steels”, *Metallurgical and Materials Transactions A*, 2000, vol. 31A, pp. 1907-1916.

169. C. Zener, “Theory of Growth of Spherical Precipitates from Solid Solution”, *Journal of Applied Physics*, 1949, vol. 20, pp. 950-953.

170. J. W. Gibbs, “*On the Equilibrium Heterogeneous Substances*”, Collective works, Longmans, Green & Co., London, 1928.

171. J. J. Thomson, “*Applications of Dynamics to Physics and Chemistry*”, London, MacMillan, 1988.

172. W. Ostwald, *Lehrbruck der allgemeinen Chemie*, 1896, vol. 2, part 1, pp. 444-465, Leipzig, Germany.

173. I. M. Lifshitz and V. V. Slyozov, "The Kinetics of Precipitation from Supersaturated Solid Solutions," *Journal of Physics and Chemistry of Solids*, 1961, vol. 19, pp. 35-50.
174. C. Wagner, "Theorie der Alterung von Niederschlägen Durch Umloesen (Ostwald-Reifung)", *Zeitschrift Zeitschr. Elektrochemie*, 1961, vol. 65, pp. 581-591.
175. W. P. Sun, M. Militzer and J. J. Jonas, "Diffusion-controlled growth and coarsening of MnS during hot deformation", *Metallurgical Transaction A*, 1992, vol. 23A, pp. 3013-3023.
176. H. O. K, "Coarsening of Grain-Boundary Precipitation", *Metallurgical Transactions*, 1971, vol. 2, pp. 2861-2865.
177. A. J. Ardell, "On the Coarsening of Grain boundary Precipitates", *Acta Metallurgica*, 1972, vol. 20, pp. 601-609.
178. J. S. Langer and A.J. Schwartz, "Kinetics of Nucleation in Near-Critical Fluids", *Physical Review A*, 1980, vol. 21, pp. 948-958.
179. R. Kampmann and R. Wagner, "*Decomposition of Alloys*: *the Early Stages*", edited by P. Haasen, V. Gerold, R. Wagner, M. F. Ashby, Pergamon Press, Oxford, United Kingdom, 1984, pp. 91-103.
180. R. Kampmann, H. Eckerlebe and R. Wagner, "Precipitation Kinetics in Metastable Solid Solutions – Theoretical Considerations and Application to Cu-Ti Alloys", *Materials Research Society Symposia Proceedings*, 1987, pp. 525-542.
181. F. Perrard, A. Deschamps and P. Maugis, "Modeling the Precipitation of NbC on Dislocations in α-Fe", *Acta Materialia*, 2007. Vol. 55, pp. 1255-1266.
182. Y. H. Choi, H. C. Shin, C. S. Choi and Y. K. Lee, "Precipitation Kinetics of NbC in Ferrite of a Nb Microalloyed Steel", *Journal De Physique IV*, 2004, vol. 120, pp. 563-570.
183. P. Hassen and R. Wagner, "High-Resolution Microscopy and Early-Stage Precipitation Kinetics", *Metallurgical Transactions A*, 1992, vol. 23A, pp. 1901-1914.
184. J. W. Cahn, "On Spinodal Decomposition", *Acta Metallurgica*, 1961, vol. 9, pp. 795-801.
185. S. M. Allen and J. W. Cahn, "A Microscopic Theory of Domain Wall Motion and Its Experimental Verification in Fe-Al Alloy Domain Growth Kinetics", Journal De Physique, 1977, vol. 38, pp. C7-51.
186. L, Onsager, "Reciprocal Relations in Irreversible Process. I.", *Physical Review*, 1931, vol. 37, pp. 405-426.

187. L, Onsager, “Reciprocal Relations in Irreversible Process. II.”, *Physical Review*, 1931, vol. 38, pp. 2265-2279.

188. J. A. Barbu and E. Clouet, “Cluster Dynamics Modeling of materials: Advantages and Limitations”, *Solid State Phenomena*, 2007, vol. 127, pp. 51-58.

189. M. Smoluchowski, “Versuch einer Mathematischen Theorie der Koagulationskinetic Kolloider Losungen”, *Zeitschrift für Physikalische Chemie*, 1917, vol. 92, pp. 129-168.

190. L. Kampmann and M. Kahlweit, “On the Theory of Precipitation II”, *Berichte der Bunsen-Gesellschaft Physikalische Chemie*, 1970, vol. 74, pp. 456-462.

191. P. G. Saffman and J. S. Turner, “On the Collision of Drops in Turbulent Clouds”, *Journal of Fluid Mechanics*, 1956, vol. 1, pp. 16-30.

192. U. Lindborg and K. Torssell, “A Collision Model for the Growth and Separation of Deoxidation Products”, *Transactions of Metallurgical Society of AIME*, 1968, vol. 242, pp. 94-102.

193. S. K. Friedlander and C. S. Wang, “The Self-Preserving Particles Size Distribution for Coagulation by Brownian Motion”, *Journal of Colloid and Interface Science*, 1966, vol. 22, pp. 126-32.

194. V. G. Levich, “*Physicochemical hydrodynamics*”, Prentice-Hall, Inc., Englewood Cliffs, NJ, 1962, pp. 213-219.

195. J. Zhang and H. Lee, “Numerical Modeling of Nucleation and Growth of Inclusions in Molten Steel Based on Mean Processing Parameters”, *ISIJ International*, 2004, vol. 44, pp. 1629-1638.

196. Y. J. Kwon, J. Zhang and H. G. Lee, “A CFD-Based Nucleation-Growth-Removal Model for Inclusion Behavior in a Gas-Agitated Ladle during Molten Steel Deoxidation”, *ISIJ International*, 2008, vol. 48, pp. 891-900.

197. H. Oikawa, “Lattice Diffusion in Iron-a Review”, *ISIJ*, 1982, vol. 68, pp. 1489-1497.

198. J. Geise and C. Herzig, “Lattice and Grain Boundary Diffusion of Niobium in Iron”, *Zeitschrift für Metallkunde*, 1985, vol. 76, pp. 622-626.

199. J. Takada, S. Yamamoto, S. Kikuchi and M. Adachi, “Determination of Diffusion Coefficient of Oxygen in γ-iron from Measurements of Internal Oxidation in Fe-Al Alloys”, *Metallurgical Transactions A*, 1986, vol. 17A, pp. 221-229.

200. J. Takada and M. Adachi, "Determination of Diffusion Coefficient of Oxygen in α-iron from Internal Oxidation Measurements in Fe-Si Alloys", *Journal of Materials Science*, 1986, vol. 21, pp. 2133-2137.

201. *Metals Handbook*, 8th edition, edited by T. Lyman, H. E. Boyer, W. J. Carnes and N. W. Chevalier, ASM, Metal Park, OH, 1973.

202. *Tekko-Binran (Handbook for Iron and Steel)*, 3rd edition, ISIJ, Maruzen, Tokyo, 1981, vol. 1, pp. 193-194.

203. N. Zhang and Z. C. Zheng, "A Collision Model for a Large Number of Particles with Significantly Different Sizes", *Journal of Physics D: Applied Physics*, 2007, vol. 40, pp. 2603-2612.

204. Y. Miki, B. G. Thomas, A. Denissov and Y. Shimada, "Model of Inclusion Removal during RH Degassing of Steel", *Iron and Steelmaker*, 1997, vol. 24, pp. 31-38.

205. Y. Miki and B. G. Thomas, "Modeling of Inclusion Removal in a Tundish", *Metallurgical and Materials Transactions B*, 1999, vol. 30B, pp. 639-654.

206. L. Zhang, S. Tanighchi and K. Cai, "Fluid Flow and Inclusion Removal in Continuous Casting Tundishes", *Metallurgical and Materials Transactions B*, 2000, vol. 31B, pp. 253-266.

207. D. Sheng, M. Söder, P. Jönsson and L. Jonsson, "Modeling Micro-inclusion Growth and Separation in Gas-stirred Ladles", *Scandinavian Journal of Metallurgy*, 2002, vol. 31, pp. 134-147.

208. M. Hallberg, P. G. Jönsson, T. L. I. Jonsson and R. Eriksson, "Process Model of Inclusion Separation in a Stirred Steel Ladle", *Scandinavian Journal of Metallurgy*, 2005, vol. 34, pp. 41-56.

209. T. Nakaoka, S. Taniguchi, K. Matsumoto and S. T. Johansen, "Particle-Size-Grouping Method of Inclusion Agglomeration and its Application to Water Model Experiments", *ISIJ International*, 2001, vol. 41, pp. 1103-1111.

210. L. Zhang and W. Pluschkell, "Nucleation and Growth Kinetics of Inclusions during Liquid Steel Deoxidation", *Ironmaking and Steelmaking*, 2003, vol. 30, pp. 106-110.

211. F. Gelbard, Y. Tambour and J. H. Seinfeld, "Sectional Representations for Simulating Aerosol Dynamics", *Journal of Colloid and Interface Science*, 1980, vol. 76, pp. 541-556.

212. J. J. Wu and R. C. Flagan, "A Discrete-sectional Solution to the Aerosol Dynamic Equation", *Journal of Colloid and interface Science*, 1988, vol. 123, pp. 339-352.

213. K. Xu and B. G. Thomas, "Particle-Size-Grouping Model of Precipitation Kinetics in Microalloyed Steels", *Metallurgical and Materials Transactions A*, 2012, vol. 43A, pp. 1079-1096.

214. H. Tozawa, Y. Kato, K. Sorimachi and T. Nakanishi, "Agglomeration and Flotation of Alumina Cluster in Molten Steel", *ISIJ International*, 1999, vol. 39, pp. 426-434.

215. K. Higashitani, Y. Yamauchi, Y. Matsuno and G. Hosokawa, *Journal of Chemical Engineering of Japan*, 1983, 116, pp. 299-304.

216. W. C. Leslie, R. L. Rickett, C. L. Dotson and C. S. Walton, "Solution and Precipitation of Aluminum Nitride in Relation to the Structure of Low-Carbon Steel", *Transactions of the American Society for Metals,* 1954, vol. 46, pp. 1470-1499.

217. F. G. Wilson and T. Gladman, "Aluminium Nitride in Steel", *International Materials Review*, 1988, vol. 33, pp. 221-286.

218. R. Radis and E. Kozeschnik, "Precipitation Kinetics of Aluminum Nitride in Austenite in Microalloyed HSLA Steels", *Materials Science Forum*, 2010, vol. 636-637, pp. 605-611.

219. R. Radis and E. Kozeschnik, "Kinetics of AlN Precipitation in Microalloyed Steel", *Modelling and Simulation in Materials Science and Engineering*, 2010, vol. 18, 055003.

220. F. Perrard, A. Deschamps, F. Bley, P. Donnadieu and P. Maugis, "A Small-Angle Neutron Scattering Study of Fine-Scale NbC Precipitation Kinetics in the α-Fe-Nb-C System", *Journal of Applied Crystallography*, 2006, vol. 39, pp. 473-482.

221. E. K. Strorms and N. H. Krikorian, "The Niobium-Niobium Carbide System", *The Journal of Physical Chemistry*, 1960, vol. 64, pp. 1471-1477.

222. S. M. He, N. H. Van Dijk, M. Paladugu, H. Schut, J. Kohlbrecher, F. D. Tichelaar and S. Van der Zwaag, "In situ Determination of Aging Precipitation in Deformed Fe-Cu and Fe-Cu-B-N Alloys by Time-Resolved Small-Angle Neutron Scattering", Physical Review B, 2010, vol. 82, 174111.

223. N. Fujita and H. K. D. H. Bhadeshia, "Modeling Precipitation of Niobium Carbide in Austenite: Multicomponent Diffusion, Capillarity, and Coarsening", *Materials Science and Technology*, 2001, vol. 17, pp. 403-408.

224. J. D. Robson, "Modelling the Overlap of Nucleation, Growth and Coarsening during Precipitation", *Acta Materialia*, 2004, vol. 52, pp. 4669-4676.

225. T. Sourmail and H. K. D. H. Bhadeshia, “Modelling Simultaneous Precipitation Reactions in Austenite Stainless Steels”, *Computer Coupling of Phase Diagrams and Thermochemistry*, 2003, vol. 27, pp. 169-175.

226. M. Perez and A. Deschamps, “Microscopic Modelling of Simultaneous Two-Phase Precipitation: Application to Carbide Precipitation in Low-Carbon Steels”, Materials Science and Engineering A, 2003, vol. 360, pp. 214-219.

227. P. Shi, A. Engström, B. Sundman and J. Ågren, “Thermodynamic Calculations and Kinetic Simulations of Some Advanced Materials”, *Materials Science Forum*, 2011, vol. 675-677, pp. 961-974.

228. N. Zhu, Y. He, W. Liu, L. Li, S. Huang, J. Vleugels and O. Van der Biest, “Modeling of Nucleation and Growth of $M_{23}C_6$ Carbide in Multi-component Fe-Based Alloy”, *Journal of Materials Science and Technology*, 2011, vol. 27, pp. 725-728.

229. I. Steimbach and F. Pezzolla, “A Generalized Field Method for Multiphase Transformations Using Interface Fields”, *Physica D*, 1999, vol. 134, pp. 385-393.

230. M. S. Park and R Arróyave, “Concurrent Nucleation, Formation and Growth of Two Intermetallic Compounds (Cu_6Sn_5 and Cu_3Sn) during the Early Stages of Lead-Free Soldering”, *Acta Materialia*, 2012, vol. 60, pp. 923-934.

231. R. Radis and E. Kozeschnik, “Concurrent Precipitation of AlN and VN in Microalloyed Steel”, *Steel Research International*, 2010, vol. 81, pp. 681-685.

232. M. Hillert, “On the Theory of Normal and Abnormal Grain Growth”, *Acta Metallurgica*, 1965, vol. 13, pp. 227-238.

233. P. R. Rios and M. E. Glicksman, “Topological Theory of Abnormal Grain Growth”, *Acta Materialia*, 2006, vol. 54, pp. 5313-5321.

234. V. Randle and D. Horton, Grain Growth Phenomena in Nickel, *Scripta Metallurgica et Materialia*, 1994, vol. 31, pp. 891-895.

235. H. V. Atkinson, “Theories of Normal Grain Growth in Pure Single Phase Systems”, *Acta Metallurgica*, 1988, vol. 36, pp. 469-491.

236. G. T. Higgins, “Grain Boundary Migration and Grain Growth”, *Metal Science*, 1974, vol. 8, pp. 143-150.

237. H. V. Atkinson, “Theories of Normal Grain Growth in Pure Single Phase System”, *Acta Metallurgica*, 1988, vol.36, 469-491.

238. R. L. Fullman, “Boundary Migration during Grain Growth”, *Metal Interface*, American Society for Metals, Cleveland, 1952, pp. 179-207.

239. T. Gladman and F. B. Pickering, “Grain-Coarsening of Austenite”, *Journal of the Iron and Steel Institute*, 1967, vol. 205, pp. 653-664.

240. P. A. Manohar, M. Ferry and T. Chandra, “Five Decades of the Zener Equation”, *ISIJ International*, 1998, vol. 38, pp. 913-924.

241. Y. Liu and B. R. Patterson, “Particle Volume Fraction Dependence in Zener Drag”, *Scripta Metallurgica et Materialia*, 1993, vol. 29, pp. 1101-1106.

242. I. Andersen and Ø. Grong, “Analytical Modeling of Grain Growth in Metals and Alloys in the Presence of Growing and Dissolving Precipitates –I. Normal Grain Growth”, *Acta Metallurgica Materialia*, 1995, vol. 43, pp. 2673-2688.

243. G. Abbruzzese, “Computer Simulated Grain Growth Stagnation”, *Acta Metallurgica*, 1985, vol. 33, pp. 1329-1337.

244. G. Abbruzzese and K. Lücke, “A Theory of Texture Controlled Grain Growth – I. Derivation and General Discussion of the Model”, *Acta Metallurgica*, 1986, vol. 34, pp. 905-914.

245. E. Bealy, B. G. Thomas, “Prediction of Dendrite Arm Spacing for Low Alloy Steel Casting Processes”, *Metallurgical and Materials Transactions B*, 1996, vol. 27B, pp. 689-693.

246. J. Reiter, C. Bernhard and H Presslinger, “Determination and Prediction of Austenite Grain Size in Relation to Product Quality of the Continuous Casting Process”, *Materials Science & Technology (MS&T 06)*, Cincinnati, USA, 2006, pp. 805-816.

247. M. M. Wolf, “History of Continuous Casting”, *Steelmaking Conference Proceedings*, 1992, vol. 75, Iron & Steel Society, Warrendale, PA, pp. 83-137.

248. A .Grill, J. K. Brimbacombe and F. Weinberg, “Mathematical Analysis of Stresses in Continuous Casting of Steels”, *Ironmaking and Steelmaking*, 1976, vol. 3, pp. 38-47.

249. C. A. Muojekwu, D. Q. Lin I. V. Samarasekera and J. K. Brimacombe, “Thermomechanical History of Steel Strip during Hot Rolling – A Comparison of Conventional Cold-Charge Rolling and Hot-Direct Rolling of Thin Slabs”, *37th NMSP Conference Proceedings*, Warrendale, PA, ISS, 1996, vol. 33, pp. 617-633.

250. M. S. Dyer, J. G. Speer, D. K. Matlock, A. J. Shutts, S. Jansto, K. Xu and B. G. Thomas, “Microalloy Precipitation in Hot Charged Slabs,” *Iron and Steel Technology*, 2010, October, pp. 96-105.

251.M. S. Dyer, “Study of Microalloy Precipitation in Hot Charged Slabs,” *M. S. thesis*, Colorado School of Mines, Golden, CO, 2010.

252. Y. Meng and B. G. Thomas, “Heat Transfer and Solidification Model of Continuous Slab Casting: CON1D”, *Metallurgical and Materials Transactions B*, 2003, vol. 34B, pp. 685-705.

253. B. Petrus, K. Zheng, X. Zhou, B. G. Thomas and J. Bentsman, “Real-time Model-based Spray-cooling Control System for Steel Continuous Casting”, *Metallurgical and Materials Transactions B*, 2011, Vol. 42B, pp. 87-103.

254. Y. M. Won and B. G. Thomas, “Simple Model of Microsegregation during Solidification of Steels”, *Metallurgical and Materials Transactions A*, 2001, vol. 32A, pp. 1755-1767.

255. K. Xu, B. G. Thomas, M. S. Dyer, J. G. Speer, D. K. Matlock, “Model of Microalloy Precipitation during Continuous Casting and Reheating”, *Iron and Steel Technology*, 2011, October, pp. 59-68.

256. W. Roberts, “Deformation, Processing and Structure”, 1982, Metal Park, OH, American Society of Metals, pp. 109-180.

257. W. T. Landford, “Some Considerations of Strength and Ductility in the Continuous Casting Process”, *Metallurgical Transactions*, 1972, vol. 3, pp. 1331-1357.

258. D. Turnbull, “Role of Structural Impurities in Phase Transformations”, *Impurities and imperfections*, Seminar Proceedings, American Society for Metals, Cleveland, OH, 1955, pp. 121-144.

259. J. H. Van Der Merwe, “Crystal Interfaces, Part I. Semi-Infinite Crystals”, *Journal of Applied Physics*, 1963, vol. 34, pp. 117-122.

260. R. G. Baker and J. Nutting: “Precipitation Process in Steels”, *Special Report No*. *64*, 1959, The Iron and Steel Institute, London, 1959, pp. 1–22.

261. H. Shoji, “Geometric Relationship between the Structures of the Modifications of a Substance”, *Zeitschrift fuer Kristallographie, Kristallgeometrie, Kristallphysik, Kristallchemie,* 1931, vol. 77, pp. 381-410.

262. Z. Nishiyama, *Science Report*, Tohoku Imperial University, 1936, 1st Ser. **25**, pp. 79.

263. W. G. Burgers: “On the Process of Transition of the Cubic-Body-Centered Modification into the Hexagonal-Close-Packed Modification of Zirconium”, *Physica*, 1934, vol. 1, pp. 561–586.

264. H. J. Frost and M.F. Ashby: "*Deformation-Mechanism Maps",* Pergamon Press, Oxford, United Kingdom, 1982, pp. 20-70.
265. L. R. Zhao, K. Chen, Q. Yang, J. R. Rodgers and S.H. Chiou, "Materials Informatics for the Design of Novel Coating", *Surface and Coating Technology*, 2005, vol. 200, pp. 1595-1599.
266. J. O. Kim and J. D. Achenbach, P. B. Mirkarimi, M. Shinn and S. A. Barnett, "Elastic Constants of Single-Crystal Transition-Metal Nitride Films Measured by Line-Focus Acoustic Microscopy", *Journal of Applied Physics*, 1992, vol. 72, pp. 1805-1811.
267. B. Morosin, "Exchange Striction Effects in MnO and MnS", *Physical Review B*, vol.1, 1970, pp. 236-243.
268. L. E. Toth, "*Transaction Metal Carbides and Nitrides*", Academic Press, New York, 1971.
269. Chase, M.W., Jr., "*NIST-JANAF Thermochemical Tables"*, Fourth Edition, *J. Phys. Chem. Ref. Data*, Monograph 9, 1998, pp. 1-1951.
270. D. V. Vechten and J. F. Liebman, "Consideration on the Selection of Artificial Tunneling Barriers", *The Journal of Vacuum Science and Technology A*, 1985, vol. 3, pp. 1881-1883.
271. E. G. King, "High Temperature Heat Contents of Vanadium Carbide and Vanadium Nitride", *Journal of the American Chemical Society*, 1949, vol. 71, pp. 316–317.
272. C. J. Smithells and E. A. Brandes, "*Metals Reference Book*", 5th edition, Butterworth's, London, 1978, vol. 1, pp. 115-177, 186-241.